METEOROLOGICAL STUDIES USING A VHF RADAR

By

Deepak K. Rajopadhyaya, M.Sc. (Nepal)

THESIS SUBMITTED FOR THE DEGREE OF

DOCTOR OF PHILOSOPHY

IN

THE UNIVERSITY OF ADELAIDE

(FACULTY OF SCIENCE)

(DEPARTMENT OF PHYSICS AND MATHEMATICAL PHYSICS)

March 1994

Preface

This work contains no material which has been accepted for the award of any other degree or diploma in any university or other tertiary institution and, to the best of my knowledge and belief, contains no material previously published or written by another person, except where due reference has been made in the text.

I give consent to this copy of my thesis, when deposited in the University Library, being available for loan and photocopying.

Deepak K. Rajopadhyaya, M.Sc.

Signed: [signature]

Date: 31·3·94

Abstract

Measurements of size distributions of hydrometeors are very important in the study of cloud micro-physics and for the improvement of radar estimates of rainfall intensities. Many experiments have been carried out in the past to develop instruments to measure the size distributions of these precipitation particles on the ground. In past decades, size distributions have been determined *in situ* by aircraft measurements, but the challenge is to measure the size distributions using remote sensing. The recent development of ground-based wind-profiler radars provides a potentially powerful tool for remotely determining size distributions of hydrometeors. This is because, with the help of vertically pointing Doppler radar, we can directly determine the fall-velocity spectrum of the hydrometeors. If the velocity can be related to the size of the falling droplets then the size distributions can be estimated using Doppler radar.

Accordingly, a technique is described which allows raindrop and ice particle size distributions to be obtained from the Doppler spectra measured by wind profiling radars. To test the accuracy of the statistical reliability, artificial data with realistic statistical properties have been generated. The method makes no *a priori* assumptions regarding the shape of the dropsize distributions. The analysis technique obtains an accuracy of around 10% in

the dropsize range between 1 and 4 mm, for data consistent with typical 50 MHz observations averaged over 5-10 minutes. There are limitations outside this range and the physical reasons for these are discussed. Simulations with multiple peaked distributions show that the technique can resolve complicated distributions well.

To estimate the ice particle size distributions, it has been assumed that the size distribution of the ice particles is exponential. It is also assumed that there are a small number of ice types present, such as aggregates of dendrites, and aggregates of plates and bullets form the bulk of the ice content in the precipitation. This simplifying assumption is needed to make the retrieval problem tractable, because the solution will not be stable if the number of parameters to be estimated is large. The simulation results showed that the size distribution can be well recovered for a wide range of exponential slopes corresponding to a wide range of rainfall rates.

A 50 MHz wind profiler located near Darwin (12.4°S and 130.9°E) is used to study the vertical motions and the precipitation structure in the convective, moat and stratiform regions of the two deep convective tropical squall lines that passed over Darwin on December 5, 1989 and Jan 12, 1990. The high temporal resolution data (90sec) shows a strong updraught below 4 km associated with warm rain processes in the leading cells. This is followed by convective downdraughts and a mature cell with weak vertical motion below 4 km, and glaciation producing a strong acceleration above 7 km. The moat region shows descent throughout the depth of the storm. The stratiform region shows the classic mesoscale up and downdraughts, with the cross-over about 1-2 km above the freezing level.

The cloud microphysical structure of the trailing stratiform region shows considerable detail. A distinct double peaked rain dropsize distribution (peaks at about 0.5 mm and 1.5 mm) is occasionally observed. There are considerable changes with time and height. The

ice particles size distributions showed that the median volume diameter varied from 0.35 to 2.17 mm. A considerable increase in size is associated with aggregation. The water content above the freezing level drops off with height. More than half of the liquid water content evaporates while descending from 3.5 to 1.3 km in the stratiform and moat regions. These changes have important implications in mesoscale circulation.

Acknowledgements

This work has been carried out under the supervision of Dr. Robert. A. Vincent and Dr. Peter T. May. Preparation of this thesis would have been almost impossible without their continuous encouragement and helpful discussion. Words cannot express my gratitude to them.

I also thank Dr.I.M.Reid, Dr.G.Elford and Dr.S.D.Eckermann for helping me at all times throughout the period of my project. I am also grateful to the late Dr.B.H.Briggs and to Dr.W.K.Hocking for their constructive comments during the initial stages of the project.

I am indebted to the Bureau of Meteorology Research Centre, Melbourne, for providing me with financial support for travel to Darwin and Melbourne and for supplying me with necessary data. Thanks are also extended to Manuel, Dugg, Brenton, Marwenna, and Alex for collecting data at the Buckland Park field station.

The continuous help of Trevor (Dr.Harris) in fixing software problems and helping in the use of IDL procedures is greatly appreciated. Thanks to Brenton (Dr.Vandepeer) for taking Trevor's place after his departure from our group.

The most tedious part of the "proof-reading" has been done by Dr. Campbell, who suggested improvements to my English in the first draft and finally Lyn helped me to give final shape of my whole thesis. From time to time Dallas and Lyn also helped me a lot.

This thesis itself will remind me about their excellent contribution to my life.

Without occasional relaxation, it is almost impossible to make significant progress in life, so I express my sincere appreciation to those who spent their valuable time with me. Thankyou to Shane (Stictly non-veg), Mike (Dancer), Brian (Slippy Lizard), Manners (Ticklish), Holdsworth (Tough guy), Steve (Tee-totaller) and lovely Lesley (Hair puller) for dragging me to the staff club, teaching me Australian slang and swear words, and playing pool and darts with me. Well done guys. Keep it up. Whoa! I almost forgot about Simon, whose office and punctuality reminded me to clean my table and not to be like a night owl. What about Ali, who always offered me something to eat when I was hungry? Another deserving of thanks is Damian (Dr. Murphy) who helped me at all times and gave me valuable driving lessons. I should not forget Laurence who helped me a lot and often told me to get on with my thesis. Thanks to Kong, Dorothy, Bridget, Young Scotty, Karen, Hon and others for their encouragement.

Special thanks go to Dr.Lesicar (big man) for pushing me to have my "crossed-eyes" operation, Dr.Murchland for operating on my eyes and John and Lyn Birchby for looking after me after these operations. My eyes will remind me of you all for ever. Whenever I needed encouragement, almost every day, I would talk to Dallas and Lesley. Their willingness to make me happy cannot be forgotten.

I should mention my brother Rupak, sisters Amsuka, Rashmi and Srijana, uncles Bahart, Ram and Krishna, and my father-in-law Herambananda and mother-in-law Subhadra for sending me encouraging letters from Nepal throughout the period of my study. My other close relatives and friends (Medini, Ganesh, Bishnu, Sajani, Yamuna, Manjari, Rebati, Prachan, Sriniwas, Sarad, Byapak, Raju, Rajeeb, Nil, Sri, Surhid, Hom, Pratap, Tulshi and their families) helped me to keep up my Nepalese language by sending me greeting cards,

jokes, letters, Nepalese news and so on. I salute my lovely Mum who could not wait for me to return to Nepal, but went to join with my lovely late Dad's soul somewhere far from this world. I pray that they are at peace.

Finally, what can I say to Laxmi (my wife), and Kanchani and Brajesh (my kids), who did not see me very much throughout the period of my study. I did not fulfill my duty as husband and father. I hope they will understand me as a crazy scientiest. Anyway, at least other people, such as Suzi, John, Lyn, Kathy, George, Malcolm, Dallas, Liz, Bickram, Himadari, Manandhar, Kus, Rakesh and Archana, tried to make them happy. Deepest appreciation to Paul (a half Nepalese and devoted guy), who went to pick up my kids almost everyday to take them around Adelaide. Thanks to all of you on their behalf.

This work has been supported by an Overseas Postgraduate Research Scholarship, University of Adelaide Scholarship and Australian Research Grant.

Contents

List of Figures

Chapter 1

Introduction

1.1 Early history

Radar (Radio detection and ranging) uses radio waves for the detection and location of material objects. When propagating waves meet an object in their path, the waves are scattered. By analysing these scattered waves, the range and approximate size of the object can be determined. Radar was developed for military purposes during World War II but since then its application has been extended widely to other areas of human activity and now radar is an essential tool in our daily life. Because of this, it is worthwhile presenting a short history of the use of radar.

We have five senses, hearing, sight, touch, smell and taste. However, there are other phenomena in nature (e.g. electric and magnetic fields) which our senses cannot detect directly. For this reason, electromagnetic waves were not discovered until the nineteenth century, when in 1886 Heinrich Hertz of Germany found experimental evidence for the existence of electromagnetic waves (in this case, radio waves). Following this, extensive research on the use of radio waves in communication was carried out, with a breakthrough by

Marconi in 1901. While he was in Scotland, he was able to detect radio signals transmitted from the other side of the Atlantic (about 5000 Km away). This successful demonstration is regarded as the beginning of the use of the ionosphere in communication. However, there is no evidence that Marconi himself understood that the ionosphere was playing a major role in reflecting the radio signals in his experiment. Also, being unaware of electromagnetic pulse theory, he used a very long wavelength in his experiment. Since then the trend has been towards the use of shorter wavelengths, which can propagate in narrow beams, allowing more reliable systems of communication.

In 1912, Eccles made an attempt to explain quantitatively the role of ionospheric plasma in the propagation of electromagnetic waves. In 1922, Marconi suggested the possibility of using radio waves to detect metallic conductors. In 1924, Larmor observed that radio waves incident obliquely on the ionosphere were reflected back to the surface of the Earth. This was explained by the ionospheric plasma having a dielectric constant less than unity and consequently refracting the waves in the direction of increasing density, thus giving experimental evidence for the existence of a conducting layer in the upper atmosphere. Shortly after Larmor's discovery, Appleton and Barnett measured the height of the reflecting layer (*ie* the ionosphere) by using radio waves.

In 1926 Breit and Tuve published details of the pulse technique, based on amplitude modulation theory, which then became the standard technique for radio soundings of the ionosphere (Beynon, 1975). Around 1930, Eckersley in the UK and Mogel in Germany observed weak echoes from irregularities in the ionosphere but were unable to explain their observations. The first reported detection of radio waves scattered by aircraft in flight was in 1930 in the United States and in 1932 by British Post Office engineers. The engineers

thought that it was due mainly to interference phenomena and did not consider the scattering of radio waves from aircraft. About the same time Marconi used radio waves of one centimeter wavelength and detected the scattering by material objects. These pioneering experiments led to the development of various types of radar.

Thus many people were involved in the development of radar and no one person can be identified as the inventor of radar, but rather the credit is shared by scientists of the United Kingdom and the United States. The work done before 1940 in each of these countries was completely independent. Early work also has been reported in Germany, France, Italy and other countries. For this reason, the early name of radar is different in different countries, such as RDF (Radio Direction Finding) in the UK, REE (Radio Echo Equipment) in the USA, RDT (Radio Detector Telimetro) in Italy, DEM (Detection Elecromagnetique) in France and so on. The word "RADAR" was first suggested in the USA in 1940 (Swords 1986) and since then it has been widely accepted.

1.2 Radar Frequencies

The practical development of pulse radar began in the USA and UK in the early 1930s. The initial choice of frequency was 6 MHZ, corresponding to a wavelength of 50 m. In the mid-1930s the wavelengths generally varied from 1.5 to 6 m (*ie* frequencies of 50-200 MHz). The trend to higher frequencies allowed a wider range of applications. By 1939, frequencies up to 600 MHz (*ie* 50 cm in wavelength) were in use and during World War II the radars used shorter wavelengths in the microwave region, which includes the frequency range 300 MHz - 30 GHz. The respective wavelengths are 1 m and 1 cm. The range of frequencies used by radar is divided into a number of bands and are presented in table 1.

Table 1: Radar Bands and their frequencies.

Band Code	Frequencies	Wavelength (cm)
Medium (MF)	0.3 - 3 MHz	1000 - 100 m
High (HF)	3 - 30 MHz	100 - 10 m
Very High (VHF)	30-300 MHz	10 - 1 m
Ultra High (UHF)	300 MHz -3 GHz	1m - 10 cm
Super High (SHF)	3 - 30 GHz	10 - 1 cm
Extra High (EHF)	30 GHz and above	1 cm and less

There are limits on the radar frequencies which we can use in practice, such as a lower limit of ~0.1 MHz, because, for smaller frequencies the wavelength would be much larger than the object to be identified and hence it would be difficult to get useful information about the object. The upper limit is due to the technical difficulties involved in producing very high frequencies. To get high resolution, it is essential to operate radars at very high frequency. After World War II, because of the continuous development of technology, very high frequency radars were installed. During the 1960s some experimental radars were operated at 70 GHz and now radars up to 10,000 GHz are used in satellite applications. Another big advantage in using a very high frequency radar is to produce a very narrow beam width. However, care should be taken in using higher frequncies because there may be a loss of signal strength due to atmospheric absorption. Today radars are used in navigation, air-traffic control, location of mineral resources, cartography, transportation, agriculture, land erosion, atmospheric research and so on. But the selection of the operational frequency of a radar depends upon the type of detection to be done. For example, in atmospheric research Doppler radars operated in the VHF and UHF bands, cms radars and mm radars

(to study non-precipitating clouds) have been used. This aspect is further discussed in the following sections. Newly developed laser ceilometers and lidars are also used to study cloud heights and other related cloud properties.

1.3 Radars in Weather Forecasting

In the early stages of the development of radar, it was widely used by the military. After World War II, radars were used in many applications on land, at sea, and in the air. During World War II, it has been reported that the radio waves transmitted by the microwave radars designed for locating distant ships, airplanes and submarines were often affected by the existence of weather "clutter". Subsequently it was found that the effect is due to the scattering of radio signals by hydrometeors. It was also found that by analysing the scattered echo, deduction of the size, shape, motion and thermodynamic behaviour of the hydrometeors is possible. This led to extensive use of these microwave radars in Meteorological research.

With the advent of radar, there was a new impetus to the study of atmospheric science. While it is still almost impossible to predict the weather, a significant advance in weather radar has come with the application of the Doppler principle to determine the full three-dimensional velocity field in regions of precipitation. The displacement in frequency of the received echo relative to the transmitted frequency is directly proportional to the component of the velocity of the precipitation toward the radar. Thus by scanning the radar in azimuth and elevation, a full three-dimensional plot of the radial component of velocity can be obtained.

1.3.1 MST\ST radars

MST radars are Doppler radars operating in the VHF or UHF bands to obtain the backscattered signal from the middle atmosphere (10-110 km height level). Here M, S, and T stand for Mesosphere, Stratosphere and Troposphere, respectively.

In the mid-1950s radars were built for ionospheric research in the Mesosphere operating in the very-high-frequency regions, such as the UHF and VHF bands. For example, the first observations of ionospheric scatter in the 75-90 km height range using VHF signals were reported by Bailey et al. (1952) and later by Villars and Weisskopf (1955), Bowles (1958) and Flock and Balsley (1967). In the same way, LaLonde (1966) recorded D-region echoes using UHF signals. These echoes are due to scattering by turbulent irregularities which are present in the gradient in electron density. Since then, extensive studies of scattering of radio waves in the VHF and UHF bands have been carried out, and in 1974 Woodman suggested the possibility of using VHF radars to determine wind velocities in the mesosphere. Woodman's work led to the wide application of VHF and UHF signals in the study of atmospheric dynamics, not only in the mesosphere but also in the troposphere and stratosphere.

These MST\ST radars operate in Doppler mode, with atmospheric dynamics investigated by recording both the amplitude and phase of the reflected signal. The radial velocity of the scattering medium can then be determined from the Doppler shifted power spectrum of the returned signal, using narrow off-vertical beams.

Later Rottger and Vincent (1978) presented evidence that VHF reflections can be used to determine horizontal wind velocities in the troposphere by spaced-antenna techniques (Briggs, 1968). In spaced-antenna techniques, two-dimensional (*ie* horizontal) wind velocities can be obtained from the movement of the diffraction pattern observed on the ground,

using a "full-correlation" analysis.

1.3.2 *Weather* radar

Weather radars are operated in the SHF band and are called "Centimetre Radars" because their wavelength is of the order of centimetres (see table 1). These are also operated in Doppler mode and they generally measure the radial speed of the hydrometeors rather than of the air. The observed echoes are composites of signals from a very large number of hydrometeors, each of which acts as a point target except for very large particles, such as hail, or for mm wavelength radars where the particles size $\sim \lambda$. The displacement in frequency of the received echo relative to the transmitted frequency is directly proportional to the component of the velocity of the precipitation toward the radar. Thus by scanning the radar in azimuth and elevation, a full three-dimensional plot of the velocity field can be obtained, provided there are suitable targets (hydrometeors) for backscatter in the region of interest. These radars can cover a wide horizontal area of up to several hundred kilometers radius. These weather radars are used extensively in studying fronts, squall lines and storms. Their capacity to map the reflectivity and the mean radial velocity inside the storm shield of clouds, with good height and spatial resolution, can be used for the early warning of the possibility of severe damage.

In a real sense there is not much difference in principle between MST\ST and Weather radar. The latter is limited to the troposphere whereas MST\ST radars are useful up to 100 km or more. In MST radars the frequency has been chosen so that it is more sensitive to clear-air echoes, whereas weather radar is more sensitive to precipitation particles. For this reason, these two types of radars produce quite different results, even though the same principle is applied in detecting echoes. However, it has been suggested that a powerful

weather radar can detect even clear-air echoes (Doviak and Zrnic, 1984). Also, MST\ST radars operated in the VHF band are much more sensitive to clear-air echoes than those operated at UHF. This will be discussed in the following chapters.

In summary, the newly developed MST radar is regarded as a powerful remote-sensing tool for the study of the three-dimensional mesoscale wind field of the statosphere and troposphere. The most recent significant advance in radar technology is the advent of weather radar, with the application of the Doppler principle to determine the full three-dimensional velocity field in regions of precipitation. Their excellent height and time resolution (and even spatial resolution in weather radar) provides an essential tool in short- and long-range weather forecasting.

1.4 Radars in cloud micro-physics

It is well known that the principle source of the influx of energy into the atmosphere is the solar radiation flux to the earth. It has been observed in many careful measurements that there is no noticeable time variation in the incoming solar radiation flux at the top of the atmosphere. For this reason, the term *solar constant* is used to specify the total energy flux on the top of the atmosphere. If this energy input is constant, then why is the short- and long-term weather different in each year? What factors produce this variability? What can intercept the incoming and outgoing heat and radiation fluxes? What factor is responsible for absorbing or supplying heat during condensation of vapour or evaporation of a water drop in the atmosphere? One reason for this variability is the cloud cover in different layers and the type of cloud present. Clouds play an important role in the earth's radiation budget (Arking, 1991). The most persistent and extensive cloud type is the cirrus cloud which has an annual average global frequency of occurrence of about 34% (Matrosov

and Kropfli, 1993). These cirrus clouds consist entirely of ice crystals in different sizes and shapes (Heymsfield and Donner, 1990).

Much of the rain which reaches the earth's surface outside the tropics results from melted ice particles (Stewart et al., 1984). A major portion of the precipitation in the tropics and mid-latitude regions falls in the mesoscale convective systems. In the tropics these systems are referred to as cloud clusters which are generally associated with a tropical storm, cyclone and tropical squall lines. The trailing stratiform regions of these systems cover a horizontal area of 50-200 km and their capacity to give widespread precipitation from the melted ice particles is very impressive. For this reason the study of cloud microphysics is essential in atmospheric research.

Many experiments were carried out to obtain the size distributions of cloud droplets and ice particles. For example, in past decades dropsize distributions were studied by using aircraft, giving information only for a short interval of time in a particular layer and sampling only a small volume of air. It was essential to develop inexpensive remote-sensing techniques. The first successful measurement of drop-size distributions using Doppler techniques with microwave radar was reported by Boyenval (1960) and Probert-Jones (1960). They calculated the velocity distributions of the drops from the observed spectra and then converted the velocity distributions to size distributions. However, due to the presence of turbulence, the observed spectra are broader than the actual spectra and hence the true distribution cannot be calculated without applying a correction for the smearing effect produced by the clear-air echoes[1]. Subsequently, Fukao et al. (1985) demonstrated the ability to detect clear-air and precipitation echoes simultaneously using VHF radar. Gossard (1988) used UHF radar to obtain the size distribution. These new applications led to an extensive use of VHF and UHF radars in the study of the evolution of the size of hydrometeors in

1. The width of the clear-air echoes give a measure of the smearing effect.

the atmosphere.

1.5 Scope of this thesis

In the previous section a few highlights of the use of radar technology in atmospheric research have been made. On going efforts are taking place to improve the application of these newly developed powerful radars in various fields. As we know, they have the capacity to detect from a small water drop or ice crystal to a huge planet. Now, this thesis mainly deals with the use of VHF radars in cloud microphysics. In the analysis part, the data collected from Darwin wind profiler and Adelaide wind profiler are used.

Before explaining its application it would be more appropriate to give a brief idea about how the radar detects echoes from our target and how they are interpreted. So, in Chapter 2, the VHF radar technology is presented in brief. Here, the way in which the Doppler and spaced antenna technique estimate the vertical and horizontal winds of the atmosphere are also included. Radars can detect the three dimensional wind field of the atmosphere. How far can these measurements be trusted? What is the discrepancy between the classical technique and this newly developed technique? What are the factors which can produce this discrepancy? To answer these questions, the intercomparison between the Adelaide VHF radar and the balloon wind measurements are presented in Appendix B.

The knowledge of the size distributions of hydrometeors with height helps to explain the evolution and evaporation of hydrometeors taking place in the atmosphere. It also helps to improve the radar estimates of rain fall intensities. So, a detail study of the retrievals of dropsize distribution and ice crystal size distributions has been carried out. Chapter 3 deals with the formation of cloud droplets and their size distributions. Here the fall-velocity relation of the droplets and the technique used to retrieve dropsize distributions

using a VHF radar are discussed. Additionally, some other important parameters of cloud microphysics such as median diameter and water content of the cloud are presented.

In Chapter 4, modelling results of the retrieval of dropsize distribution and their accuracy is presented. In addition to this some results of the retrievals of dropsize distribution from the Adelaide and Darwin VHF radars are also included.

Chapter 5 deals with the formation of ice crystals in natural clouds. Here, the types of ice crystals, their dimension, fall velocity relations and the technique used to retrieve ice crystals size distributions using a VHF radar are discussed. Finally, height profiles of ice crystal spectra observed by the Darwin wind profiler are presented.

The details of the retrievals of ice crystal size distribution with height and time using the spectra obtained from Darwin VHF radar and the accuracy of the technique is presented in Chapter 6.

The major portion of rainfall in the tropics and mid-latitudes falls in the mesoscale convective regions. Chapter 7 reviews the previous work on mesoscale convective systems, such as squall lines and storms. Here the life cycle of these systems, the vertical up- and down-draught and their relation to precipitation intensity and heating rates are discussed.

Case studies of the squall line passed over Darwin on 5 Dec 1989 and 12 Jan 1990 have been carried out using VHF radar and weather radar and are presented in Chapter 8. Here the vertical profiles of vertical velocity in the convective and stratiform regions, size distribution profiles of raindrops and ice particles, profiles of liquid water content and ice water content are estimated. The heating and the cooling due to vapour deposition and evaporation are also discussed.

Finally, the summary of this thesis with recommended further studies are presented in Chapter 9.

1.6 Conclusion

The discovery of radio waves by Hertz and Marconi led not only to the development of a powerful tool for the detection of material objects in their path but also to a revolution in the study of atmospheric science. No longer limited to military use, it now contributes to the acquisition of a global picture of the earth, with excellent resolution, the study of environmental degradation such as deforestation, soil erosion, and so on. Automatic braking systems in vehicles, agricultural planning for better production, more economical flights following jet streams, reliable navigation and air travel, are now within our control.

The rapid development of this technology in the VHF and UHF bands in the past 2–3 decades helps in the study of many interesting atmospheric phenomena such as mesoscale dynamics of the atmosphere (especially in the stratosphere and troposphere), small and large-scale clear-air turbulence, momentum fluxes, gravity waves, meteor echoes in the mesosphere and so on. The capacity of weather radar to present a comprehensive picture of cyclones, storms and squall lines plays a vital role in short- and medium-range weather forecasting.

The estimation of dropsize distribution using VHF radar has just begun in the past 6-7 years. The shape of the distributions and the accuracy of their estimation is still uncertain. This thesis deals with these problems and a technique is developed to retrieve dropsize distributions using the VHF radar. Here the first attempt to estimate the size distributions of ice crystals using VHF radar is made. The techniques are applied to study the two deep convective motions which passed over Darwin profiler on Dec 5, 1989 and Jan 12, 1990. So, it is expected that this thesis will definitely give a significant contribution towards the application of radar technology in atmospheric science.

Chapter 2

Radar techniques

2.1 Introduction

MST radar can observe almost the entire middle atmosphere up to 100 km, except the region from 30-60 km. From about 60-100 km the main source of scattering is fluctuations in the refractive index caused by variations in electron density. Below 30 km the atmosphere is regarded as neutral, but it is still possible to detect a signal scattered from this region. In the troposphere, the major sources of varying radio refractive index are variations in humidity, pressure and temperature. It has been assumed that the echoes are mainly due to scattering of radar signals by small-scale refractive-index flutuations with dimensions of half the radar wavelength (coherent scatter) or from a random array of precipitation particles (incoherent scatter). In this chapter the various parameters responsible for variations in radio refractive index in the neutral atmosphere are discussed. To give a brief idea about how the radar echoes can be studied in terms of radar parameters, the radar equation will be presented. For practical applications, the Doppler and spaced-antenna techniques used to obtain the windfield of the atmosphere will be explained quantitatively.

2.2 Radio refractive index

The strength of the electric field in a given medium depends upon its dielectric permittivity ϵ. The relative permittivity (or the dielectric constant) ϵ_r of the medium is defined by

$$\epsilon_r = \frac{\epsilon}{\epsilon_0} \tag{2.1}$$

where $\epsilon_0 = 8.85 \times 10^{-12}$ F m^{-1} and is called the dielectric permittivity of free space. Similarly the strength of the magnetic field in a given medium depends upon its permeability μ. The relative permeability (μ_r) of the medium is defined by

$$\mu_r = \frac{\mu}{\mu_0} \tag{2.2}$$

where $\mu_0 = 4\pi \times 10^{-7}$ Hm^{-1}. The value of the relative permeability of the air is nearly equal to unity (Bean and Dutton, 1968). The radio refractive index n of a given medium can be defined in terms of two dimensionless quantities, ϵ_r and μ_r, by

$$n = \sqrt{\mu_r \epsilon_r}. \tag{2.3}$$

The radio refractive index of the atmosphere for non-ionised air can be related to the temperature, pressure and humidity of the air (Tararski, 1961; Bean and Dutton, 1968). For microwave radars, the radio refractive index for the neutral atmosphere can be expressed in terms of these atmospheric parameters (Tararski, 1961) by

$$n - 1 = 10^{-6}[79/T(P + 4800e/T)]\,. \tag{2.4}$$

For VHF radars, Gage and Balsley, 1980 gave a slightly different expression

$$n - 1 = \frac{3.73 \times 10^{-1} e}{T^2} + \frac{77.6 \times 10^{-6} P}{T} - \frac{N_e}{2N_c} \tag{2.5}$$

where e is the vapour pressure in millibars (mb), T is the absolute temperature in Kelvin, P is the atmospheric pressure (mb), N_e is the number density of electron m^{-3} and N_c =

$1.24 \times 10^{-2} f(\mathrm{MHz}^2)$ is the critical plasma density and f is the radio frequency. As the radio refractive-index of the air is only slightly greater than unity, it is more convenient to express it by subtracting 1, as done on the left hand side of eqns. 2.4 and 2.5. The first term of the right hand side represents the contribution from the water vapour (moisture). This term gives a significant contribution in the lower troposphere, but above about 6 km its contribution is usually negligibly small (Tsuda et al., 1986). The second term which represents the contribution from dry air, is important up to around 50 km (Gage and Balsley, 1980). The third term gives the contribution from free electrons in the atmosphere. Above 60 km their contribution becomes greater and greater because the electron density increases rapidly with height.

The complete understanding of the radio refractive index of the atmosphere is very essential because the path followed by a radio wave in the atmosphere is determined by the variation of the refractive index along the path. The variation of radio refractive index can be defined by a term called the gradient of "generalised refractive index", M (Ottersten, 1969)

$$M = M_d \left[1 + \frac{15500q}{T} \left(1 - \frac{1}{2} \frac{\frac{\delta \ln q}{\delta z}}{\frac{\delta \ln \theta}{\delta z}} \right) \right] \tag{2.6}$$

where , M_d stands for the dry-air term and is expressed as

$$M_d = -77.6 \times 10^{-6} \frac{P}{T} \left(\frac{\delta \ln \theta}{\delta z} \right); \tag{2.7}$$

$q = e/1.62\,P$ and is called the specific humidity; $\theta = T(1000)/P)^{0.286}$ and is the potential temperature. With VHF radars pointing away from the zenith the scatter is from isotropic eddies and is proportional to the strength of the turbulence rather than to M^2.

Why does the radio refractive-index in the neutral atmosphere depend upon the humidity, temperature and pressure? This is because the refractive index of a given medium is proportional to the density of molecules in the medium and their polarization. Those

molecules which can produce their own electic field without any external field are called polar molecules. These have a permanent displacement of opposing charges within their internal structure, producing a dipole electric field which can reach far beyond their interatomic distance. Water molecules are polar, but dry air molecules are nonpolar. However, the latter are polarised by the action of an external field, such as radio waves.

2.3 The radar equation

The principle of radar is to transmit a narrow beam of electromagnetic waves in the radio-frequency range into the atmosphere and observe a reflection. When this pulse (or beam) is intercepted by an object whose refractive index is different from that due to the air, then a current is induced in the object, generating a new signal and so scattering some of the energy incident upon it. Part of the scattered component will be directed back to the receiver, where it will be detected if this backscattered power is sufficiently large compared to the receiver noise. Information about the target can be obtained by measuring this reflected (or back scattered) power.

The radar equation or radar range equation gives the power P_r reflected from the atmosphere (target) in terms of radar parameters.

If S_r is the density of the received signal power then we define

$$P_r = A_{eff} S_r \tag{2.8}$$

where A_{eff} is the effective area of the antenna. It can be shown that, (see Gage and Balsley, 1980)

$$P_r = \frac{P_t A_{eff}^2}{4\lambda^2 R^2} |\rho|^2 \tag{2.9}$$

where P_t is the transmitted power, λ is the radar wavelength, R is the distance to the scattering layer and $|\rho|^2$ is the power reflection coefficient. This is the radar equation first derived by Friend, 1949, quoted by Gage and Balsley, 1980. By measuring the time interval Δt between the pulse transmission and its reception, the range of the target, R can be determined by $R = \frac{c\Delta t}{2}$, where c is the velocity of the light.

For isotropic scattering, $|\rho|^2 = \Delta R\,\eta$ and hence

$$P_r = \frac{P_t A_{eff}^2 \eta \Delta R}{4\lambda^2 R^2} \tag{2.10}$$

where ΔR is the range resolution and η is the radar reflectivity. The above eqn. 2.10 is for monostatic radar. For bistatic radar a factor of two in the effective antenna has to be used because of the use of different size antennaefor transmission and reception (May, 1990). More precisely, if $A^t \neq A^r$ then

$$A_{eff} \approx \frac{2\,A^t\,A^r}{A^t + A^r}. \tag{2.11}$$

2.4 Echo detection and interpretation

In the past two decades, VHF radars have been used as "*wind profilers*" to determine the wind vector in the troposphere and lower stratosphere.

The exact mechanism by which the radar echoes are produced in the electrically neutral atmosphere is still uncertain. For radars working at off-vertical angles, scattering from irregularities generated by isotropic turbulence is regarded as the main mechanism, whereas for radars working at vertical incidence, Fresnel (or Partial, or Specular) reflection plays a vital role.

The importance of Fresnel reflection for the radars operating in the VHF band was first cited by Gage and Green (1978) . Their observations of the enhancement in the returned radar signal was confirmed later on by Rottger and Liu (1978), and Rottger and Vincent

(1978). There are two major techniques used to determine the mean wind in the atmosphere using wind profilers: (i) the Doppler beam swinging technique (DBS) and (ii) the spaced antenna technique (SA).

2.4.1 The Doppler beam-swinging technique

The method involves measuring the mean Doppler shift for the signal returned to the radar by backscatter. If we assume that a bulk motion carries the scatterers (or reflectors) in the radar volume at range R, then the rate of change of the phase of the returned signal $\frac{\delta\phi}{\delta t}$ (Rottger, 1984a) is

$$V_r = \frac{\lambda}{4\pi}\frac{\delta\phi}{\delta t} \tag{2.12}$$

where $V_r = \frac{dr}{dt}$ and is the radial velocity in the direction of the radar beam. However, to represent the average value of the wind within the radar volume, in the above eqn. 2.12, V_r and $\frac{\delta\phi}{\delta t}$ have to be replaced by averages of all the targets within the volume.

The mean rate of change of phase for the scatterers is, (Woodman and Guillen, 1974)

$$\frac{d\,\Delta\phi}{dt} = \frac{1}{2\pi\delta t} tan^{-1}\left[\frac{Im(\rho(\delta t))}{Re(\rho(\delta t))}\right] \tag{2.13}$$

where $\rho(\delta t)$ is the autocovariance function of the complex time series at time shift δt. Im and Re stand for imaginary and real parts of the complex quantity. But the autocovariance function of a time series is the Fourier transform of the power spectrum of that series (Bracewell, 1978). Hence, if T is the data length of the time series, then we can write

$$\rho(\delta t) = \sum_{i=1}^{n} P(f_j) e^{2\pi i f_j \delta t}, \quad f_j = \frac{j-1}{T}\,. \tag{2.14}$$

Finally, substituting from eqns. 2.13 and 2.14 in 2.12 and assuming the term inside the [ ]

brackets is much less than unity, we arrive at

$$v_r \approx \frac{\lambda}{2} \frac{\sum_{i=1}^{n} f_j P(f_j)}{\sum_{i=1}^{n} P(f_j)}. \tag{2.15}$$

From this equation, the calculation of the vertical velocity is straight forward, if the radar beam is pointed vertically. To obtain the horizontal velocities, we calculate the radial velocity of the scatterer for the off-vertical beam and then, by taking its component in the horizontal direction, we can estimate the horizontal winds. However, if the off vertical pointing angle is small, the effects of horizontal variations in the wind field are reduced. Additionally, it maximizes the aspect sensitivity of the scatterers giving enhanced power from near the zenith. As pointed out by Strauch (1983) and Vincent(1984), there is an optimum beam pointing angle because at VHF band ($\sim$ 50 MHZ), the strong aspect sensitivity of the scattering can cause the effective pointing beam direction to be smaller than the physical direction. Additionally, the optimum off vertical beam pointing angle is determined by the product of beam pattern and the angular distribution of the scatter. The recommended off vertical pointing angle for radars operating at $\sim$ 50 MHZ is 10–15°. It should be noted that if the signal falling in the sidelobe is significant, it has to be rejected in the analyses. This zenith angle dependence of the echo power in the troposphere and stratosphere has been confirmed by Tsuda et al. (1986).

2.4.2 The Spaced Antenna Technique

The Spaced-Antenna (SA) Technique was developed in the 1950s to enable the analysis of ionospheric data. It was first proposed by Mitra in 1949, as quoted by Solvang et. al (1977). However, the first detailed analysis technique, the so called 'Full correlation analysis', was developed by Briggs et al. (1950) and then extended by Phillips and Spencer (1955). Since

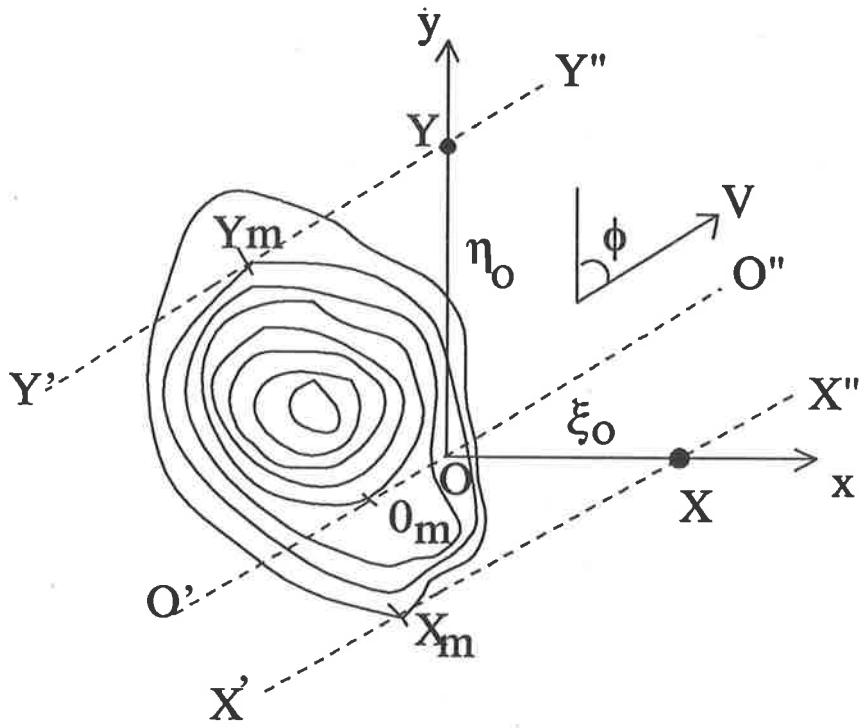

Figure 2.1: An example of a diffraction pattern produced by the interaction of radar echoes scattered by variations of radio refractive index in the atmosphere. The pattern in the atmosphere is moving with velocity, V, and the three ground based sensors are used to detect the diffraction pattern.

then this technique has been widely utilized and an ongoing effort has been made to improve the SA system and data handling procedures.

The SA technique involves a transmitter which emits an electromagnetic pulse to the atmosphere and the study of the scattered echoes detected by three receiving antennas forming a triangle. The initial assumption of the analysis is that the atmospheric irregularities have a certain shape and are random in nature and moving in a fixed direction with constant speed without changing their shapes. It is more convenient to represent these patterns by contour lines, as shown in Fig. 2.1. for a typical pattern moving at an angle ϕ with velocity V. The pattern is detected by three sensors O, X, and Y forming a right

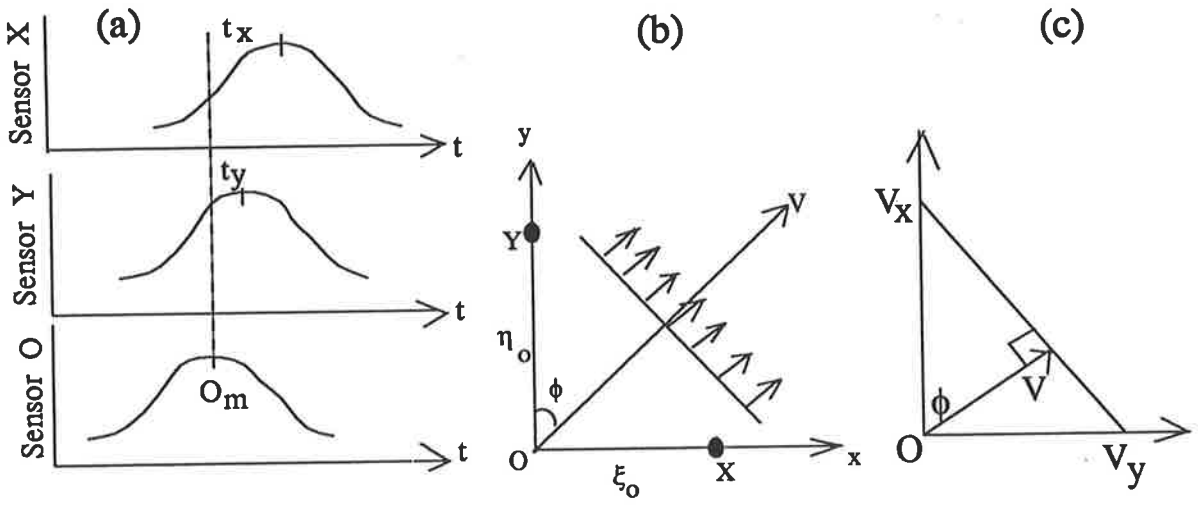

Figure 2.2: (a) Time records of a typical crest obtained by three sensors (b) Simple representation of the diffraction pattern by a line of maximum which is perpendicular to the velocity vector V (c) Geometrical construction to obtain the velocity vector from its trace velocities in the x- and y-directions.

angled triangle. The separation between O-X and O-Y are ξ_0 and η_0 respectively. If the pattern is very large compared with the separation between the sensors, then the line of maximum $X_m 0_m Y_m$ will be almost straight. This assumption may lead to a serious error which will be explained later. As the line of maximum moves in the direction 0'0" it will be detected first at 0, then at Y after a time interval t_y and then at X after t_x, producing the signals as shown in fig. 2.2a.

So the sensor Y will record a section of line of maximum in the direction Y'(Y_m)Y" and in the same way sensor X will record along X'(X_m)X", which is parallel to both 0'(0_m)0" and Y'(Y_m)Y". Thus, fig. 2.1, can be simply represented by Fig. 2.2b with the assumption of a line of maximum perpendicular to V. By measuring the time intervals t_x and t_y (see Fig. 2.2a) the trace velocities V_x and V_y can be determined and the velocity vector V (see Fig. 2.2c) can be related to V_x and V_y by the relation,

$$V = \frac{V_x V_y}{\sqrt{V_x^2 + V_y^2}} . \tag{2.16}$$

When these patterns have no systematic elongation in any particular direction, average time displacements should be the same whereas individual time displacements may vary. By using the average time displacements in Eqn. 2.16 we can estimate the average velocities, which we generally call the "apparent velocities".

These do not represent the true velocities because the patterns may be elongated in a particular direction and they may change as they move. The true velocities of the pattern can be obtained by using a full correlation analysis. A short description of the method is presented in Appendix A. For detailed description see Briggs (1984).

2.4.3 Precipitation measurements

In the previous sections, we have seen that radar backscattering can be used to get substantial information about the clear air. Backscattering is also capable of giving a comprehensive picture of precipitation particles in the atmosphere, because the scattered signal (or the Doppler spectrum) contains information about both the air motion and the fall speed of precipitation particles. For scatter from particles which are small compared to a wavelength, the radar reflectivity is a function of D^6 where D is the diameter of spherical particles such as raindrops. A term ,Z, reflectivity factor is defined as

$$Z = \frac{K}{R^2}\frac{\pi^5}{\lambda^4}\left(\frac{|\epsilon_r - 1|}{|\epsilon_r + 2|}\right)^2 P_r \tag{2.17}$$

where K is a constant which depends upon the parameters of radar, λ is the wavelength, ϵ_r is the dielectric constant of the medium and R is the target range. The reflectivity factor also related to the drop diameter by the relation, (Doviak and Zrnic, 1984)

$$Z = \int_0^\infty N(D) D^6 dD \tag{2.18}$$

where N(D) is the number of drops within the radar volume in the diameter range between D and D+dD. Thus by studying the backscattered signal it is possible to obtain information on the size distribution of the hydrometeors. This aspect will be discussed in detail in Chapters 3, 4, 5 and 6.

2.5 Conclusion

Thus, the observed backscattered power caused by the variation in the gradient of radio refractive index, can be used in atmospheric research using radar equations. As a further application, the windfield of the atmosphere can be determined by using the DBS and SA methods. Arguments have been made about the accuracy of these two methods. Briggs (1980) mentioned that basically the DBS and SA methods are the same but the main advantage of SA over DBS is that the Fresnel reflection from horizontally stratified turbulence structures in the troposhere and stratosphere is manifest at VHF, and SA gives spatial pattern in additon to temporal pattern.

Radars are not only able to obtain the wind information, but also able to obtain precipitation information from the atmosphere, because the backscattered power depends on the sixth power of the diameter of the precipitation particles. It is also possible to derive further information about a target by measuring the polarization of transmitted and received pulse. This cross-polarization technique can be used to obtain the axial ratio of the particles, giving some idea about the type of precipitation particles present in the atmosphere.

Chapter 3

Cloud droplets and their size distributions

3.1 Introduction

In general a cloud is an assembly of very small droplets with a number density of about 100 per cm^{-3} and a radius of about 10 μm (Rogers and Yau, 1991). This number density can vary from one type of cloud to another; for example, for continental clouds the drop number density is 300-600 cm^{-3} whereas for maritime cumulus it is 50-300 cm^{-3}. The two main processes taking place in the atmosphere for the growth of these cloud droplets are

(1) the diffusion of water vapour to and its condensation upon their surfaces

(2) Collision and coalescence of droplets.

Experimental evidence shows that the droplets can grow up to about 25 μm by condensation and diffusional processes. When the drops exceed 25 μm the rapid growth of droplets by collision and coalescence process can be observed. These processes can be found qualitatively

and quantitatively in many textbooks of cloud physics. (eg. Mason, 1971).

This chapter deals mainly with the size distribution of cloud droplets because, by using radars, we can estimate the drop size distributions, which are related to very important parameters such as the rainfall intensity, liquid water content and so on. We begin with the droplet fall-velocity relation which is the most important step in the radar precipitation echo interpretation. Then the estimation of the dropsize distribution using various radars will be discussed in detail. Finally, various proposed models of the dropsize distribution and of the distortion of the raindrop will be discussed.

3.2 Droplet fall-velocity relation

The fall velocity of water drops of various sizes was first measured by Lenard in 1904 (quoted by Mason, 1971) in the range from .01 to .13 grams, by suspending them on a blast of air produced by a blower. In 1909 Schmidt measured the much smaller velocities of drops in the range from 0.35×10^{-4} to .04 grams (diameter range 0.4 to 3.4 mm). More accurate measurements were made by Laws (1941), using electronic and optical techniques. Since then many laboratory experiments have been carried out to develop empirical relationships which allow the size of the droplets to be calculated from their fall speed (Gunn and Kinzer, 1949; Imai, 1950; Kumai and Itagaki, 1954; du Toit, 1967; Foote and du Toit, 1969).

For a droplet diameter D falling freely at its terminal velocity w in the air, its weight (mg) must be balanced by the viscous drag of the air. Hence, (Gunn and Kinzer, 1949)

$$\frac{1}{6}\pi D^3(\rho\prime - \rho)g = \frac{1}{2}\rho w^2 \eta A \tag{3.1}$$

where ρ' is the density of the drop, ρ the density of the air, g the acceleration due to gravity, η the dimensionless drag coefficient and A the projected area of the drop ($\pi D^2/4$).

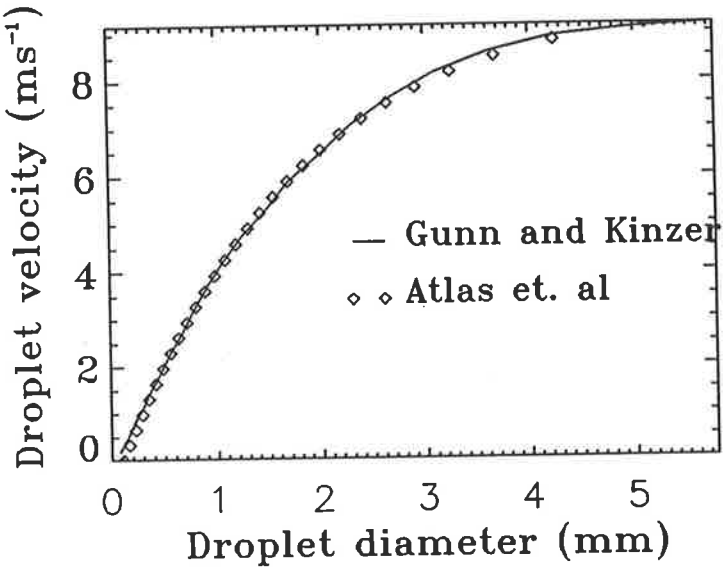

Figure 3.1: The terminal velocity of a distilled water droplet in stagnant air. The data are from the original measurements of Gunn and Kinzer, 1949, at air temperature 20°C, pressure 760 mm of mercury, and humidity 50%.

McDonald(1960), and Cornford (1965) and Foote and du Toit, (1967), Mason (1971) have addressed the relationship between the Reynolds number and the terminal velocity. The Reynolds number R_e is given by (Foote and du Toit, 1967)

$$R_e = \frac{D\,w}{\nu} \tag{3.2}$$

where ν is the coefficient of viscosity of the air.

The main problem in using Eqn. 3.1 is to find an accurate value of the drag coefficient η. By putting an assumed value of w in Eqn 3.2, one can estimate R_e. Using a standard plot of R_e vs. η obtained from the wind-tunnel experiments (Foote and du Toit, 1967), the drag coefficient can be estimated. Inserting this drag coefficient, a new value of w is determined. The process is repeated for a few iterations until convergence is obtained. To avoid this iterative process an approximate analytic solution to the fall speed data of Gunn

and Kinzer (1949) was given by (Atlas et al, 1973)

$$w(D) = 9.65 - 10.3\,exp(-600D) \tag{3.3}$$

where w and D are in m s^{-1} and m respectively.

In Fig. 3.1, we can see that the discrepancy between 3.3 and Gunn and Kinzer's original data is extremely small. If D lies between 6×10^{-4} and 5.8×10^{-3}m, the estimate of the fall velocity from Eqn. 3.3 deviated by less than 2% from the data obtained by Gunn and Kinzer. Atlas and Ulbrich (1977) gave a power law fit to Gunn and Kinzer's data for the diameter range from 5×10^{-4} to 5×10^{-3}, this being

$$w(D) = 386.6D^{0.67}. \tag{3.4}$$

Rain drops fall faster at upper levels in the atmosphere than nearer to the ground, because at-upper levels air density is lower, causing less viscous drag on the drops. The necessary correction, calculated numerically by Foote and du Toit (1967) is given by

$$w(\rho) = w(\rho_o)10^Y \left[1 + 0.0023\left(1.1 - \frac{\rho}{\rho_0}\right)(T_0 - T)\right] \tag{3.5}$$

where T and ρ stand for the temperature and density of the air. ρ_o and T_o represent the the surface air pressure of 1013 mb and temperature of 20°C. Y is given by

$$Y = 0.43\,log_{10}\left(\frac{\rho_0}{\rho}\right) - 0.4\left[log_10\left(\frac{\rho_0}{\rho}\right)\right]^{2.5}. \tag{3.6}$$

Neglecting small terms the approximate form of Eqn 3.5 is

$$w(\rho) = w(\rho_0)\left(\frac{\rho}{\rho_0}\right)^{-0.4}. \tag{3.7}$$

Beard (1985) argued that exponent of $\frac{\rho}{\rho_0}$ should be -0.45. How can the terminal velocity obtained in the laboratory using distilled water be matched with the terminal velocity of a

rain drop falling freely in the atmosphere? For this, Gunn and Kinzer commented that the mechanical vibrations and distortions of the falling droplet from the distilled water can be compared with the naturally falling raindrops because the distilled water has normally high surface tension compared to undistilled water. However, Beard and Pruppacher (1969) reported that while their estimates of terminal velocities agree quite closely with those reported by Gunn and Kinzer for larger drop diameters, Gunn and Kinzer's values appear to be slightly larger for small drops. They said that this may be due to the fact that in Gunn and Kinzer's experiment, the environmental air in which the drops were falling was not water-saturated, but had a relative humidity of only 50%. Many experiments have been carried out to study the terminal velocity of smaller drops, for which it is found that Stoke's law applies i.e. the viscous force on a sphere falling freely at a constant speed is equal to $6\pi a\eta V$, where a is the radius of the drop. Replacing radius with diameter and equating the viscous force with the downward force due to gravity (neglecting upthrust due to air) we can write (Beard and Pruppacher, 1969 and Gossard et. al., 1990)

$$D = \sqrt{\frac{18\eta V_t}{\rho g}} \quad \text{for } V_t < 0.4\text{ms}^{-1}\,. \tag{3.8}$$

Gossard et. al. (1990) also suggested that

$$D = 0.2V_t \quad \text{for } 0.4 \leq V_t < 2.75 \tag{3.9}$$

and for diameter greater than 2.75, they used Eqn 3.3.

Gossard (1988) found another empirical relationship by applying a numerical fit to the curve found by du Toit (1967), using data from Gunn and Kinzer for $w \leq 3\,\text{ms}^{-1}$

$$D \approx 0.122w + 0.0206w^2\,. \tag{3.10}$$

In this work the velocities have been calculated by using Eqn. 3.3 and the correction is applied for various altitudes using Eqn. 3.7. The work of Gunn and Kinzer is used

because it is regarded as the most complete so far and has been widely used. Supporting this, Gossard et al (1990) quoted that even though Eqns. 3.3 and 3.7 were developed a long time ago, with their revision they found that the velocities calculated from Eqns. 3.3 and 3.7, gives one of the lesser errors (provided there is no turbulence). Thus, by using these accepted empirical relationships, the dropsize distributions can be estimated accurately from the fall-velocity spectrum. The deviation for small drops is not significant, since the 50 MHz wind profiler used in the present study is not sensitive to very small drops.

3.3 Dropsize distributions

In 1895 Wiesber first measured the size of rain drops by allowing the drops to fall on a filter paper. In 1904 Bentley measured the drop diameter by allowing the drop to fall into a layer of flour (Pruppacher and Klett, 1978). In order to obtain the size of the rain drops, many experiments have been carried out using various techniques. It has been found that rainfall is never composed of drops of uniform size, but that there is always a distribution of many different sizes. Even for the same rainfall rate, the size of the drops may vary from one instant to another. So the estimation of the size of individual drops has no meaning and in practice would be almost impossible to carry out. Since there is always a distribution of drop-size, meteorologists are keen to calculate the size-distribution of drops in a sample volume of cloud.

3.3.1 Exponential distributions

An early analysis of the rain dropsize distribution was made by Marshall and Palmer (1948). If $N(D)$ is the number of drops in the diameter range betwen D and $D + dD$, then from

the distribution of Marshall and Palmer (1948)

$$N(D) = N_o e^{-\lambda D} \tag{3.11}$$

where N_o is the absolute number of drops and λ is the slope of the curve between diameter (D) and Log N(D). The values given by Marshall and Palmer (1948) for widespread rain are

$$\lambda = 4.1\, R^{-0.21}\, mm^{-1} \tag{3.12}$$

$$N_0 = 8 \times 10^3\, m^{-3}\mathrm{mm}^{-1}\,. \tag{3.13}$$

The observational technique of Marshall and Palmer was really impractical, and painstaking too, because they used coloured marks left on dyed absorbent paper by falling rain drops. Since then many experiments have been carried out in order to develop a standard instrument, called disdrometer, to measure the dropsize distributions on the ground.

In past decades, dropsize distributions have been determined *in situ* by aircraft measurements. Despite its high speed, an aeroplane can only explore a small volume of air in a given time compared to that which is ideally sampled for the study of the meso-scale convective systems in the atmosphere. Again, the size distribution of drops with height is now a standard measurement contributing to a complete picture of a convective cell, but it can be obtained directly only by using a number of aircraft simultaneously, which is not only difficult to manage, but also expensive. So the challenge is to measure the dropsize distributions of a large volume using remote sensing.

3.3.2 Use of micro-wave radars

In the early 1940s meteorologists began to realise that radars were capable of detecting storms, cyclones and other meso-scale convective phenomena. They also found that this

new radar technology was able to sample a large volume of a convective system, compared to that sampled by aircraft. The dimensions of the volume sampled by the radar is determined by the radar pulse length, its beam-width and the range of the volume explored. To give a rough idea of the volume sampled by the radar, at 100km range a 2° conical beam would have a circular cross-section of diameter 3.5 km. By the late 1950's attempts had been made to estimate dropsize distributions using Doppler radar. This was made possible by vertically pointing Doppler radar, with which the reflectivity weighted fall-velocity spectrum of the hydrometeors can be directly measured. If the velocity can be related to the size of the falling droplets, then the dropsize distributions can be estimated. Boyenval(1960), Probert-Jones (1960) and Lhermitte (1960) achieved remarkable success in measuring dropsize distributions using Doppler radars. Later on Rogers and Pilie (1962), Wilson (1963), Caton (1963, 1966), Battan (1964), Du Toit (1967), and Gorelik et al (1967) as quoted by Gossard (1988), and Rogers (1967) studied the size distributions of rain drops using Doppler radars in various atmospheric conditions.

However, all these experiments, based on microwave radar, were not sensitive to the clear-air vertical velocity. Atlas *et al.* (1973) pointed out that the vertical velocity is a crucial factor for accurately determining the droplet diameter. Hence the estimation of dropsize distributions from the observed fall-velocity spectrum is straight forward in stagnant air, but complications arise in the presence of mean vertical motions and clear-air turbulence in the atmosphere. To correct for the effects duc to turbulence and mean vertical motion, an accurate determination of the clear-air vertical velocity characteristics is essential.

3.3.3 Use of VHF/UHF radars

The effect of vertical motion on the interpretation of the radar precipitation echo may be solved by wind profilers, which are Doppler radars working in the VHF or UHF bands. These radars are designed mainly to detect backscatter from clear air and to measure profiles of the three-dimensional wind vector through the troposphere and lower stratosphere. As described below, these profilers can be used as an accurate ground-based tool to obtain the dropsize distribution in the atmosphere.

Fukao *et al.* (1985), and Wakasugi *et al.* (1986, 1987) pointed out that VHF Doppler radars are capable of simultaneously detecting two distinct echoes, one from the clear-air turbulence and the other from hydrometeors. They described a method to remove the spectral broadening effect of turbulence and finite beam width as well as mean vertical motion from the precipitation spectra. There are two basic approaches to the estimation of the dropsize distributions from the observed spectra; one assumes a particular shape of the dropsize spectrum and another assumes a random shape. Wakasugi *et al.* (1986, 1987) fitted a spectrum based on the Marshall-Palmer (1948) distributions to the observed spectra by a least-squares method. The main problems of this method are the need for an initial guess of the parameters in the theoretical fitting process and the restriction involved in assuming the Marshall-Palmer (1948) distribution itself. This assumption essentially prevents the study of many interesting effects, such as the evolution of multi-peaked dropsize spectra.

This successful demonstration by Wakasugi *et al.* provided motivation for many workers to improve radar technology to study cloud properties. Gossard (1988) described a method to determine the dropsize distribution by separating the clear-air echo and the precipitation echo for a UHF radar, requiring no assumptions about the shape of the dropsize distributions, but he gave more emphasis to the small-diameter regime. Sato *et al.* (1990) used

a method similar to that of Wakasugi*et al.* (1986) to estimate the dropsize distributions using VHF radar, and developed a computer algorithm to find the initial guess involved in the process of fitting a curve directly to the original spectra. Currier *et al.* (1992) corrected for the effect of turbulence and mean vertical velocity on the precipitation spectra observed by a 915-MHz radar, using information obtained by a 50-MHz radar and an analysis which generalised the model dropsize distributions to a sum of Gamma distributions. They also deduced the rainfall intensities from the dropsize distributions of the hydrometeors and compared them with actual rainfall data obtained from an *in-situ* tipping-bucket rain gauge. However, in their estimations, the validity of the assumption of beam broadening due to clear-air and beamwidth effects in the spectra, obtained by two different radars operating at two different frequencies, is difficult to judge and again a fairly explicit distribution shape is assumed. Rogers *et al.* (1992) compared the dropsize distributions obtained by aircraft measurements with the dropsize distributions estimated using UHF radar data and analysed using the Gossard technique. They found that the results were in good agreement with each other.

Although profilers operating at 915 MHz are more sensitive to scatterers from precipitation (making them excellent tools for low rainfall rate studies such as those of Gossard, 1988), observations with a 50-MHz system have the advantage of always being able to detect the clear-air echo. As shown in Fig. 3.2, in the UHF band at operating frequency of around 400 or 915 MHZ (corresponding to wavelengths $\approx$ 70 cm or 30 cm), the contribution from the precipitation echo in the total backscatered power is much higher than the contribution from the clear-air echo. So the precipitation peak dominates the clear-air peak and hence it would be difficult to separate the two. In the VHF band at 50 MHZ, the clear-air echo is about the same strength as the precipitation echo in heavy rain. In general, it has been

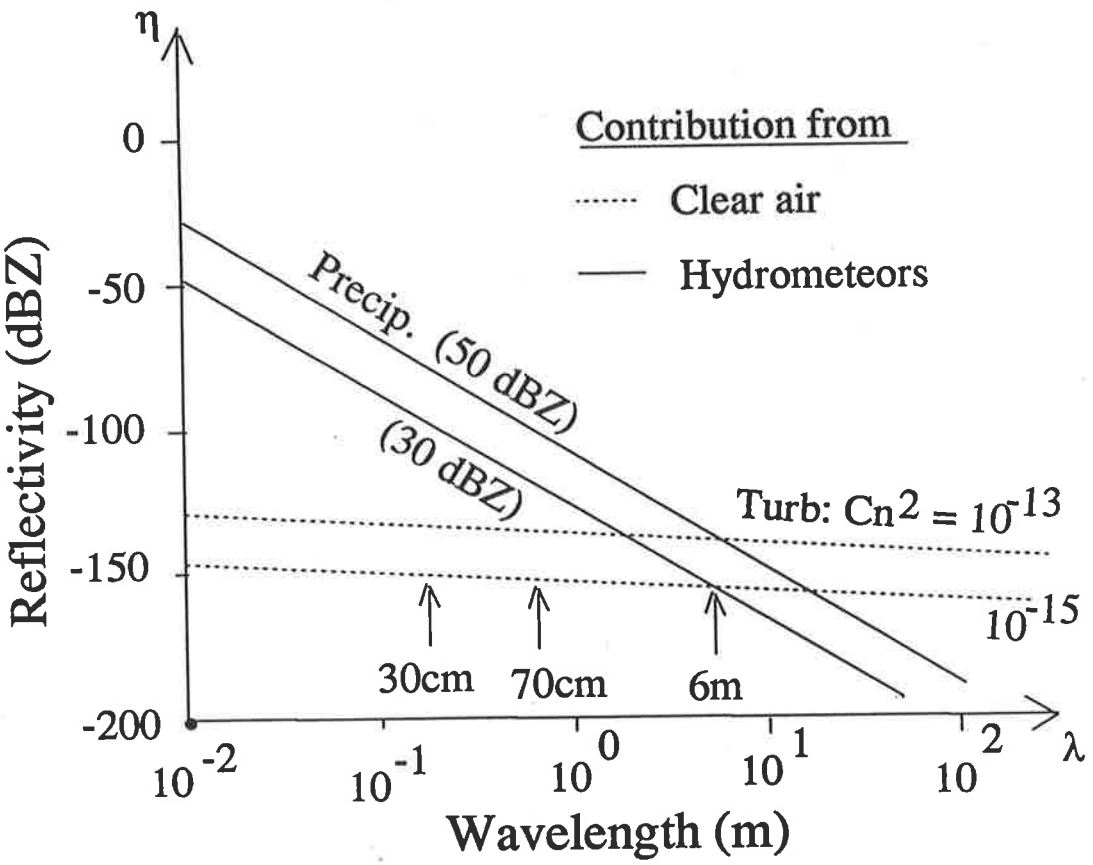

Figure 3.2: The radar reflectivity due to clear-air turbulence and hydrometeors in various ranges of operating frequencies

observed that the clear-air echo is much stronger than the precipitation echo.

Now, the backscattered power due to hydrometeors depends upon the size, type, and number density of the hydrometeors in the sampled volume. The radar-reflectivity factor Z due to the hydrometeors varies as the sixth power of the diameter of the hydrometeors, summed over all the hydrometeors per unit volume, and is expressed as (see Doviak and Zrnic, 1984)

$$Z = \int_0^\infty N(D) D^6 dD \,. \tag{3.14}$$

The backscattered power spectrum S(w) as a function of vertical velocity, w, in precipitation conditions is the sum of the backscattered power spectrum from the clear-air turbulence, G(w), and from the droplets, P(w). However, due to the effect of turbulence, beam-broadening, wind shear and window effects, the precipitation spectrum is broader than the true-reflectivity weighted fall-speed spectrum, P(w), which we wish to estimate. Now, the observed spectra may be represented by the convolution of the clear-air echoes and the precipitation echoes. Hence S(w) can be expressed as (e.g., Wakasugi *et al*, 1986).

$$S(w) = G(w - \overline{w}) + G(w) * P(w - \overline{w}) + n\,. \tag{3.15}$$

The asterisk ($*$) stands for the convolution operation, $\overline{w}$ for the mean vertical wind, and n is the noise level. Here

$$G(w) = A_0 \exp\left(-\frac{(w - \overline{w})^2}{\sigma^2}\right) \tag{3.16}$$

$$P(w) = \frac{1}{Z} N(D) D^6 \frac{dD}{dw} \tag{3.17}$$

where A_0 and σ are the amplitude and spectral width of the clear-air spectrum respectively. The factor dD/dw can be determined from Foote and du Toit's (1969) fall-speed relation

$$w(D) = (9.65 - 10.3\exp(-600D))\left(\frac{\rho}{\rho_0}\right)^{-0.4} \tag{3.18}$$

where w and D are in ms^{-1} and m respectively. The symbols ρ_0 and ρ represent the respective densities of air at sea level and at the height of the observation.

The backscattered power spectra due to the clear air and precipitation particles are explained briefly in Fig. 3.3. The Gaussian shape of the clear-air turbulence $G(w)$ is shown in Fig. 3.3 (a). Here the offset $\overline{w}$ of the Gaussian peak is associated with the mean background wind. A precipitation echo $P(w)$ in the absence of turbulence and vertical velocity is shown in Fig. 3.3b. The peak of the precipitation echo lies at a velocity w_1. In the presence of

turbulence, this precipitation echo will be broader because of the turbulent motions in the atmosphere which smear out the precipitation echo $p(w)$ as shown in Fig. 3.3c. Analytically it is the convolution of $P(w)$ and $G(w)$. In this case the peak position is not at w_1, but at $\overline{w} + w_1$. Clearly, the larger the turbulence, the greater the smearing effect. Finally, the Fig. 3.3d represents the total backscattered power which we observe by the ground-based sensors. Here the position of the precipitation echo is at $\overline{w} + w_1$. In these diagrams it is clear that in the interpretation of radar echoes, we need to correct for the broadening of the precipitation echo in order to calculate the reflectivity-weighted fall-speed spectrum.

To remove the broadening effect due to the beamwidth and turbulence in the precipitation part of the spectrum, a deconvolution operation of the precipitation echoes with clear-air echoes of unit area is carried out. Two methods of deconvolution were tested. These are

(i)a Fourier transform (FT) technique, and (ii) an iterative technique.

In the FT technique, if $s_1(t)$ is the population power spectrum, and $S_1(\tau)$ is its FT, then

$$S_1(\tau) = \frac{H}{G} \tag{3.19}$$

where H and G are the FTs of the observed precipitaton echo h and the clear-air echo g respectively. In this method, to avoid division by a very small number and so catastrophically amplify the noise, the spectra H and G have to be truncuated. As the most important information lies in the central part of the series, we can apply a low-pass filter to the FT by removing the high frequency components.

In the iterative technique, the deconvolution is achieved by a series of convolutions and the population spectra are estimated by (Cooper, 1977)

$$h_{i+1} = h_i * g - h \mid_{i=0.....\infty} \tag{3.20}$$

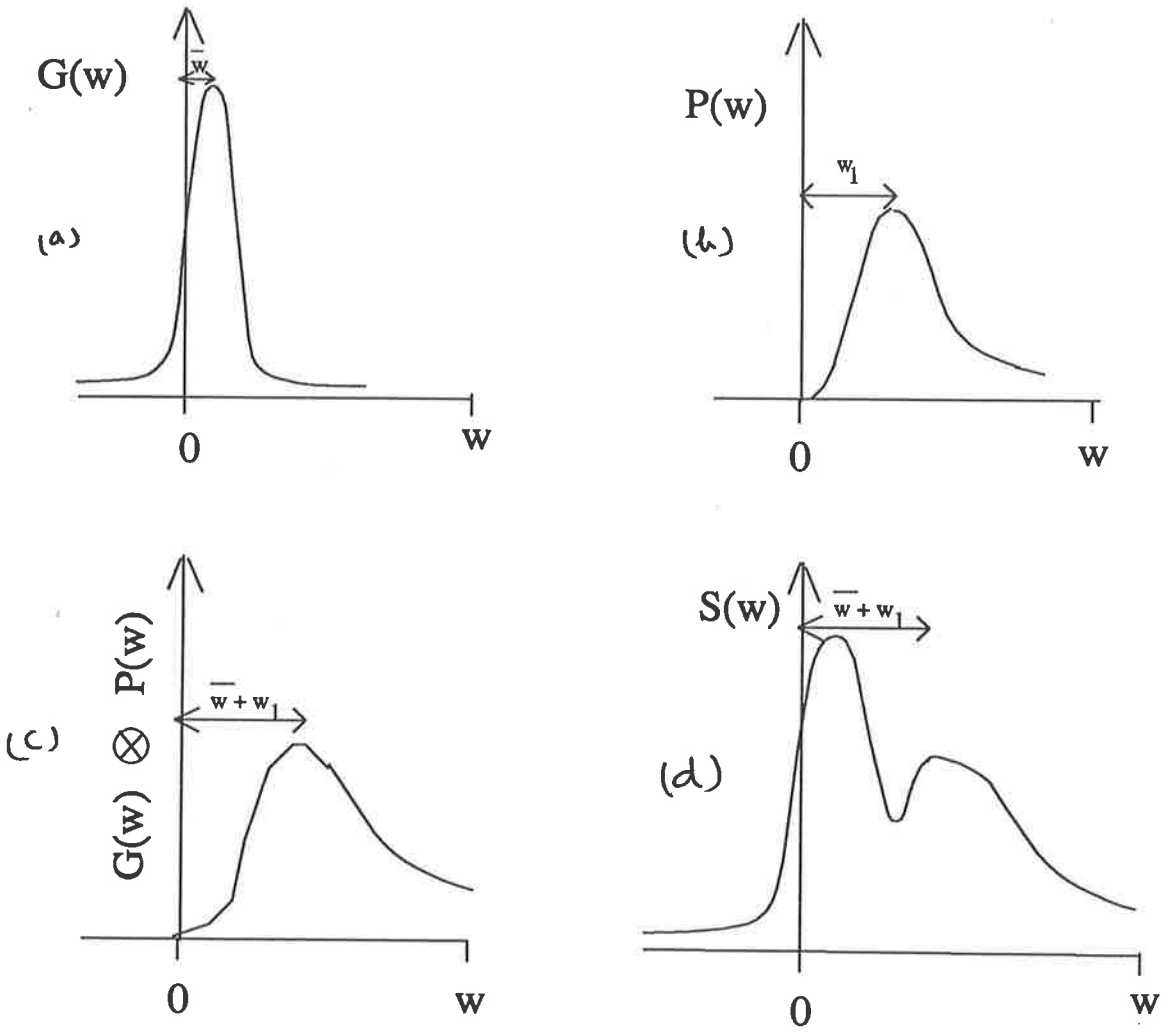

Figure 3.3: The radar reflectivity due to a) clear-air turbulence, b) hydrometeors, c) hydrometeors in turbulent conditions and d) clear air and hydrometeors.

where h is the observed precipitation echo and g is the clear-air echo. Here the successive approximations are made by repeated substitution of new estimates of h_i. In the absence of noise, h_{i+1} converges to $S_1(w)$ as $i \rightarrow \infty$. In practice, however, only a few iterations are appropriate so that the high-frequency terms in the FT are diminished. Repeated iterations include more high-frequency information and the noise is amplified. Cooper (1977) notes that the iterative technique is equivalent to a FT technique with a smooth weighting of the deconvolved spectra, rather than a straight truncation.

3.4 Deviation from exponential shape

The departure of the raindrop size distributions from the predicted exponential form has been reported by many investigators. If sufficient averaging in space and/or time is performed, the size distributions eventually tends to an exponential. However, Waldvogel (1974); Joss and Gori (1978); Gori and Geotis (1981); and Donnadieu (1982) as quoted by Ulbrich (1983) commented that a large and sudden change in N_0 can occur from moment to moment within a convective cell. They have further pointed out that these rapid variations in N_0 are independent of those occuring in λ. Clearly, this variation in the drop size distribution can affect the radar estimation of rainfall intensity. Since the drop forming process is affected by many physical processes, departures from the exponential form are expected. It is therefore essential to study the deviations of N_0 and λ from the values given by Marshall and Palmer. Other models have been proposed to deal with this descrepancy from the exponential distribution.

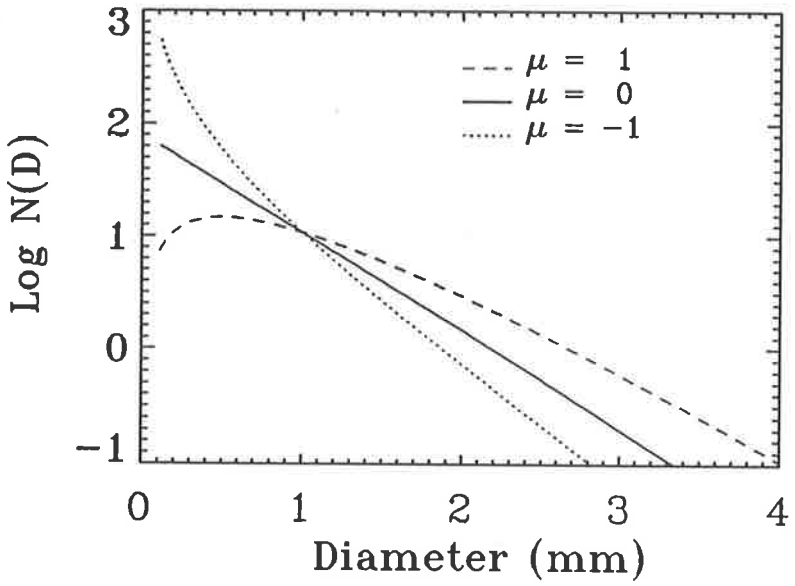

Figure 3.4: An example of a dropsize distribution for typical values of λ and N_0 of 2.0 mm^{-1} and 8000 $m^{-3}mm^{-1}$. The solid line is an exponential distribution, the broken and dotted lines are for values of μ of +1 and -1.

3.4.1 Gamma distribution

The gamma distribution was first proposed for dropsize spectra by Khrgian et al. (1952), then elaborated by Sulakvelidze (1969) and Sulakvelidze and Dadali in 1971 (Ulbrich, 1983). The gamma distribution has the form (see Ulbrich, 1983)

$$N(D) = N_o D^{\mu} e^{-\lambda D} \tag{3.21}$$

where the exponent μ can take any positive or negative value. The coefficient N_o has units of $m^{-3}mm^{-1-\mu}$. Eqn. 3.21 deals with 3 drop size distribution parameters, N_o, λ, and μ rather than just the N_o and λ involved in the exponential distribution. Atlas et al. (1984) pointed out from their simulations that this three-parameter technique can often give a good approximation of the observed rain dropsize spectrum. To illustrate these exponential

and gamma distributions, an example of the dropsize distribution is shown in Fig. 3.4. The solid line ($\mu = 0$) represents an exponential distribution. The broken line ($\mu = 1$) represents a Gamma distribution with its shape concave upward. Clearly, there are a greater number of large drops than predicted by the Marshall and Palmer distribution. Similarly, the dotted line for $\mu = -1$ represents a Gamma distribution with shape concave downward. Such types of distribution can be observed when there are fewer large drops compared to the Marshall and Palmer distribution.

3.4.2 Truncated exponential distribution

So far we have assumed that the drop diameters vary from 0 to infinity, which is unrealistic. Errors in the estimation of the size distribution would be low if the value of λ is large. However, when the size distribution curve is flat (for small values of λ), this assumption of the existence of all sizes of drops may produce a very large error. For this reason it is common to use a maximum value, D_max, of the diameter in the exponential distribution. Hence

$$N(D) = N_o e^{-\lambda D} \qquad \text{for} \qquad D < D_{max}$$

$$\text{N(D)} = 0 \; . \qquad \text{for} \qquad D > D_{max}$$

3.4.3 Three peak model

This approach is different from the use of the exponential and Gamma distributions and is based on physics of drop breakup. This model is useful in visualizing the collisional breakup and coalescence of raindrops. Low and List (1982) observed three different types of breakup: filament, sheet and disk. According to List and McFarquhar (1990), if the number density of the raindrops is plotted against the logarithm of the diameter, the equilibrium raindrop

size distribution should have three peaks. Willis (1984) has also reported a three-peak distribution above the cloud base in a hurricane system and later on List et. al (1988) observed spectra similar to the 3-peak model.

Is there any interrelation between the 3 types of breakup and the 3 observed peaks? Valdez and Young (1985) and Brown (1988) investigated the 3 different types of breakup observed by Low and List (1982). Later on List and McFarquhar (1990) concluded that the equilibrium raindrop size distributions with three peaks in number concentration result from different breakup and coalescence modes. Further, they concluded that filament breakup produces a peak in the small-diameter regime and sheet breakup a peak in the medium-diameter regime, but disk breakup does not significantly affect the 3-peak distributions. They argued that the peak in the large-diameter regime is produced by many types of interaction and hence it is not as sharp as the other two peaks.

3.5 Multiple peak

The exponential distribution has been used widely because it is well established and, since there are only two parameters to deduce, it is simple to use in a quantitative manner. Use has also been made of other proposed models such as the truncated, gamma and three-peak models. But in many situations there is still a discrepancy between the proposed theoretical model and the observed dropsize distribution.

As noted there has been significant theoretical work suggesting much more complicated dropsize distributions can occur, such as multiple-peaked spectra (e.g., Valdez and Young, 1985; List *et. al.*, 1987, List and McFarquhar, 1990). Examples from disdrometers and Doppler radars showing more than one precipitation peak in the spectrum have been reported (Zawadzki and Antonio, 1988; Steiner and Waldvogel, 1987; Gossard *et. al.*, 1990).

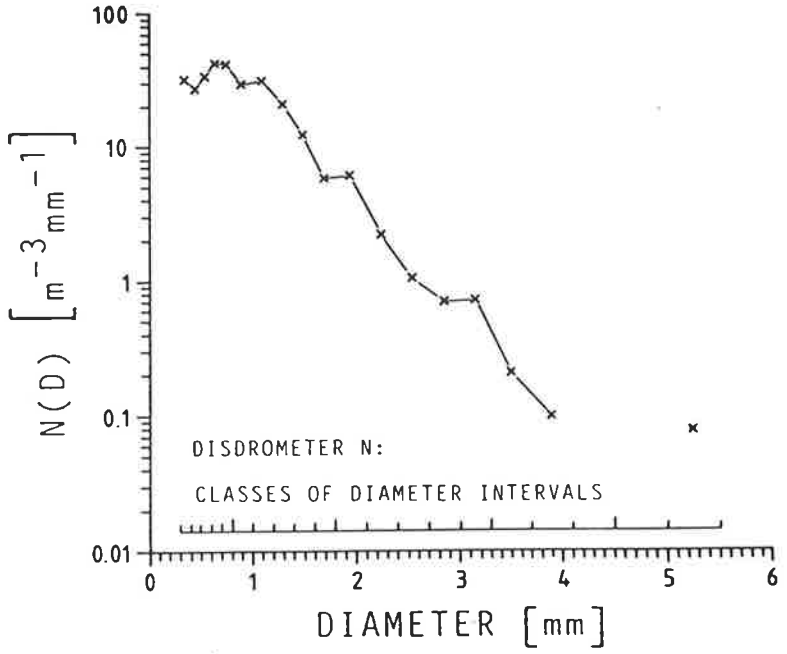

Figure 3.5: Raindrop size distribution measured on 16 August 1983 from 18:21 until 18:49 local standard time. [After Steiner and Waldvogel, 1987]

These observations clearly indicate that actual spectra may have multiple peaks.

The evolution of peaks in the dropsize spectrum is due to various physical processes taking place in the atmosphere and hence a simple theoretical approach can not adequately explain these multiple-peak distributions. One example of a multiple peak distribution which was observed on 16 August 1983 is shown in Fig. 3.5 (Steiner and Waldvogel, 1987). Peaks can be seen clearly for drop diameters of 0.7, 1.1, 1.9 and 3.2 mm.

3.6 Other important parameters

By knowing the parameters of the rain dropsize distribution N_o and λ, we can easily obtain the other important parameters in relation to cloud and its optical properties.

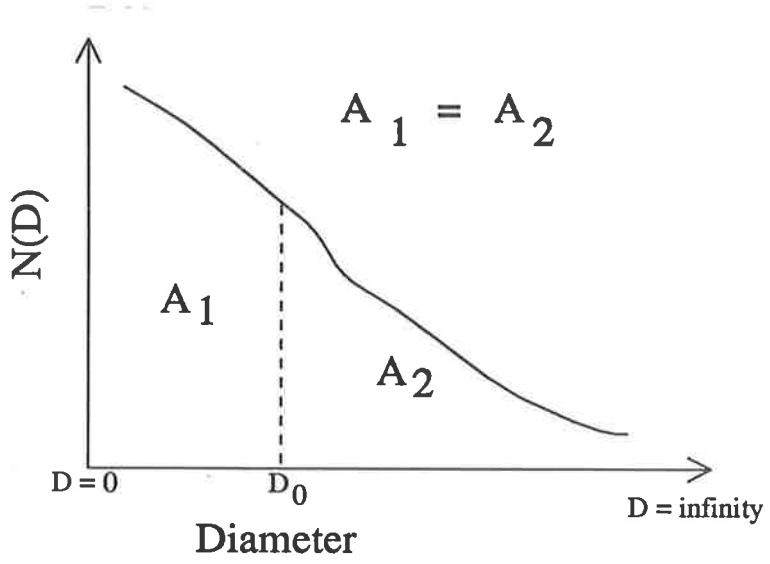

Figure 3.6: An example of a drop size distribution curve showing the median drop diameter D_0 which divides the distribution curve into two equal areas, labelled A_1 and A_2.

3.6.1 Median drop diameter

The area A under the distribution curve is

$$A = \int_0^\infty N(D)dD. \tag{3.22}$$

Assuming the dropsize distribution is an exponential,

$$A = \int_0^\infty N_0 e^{-\lambda D} dD = \frac{N_0}{-\lambda}\left[e^{-\lambda D}\right]_0^\infty. \tag{3.23}$$

The median drop diameter D_0 divides the size distribution curve such that the area on each side of it is the same. Hence form fig 3.6,

$$\frac{N_0}{-\lambda}\left[e^{-\lambda D}\right]_0^{D_m} = \frac{N_0}{-\lambda}\left[e^{-\lambda D}\right]_{D_m}^\infty. \tag{3.24}$$

Simplifying gives,

$$D_m = \frac{\ln 2}{\lambda}. \tag{3.25}$$

Liquid water content

An important parameter in studying radar estimates of rainfall intensity is the liquid water content, M, of the cloud at various levels. This can be defined in terms of the size distribution function

$$M = \frac{\pi \rho_w}{6} \int_0^\infty D^3 N(D) dD \tag{3.26}$$

where ρ_w is the density of the drop.

Apart from the rainfall estimation, knowledge of the spatial distribution of liquid water content within the cloud helps to indicate the degree of mixing between rising cloud and its drier environment. Changes in water content are important in the study of the thermodynamic behaviour of the cloud because these changes are associated with the large energy changes taking place in the cloud.

In past observations it has been found that the liquid water content of the cloud can have a minimum value of 0.05 g m^{-3}, ranging to a maximum value of 5.0 g m^{-3}. For stratiform clouds the liquid water content is in the range from 0.1 to 1.0 g m^{-3}, with 0.1 g m^{-3} being the most likely, where as for convective clouds it varies from 0.5 to 2 gm m^{-3}.

Median volume diameter

The median volume diameter D_0 divides the drops into two size ranges for which the total water volume is the same and it can be shown (as in §) that (Appendix C)

$$D_0 = \frac{3.67}{\lambda}. \tag{3.27}$$

Since the physical meaning of D_0 is very easy to understand, often the exponential distribution of dropsize is expressed as a function of D_0 rather than λ, *i.e.*

$$N(D) = N_0 \times exp(\frac{-3.67D}{D_0}). \tag{3.28}$$

Rainfall intensity

The rainfall rate R is the flux of precipitation through a horizontal surface and is measured in terms of the volume flux of water $m^3cm^{-2}sec^{-1}$=$msec^{-1}$ generally expressed in mm h^{-1}. Hence it is clear that the rainfall intensity is the depth of water per unit time. In terms of N(D), it can be defined as

$$R = \frac{\pi}{6}\int_0^\infty N(D)D^3w(d)dD. \tag{3.29}$$

As an example, a rainfall rate of about 25 mmh^{-1} is a clear sign of the presence of a convective cell in the atmosphere. The rainfall rate also can be evaluated from the reflectivity factor Z. For an exponential distribution, Eqn. 3.14 can be expressed as (Rogers and Yau, 1991)

$$Z = N_0\frac{6!}{\lambda^7}. \tag{3.30}$$

Substituting from 3.12, this reduces to

$$Z = N_0\frac{6!}{41^7}R^{1.47} \tag{3.31}$$

which is in the form of a power law $Z = aR^b$ and is generally called the Z-R relation. Meteorologists use various empirical relations. For example Marshall et al. (1955) suggested for stratiform rain,

$$Z = 200R^{1.6} \tag{3.32}$$

where R is in mm h^{-1} and Z is in $mm^6\,m^{-3}$. From observations made in 1967, Joss and Waldvogel (1970) gave a relation

$$Z = 300R^{1.5}. \tag{3.33}$$

These relations vary from place to place and from one system to another.

3.7 Shape of the rain drop

It is well known that the potential energy due to intermolecular forces in a given volume will be a minimum when it is a perfect sphere. Thus rain drops should be spherical in shape. In past observations, it was found that rain drops of diameter less than 0.35 mm are spherical. From 0.35 to 1mm, the shape is approximately an oblate spheroid, whereas the drops of diameter larger than 1mm are flattened with a concave base. Now, which factor is responsible for producing distortion in the raindrop?

As the raindrop falls freely in the atmosphere, aerodynamic forces cause vibration and spin of the drop. This leads to deformation of the drop from its spherical symmetry (Gunn and Kinzer, 1949). If the drops are sufficiently large, the vibration and resultant deformation break up the drops. The vibration of the drops has also been observed by Volz (1960) using a photographic technique at night. For large drops, collisions with surrounding small drops are enough to maintain oscillations (Beard et al., 1983; Johnson and Beard, 1984). Thus it is clear that the most common factors responsible for the distortion of rain drops are the equilibrium aerodynamic effect and transient drop collisions. Beard et al. (1991) commented that in small drops another factor responsible for the distortion is the periodic shedding of eddies in the wake. However, not much work has been done to study the effect of these factors in producing the distortion of raindrops.

The shape of the drops can be studied by dual polarisation radar. The measurement technique is the so-called differential polarisation technique. (Z_{DR}) is the difference in the backscattered power and is measured by radar pulses having vertical and horizontal polarizations. This measurement in the rain is directly related to the axis ratio of the raindrops. Beard et al. (1991) studied the role of eddy shedding using this technique and found that eddy shedding can produce oscillation of larger drops.

The interpretation of the data using radars in precipitation conditions depends upon the shape of the rain drop. Since the rain drop is usually non-spherical, the exact diameter of the droplet has no meaning but rather it is represented by an equivalent drop diameter. It must be remembered that in previous expressions, the diameter D is the equivalent drop diameter which has been estimated from its mass and not the actual diameter.

3.8 Conclusion

On account of the departure of the drop from a spherical shape the numerical calculations of the terminal fall velocity are complicated. However, with much experimental evidence now available, the droplet fall velocity relations are well established for small and large drops.

The study of the size distribution of raindrops is now common from both a theoretical and practical point of view. Zawadzki and Antonio (1988) commented further about the importance of the study of dropsize distributions, saying momentum carried by the raindrops is transferred to the soil upon impact and stimulates soil erosion while pollutants are swept out of the air by the falling raindrops.

The physical mechanisms which affect the size of the drops are micro-physical processes such as condensation, accretion of cloud droplets, evaporation, collision-coalescence, collisional breakup and aerodynamic breakup. Clearly, evaporation and collision-coalescence reduce the small-drop concentration whereas collisional and aerodynamic breakup will reduce the large drop concentration within the cloud volume. The distribution is also controlled by the cloud dynamics that determine the cloud dimensions, the degree of mixing with the environment, the distribution of vertical velocities, the scale and intensity of turbulence and the time interval for which the drops remain within the cloud volume.

Thus the growth of precipitation in nature is a complicated physical process because of

the existence of air turbulence and of different average air motions. Additionally, internal circulation within the drop produced by the viscous drag between the surface and the air has been theoretically predicted. This makes the study of cloud parameters more complicated. The ground-based Doppler radar is now widely used as an essential tool to understand these processes. There is no doubt that the clear-air information obtained by VHF radar make it a potentially powerful tool for remotely determining dropsize distributions. However, on-going efforts are still being made to develop an accurate technique to study the cloud optical properties governed by many complicated physical processes.

Chapter 4

Retrievals of dropsize distributions

4.1 Introduction

In the last 6-7 years, retrievals of dropsize distributions using VHF and UHF radars have been carried out all around the world, but the accuracy of the technique is still uncertain. The uncertainty arises mainly because of the following two factors:

(a) inadequate information about the shape of the precipitation spectra, and

(b) broadening of the precipitation spectra due to various physical processes.

The shape of the precipitation spectrum is still not fully understood. It is well known that the Marshall-Palmer (1948) distribution is not general enough to explain most observed precipitation spectra accurately. Apart from the Marshall-Palmer distribution, discussed in Chapter 3, all other proposed models including gamma distributions, and theoretical work, suggest the existence of more complicated distributions of dropsize, such as a three-peak

model. Due to the difficulty in understanding the exact shape of the precipitation spectra, it is worthwhile calculating the dropsize distributions without assuming any particular shape for the precipitation echo. So, in the present study, emphasis will be given to a dropsize distribution with an arbitrary shape rather than to a particular model.

Removal of spectral broadening of the precipitation echoes is now recognized as an important step in the retrieval process, but the effects of the broadening due to turbulence, beam width and the range resolution are still not fully understood (Sato et al., 1990). The effects of these sources of broadening on the spectral width of radar echoes were discussed by Hocking (1983). The accuracy of the technique in estimating the dropsize distributions depends on the removal of these broadening effects. However, a comprehensive study of the accuracy of the technique has not yet been carried out.

The problem is to recover the population spectra after consideration of realistic statistical variations of the radar signal. So, in the present work, a technique is developed to estimate dropsize distributions using a technique similar to that adopted by Gossard (1988). An examination is made of two different methods of deconvolution that must form part of the technique, and of their relative advantages.

Validation of the technique is performed using simulations with realistic spectral shapes and signal statistics. An error analysis is also included for the further validation of the technique.

4.2 Retrieval technique

In this retrieval method, the clear-air and precipitation peaks are separated. The spectra are cutoff at the position of minimum signal strength between the clear-air peak and the precipitation peak. A tail is extended in the precipitation part to represent a complete

precipitation echo (to eliminate sharp edges from the observed spectrum). Drops with fall speeds in this "tail" obviously cannot be measured as they are obscured by the clear-air signal. A Gaussian curve is fitted to the clear-air part.

It should be noted that there is a physical limit to the size of the droplet that can be measured by a radar. Below this value, the droplet fall velocity is much smaller than the variations in radial wind. Their size cannot be determined even though there are so many of them, because their backscatter is small compared to that from the clear air. So, in the small-diameter regime, the scattering from the droplets helps to increase the magnitude of the atmospheric turbulence component in the observed backscattered spectrum (Sato *et al.*, 1990). In non-precipitating cloud, liquid resides in the small drops, proper handling of the back scattered power near $w = 0$ is very important if radars are to be used to deduce dropsize distributions and cloud liquid water content (Gossard, 1988).

At the large dropsize end of the spectrum, droplets growing by collision rarely exceed 6 mm because, beyond this limit, they are unstable and break up into smaller droplets. Droplets larger than 10 mm in diameter are hydrodynamically unstable and break up, even in a laminar air flow (Pruppacher *et al.*, 1978).

In order to study the possibility of measuring such dropsize distribution spectra, the various minimum and maximum limits of the diameter of the rain drops in the model are considered.

In order to test this technique, artificial data with realistic statistical properties were generated. It is assumed that:

(a) The shape of the spectrum associated with the clear air echoes is well approximated by a Gaussian distribution (Tennekes and Lumley, 1973).

(b) The distribution of precipitation echoes in the model spectrum is based on an exponential distribution, the so called Marshall-Palmer distribution (Marshall & Palmer, 1948), although this was systematically varied in the simulations.

(c) The spectral amplitude is Rayleigh-distributed.

In order to consider realistic statistical variations, a power spectrum of 4096 points is obtained using equation (3.15), and then a random numbers sequence N of the same length is generated with a uniform distribution in the range [0, 1] (Zrnic, 1975; May and Strauch, 1989). Each spectral component is multiplied by -ln (N), which produces power spectral coefficients that follow an exponential distribution. Taking the square of each component of the spectral values gives the spectral amplitude. Similarly, 2π times each component of N gives the phase. The quadrature and in-phase components are calculated to form a complex series. The following mathematical expressions explain these steps.

If $S_1(w)$ is a power spectrum without considering realistic statistical variations, then we define the spectral amplitude, A and phase, ϕ by the following eqns:

$$s(w) = - S_1(w) \log(N) \tag{4.1}$$

$$A = \sqrt{s(w)} \tag{4.2}$$

$$\phi = 2\,\pi\,N \tag{4.3}$$

where s(w) is an exponentially distributed power spectrum and N represents values from a random number distribution from 0 to 1 and equal in size to $S_1(w)$. Quadrature and inphase components of the spectral series are

$$X = A \sin \phi \tag{4.4}$$

$$Y = A \cos \phi\,. \tag{4.5}$$

Now, the complex series (Z) is

$$Z = X + iY \tag{4.6}$$

and a time series is obtained by taking the inverse FT of Z. Samples of 256 points are taken from the time series for analysis. The estimated mean power spectrum, is obtained by averaging 16 of the 256-point spectra. One of the model backscattered power distributions for precipitating conditions, without considering realistic statistical variations, is shown in Fig. 4.1a. Marshall and Palmer's (1948) derived values of λ and N_0 were used (eqns. 3.12 and 3.13). The rainfall rate, R, is taken as 20 mm h^{-1}, the spectral width as 0.5 m s^{-1}, and the mean vertical background wind as 0.5 m s^{-1}. Fig. 4.1b is the model spectrum after the addition of realistic statistical variations, and with 16 spectra averaged together. A model spectrum without the consideration of realistic statistical variations is shown by dotted lines.

The noise was subtracted from the spectrum (not shown in Fig. 4.1) in order to recover the dropsize distribution from the radar spectrum, and the analysis then proceeded in the following four steps:

- Location of the position of the clear air peak;
- Determination of the contribution from the clear-air turbulence;
- Separation of the precipitation echo from the composite spectrum;
- Correction for the spectral broadening of the precipitation echoes due to turbulence and finite beam width by deconvolving the precipitation peak by the Gaussian fitted to the clear air peak.

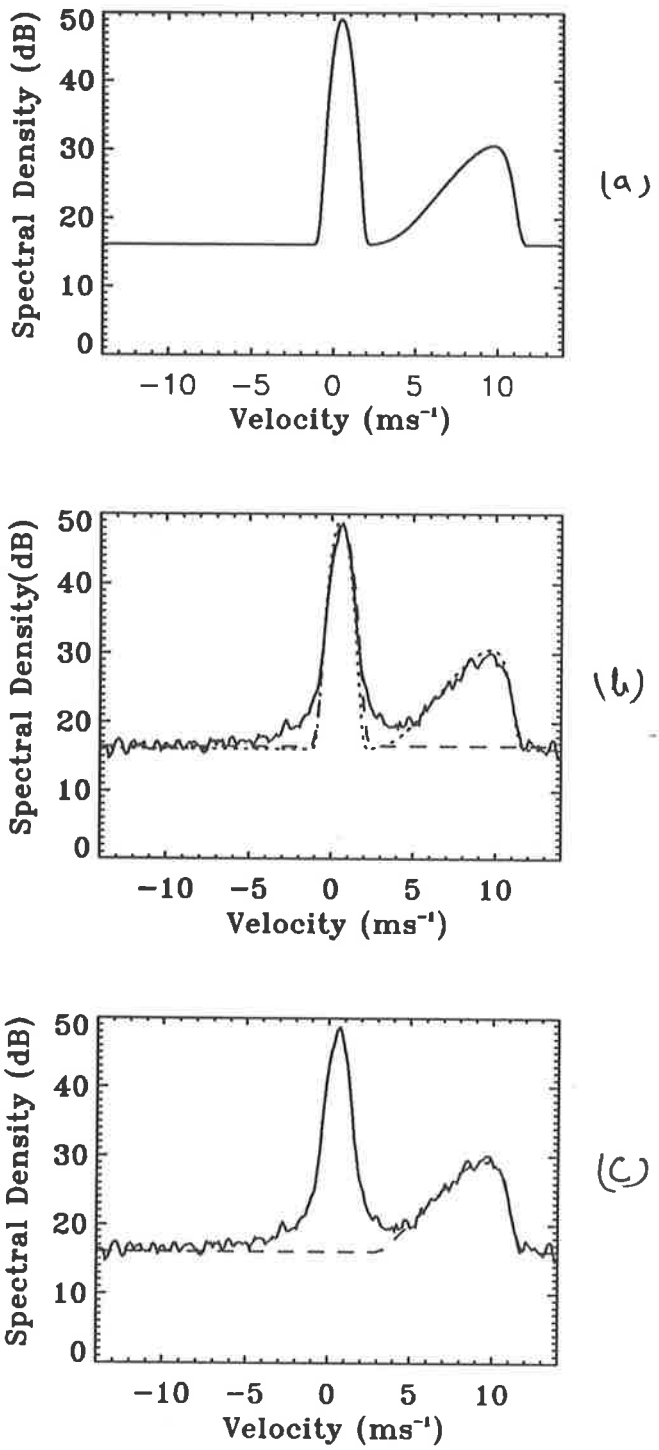

Figure 4.1: (a) Model clear-air and precipitation spectra without realistic statistical variations. (b) as for (a), with realistic statistical variations added, and a fitted Gaussian distribution for the clear-air part (dotted lines). (c) The model precipitaton echo after the truncation of the clear-air part, and with an extended tail added.

To locate the position of the clear-air peak, the first moment is determined from the clear-air echoes. This first moment represents the mean vertical motion $\overline{w}$ of the atmosphere. In this simulation the spectrum was shifted by $\overline{w}$ so that the clear-air peak was at zero vertical velocity (not shown in Fig. 4.1).

To obtain the contribution from clear-air turbulence in the composite spectrum, a Gaussian curve is fitted to the clear-air part of the spectrum, as shown by broken lines in Fig. 4.1b. The next step is to find the contribution from the precipitation particles. As shown in Fig. 4.1c, the precipitation peak is truncated at the position of minimum power between the clear-air and precipitation peaks and a smooth tail is added (broken lines). To remove the broadening effect from the precipitation echo, deconvolution techniques are used. So, the next question to be addressed is how to find the best method of deconvolution to recover the dropsize spectra.

4.2.1 Deconvolution by Fourier and iterative techniques

The relationships used in Fourier and iterative techniques have already been given in equations 3.19 and 3.20. In the Fourier-method deconvolution technique, a problem is caused by the truncation of the FT of the precipitation spectrum, which produces spectral sidelobes in the recovered spectrum. Because of this, the method has limitations, especially in the small- and large-diameter regimes.

Fig. 4.2 shows an example of a deconvolved precipitation spectrum (solid lines), compared with the population spectrum (dotted lines). We can see clearly that the population spectrum can be recovered reasonably well by the Fourier technique. However, the deconvolved spectrum is still wider than the population spectrum. This is probably due to the

windowing effect associated with the truncation of the FT form of the precipitation spectrum. This is not difficult to understand, since the truncation is equivalent to convolution of the spectrum with a window function which is the FT of the truncating "window".

Fig 4.4 shows an example of a deconvolved precipitation spectrum (solid lines) using the iterative technique, compared with the population spectrum (dotted lines). We can see clearly that with the iterative technique, the deconvolved spectra were found to be even wider than those obtained by the Fourier technique. This implies that the Fourier transform method is better than the iterative technique.

However, the iterative technique is much simpler than the FT technique because in the latter there is a problem in selecting an appropriate length into which the FT form of the precipitation echoes is to be subdivided. The accuracy depends upon the length of data

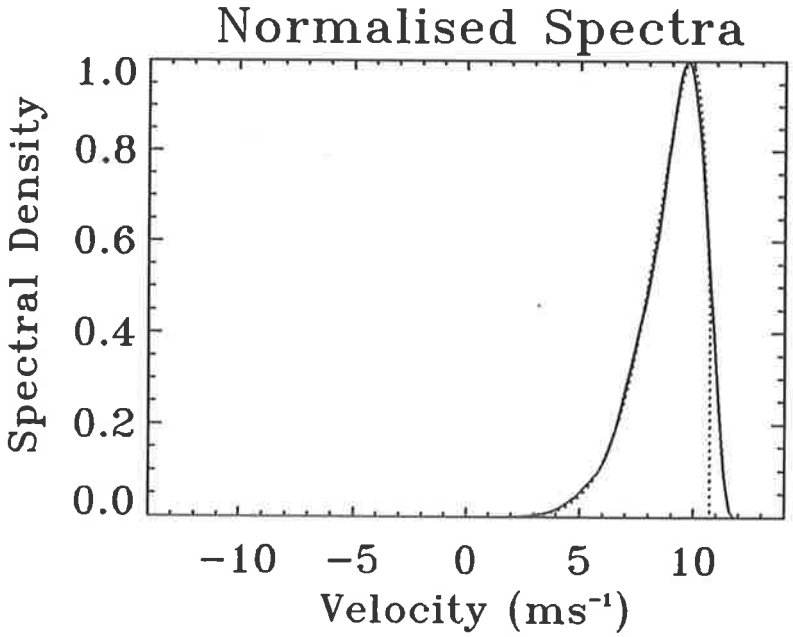

Figure 4.2: The recovered population spectra using the FT method (solid lines) and model population spectra (dotted lines). The clear-air spectral width was 0.5 ms^{-1}.

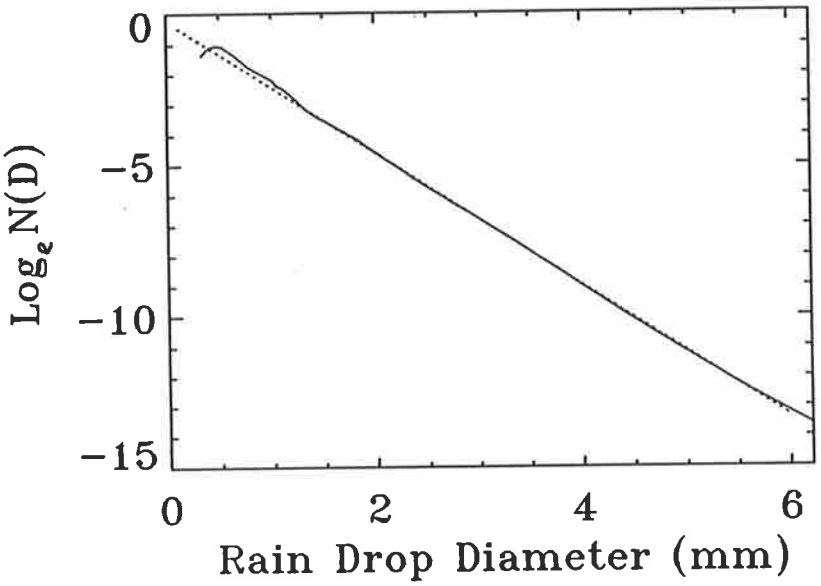

Figure 4.3: The recovered dropsize distribution using the FT method (solid lines) and model population spectra (dotted lines). The clear-air spectral width was 0.5 ms^{-1}.

used in deconvolution and it is hard to find the correct length of the data which has to be used in the deconvolution process based on the FT technique.

As noted, the iterative technique is equivalent to the FT technique with a different truncation function, but it appears as if this window is narrower than the FT window (implying convolution with a broader function) for a small number of iterations. Both techniques effectively filter the spectrum and neglect the higher-frequency components of the dropsize distributions. Since we are losing all the information lying in the higher frequency parts of the population spectra, the retrieved dropsize spectra are smoother than in the model. On the other hand, with the iterative technique, the sidelobe problem does not exist as the truncation function is smoother.

In this work, the dropsize distributions are estimated using both techniques. As an

example, Figs. 4.3, and 4.5 show the calculated values of dropsize distributions after re-

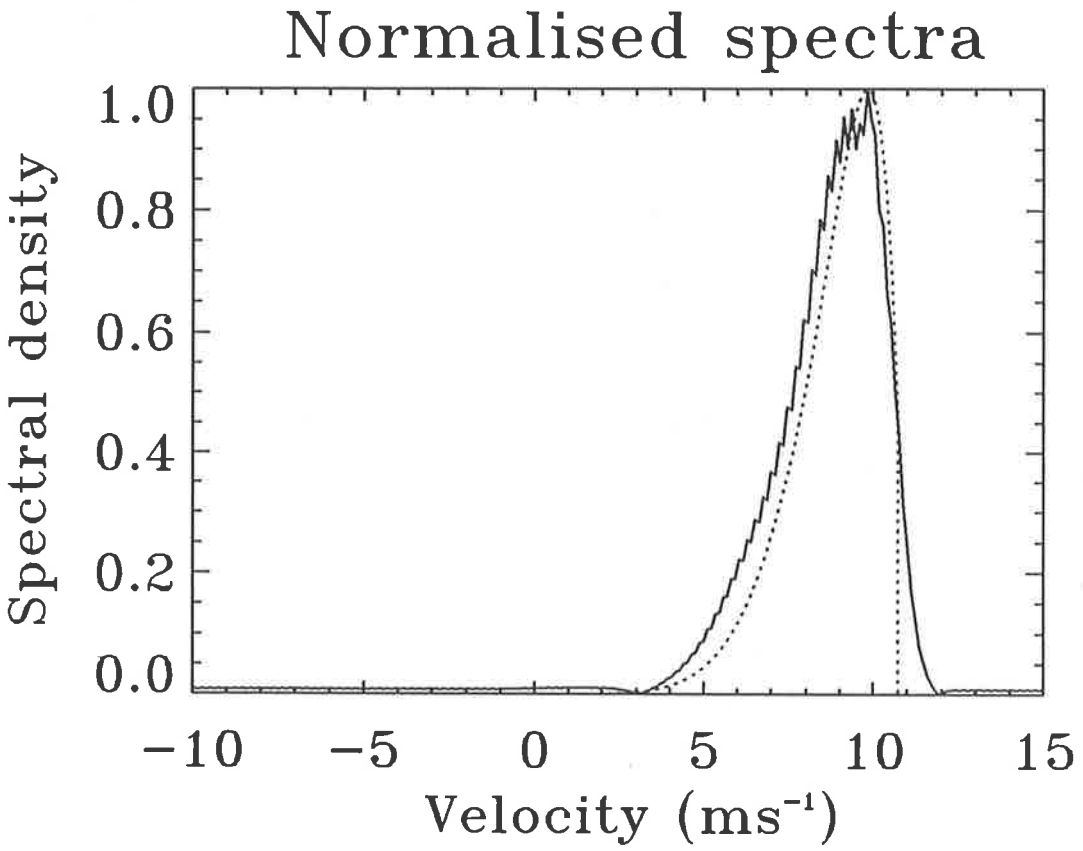

Figure 4.4: The recovered population spectra using the iterative method (solid lines) and the model population spectra (dotted lines). The clear-air spectral width was 0.5 ms^{-1}.

covery of the population spectrum using the Fourier-transform technique and the iterative technique. The dropsize distribution calculated using the iterative technique departs significantly from the model dropsize distribution, especially in the smaller diameter regime. The results from the Fourier technique are seen to be in better agreement with the model spectrum.

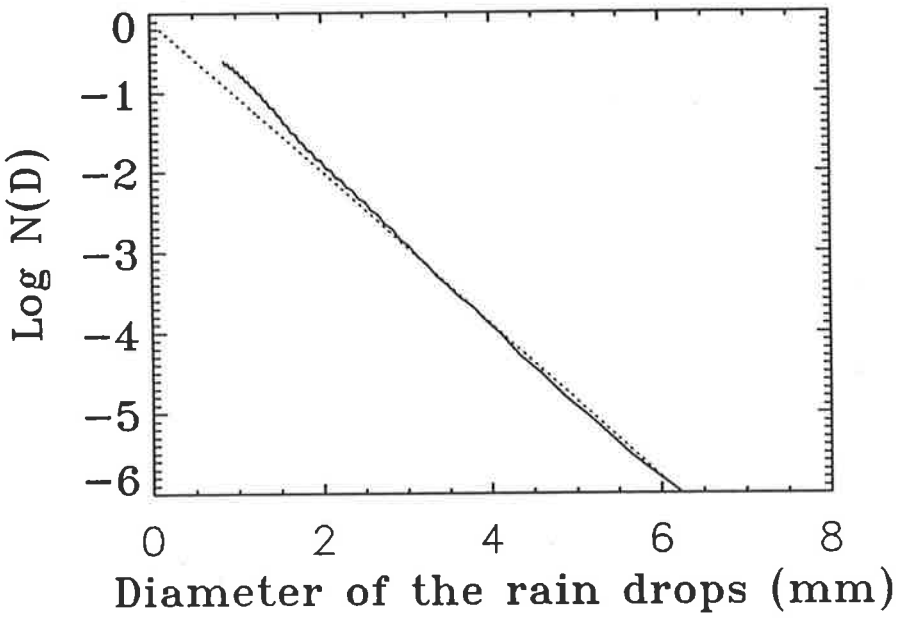

Figure 4.5: The recovered dropsize distribution (solid lines) using the iterative method and model population spectra (dotted lines). The clear-air spectral width was 0.5 ms^{-1}.

4.3 Error analysis

The accuracy and limitations of the retrievals are now explored in more detail. Firstly, suppose the dropsize distributions are exponential, as for the Marshall-Palmer (1948) distribution, but are sharply truncated at some maximum dropsize. Can the above methods retrieve this distribution?

Fig. 4.6, 4.7, and 4.8 show results where the maximum dropsize is truncated at 2, 4, and 6 mm, respectively. Results of 100 simulations using the FT technique are plotted on each graph (solid lines) in order to estimate the deviation from the mean value. The truncated exponential distribution (dotted lines) can be seen clearly in the 0 - 2 mm plot. There is a slight departure of the dropsize distribution in the 0 - 2 mm plot from the exponential distribution but this

departure can not be seen in the 0 - 4 and 0 - 6 mm plots. From the simulations the cutoff

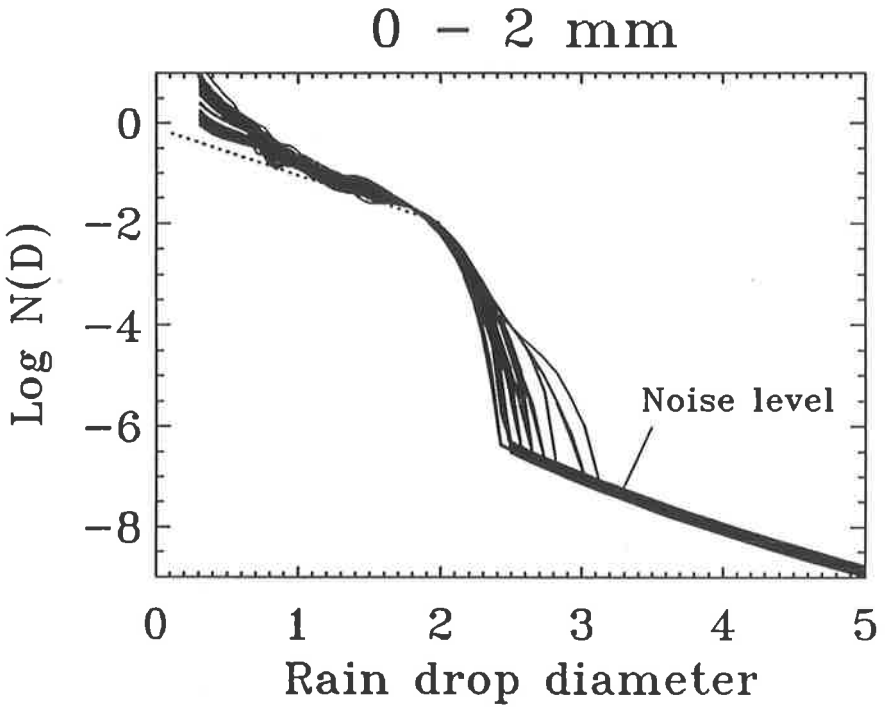

Figure 4.6: The results of 100 successive simulations where the dropsize distribution spectrum has had drops with diameters greater than 2 mm removed. The dotted line for the truncated exponential distributions.

in the dropsize distributions can be seen up to 3 mm. At 4 mm, the cutoff can be seen most of the time, but often appears as just a steepening of the decrease with drop diameter. Above 4 mm in diameter the effect of the cutoff is hard to see. This can be understood by considering the terminal velocity of droplets of different sizes. For larger drops the velocity changes only slowly, *e.g.* the terminal fall speed (referring to Fig. 3.1) for drops of 4, 5, 6, and 7 mm diameter is 8.72, 9.13, 9.37 and 9.50 ms^{-1} respectively, at sea level. Given that we have some residual broadening of the fall-speed spectrum, such small changes are difficult to resolve.

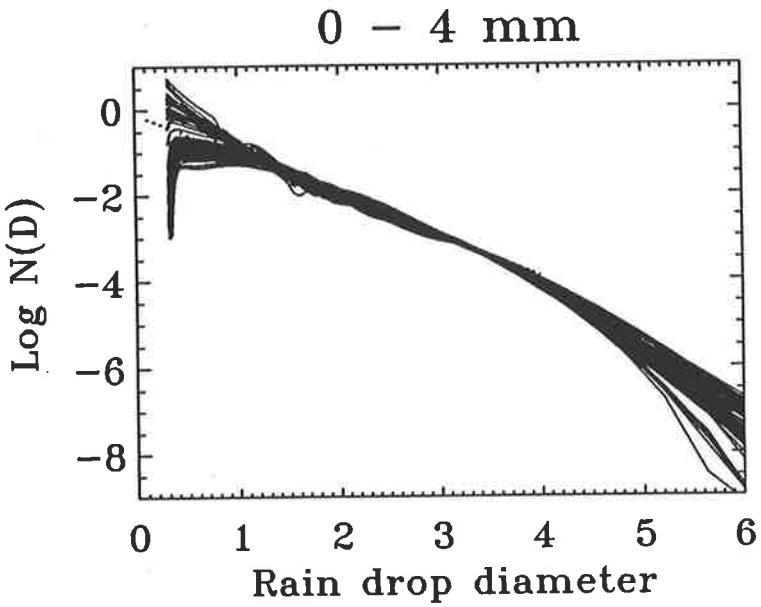

Figure 4.7: As for Fig. 4.6, but for drops with diameters greater than 4 mm removed.

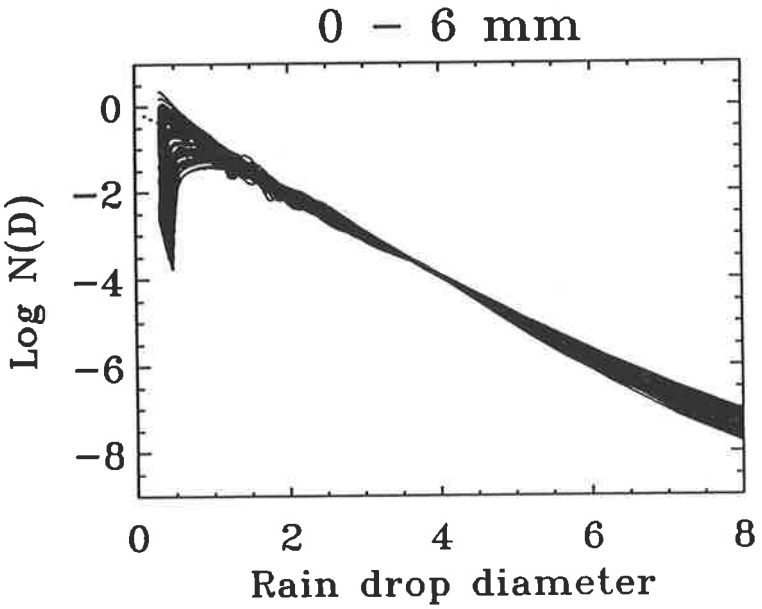

Figure 4.8: As for Fig. 4.6, but for drops removed with diameters greater than 6 mm.

The calculated dropsize distribution (solid lines) and associated departures (dotted line) from the mean values are plotted in Figs. 4.9, 4.10 and 4.11. The mean dropsize distributions are the results of hundreds of simulations performed for Figs. 4.6, 4.7, and 4.8. using various cutoff values. The departures are taken as two standard deviations from the 100 different simulated values.

The relative difference (broken line) of the recovered dropsize distribution from its model spectrum is also shown on these graphs. It can be seen from these plots that the departures from their mean values are small. The relative difference from the model spectrum becomes large only as the small-diameter regime is approached *i.e.*, as the truncation point of the spectrum is reached.

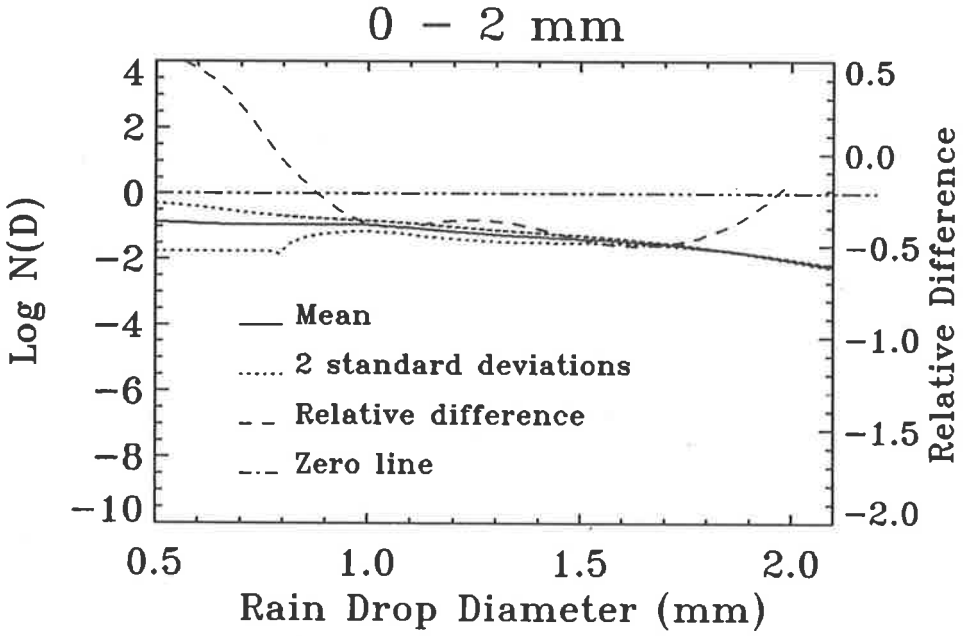

Figure 4.9: Departures (two standard deviations indicated by dotted lines) from the mean (solid line) dropsize distribution of 100 simulations and the relative difference (broken line) from the model spectrum for a cutoff value of 2 mm. This plot is useful only within the cutoffs where there are significant numbers of drops.

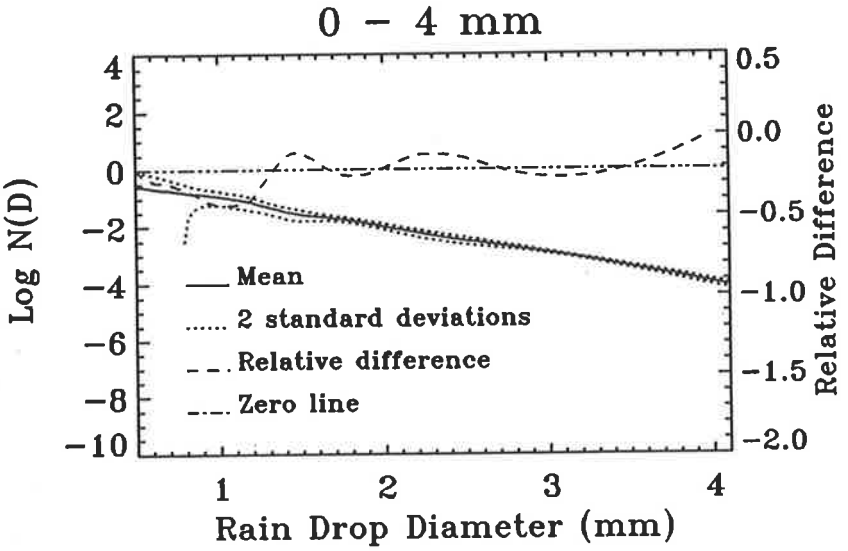

Figure 4.10: As for Fig. 4.9, but for a cutoff value of 4 mm.

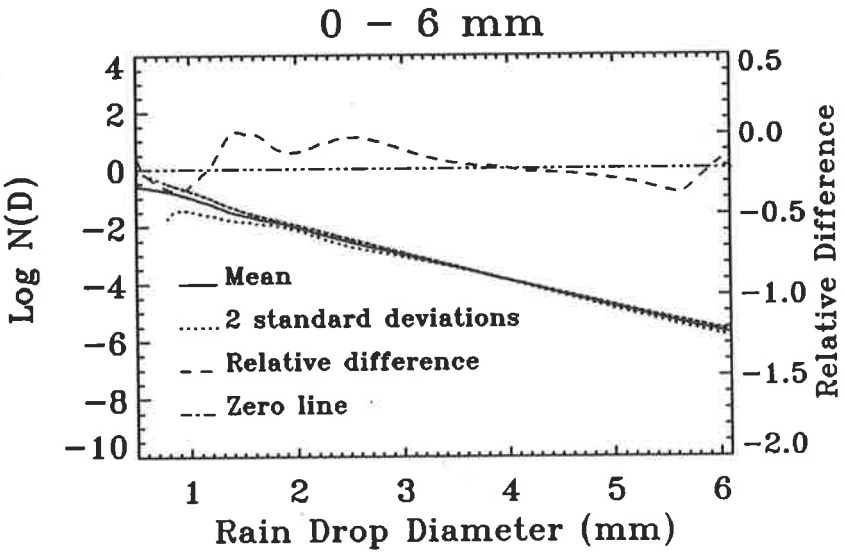

Figure 4.11: As for Fig. 4.9, but for a cutoff value of 6 mm.

For example, in the 6-mm cutoff plot (Fig. 4.11), for diameters greater than 0.5 mm, the relative error is less than 20 % and, above 3 mm, the relative error is less than 10 %. In the 4 mm cutoff plot (Fig. 4.10), the relative error above 0.5 mm is less than 10 %, except for one or two points at the end. However, in the 2 mm cutoff plot (Fig. 4.9), the relative error is larger (20 - 30 %). This illustrates that there is some limitation to the method in the small-diameter regime. This departure can also be seen in Fig. 4.6.

As mentioned earlier, the radar cannot detect drops of diameter less than a certain limit. To study this effect, drops smaller than a threshold value were removed from the model spectrum, and then the dropsize distributions were recalculated for various thresholds and for a clear-air spectral width of 0.5 ms^{-1}.

Fig. 4.12 and 4.13 show the dropsize distributions with thresholds at 1 mm and 3 mm. In these simulations, it was found that the cutoff below 1 mm in diameter is hard to determine, and between 1.0 and 1.5 mm the existence of the cutoff is sometimes not observed. However, above 1.5 mm in diameter, the cutoff in the dropsize distributions is easily detectable for this clear-air spectral width.

The precise limits on the minimum resolvable dropsize will clearly depend on such factors as the relative amplitudes of the two peaks (as larger precipitation peaks mean that smaller drops can be resolved), and the width of the clear-air peak itself. As the clear-air peak broadens, the minimum resolvable diameter will increase. However, the value of the width and the relative amplitudes chosen in the simulations presented here are typical of what we have observed in stratiform rain with 50 MHz profilers in Darwin and Adelaide. Note also that this technique will be applicable to profilers operating near 400 and 900 MHz, but with these higher frequency profilers the relative magnitudes of the two peaks will be very different. Smaller drops can be detected, but for more intense rain the clear air peak

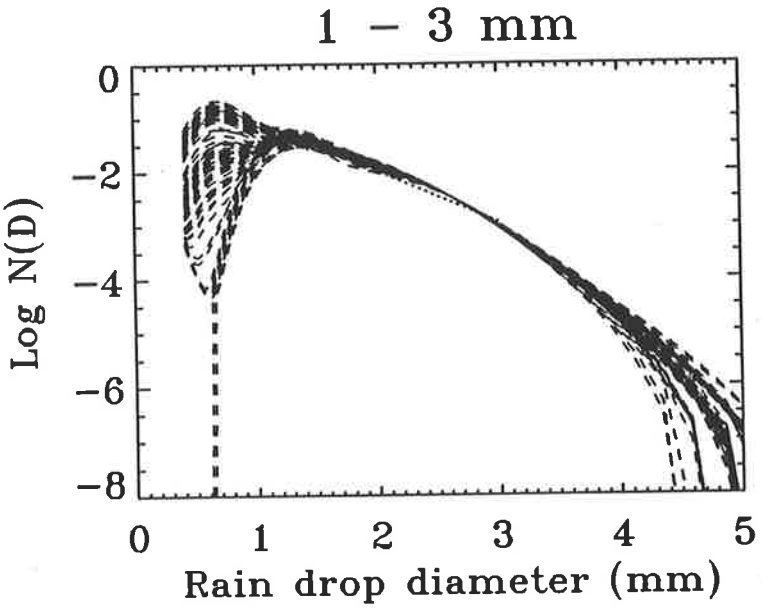

Figure 4.12: The results of 100 simulations with dropsizes between 1–3 mm included in the model.

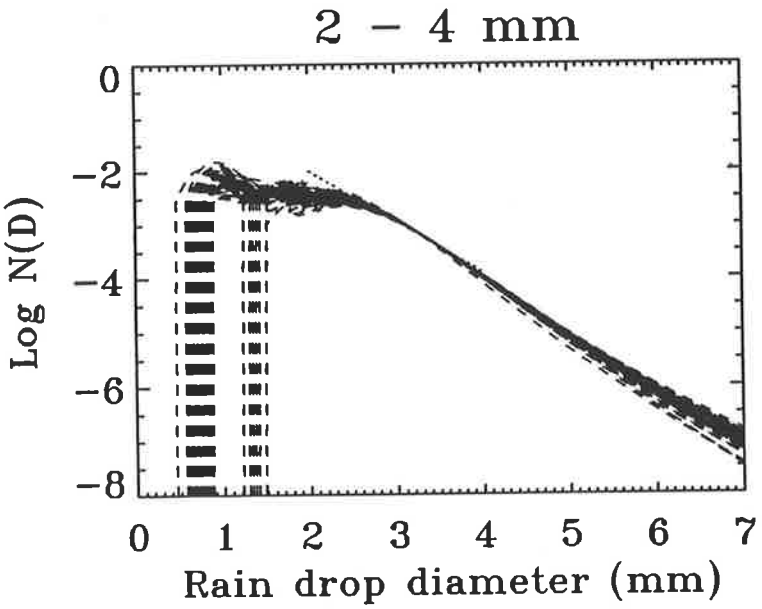

Figure 4.13: As for Fig. 4.12, but for the diameter range 2–4 mm.

may not be visible at the higher frequencies, so that retrievals will require mixed-frequency techniques (e.g., Currier *et al.*, 1992).

4.3.1 Effect of the clear-air spectral width

What would be the effect of the clear-air spectral width on this retrieval technique? To what extent can the clear-air spectral width be used? One expects that the broader the clear air echo, the greater the smearing effect in the precipitation echo and the smaller the likelihood of recovering the population spectra with the inclusion of realistic statistical variations.

To deal with these problems, a series of simulations have been carried out by changing the spectral width from 0.5 to 2 ms^{-1} in the steps of 0.5 ms^{-1}. It was assumed that in the lower-diameter regime, there were no drops smaller than 2 mm in diameter. Similarly in the upper diameter regime, the maximum diameter was taken as 6 mm. Can we see the cutoff at 2 mm in all spectral widths?

Fig. 4.14 shows the result of one hundred simulations for the spectral width of 0.5 ms^{-1} (upper diagram) and 1.0 ms^{-1} (lower diagram). Here the dropsize distribution has been plotted against the diameter of the drop. The dotted line represents the model dropsize distribution. The cutoff can be seen clearly when the clear-air spectral width is 0.5 ms^{-1}. When the clear-air spectral width is 1.0 ms^{-1}, the cutoff can frequently be seen. However, when the spectral width is greater than 1.0 ms^{-1} the cutoff is hard to see.

The same is true for another set of results of one hundred simulations (Fig 4.1) for a clear-air spectral width of 1.5 ms^{-1} (upper diagram) and 2.0 ms^{-1} (lower diagram). Here, at 2.0 ms^{-1} the departure from the model dropsize distribution is random, not only in the

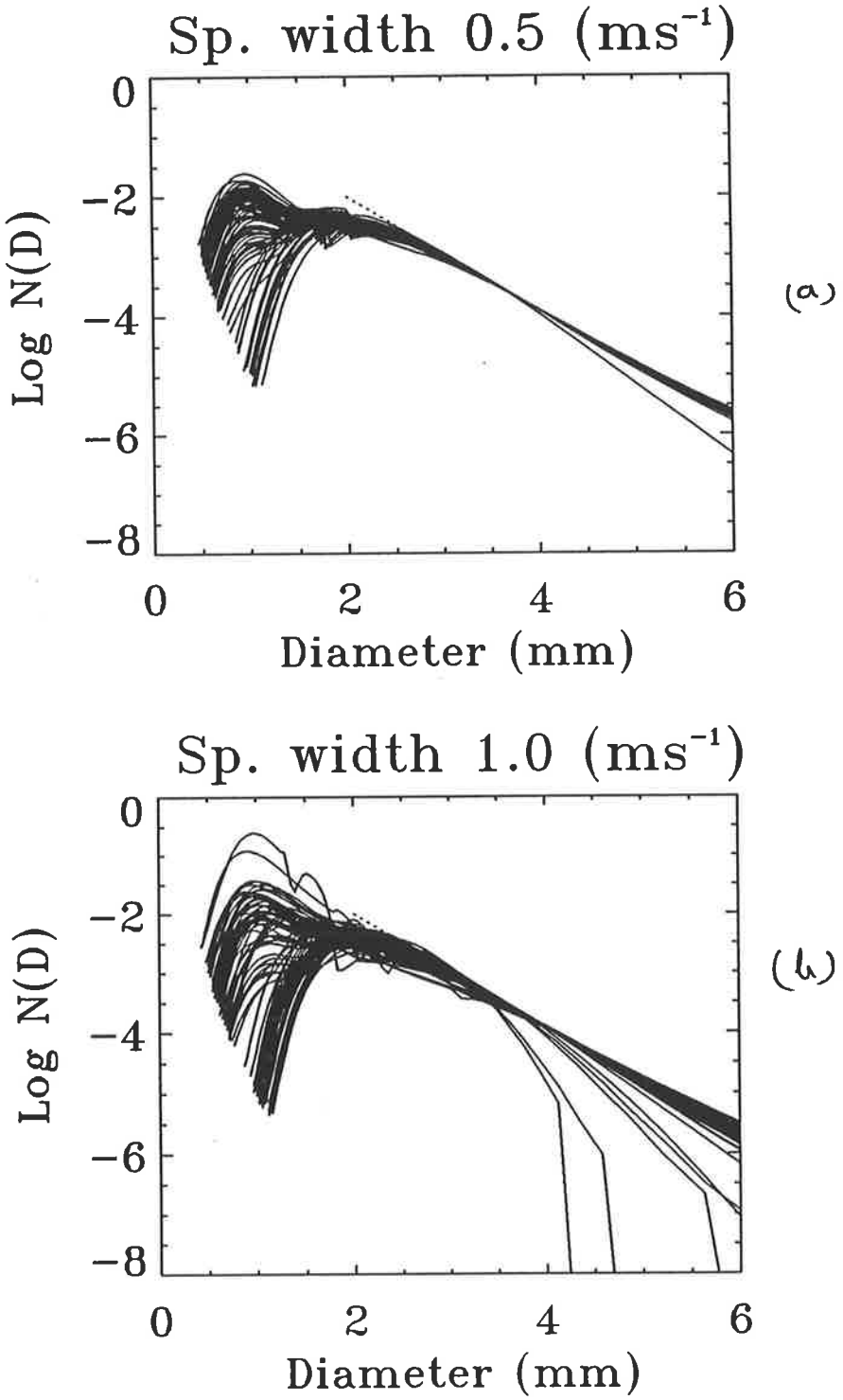

Figure 4.14: The recovered dropsize distribution (solid lines) and model population spectra (dotted lines). The clear-air spectral width was (a) 0.5 ms^{-1}, and (b) 1.0 ms^{-1}.

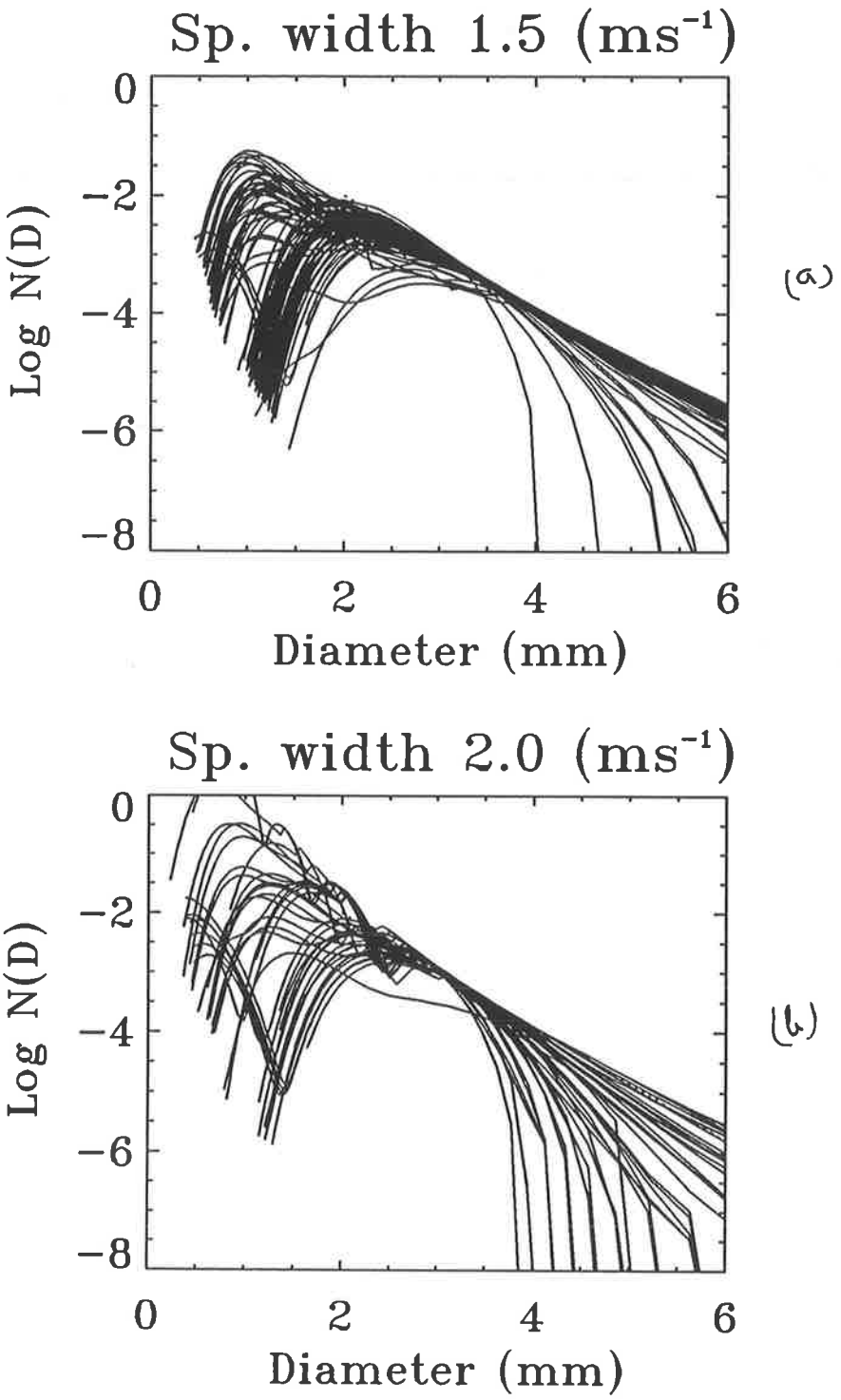

Figure 4.15: The recovered dropsize distributions (solid lines) and model population dropsize distributions (dotted lines). The clear-air spectral width was (a) 1.5 ms^{-1}, and (b) 2.0 ms^{-1}.

lower diameter regime but also in the upper diameter regime, and very large even well below the upper limit of 6-mm diameter. This simulation clearly gives evidence that when the spectral width is around 1.5 ms^{-1} or greater, the retrieved values of the dropsize distribution are not reliable.

4.3.2 Multiple-peaked spectra

As discussed in § 3.5, "the real dropsize spectrum may have multiple peaks". The presence of such distributions suggests that the approach to dropsize retrievals here may be superior to that in which a particular spectral form is assumed. It needs to be demonstrated that multiple-peaked spectra can indeed be resolved, given the limitations in the retrieval method.

A series of simulations was carried out in which there were two distinct peaks associated with the distribution. To produce multiple peaks, two truncated exponential distributions were used, these being:

$$N_1 = N_0 \times e^{-\lambda_1 D} \qquad \text{for} \qquad 0 < D < 1.5\,\text{mm} \tag{4.7}$$

$$N_2 = N_0 \times e^{-\lambda_2 D} \qquad \text{for} \qquad 1.5 < D < 10\,\text{mm} \tag{4.8}$$

The true reflectivity weighted precipitation echo is (eqns. 3.14 and 3.17)

$$P_1(w) = \frac{1}{Z_1} N_1(D) D^6 \frac{dD}{dw} \qquad \text{for} \quad 0 < D < 1.5\text{mm} \tag{4.9}$$

$$P_2(w) = \frac{1}{Z_2} N_2(D) D^6 \frac{dD}{dw} \qquad \text{for} \quad 1.5 < D < 10\,\text{mm} \tag{4.10}$$

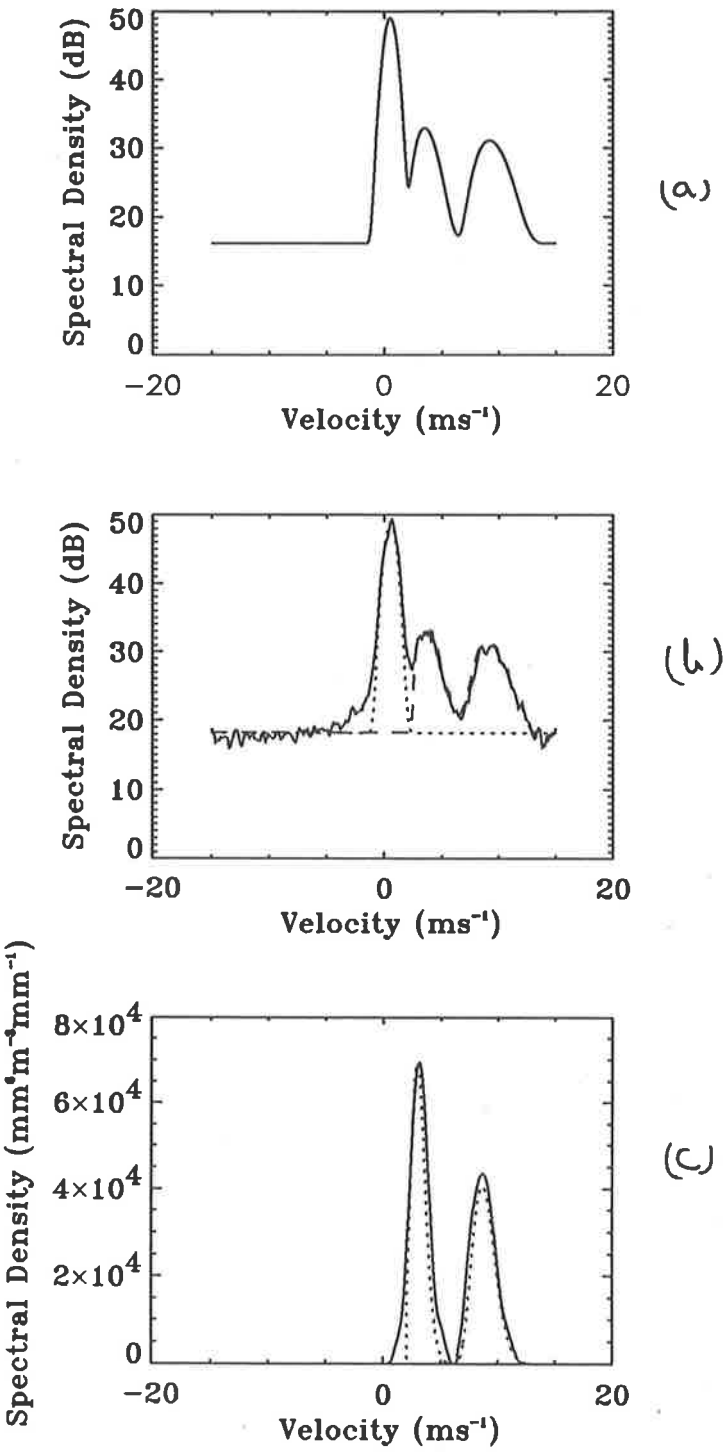

Figure 4.16: Double peak spectra with and without inclusion of realistic statistical variations (a)Population model for double-peak spectrum, (b) "observed" spectrum, and (c) reflectivity-weighted fall-speed spectrum of hydrometeors after the deconvolution process.

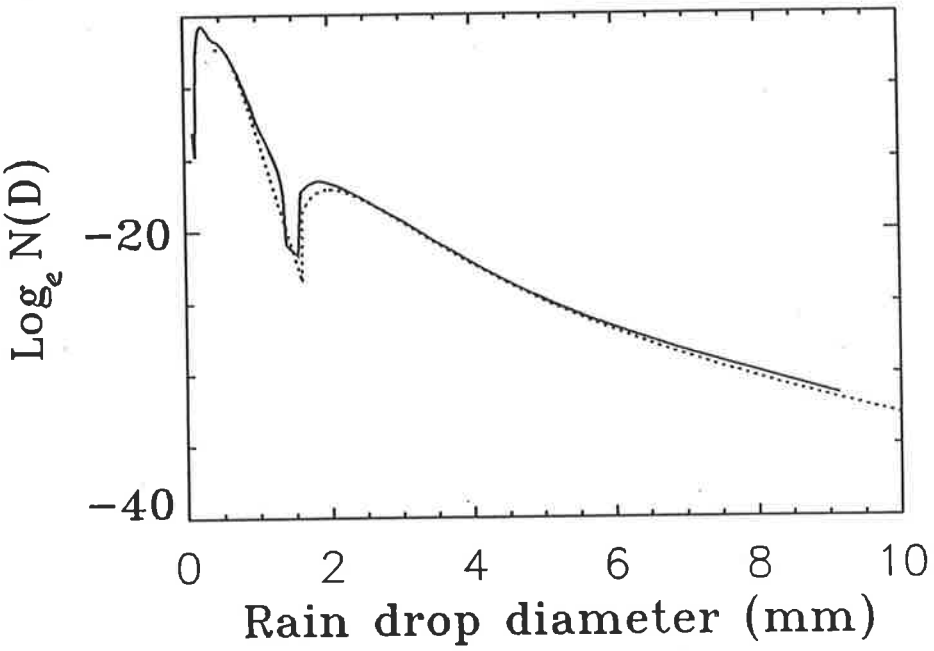

Figure 4.17: The recovered multiple-peaked dropsize distributions (solid lines) and model multiple-peaked population spectra (dotted lines).

Finally the multiple-peak spectrum is calculated using eqn. 3.15. As an example, Fig. 4.16 shows, respectively, the population model spectrum (Fig. 4.16a), the model spectrum with realistic noise (Fig. 4.16b), and the deconvolved reflectivity-weighted fall-speed spectrum (fig 4.16c). Here a clear-air spectral width of 0.5 ms^{-1} and a mean background wind of 0.5 ms^{-1} were used. The two peaks can be clearly seen in the raw data, and the deconvolution procedure clearly captures them both. The results of 100 simulations of the full retrieval process are shown in Fig. 4.17, and it is clear that the technique can resolve the two peaks with an accuracy similar to that obtained for simpler distributions. Of course, similar restrictions to those discussed earlier will apply at small-and large-drop diameters.

4.3.3 Strong precipitation echo

As discussed in §3.3.3, when a centimetre-wavelength radar is used, the precipitation echo predominates over the clear-air echo in the radar backscattered spectrum. This phenomenon can be explained quantitatively. If η is the radar reflectivity and Z is the radar reflectivity factor for the prevailing precipitation conditions, (Gossard and Strauch, 1983)

$$\eta = 0.93 \left(\frac{\pi^5}{\lambda^4}\right) Z . \tag{4.11}$$

where λ is the radar wavelength. The backscatter from the clear air turbulence is (Gossard and Strauch, 1983)

$$\eta = 0.38 \left(\frac{1}{\lambda^{\frac{1}{3}}}\right) C_n^2 . \tag{4.12}$$

From 4.11 the backscatter from the droplets increases with the decrease in the radar wavelength, whereas from 4.11 this increase in backscatter from the the clear-air turbulence is much smaller. For this reason, precipitation echoes are strong enough for detection by weather and UHF radars even if there is only drizzle in the atmosphere.

Is the retrieval technique capable of solving the case where the precipitation echo is much larger than the clear-air echo? Simulations were performed by changing random numbers in the retrieval technique. Fig. 4.18a is an example where the clear-air echo is 5 db less than the precipitation echo for typical values of λ and N_0 of 2.0 mm^{-1} and 8000 $m^{-3}mm^{-1}$. The

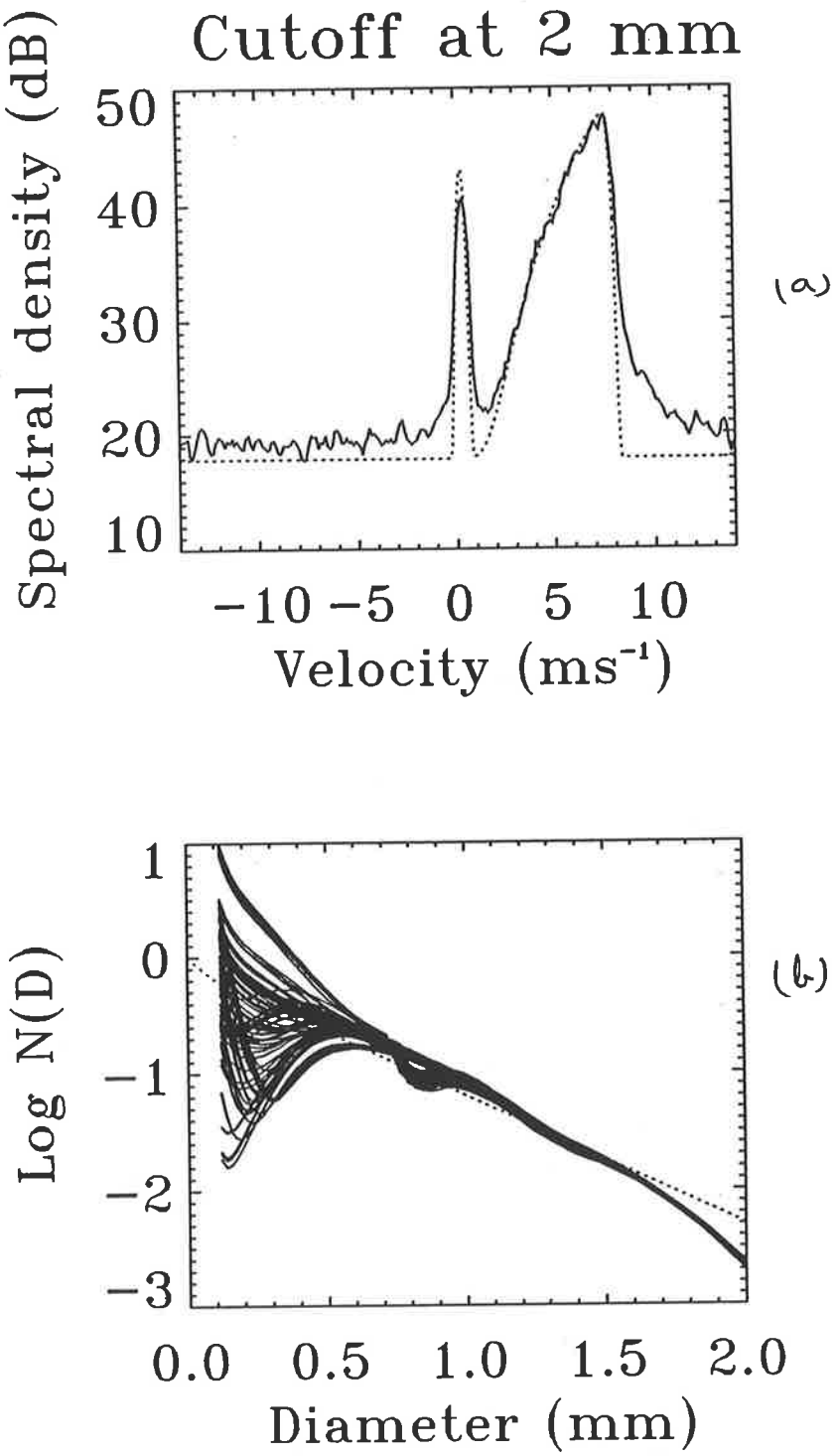

Figure 4.18: (a) An example of a model backscattered spectum where the precipitation echo is larger than the clear-air echo, for a typical value of clear-air spectral width of 0.2 ms^{-1}. (b) Dropsize distributions estimated from one hundred simulations (solid lines) and a population dropsize distribution (broken lines) with λ and N_0 of 2.0 mm^{-1} and 8000 $m^{-3}mm^{-1}$.

Here the scale in the x-axis has been stopped at 2mm, because the deviation from the model spectrum were almost the same as in previous figures 4.6, 4.7 and 4.8. There are some problems of underestimation of the size distribution of dropsize near and beyond the cutoff values.

spectral width was 0.3 ms^{-1} and the mean background wind was 0.1 ms^{-1}. To give more attention to the small diameter regime, a maximum drop diameter of 2 mm was chosen.

Fig. 4.18b is a result of one hundred simulations. The retrieved dropsize distributions are shown by solid lines and the true dropsize distribution by broken lines. The size distributions can be retrieved to a diameter as small as .2–.3 mm but the accuracy in this small-diameter regime is low. A cutoff at 2 mm in diameter is also clearly visible.

4.4 Real data analysis

The precipitation echoes were detected using Adelaide VHF radar for the first time on September 30, 1993. The observations were taken during the passage of cold fronts. The precipitation echo was detected many times during the 24 hr radar operation, but was not continuous for more than 15 minutes at anyone time.

The radar specification is given in Table 4.1

Table 4.1

Adelaide profiler specifications	
Latitude	35° S
Longitude	138° E
Tx. Frequency	54.1 MHz
Direction	Vertical
PRF	4096 Hz
No. of coherent integration	256
No. of points transferred per data set	1024
Averaging time	2 mins

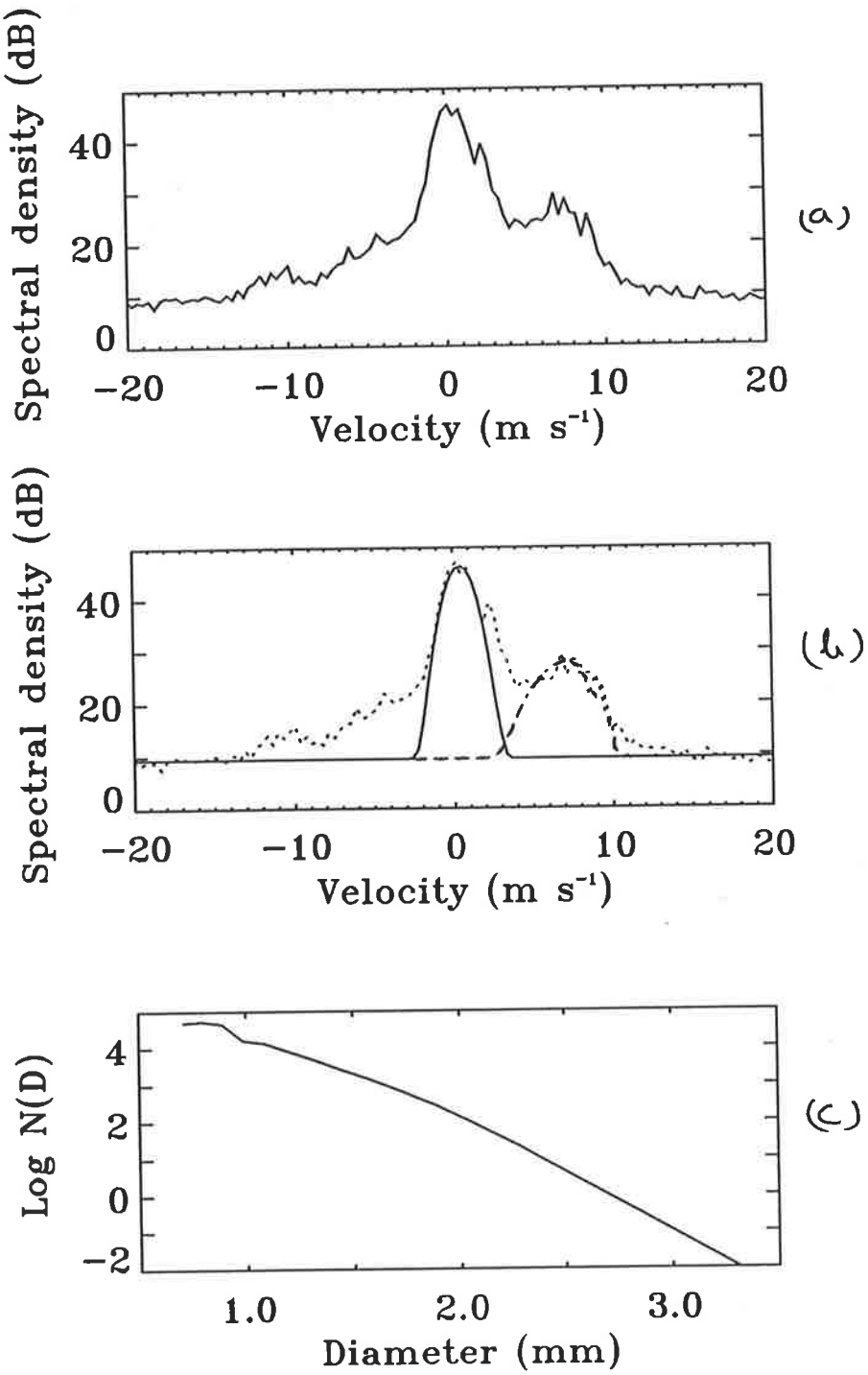

Figure 4.19: Observed power spectrum using Adelaide VHF radar (a) The clear air and the precipitation echoes(b) Fitted Gaussian spectrum (solid line) and precipitation spectrum with an extended tail (broken lines) (c) Dropsize distribution.

Fig. 4.19a is a velocity power spectrum observed on 30 September, 1993 at a height of 2.5 kms. Here the peak of the precipitation echo is $\sim$ 13 dB less than the peak of the clear air echo. The precipitation echo was detected only in the lower heights from 2 to 3.5 km.

To estimate the dropsize distributions, the technique described in § 4.2 is used. A Gaussian spectrum (solid line) fitted to the clear-air part of the power spectrum, separated precipitaion echo (broken lines) from the power spectrum and the complete power spectrum (dotted lines) are shown in Fig. 4.19b. The estimated size distributions is shown in Fig. 4.19c. It should be noted that these values of size distribution are only the relative values.

The Adelaide VHF radar cannot detect the echo below 2 km, whereas the melting layer in the Adelaide lies somewhere between 1.5-2.5 km. For this reason, a low level radar is essential in order to determine the height profiles of dropsize distributions.

4.5 Conclusion

A technique is demonstrated for the recovery of rain-dropsize distributions, after addition of realistic statistical variations. No particular shape of the precipitation spectrum is assumed, so the technique is quite general in its application. The technique is shown to have good statistical accuracy ($\sim 10-20\%$) for reasonable averaging, especially in the dropsize region ranging from about 1.5 to 4 mm. With this technique, the existence of cutoffs in the spectrum can be identified over a wide range of drop diameters. It was also found that the accuracy of the technique depends upon the spectral width of the clear-air echo. If the clear-air spectral width is about 1.5 ms^{-1} or more, the reliability of the recovered values will be reduced. It is also demonstrated that this technique can resolve multiple peaks in the back-scattered spectrum.

The technique is also applied to analyse Adelaide VHF radar data and further application of this technique to obtain the height profiles of dropsize distribution in deep convective storms in Darwin will be discussed in chapter 8.

There are, however, significant limitations at the very small and very large ends of the dropsize distribution. This is mainly due to the existence of sidelobes in the recovered spectra and small variation of fall speed from the large diameter and the finite width of the clear-air echo. The recovered spectra are also somewhat broader than the population spectra. Hence more work needs to be done to overcome these limitations. This technique can be extended to include simulations based on data obtained by 915-MHz profilers, where the precipitation echo is much stronger than the clear-air echo for any rain except very light rain. Mixed 50/915-MHz profiler observations are also a field for further work. More detailed study can also be done by including other related meteorological parameters in the analysis.

This technique should have applications in the study of cloud microphysics. The measurements have direct implications for such diverse applications as rainfall estimation from weather radars and the calculation of cloud optical properties. The technique is being applied to 50-MHz radar measurements taken during stratiform rain conditions at locations in both low- and mid-latitudes.

Chapter 5

Ice particles in natural clouds

5.1 Introduction

Ice crystals are likely to form once cloud rises to an altitude where the ambient temperature is less than 0°C. This phase transition from existing water drops or supersaturated vapour can take place by two common processes–the freezing of droplets and direct deposition of vapour to the solid state. In the cloud, the water mass is distributed as a large number of tiny drops and each one has to come in contact with a ice nuclei to change its phase. For this reason, in some cases, liquid droplets at -40°C have been observed in natural clouds. This resistance to freezing is different from our common experience, where water freezes at or below 0°C. At lower temperatures in the atmosphere, the droplets will change their phase only when they are contaminated with foreign particles called "ice nuclei", in a process called hetereogeneous nucleation. However, below -40°C, the drops freeze without solid nuclei in a process called homogeneous nucleation (Rogers and Yau, 1991). Ice crystals generally appear in natural clouds when the temperature drops below -12°C and thereafter they begin to grow. The growth of these ice crystals to particles which are large enough to

1. Ice crystals are likely to form when the ambient temperature drops below 0°C. However, their occurrence and growth are much more pronounced when the temperature of the air drops below 12°C

yield precipitation in a supercooled cloud has been described by many investigators in the last 4-5 decades.

The three main processes taking place in the atmosphere which contribute to the growth of these ice crystals are:

(1) water vapour deposition to the ice particles (deposition)

(2) collision with and freezing of drops on the ice particles (riming or accretion)

(3) collision of ice crytals with other crystals (clumping or aggregation).

These processes are described, qualitatively and quantitatively, in many textbooks on cloud physics (e.g., Mason, 1971; Rogers and Yau, 1991; Young, 1993 and so on)

This chapter deals mainly with the types of ice crystals, their concentrations and the fall-velocity relations. Finally, to give a brief assessment of the possibility of the use of VHF radars to study the growth of ice crystals and their size distributions, some observed spectra during precipitation conditions will be presented, showing their variation with time and height.

5.2 Types of ice crystals

Observations show that ice crystals in natural clouds occur with a large variety of shapes and with different densities. Their beautiful appearance, such as hexagonal or with six arms, drew the attention of scientists from the 15th century onwards. Why should they be six sided or have six arms? The simple answer is that this symmetry comes from the basic crystalline structure of ice.

In the seventeenth century, Hooke (1635-1703) first studied the forms of snow crystals under a microscope. Neuhaus (1855-1915) used microphotograpy to study the shape of

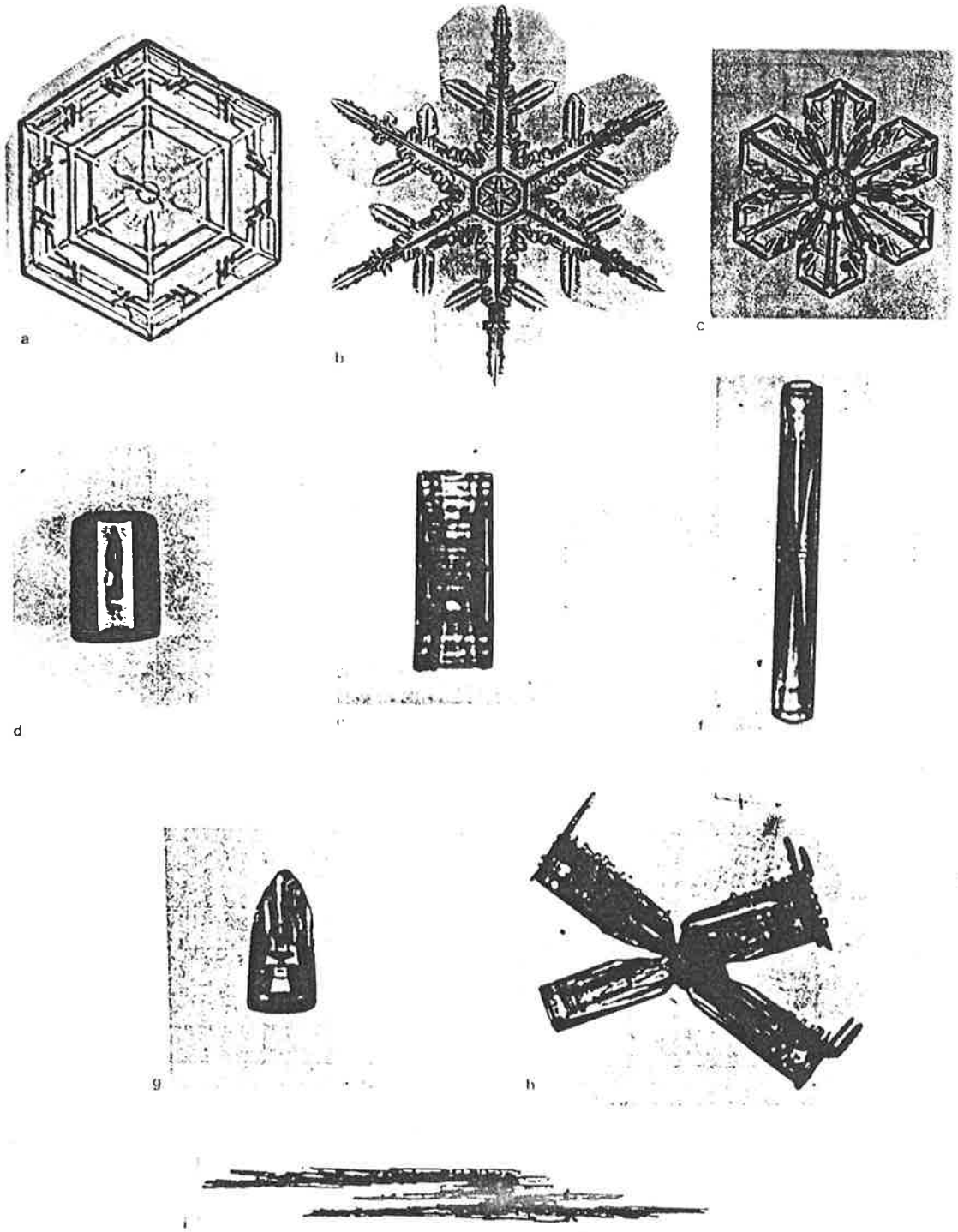

Figure 5.1: Various shapes of ice crystals: (a) simple plate (b) dendrite (c) crystal with broad branches (d) solid column (e) hollow column (f) sheath, (g) bullet, (h) combinations of bullets (i) combinations of needles (From Pruppacher and Klett, 1978).

ice crystals. The most complete collections of snow crystals were presented beautifully by Bentley and Humphreys in the United states in 1931 and Nakaya in Japan (published in 1954 from his life work). There are three fundamental shapes of ice crystals, namely needles, columns and plates. The needles occur singly or in bundles, columns include pyramid types and bullets, whereas plates include simple hexagons, sectored hexagons, stars and highly branched dendrites. In 1949 the International Commission on Snow and Ice (ICSI) classifed ice crystals into 10 different major catagories, being plates, stellar crystals, columns, needles, spatial dendrites, capped columns, irregular particles, graupel, ice pellets and hail. Later on Magono and Lee (1966) found many subdivisions of each type and classified ice crystals into 80 different types. To discuss all these crystal types is beyond the scope of this thesis. However, to give a brief idea about the appearance of ice crystals, some of the typical major forms are shown in Fig. 5.1

5.3 Ice crystal nuclei

A cubic metre of atmospheric air may contain 10^{11} particles, but there may be just 10-100 (as low as) active ice nuclei. What are the souces of these nuclei? Why are only a specific type of nuclei more active in the ice nucleation process? What is the size of ice nuclei? To answer these questions many experiments have been carried out in a variety of ways, such as:

a) testing various ice nuclei material in the laboratory

b) collecting ice samples from the natural clouds and identifying them

c) observing spatial and temporal variations of the concentration of ice nuclei in the atmosphere.

There is still uncertainty about these active chief sources of atmospheric ice nuclei. Some

investigators have suggested that they come from the outer space and others that they come from the surface of the earth, such as soils, industrial products, dust particles etc. Many investigators found that most ice nuclei are dust particles and basic clay minerals, such as kaolinite, halloysite or closely related structure of these kinds. Gokhale and Goold (1968) reported that the meteoritic samples are less efficient as ice-nuclei compared with clay particles. Generally, the size of ice nuclei is less than 0.01 micron (μ). However, large nuclei of the order of 1 μ are often observed.

Ice crystals formed in the laboratory by artificial seeding have regular hexagonal shapes, but in natural clouds various kinds of irregular crystals are observed. Is there any relation between the type of snow crystals and their nucleation from specific nuclei? Great effort has been made to identify ice nuclei in natural clouds in many different geographical and meteorological situtions and it is concluded that the types of crystals formed do not depend on the type of nuclei present, but depend solely on the ambient conditions such as temperature and humidity.

5.3.1 Dependence on temperature

Many investigators have made an attempt to relate the occurrence of various crystals to the ambient temperature. The first reported observation of this kind, quoted by Pruppacher and Klett (1978), was by Scoresby in 1820. He presented the first detailed description of a large number of different snow crystals and noticed a dependence of shape on temperature. From observations made in the Antarctic, Hein, as quoted by Mason (1971), indicated in 1914 that prisms occur with lower temperatures (-23 to -27°C) than plate-like crystals (-12 to -18°C).

The most complete presentation of ice crystals at different heights (from the troposphere

to the cirrus level) and temperatures has been made by Weickmann (1947). His aircraft observations showed that below -25°C, in cirrus and medium-level cloud, prismatic crystals are likely to form. Their form is due to growth along the principal axis normal to the basal face. Between -10°C and -20°C, star-shaped crystals called dendrites with six arms are commonly detected. These result from directional growth (propagation) along secondary axes (i.e., propagation of the prism faces). Just below 0°C needles, which have a tendency to grow along their principal axis, are most common. Some experiments even showed that the needles are formed under a very strong electric field, but the dependence of shape of the ice crystal on the existing electric field is poorly understood. Anyway, this strong dependance of crystal shape on the ambient temperature has been verified by numerous experiments carried out in different parts of the world. A brief summary is presented in Table 5.1

Table 5.1

Ice crystals and ambient temperatures After Kepler (1966) and Mason (1971)	
Temperature °C	Ice crystals
0 to -3	Thin Hexagonal plates and some trangular shapes
-3 to -5	needles
-5 to -8	hollow prismatic columns
-8 to -12	hexagonal Plates, sector stars
-12 to -16	Stellar dendrites
-16 to -25	Prisms and plates
below -30	Hollow prisms

5.4 Dimensions of ice crystals

Since ice crystals are not spherical but rather have the form of hexagonal plates, stars, needles, etc, a diameter cannot be assigned to them. Magono and Lee (1966) carried out an extensive study as presented in Table 5.2, where the length L, height h, diameter d, and width W, are in microns.

Table 5.2

Ice crystals and their dimensions	
After Magono and Lee (1966)	
Ice crystals	Dimensional relation
needles	$W = 1.1\,L^{0.61}$
plates	$h = 2.02\,d^{0.45}$
Stellar	$h = 2.03\,d^{0.43}$
Dendrites	$h = 2.80\,d^{0.38}$
Thick plates	$h = 0.40\,d^{1.02}$

5.5 Ice crystal concentrations and densities

If a supercooled cloud containing 1 gm^{-3} of liquid water was converted entirely to ice crystals, the number of ice crystals would vary from 10^4 to as high as 10^7 m^{-3} (Reynolds, 1952), depending upon the shape of the size distribution,

Jiusto and Weickmann (1973) measured a flux of approximately 5000 to 40 0000 ice crystals m^{-2} s^{-1} on the ground. The values are an order of magnitude higher than for rain drops, which generally have a flux of 1000 drops m^{-2} s^{-1}. Gunn (1967) reported that the typical flux of crystals in snowstorms was varying from 2000 to a maximum value of 10^5

$m^{-2}\ s^{-1}$.

A study of Mossop and Ono (1969) showed a variation of ice-crystal concentrations from 6×10^3 m^{-3} to 1.2×10^5 m^{-3} in stratocumulus and altostratus clouds in northern New South Wales, Australia. Later, a detailed study carried out by Mossop et al. (1972) on the Australian mainland, showed that in some cumulus clouds, the concentration of ice crystals was of the order of 10^5 m^{-3}. They also found that the maritime clouds can have an even higher concentration. An average concentration of 10^4 m^{-3} has been reported over a horizontal distance of several kilometers (Mossop et al., 1972).

Ice crystals generally fall as snowflakes which result from the aggregation of ice crystals. In general there will be 10 to a 100 ice crystals per flake.

The density of graupel varies from 0.13 to 0.7 g cm^{-3} whereas the density of densely rimed columns vary from 0.02 to 0.27 gm cm^{-3} (Locatelli and Hobbs, 1974). The density of dendritic crystals varies from 0.2 to 0.7 g cm^{-3}.

5.6 Fall-velocity relation

An understanding of the terminal velocity of ice crystals is very important in the study of ice-crystal growth and evaporation in clouds and in the estimation of precipitation rates. It is a fundamental parameter in the study of the ice-precipitation mechanism, and in the determination of size distributions of hydrometeors using radar.

Many experiments were carried out to determine the terminal velocities of ice crystals, but none of them applies to all kinds of crystals. This is because ice crystals have 80 different types (Magono and Lee, 1966) and each of these types may exist over a wide range of sizes and with various degrees of riming and aggregation, each with their own fall-velocity size relations. The first measurements of the terminal velocity of ice crystals in

natural cloud were carried out by Nakaya and Terada (1935) and later measurements were made by Magono (1951), Langleben (1954), Nakaya (1954), Litvinov (1956), Bashkirova and Pershina in 1964 (quoted by Zikmunda and Vali (1972)), Magono and Nakamura (1965), Brown (1970), Holroyd (1971), Jiusto and Bosworth (1971), Zikmunda (1972), Zikmunda and Vali (1972), Heymsfield (1972), Kajikawa (1972, 1975, 1982, 1989), Locatelli and Hobbs (1974), Heymsfield and Kajikawa (1987), and Beard and Heymsfield (1988).

With the various ice-crystal types taken into consideration, we need to convert the fall-velocity spectra to its size distributions. Magono (1951) first tried to deduce the terminal velocities from a theoretical standpoint. Later, he developed a relation between the velocity w and diameter d of the melted crystal or aggregates of crystals, for non-rimed aggregates:

$$w = 1.32 \left(\frac{d}{0.08 + 0.63\, d} \right) \tag{5.1}$$

and for rimed aggregates:

$$w = 1.94 \left(\frac{d}{0.08 + 0.63\, d} \right) \tag{5.2}$$

where w and d are measured in ms^{-1} and mm. These relations can apply to only one type of ice crystal or aggregate because they depend only upon the size of the crystals and not on their type.

5.6.1 X–R_e method

As quoted by Brown (1970) in 1950 Best related the Reynold's number R_e to the drag coefficient C_d by

$$X = C_d\, R_e^2 \tag{5.3}$$

where X is the Davies Number (Beard and Heymsfield, 1988). The drag force F_d on the ice crystals is

$$F_d = \frac{1}{2} C_d \rho_a A w^2 . \tag{5.4}$$

The downward force acting on the crystal is

$$F_g = (\rho_c - \rho_a) V g \tag{5.5}$$

where V is the volume of the crystal.

At the terminal velocity w, $F_d = F_g$. Solving for C_d, we get

$$w = \left[\frac{2g(\rho_c - \rho_a)V}{C_d \rho_a A}\right]^{\frac{1}{2}} . \tag{5.6}$$

This expression is not suitable for estimation of the terminal velocity of ice crystals because of the difficulty in calculating drag coefficients for ice crystals of various shapes. It is essential to eliminate C_d from the computational process.

Substituting C_d from 5.6 and $R_e = \frac{dw}{\nu}$ (see eqn. 3.2) in eqn. 5.3, we get

$$X = \frac{2d^2 g V}{\nu^2 A}\left(\frac{(\rho_c - \rho_a)}{\rho_a}\right) \tag{5.7}$$

which is independent of the terminal velocity w. Here ν is the coefficient of viscosity of the air.

An empirical $X - R_e$ relation for plate-like crystals and graupel is (Heymsfield and Kajikawa, 1987)

$$R_e = a X^b \tag{5.8}$$

where a and b are constants.

The estimated value of X is used in eqn. 5.8 to find R_e and then the terminal velocity w can be estimated from $R_e = \frac{dw}{\nu}$.

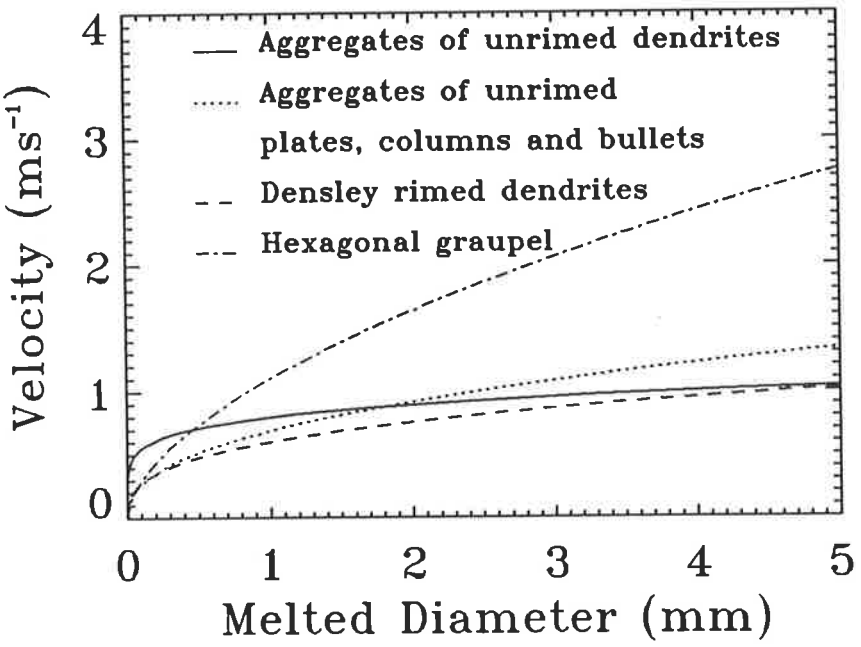

Figure 5.2: Fall velocities of various ice crystals. The values of a and b are taken from Table 5.4.

5.6.2 V-d power-law method

A more realistic relation has been developed by Langleben (1954):

$$w = K\, d^{0.31} \tag{5.9}$$

where K is a constant whose value depends upon the type of crystal. Since then a generally accepted power law relating the terminal velocity w of ice crystals, and their melted diameter D has been developed. It is

$$w = a\, D^b \tag{5.10}$$

where, a and b are constant values determined by the ice crystal density and geometry.

Nakaya (1954), who made a detailed study of various ice crystals, found that the terminal velocities of dendritic and powder-snow crystals remained constant over a wide range of diameters. Brown (1970) measured the terminal velocities of various ice crystals using more sophisticated equipment and found consistently higher values than those obtained by Nakaya. He also estimated the values of a and b for numbers of different types of ice crystals. Locatelli and Hobbs (1974) measured a large number of ice crystals, giving more attention to the effect of riming and aggregation because ice crystals tend to fall as a cluster *i.e.*

Table 5.3

Type of ice crystals and values of a & b.
(After Locatelli and Hobbs, 1974)

Type	constant, a	constant, b
Lump graupel (ρ, 0.05 to 0.10)	1.16	0.46
Lump graupel (ρ, 0.10 to 0.20)	1.30	0.66
Lump graupel (ρ, 0.20 to 0.45)	1.50	0.37
Conical graupel	1.20	0.65
Hexagonal graupel	1.10	0.57
Densely rimed columns	1.10	0.56
Densely rimed dendrites	0.60	0.33
Unrimed side planes	0.81	0.11
Aggregates of unrimed dendrites	0.80	0.16
Aggregates of rimed dendrites	0.79	0.27
Aggregates of unrimed plates columns,bullets and side planes	0.69	0.41

snow and not as individual crystals. The experimentally determined values of a and b for various ice crystals are presented in Table 5.3. Here the velocity and diameter are in ms^{-1} and mm respectively. Using this power-law equation 5.10, the fall velocities of various ice crystals are plotted against their diameter in Fig 5.2. It can be seen that compared with other ice crystals, graupel falls most quickly . In this thesis, a study of ice crystals in stratiform cloud is carried out, in which mainly dendrites and plates are taken into consideration. From Fig. 5.2, below 1.9 mm diameter, the fall velocity of unrimed dendrites is greater than that of unrimed plates, whereas above 1.9 mm the fall velocity of rimed dendrites is less than that of unrimed plates, even up to 5 mm diameter.

5.6.3 Other methods

To relate the fall velocity w of snow particles to their melted diameter D, Gossard et al. (1992) used a different relation which was developed by Magono and Nakamura in 1965. This is,

$$w = 8.8\,[(\rho_s - \rho_a)(0.1)\,D]^{\frac{1}{2}} = 2.78(\rho_s - \rho_a)^{\frac{1}{2}}\,D^{\frac{1}{2}} \tag{5.11}$$

where D is in mm and the snow density ρ_s and air density ρ_a are in g cm^{-3}.

Lin et al. (1983) used a relation for riming hexagonal crystals which is also a power law:

$$w = 1.53 \times D^{1/4} \tag{5.12}$$

where the fall velocity is in ms^{-1} and D is in mm.

In all situations, the fall-velocity can be converted to their size by using their empirical equations.

5.6.4 Altitude correction

Ice crystals fall faster at upper levels in the atmosphere than at the surface because, at upper levels, the atmospheric density is low and so there is less viscous drag due to air on the ice particles. The necessary correction factor f to be applied is (Beard, 1977)

$$f = \frac{w}{w_0} = \left(\frac{\eta_0}{\eta}\right)^{2b-1} \left(\frac{\rho_0}{\rho}\right)^{1-b} \tag{5.13}$$

where b is a constant and ρ_0 and ρ are, respectively, the atmospheric densities at the surface and at the height of observations. Similarly, η_0 and η are the respective coefficients of viscosity of the air at the surface and at the height of observation. From the ideal gas equation

$$\frac{\rho_0}{\rho} = \left(\frac{p_0}{p}\right)^{1-b} \left(\frac{T_0}{T}\right) . \tag{5.14}$$

Using 5.14 in 5.13 and expressing η in terms of temperature, (see Beard and Heymsfield, 1988), eqn. 5.13 can be written as,

$$f \approx \left(\frac{p_0}{p}\right)^{1-b} \left[1 + (1-b)\frac{\Delta T}{T_0} - 0.805(2b-1)\frac{\Delta T}{T_0}\right] . \tag{5.15}$$

Observations show that the temperature adjustment factor for the precipitation particles is very small compared to the pressure factor. In eqn. 5.15, the temperature factor will vanish when the coefficients of $\frac{\Delta T}{T_0}$ are equal, that is when

$$1 - b = 0.805(2b - 1) \tag{5.16}$$

which gives $b = 0.69$ and, from eqn 5.15,

$$f = \left(\frac{p_0}{p}\right)^{0.31} . \tag{5.17}$$

The values of b obtained by Beard and Heymsfield (1988) for various plate-like crystals and graupel ranged from 0.42 to 0.999. Lin et al. (1983) used a power of 0.5 instead of 0.31 for riming hexagonal crystals.

Because of the random collision processes involved in snowflake aggregations and the existence of different shapes and densities, an exact fall-velocity relation cannot be expected. For this reason, in this study, the power of $\frac{p_0}{p}$ is taken as 0.4 as this value has been widely used in past observations, especially in the study of the size distributions of rain drops.

Hence eqn. 5.15 becomes

$$f = \left(\frac{p_0}{p}\right)^{0.4} \tag{5.18}$$

This gives the corrected velocity at pressure p as

$$w(p) = w_0 \left(\frac{p_0}{p}\right)^{0.4} . \tag{5.19}$$

5.7 Most likely crystal types

In section § 5.2 it has already been mentioned that the occurrence of various types of ice crystal is a function of temperature. In this section, the ice crystals most likely occurring in various cloud type will be discussed. In past observations, it was noticed that, in proceeding from high-via medium- to low -level clouds, there is a gradual transition of crystals from prisms to thick plates and then to thin hexagonal plates. However, the crystals in the same type of cloud, but with different temperature, liquid water content, and water-vapour concentrations, may be different. Table 5.4 gives an average picture of likely crystals in various clouds. This summarizes results obtained by Weickmann in 1947 as quoted by Mason (1971).

Table 5.4

Cloud types	Ice crystals
Nimbostratus	Thin hexagonal plates
Stratocumulus	Star-shaped crystals
Stratus	showing dendritic structures
Altostratus	Thick hexagonal plates
Altocumulus	Prismatic columns,
	single prisms and twins
Cirrus	Clusters of prismatic columns
	and some single hollow prisms
Cirrostratus	Individual complete prisms

Rimed crystals are likely to form when the ambient temperature is relatively mild and tend to be produced by convective clouds. This indicates that they require high super-cooled liquid water content and scarcity of ice nuclei.

5.8 Rotational and horizontal motions: Dendritic crystal dominance

Most crystals fall with several different types of rotatory motions. Rotations occur about the minor axes of the crystal in both the vertical and horizontal planes and occasional rotation about the major axis can also be observed . Some of the results of Zikmunda and Vali (1972) on the rotational motion of ice crystals will be discussed here. They found that the average angular velocity of rotation of a rimed column crystal in the vertical plane was

14 rad s^{-1}, with the highest values being 45 rad s^{-1}. Rotations of the major axis about the vertical were also quite common for some types of crystals, with angular velocities ranging from 200 to 400 rad s^{-1}. Some crystals may even show a reversal of the sense of rotational motion. This indicates the existence of rotatory oscillations about an axis. However, they were unable to detect such a rotational motion for planar type crystals with broad branches. Occasionally, spiralling types of motions occur which cause tumbling of the crystals, which otherwise generally fall with their crystal plane horizontal. On the other hand, Jiusto and Weickmann (1973) did mention that most dendrites rotate as they fall.

Does the rotational motion affect the fall velocity of the crystal? Is there any relationship between the change in fall velocity and the crystal aggregation processes? Which crystal type is most likely to take part in aggregation processes?

From past observations it was found that when the major axis deviates from the horizontal position, the fall velocity generally increases with increasing angle of deviation (Zikmunda and Vali, 1972). Thus rotational motion is an important factor in the differential fall velocity of the crystal. Most studies of the aggregation of ice crystals in natural clouds had been based upon modelling the well-known studies of cloud and raindrop coalescence in which the rate of collision between the two drops was determined by their geometric cross-section, differential fall speed and mutual collection efficiency (Passarelli and Srivastava, 1979).

A clear understanding of the falling motion of snow flakes in the atmosphere is very important in order to study the aggregation processes in the clouds. This is because unstable motions, such as oscillatory, rotational and horizontal, are responsible for an increase in the collision efficiency (Rogers, 1974 as quoted by Kajikawa, 1982 and Passarelli, 1978). Supporting this statement, Kajikawa (1982, 1989) measured the horizontal components of

various ice crystals from the rotational falling motion of the snow flakes and found that the variation of horizontal velocity plays an important role in aggregation processes, whereas the effect of variation in the vertical velocity on aggregation is negligible.

From past observations it has been found that the larger snow flakes, consisting of 10 to 100 crystals, usually consist of loosely packed dendritic crystals and some thin plates (Jiusto and Weickmann, 1972) whereas snowflakes consisting of thick plates and prisms are rather uncommon (Magono, 1953; Jiusto and Bosworth, 1971). Most recently during "lake-effect" snow storms in Michigan, Braham (1990) also observed large concentrations of spatial dendrites and aggregates of dendritic forms. Do dendritic crystals favour the aggregation processes? If so, they should possess higher aerodynamic collection efficiencies than other compact crystals. However, the scope of this section is not to concentrate on the aggregation processes, but only to give a brief idea about the crystal types which can be detected most commonly in natural clouds.

5.9 Use of windprofilers to study ice particles

So far, the dependence of crystal shapes on the ambient conditions, their fall velocities and their dimensions have been discussed. All this discussion is based on *in situ* experiments, either the observations on the ground or using an aircraft. Again, as discussed in the dropsize study, despite its high speed, an aircraft can only explore in a given time a volume of air which is small compared to that which needs to be sampled for the study of mesoscale convective systems in the atmosphere. For this reason, it is desirable to develop a remote sensing technique to tackle this problem. A windprofiler operating at VHF or UHF may be a useful tool for the study of ice particles' fall velocities, and hence their crystal forms and size distributions, because significant ice echoes have been observed recently using a

windprofiler at 50-MHz (May, 1991).

Table 5.5

Darwin profiler specifications	
Latitude	12.43°S
Longitude	130.95°E
Tx. Frequency	49.92 MHz
Direction	15°E
Tx. Pulse	15 μs
Spectral points	256
Averaging time	60 mins

The data taken by a wind profiler situated in Darwin was analysed in order to see the backscattering due to ice particles. The radar specifications are presented in Table 5.5. As an example, a strong convective cell passed over the windprofiler on 11 Nov 1990. Figs. 5.4 and 5.5 show 30 minutes and 2 hours of averaged "stacked" spectra observed on 11 November 1990 in the early morning. These observations were taken in the trailing stratiform regions of a strong meso-scale convective squall line. Here a significant ice echo was detected for periods of almost 4 hours in stratiform regions of the tropical squall lines. The very strong echo, the "bright band" at the lower heights, between 4 and 5 km, corresponds to the scattering from the freezing level. When the ice begins to melt on the surface of ice crystals or on the aggregates of ice crystals, the gradient of refractive index between the two surfaces will be very large and hence the radar detects it as a big drop. For this reason, a very strong echo was observed in the melting level where the peak position is greater than at 2 ms^{-1}. But above the melting layer, the peak position of the ice echo is somewhere around 1.3 ms^{-1}. Significant ice echoes were observed up to a height of 10.5 km.

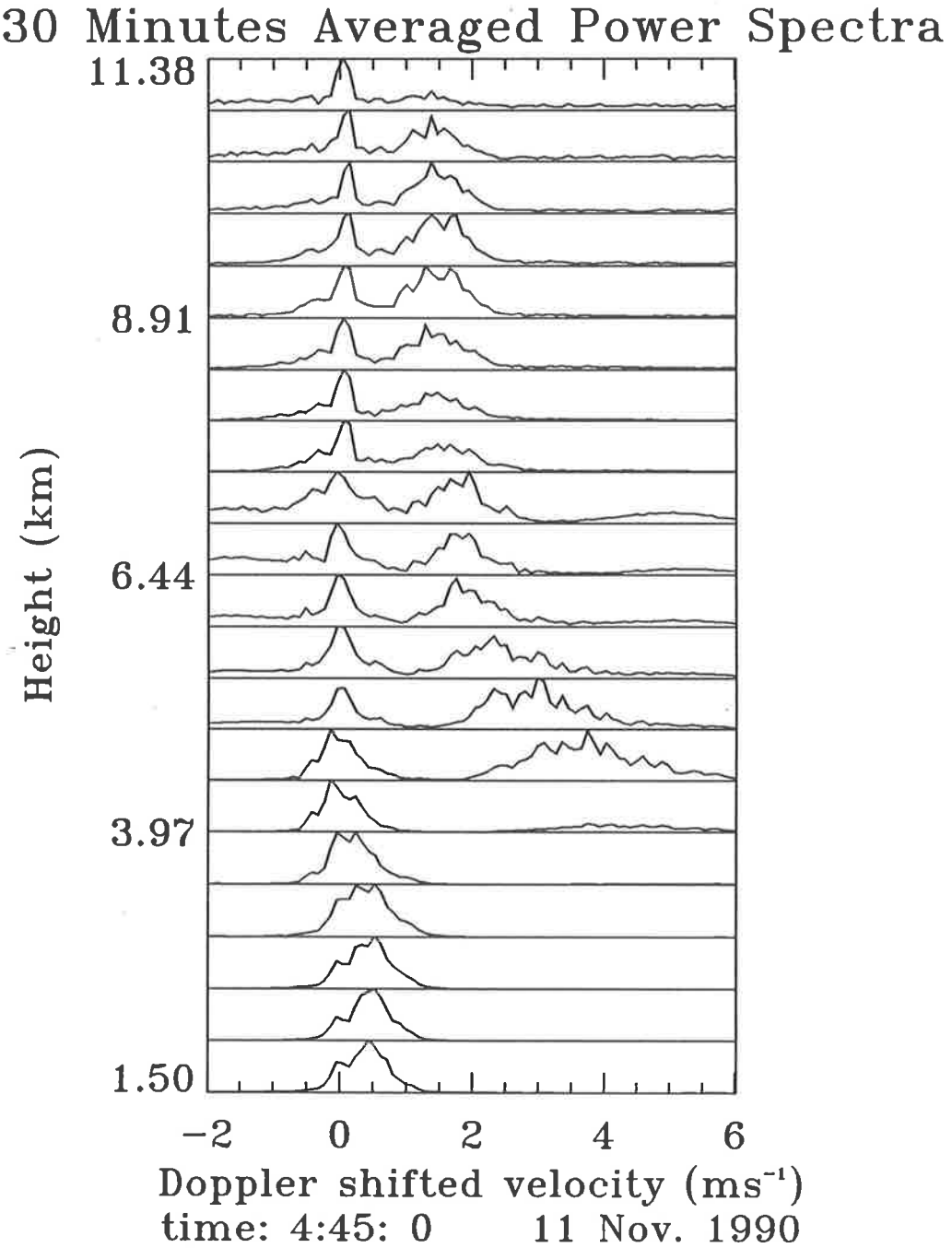

Figure 5.3: Examples of VHF Doppler "stacked" spectra observed on 11 November 1990, averaged over an interval of 30 minutes.

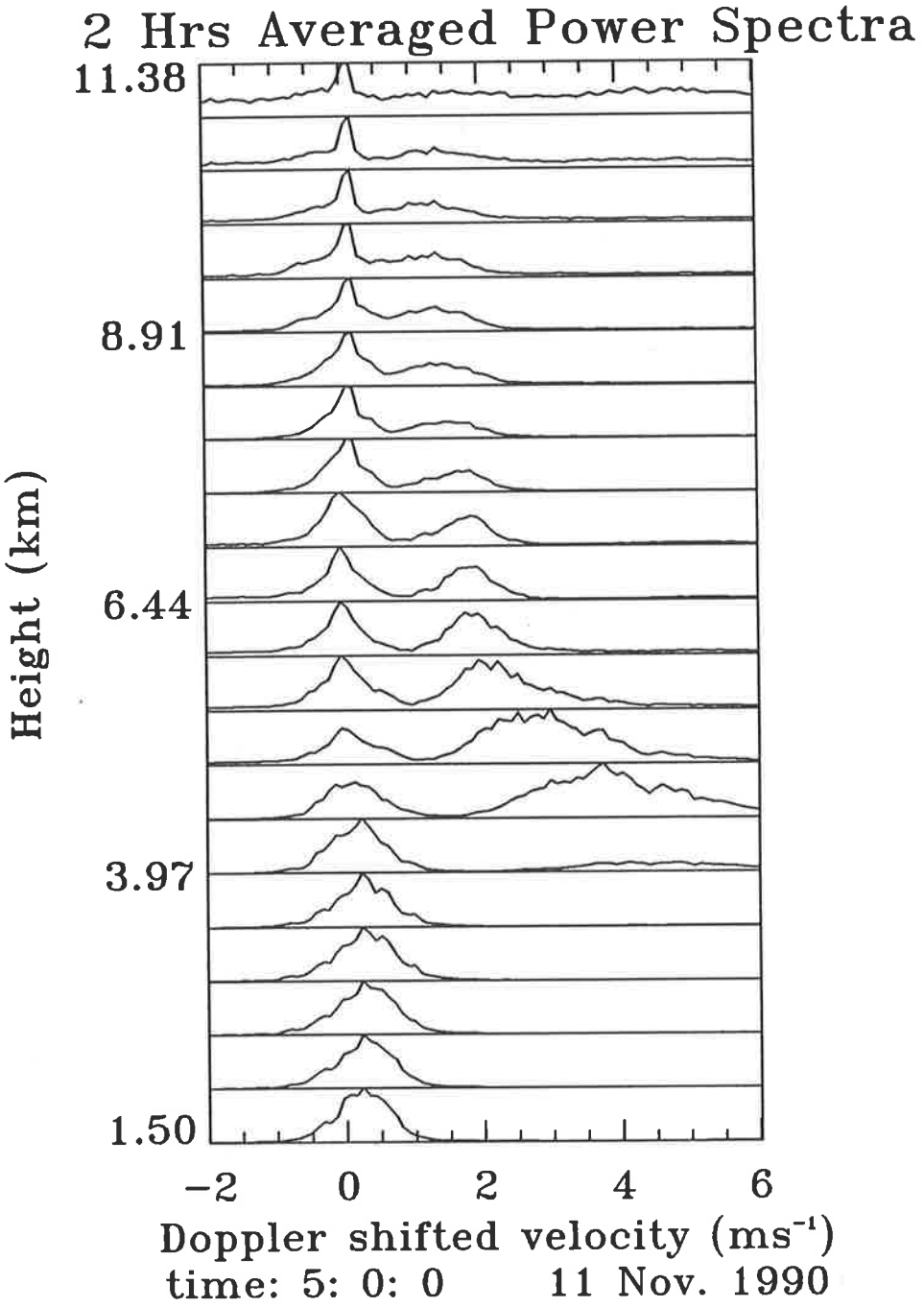

Figure 5.4: Examples of VHF Doppler "stacked" spectra observed on 11 November 1990, averaged over an interval of 2 hours.

The ice echo was not visible in the convective regions of the cells, presumably due to the large variance of the vertical motions within the cell smearing out the ice echo.

This observation clearly indicates that wind profilers operating at a frequency of 50 MHz are capable of detecting two distinct simultaneous echoes, one from the clear-air turbulence and one from the ice particles, provided that the clear-air spectral width and the mean vertical motion are both small. This is because the ice particles' fall-speed is also small and their echo lies in a region close to the clear-air echo in the observed spectra. These echoes also offer the opportunity to estimate the ice-crystal size distributions using the VHF wind profiler.

5.10 Conclusion

The fundamental shape of the ice crystals is hexagonal. However, there are an infinite number of variations ranging from flat six sided plates to six branched crystals and six sided prisms and so on. Generally the ice particles observed on the ground are not perfect. The collision between the crystals, melting and riming can lead to these irregularities.

The information on the motion of ice crystals is an essential factor in the understanding of the precipitation forms above the ground. As theoretical models of cloud and precipitation processes have become well established, the study of the relationship between the fall speeds, masses and dimensions of various ice crystals has become more important. The terminal fall velocity of ice crystals is a function of crystal orientation, crystal diameter, and axis ratio. However, a complicated spread of terminal velocities of ice crystals has been observed and it has been suggested that the mass distribution and crystal shape are responsible for complicated fall patterns.

It is well understood that dust particles play an important role in the formation of ice

crystals. However, many researchers have reported the existence of supercooled drops below 0°C . It clearly indicates that only a small number of dust particles present in the natural cloud take part in the nucleation processes. It also indicates that particular types of dust particles are essential to initiate the phase change.

The concentration of crystals per cubic cm in natural clouds may differ from one cloud type to another by a factor of 10^3.

No matter whether the crystals are formed from the supercooled drops or from the vapour, meteorologists are more interested in the type of ice crystals present in natural clouds. The discussion on the dependence of crystal form on temperature gives a brief idea of how the ambient conditions determine not only the growth rate, but also the form of the crystals. As a growing crystal penetrates through the various parts of the cloud, its crystal form will change according to the changing ambient conditions and during this time the crystals can pass through many stages such as diffusion, riming and aggregation. An understanding of these processes is necessary to estimate the density and eventually the mass of the crystals which depend upon their type, aggregation and the riming.

Excess vapour density over ice is a maximum at about -15°C, which is also the temperature of the maximum growth rate. The preferred crystal types in this growth region are seen to be dendrites and sectors. A clear understanding of the three dimensional velocity vector and rotational motions is essential in explaining the dominance of dendritic crystals in the aggregation processes. However, a complete explanation of this dominance has not yet been made.

The size distribution of cloud droplets is determined not only by the micro-physical processes of crystal growth by sublimation, riming and aggregation, but it is also affected

by the cloud dynamics, such as the degree of mixing with the environment, the distribution of vertical and horizontal velocities within the cloud, the period for which the individual crystals remain in the cloud, the three dimensional fall velocity of the crystal and its rotational motion during its fall, the intensity of turbulence and so on. Knowledge of the evolution of solid hydrometeors with time and height can make a significant contribution to the understanding of the phase change, the latent heat release within the cloud and the rainfall intensities on the ground.

In the past 4-5 decades, on-going efforts have been made to understand these processes, from both a practical and theoretical point of view. However, not much work has been done in the study of ice-crystals size distributions using ground-based instruments.

In this section, it has been shown that the windprofiler may be a powerful remote sensing tool in the study of ice crystals in natural clouds and this will be discussed further in Chapter 6.

Chapter 6

Retrievals of ice particle size distributions

6.1 Introduction

It is well known that the measurement of size distributions of cloud particles is very important for the study of cloud optical properties and for the improvement of radar estimates of rainfall intensities. In the latter case the amount of precipitation reaching the ground, in the form of rain and snow, is strongly affected by the vertical velocities, size distributions and the nature of the cloud particles.

Many experiments have been conducted to obtain the size distributions of liquid particles using Microwave Doppler radar, but so far little work has been done using such radars to obtain the size distributions of solid particles within cloud. These microwave radars are not sensitive to the clear-air velocity spectrum. The importance of the correction in the retrieval technique for beam broadening due to clear-air turbulence, along with a brief

discussion of the profiler's capacity to detect two distinct, simultaneous, signals (one from clear-air turbulence and the other from hydrometeors) have been discussed in Chapter 3 and 4. Recently, a range of numerical techniques have been developed to obtain liquid-drop size distributions from VHF and UHF radar observations (*e.g.* Wakasugi *et al.*, 1986, 1987; Gossard, 1988; Sato *et al.*, 1990; Currier *et al.*, 1992; Rajopadhyaya *et al.*, 1993). The possibility of the use of wind profilers to estimate the size distributions of solid particles (ice crystals) has yet to be explored.

The first problem in determining the size distribution is to obtain the fall-velocity of the solid hydrometeors. As explained in Chapter 5, many experiments have been carried out to determine the terminal velocities of ice crystals, but all depend on the kind of crystals, their degree of riming, and their densities, etc. Note that Magono and Lee (1966) classified ice crystals into eighty different types and each type may exist over a wide range of sizes with various degrees of riming and aggregation, each with their own fall-velocity size relation. These fall-speed relations refer to the melted crystal diameter. So, the conversion of the fall velocity spectrum of solid hydrometeors to their size distribution spectrum is more complicated than in the case of liquid hydrometeors (*i.e.* rain drops).

In this chapter, a technique is developed to calculate the size distributions of ice crystals using 50-MHz wind profiler data. As an application of this retrieval technique and to demonstrate that a simple parameterisation of the ice distribution is adequate to explain the observed Doppler spectra well, the results obtained by analysing some real data from Darwin (12.43°S and 130.95°E) are also presented.

To test the statistical reliability of the technique, model ice-echo spectra are generated with realistic statistical variations. The size spectra are then retrieved by a least-squares method. The parameters involved in the fitting process are varied through a wide range of

their possible values and then the size spectra are recovered for each combination. Special care is taken to investigate the effects of different intensities of turbulence on the model ice-echo spectrum by systematically changing the width of the clear-air spectrum from 0.1 ms^{-1} to 0.5 ms $^{-1}$. Finally, the limitations of the technique are discussed.

6.2 Shape of ice crystal size distributions

The size distributions of aggregates of ice crystals were first presented by Gunn and Marshall (1958). They found an exponential distribution for a wide range of rainfall intensities. The exponential distribution is

$$N(D) = N_0 \exp(-\lambda D)\,. \tag{6.1}$$

Note that in Eqn. 6.1, the diameter D refers to the physical diameter of the particles, while the relations for fall speed etc. usually refer to the "melted diameter", hereafter simply referred to as "diameter". It is assumed here that the melted and physical diameter are proportional. Gunn and Marshall (1958) give the following relationships for N_0 and λ as functions of r:

$$N_0 = 3.8 \times 10^3 r^{-0.87} \tag{6.2}$$

$$\lambda = 2.55 r^{-0.48} \tag{6.3}$$

where, N_0 is the intercept of the plot of size distribution versus diameters in $m^{-3}mm^{-1}$ and r the precipitation rate in mmh^{-1}, λ is the slope in mm^{-1}, measured in terms of the water-equivalent depth of the accumulated snow.

In an extensive study of snowflake aggregates, Sekhon and Srivasta (1970) confirmed Gunn and Marshall's results, but with slightly different relations between λ , N_0, and r.

They also reanalysed data obtained by previous investigators and found that

$$N_0 = 2.5 \times 10^3 r^{-0.94} \tag{6.4}$$

$$\lambda = 2.29 r^{-0.45} . \tag{6.5}$$

Most recently, Braham (1990) used aircraft measurements to show that during lake-effect snow storms, the shape of the size distribution spectra of solid hydrometeors (>1 mm in diameter) is exponential, confirming previous findings.

6.3 Retrieval technique

This section deals mainly with the procedure that is developed in this thesis to retrieve information about ice crystals size distribution in the natural clouds. As there are many types of ice crystals, moving with different fall velocities and having different aggregations, the following assumptions have been made to simplify the model:

(a) Spectral broadening, due to the beam width, radar-range resolution, and turbulence, are the same for both the clear-air and precipitation echoes.

(b) The spectral shape of the clear-air echoes is well approximated by a Gaussian distribution (Tennekes and Lumley, 1973).

(c) The distribution of precipitation echoes in the model spectrum is based on an exponential size distribution of the ice crystals.

(d) A small number of ice-crystal types is present, i.e. aggregates of dendrites and aggregates of bullets, plates etc. form the bulk of the ice content in the precipitation. This simplifying assumption is needed to make the retrieval problem tractable. More complicated distributions have been observed (e.g. Dowling and Radke, 1990). A

retrieval using a single fall-speed relation allowing a complicated distribution shape will have large errors because it cannot allow for different crystal and aggregate types.

The first two assumptions have already been considered in retrieving dropsize distributions (Chapters 3 and 4). The third assumption about the exponential distributions is based on past observations(§ 6.2). It is the most widely used distribution for widespread rain and snow. However, the size distribution of hydrometeors is not fully understood. It is possible that the distribution deviates from the proposed exponential model in some atmospheric conditions.

It has also been assumed that there is a small number of ice types present. The selection of likely types (dendrites and plates) is made *a-priori* based on the sort of atmospheric system being analysed: here the trailing stratiform region of a tropical squall line is used. This aspect has been already discussed in chapter 5. However, a more detailed explanation is given in § 6.3.1

The backscattered power from the solid hydrometeors depends upon the size, type, and number density of the hydrometeors in the pulse volume. The radar-reflectivity factor Z due to the hydrometeors, varies as the sixth power of the diameter of the hydrometeors and is summed over all the hydrometeors per unit volume (see chapter § 3.3.3)

$$Z = \int_0^\infty N(D) D^6 dD \tag{6.6}$$

where $N(D)$ is the number of ice particles in the diameter range between D and $D + dD$.

The backscattered power spectrum $S(w)$ as a function of the vertical velocity w in the presence of precipitation particles (here, solid hydrometeors), is equal to the sum of the backscattered power spectrum $G(w)$ from the clear-air turbulence, and $P(w)$ from the solid precipitation particles. However, because of the effects of turbulence, beam-broadening,

wind shear and power-spectral window, the precipitation spectrum is broader than the true reflectivity-weighted fall-speed spectrum $P(w)$ which we wish to estimate. The observed precipitation spectrum may be represented by the convolution of the clear-air echoes and the precipitation echoes. Hence $S(w)$ can be expressed as (see Eqn. 3.15)

$$S(w) = G(w - \overline{w}) + G(w) * P(w - \overline{w}) + n. \tag{6.7}$$

The asterisk $(*)$ stands for the convolution operation, $\overline{w}$ is the mean vertical wind calculated from the clear-air peak, and n is the noise level. Here

$$G(w) = A_0 \exp\left(-\frac{(w - \overline{w})^2}{\sigma^2}\right) \tag{6.8}$$

$$P(w) = F_1(w) + F_2(w) + F_3(w) + ... \tag{6.9}$$

$$F(w) = \frac{1}{Z} N(D) D^6 \frac{dD}{dw} \tag{6.10}$$

where A_0 and σ are, respectively, the amplitude and spectral width of the clear-air spectrum. $F_i(w)$ represents the true reflectivity-weighted fall-speed spectrum due to an ice crystal of type i, and $P(w)$ represents the true reflectivity-weighted fall-speed spectrum of all types of ice crystals available in the pulse volume.

6.3.1 Small ice-particle types

The diffusion of water vapour, droplet riming, and crystal aggregation are the three major ice-crystal growth mechanisms in natural clouds. The types of ice crystals present are determined by these mechanisms. Apart from this, they also depend upon the strength of up- and down-drafts, liquid-water content, humidity, cloud thickness, temperature, ice nuclei and so on. So, the basic problem is to decide which ice-crystal types to include in

the model.

To include all the types mentioned by Magono and Lee (1966) is not practicable because it will overspecify the problem. The solutions to the retrieval would be unstable. To include even the ten different ice-crystal types adopted by the International Commission on Snow and Ice (§ 5.2) is not practicable because the number of parameters to be estimated should be sufficiently small, to ensure the solution is stable. Therefore we must make *a-priori* assumptions about the likely cloud microphysics.

Graupel and hail are the fastest falling crystals. To simplify the problem, we assume that graupel, ice pellets, and hail will have fallen out of the region of active convection and so we do not need to consider them, especially in the stratiform regions of squall lines and storms. Likewise, the radar will not detect small crystals as the D^6 dependence will ensure that they are virtually invisible to the radar and because of their low fall speeds relative to the air, their absolute fall-velocities and hence radar echoes are almost the same as for clear-air turbulence.

With the support of various other experiments discussed in chapter 5, it has been suggested that the most commonly observed snowflake aggregate consists of planar-type crystals with dendritic features. Hence, the simulations for this thesis include aggregates of dendrites and other types *e.g.*, aggregates of plates, columns and bullets. It is assumed that the particles are not heavily rimed, since there should be little super-cooled water in the stratiform region. This is because small vertical velocities are observed in the stratiform region.

With the various ice-crystal types taken into consideration, the fall-velocity spectrum can now be converted to the corresponding size distribution. A generally accepted power law relating the terminal velocity, w, of an ice crystal and its melted diameter, D, is used

(See eqn. 5.10). Reproducing it here, the terminal velocity is given by

$$w = aD^b. \tag{6.11}$$

It can also be written as

$$D = \left(\frac{w}{a}\right)^{\frac{1}{b}}. \tag{6.12}$$

Referring to Table 5.3, the values of a and b experimentally determined by Locatelli and Hobbs (1974) are, for aggregates of plates, columns and bullets, $a = 0.69$ and $b = 0.41$ whereas, for aggregates of dendrites, $a = 0.8$ and $b = 0.16$.

These values are used mainly to study ice particles of diameter greater than 1 mm at the ground. At upper level (altitude greater than 6-7 km), the diameter would generally be less than 1 mm provided there is only cirrus type cloud present. In the present study the greater fall-speed was observed and this is due to the the trailing stratiform cloud formed by deep convective motion of a tropical squall line.[1]

The necessary correction to this velocity for the lower pressure at greater heights is made using Eqn. 5.19. From eqn. 6.12, the derivative of D with respect to $w(p)$ is given by

$$\frac{dD}{dw} = \left(\frac{1}{b}\right)\left(\frac{D}{w(p)}\right) \tag{6.13}$$

where $w(p)$ is the terminal velocity of ice crystals at pressure p.

It should be noted that a radar can only detect crystals of diameter greater than a certain minimum value. As mentioned earlier, below this value, the crystal's fall velocity would be much smaller than the variations in radial wind, and hence the detection by a profiler of the mean motion due to the fall of such small crystals is unlikely. Thus scattering from crystals in the small-diameter regime helps to increase the magnitude of the atmospheric turbulence component in the observed backscattered spectrum (Sato *et al.*, 1990).

1. Fall speeds of 1-2 ms^{-1} were observed at an altitude greater than 6 km. These values are generally greater than the expected values in the cirrus type cloud.

A search is made for the best fit of the "model spectrum" by varying the parameters N_0 and λ for each of the ice-crystal types, taking into account the above effects, and using a least-squares fitting method. This approach is similar to that of Wakasugi *et al.* (1986), except that more than one precipitation type must be considered. However, due to the many parameters involved in the fitting process, we have first estimated the clear-air spectral width which is twice the half width of a Gaussian to the 1/e point of the clear air peak. Here the spectral width is calculated from the first side of the Gaussian curve and care has been taken to account for the contamination from the precipitation echo. First we fitted the Gaussian curve alone and then, keeping the Gaussian parameter and noise level constant, the precipitation echo is fitted. Additionally, to keep the equations stable, the maximum diameter of plates has to be limited depending upon the position of the precipitation peak and the initial guess of the ice parameters. Otherwise, the contamination of the echo due to one ice-type on that of another will be very large.

Various least-squares fitting techniques were examined, with the best results obtained using the "grid-search" method described by Bevington (1969). An initial estimate of the desired parameters is made and the fitted spectrum is evaluated numerically. The technique then minimizes the χ^2 difference between the fitted and actual spectrum for each parameter separately. The process is iterated with the new parameters until the absolute value of the minimum in χ^2 is sufficiently small.

Clearly, the method is tedious and time consuming. In many cases, the estimated ice parameters were found to be different from one run to another when a slight change in the initial guess of the parameters was made. This was due to the observed strong clear-air echo. For this reason, an initial guess of the clear-air spectrum is made and the clear-air echo is fitted to the spectrum. Then, keeping the parameters of the clear-air echo constant,

the precipitation echo is fitted by the grid search method. Here careful attention has been paid to consideration of the contamination by the ice echo of the clear-air echo.

The use of a finite data length broadens the spectrum slightly (Waksugi et al., 1987). This window effect can be included in the retrieval assuming the observed spectrum, $S(w)$ is a convolution of the "actual" spectrum, $S_1(w)$, with the window function, *i.e.*

$$S(w) = S_1(w) * W(w). \tag{6.14}$$

Here the window function, $W(w)$, is the sinc-squared function. However, this is a relatively small effect.

6.4 Fitting to real data

A well developed continental-type squall line crossed over Darwin on Nov. 11, 1990 (May, 1991). This storm featured an extensive, fairly uniform, stratiform region covering a 200-km wide strip behind the leading convection. While the stratiform area was overhead, well-defined precipitation echoes were visible in the Doppler spectra both above and below the freezing level (Figs. 5.3 and 5.4).

The solid line in Fig. 6.1a is the 1 hr-averaged power spectrum observed by the wind profiler in Darwin between 05:00 to 06:00 local time at an altitude of 6444 m. Here the mean vertical wind was 0.2 ms^{-1}. The strong ice echo (second peak) was clearly visible even on a linear scale. The peak of this precipitation echo is somewhere around 1.75 ms^{-1}. To recover the size spectrum from this observed power spectrum an initial guess of the parameters involved in the fitting process was made after careful consideration of the positions of the clear-air and precipitation peaks, their amplitudes, and their spectral widths. The power spectrum is calculated using Eqn. 6.7 and the windowing effect is then taken into account.

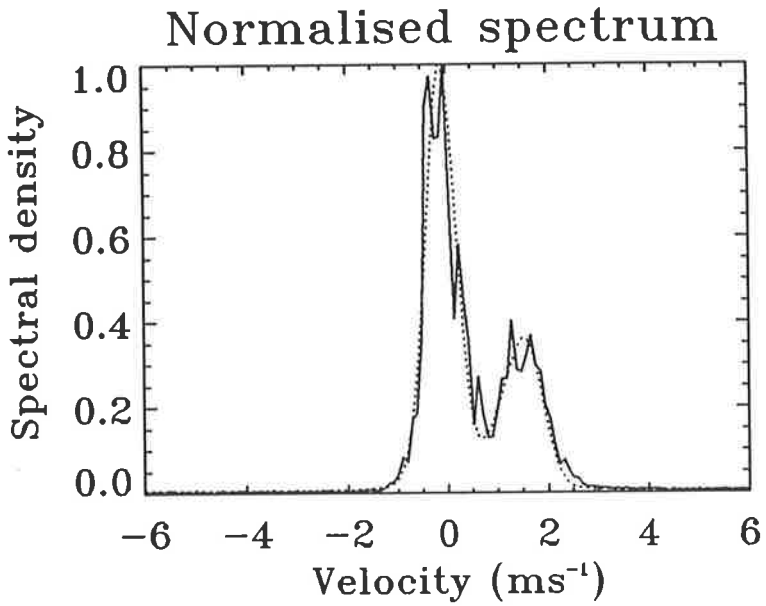

Figure 6.1: The recovered population spectrum (solid line) using a least-squares method and the actual spectrum (dotted line) observed on 11 November 1990 at Darwin at an altitude of 6444 m.

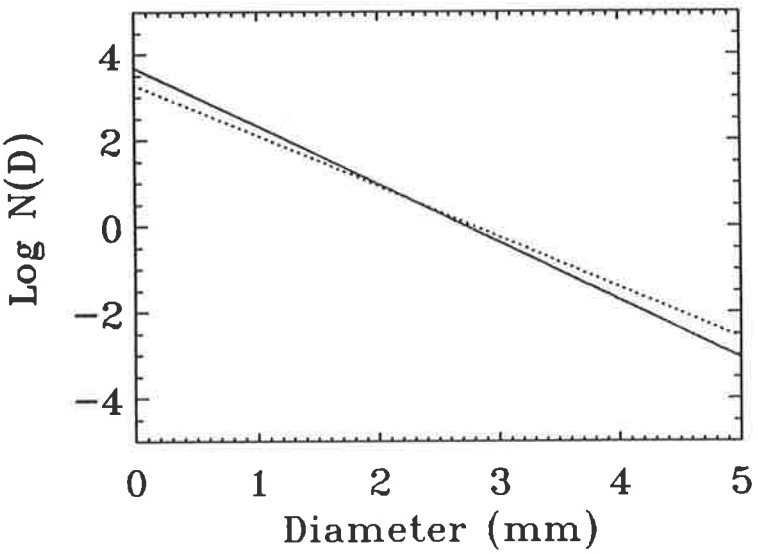

Figure 6.2: The estimated relative size distributions of plates (solid line) and dendrites (dotted line) for the spectrum shown in Fig. 6.1

Finally, applying the least-squares method produced the fitted spectrum shown by the dotted lines. The fitted spectrum almost coincides with the observed spectrum except in the large-diameter regime. The estimates of the relative size distributions $N(\gamma)$ of the ice crystals are shown in Fig. 6.2. Here the solid line corresponds to plates and the dotted line to dendrites. It can be seen from these curves that there are large concentrations of plates, bullets and columns relative to the dendritic crystals in the smaller-diameter regime. However, in the larger diameter regimes, the concentrations of dendritic crystal's are larger than those of plates, columns and bullets. It should be noted that, since the radar system was not calibrated for reflectivity, we cannot estimate the *absolute* values of N_0, so only relative values are shown. The good fit in this example clearly indicates the possibility of the use of this technique to estimate the size distributions of solid hydrometeors in natural clouds.

The variation of ice-crystal size distributions with height is essential for the study of the evaporation and aggregation processes, to estimate the water content in the cloud, and to estimate the heating rate at various altitudes. Additionally, the variation of hydrometeoric distributions with time give a clear picture of the development of a meso-scale system.

Plots of the slopes of the retrieved distributions as a function of height are shown in Fig. 6.3 for four successive times. It is clear that there is a tendency for λ to increase with increasing height, which means that the fall velocities were decreasing and the precipitation echoes were getting closer to the clear-air echoes. This indicates that there were larger numbers of very small ice-crystals at the upper levels and that the aggregation process was rapid. At the start of the observing interval (03:15 local time) the increase in the value of λ with height is slow for both dendrites and plates. However, after one and a half hour (at

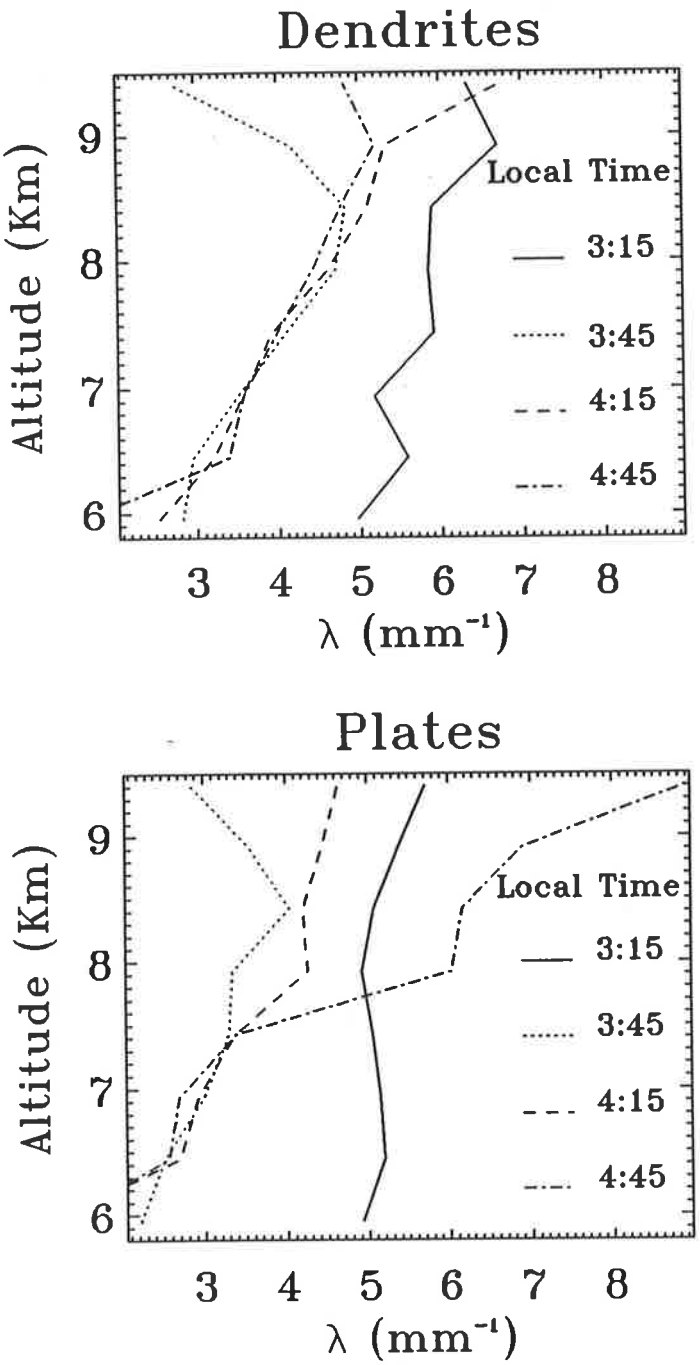

Figure 6.3: Profiles of the recovered values of the size distribution slope λ with height and time for dendrites (upper diagram) and plates, bullets and columns (lower diagram).

04:15), the rate of increase of λ with height is rapid.

Above 9 km the behaviour of the slope of the distribution curve is just the opposite *ie* there is a decrease in the value of λ with height for dendrites, except at 3:15 local time. This suggests that there should be large crystals at the upper levels compared to the lower heights. This increase corresponds to a slight shift of the precipitation peak towards the higher velocity range at the upper level (see Figs. 5.3 and 5.4). However, plates, columns and bullets do not show this type of trend (*ie* a decrease in the value of λ with height above 9 km) except at 4:15 local time.

At the lowest height (5.8 km) the median diameter of both dendrites and plates was around 0.13 mm which corresponds to a λ value of 5 mm^{-1} at 3:15 local time, but after half an hour (at 3:45) the median diameter of the dendrites had increased to around 0.35 mm, whereas it became 0.3 mm for plates, columns and bullets. This observation clearly suggests that there is a rapid growth of solid hydrometeors within half an hour at lower levels and this trend was evident at almost all heights. Over-all, λ changes from 7.0 at the upper levels to 2.0 near the freezing level corresponding to a change in the median melted crystal diameter of about 0.1 mm at upper levels to 0.35 mm near the freezing level, *i.e.* showing considerable growth as they fall.

How precise are these retrieved values? It is shown below that the precision depends on the spectral width of the clear-air echo. For reference, the width of the spectral peak shown in Fig. 6.1 is 0.35 ms^{-1}. The absolute accuracy also depends on the validity of the assumptions outlined in § 6.3.

6.5 Precision of the Technique

6.5.1 Simulated data

In order to test the stability of our analysis of real data, the model described in § 4.2 was used to generate artificial data with realistic statistical properties. As explained for the retrieval of dropsize distributions, a power spectrum of 4096 points was obtained using equation (6.7), and then a series of same length of random numbers N taken from a uniform distribution in [0, 1] was generated (following Zrnic, 1975; May and Strauch, 1989). Each value of the spectral components is multiplied by $-\ln N$, which results in power-spectral coefficients with an exponential distribution. Taking the square root of each component of the spectral values gives the spectral amplitude. Similarly, 2π times each component of N gives the phase. The quadrature and in-phase components are used to form a complex series, and a time series is obtained by taking the inverse Fourier Transform. Samples of 256 points are taken from the time series for analysis. The estimated mean power spectrum, is obtained by averaging the sixteen 256-point spectra.

An ice crystal cannot grow to a very large size because its growth is limited by many physical processes. Therefore, there should be a cut-off at a certain maximum value of crystal size. In this model spectrum, a cut-off in the large diameter regime has been taken as 3 - 5 mm, depending upon the type of crystal under consideration.

6.5.2 Results

In the simulations, two separate model spectra are developed. (Figs. 6.4a, 6.4b) for dendrites and plates using Eqn. 6.7. The clear-air spectral width is taken as 0.2 ms^{-1} and the background wind as 0.15 ms^{-1}. For dendrites and plates, the values of λ are 2.2 and

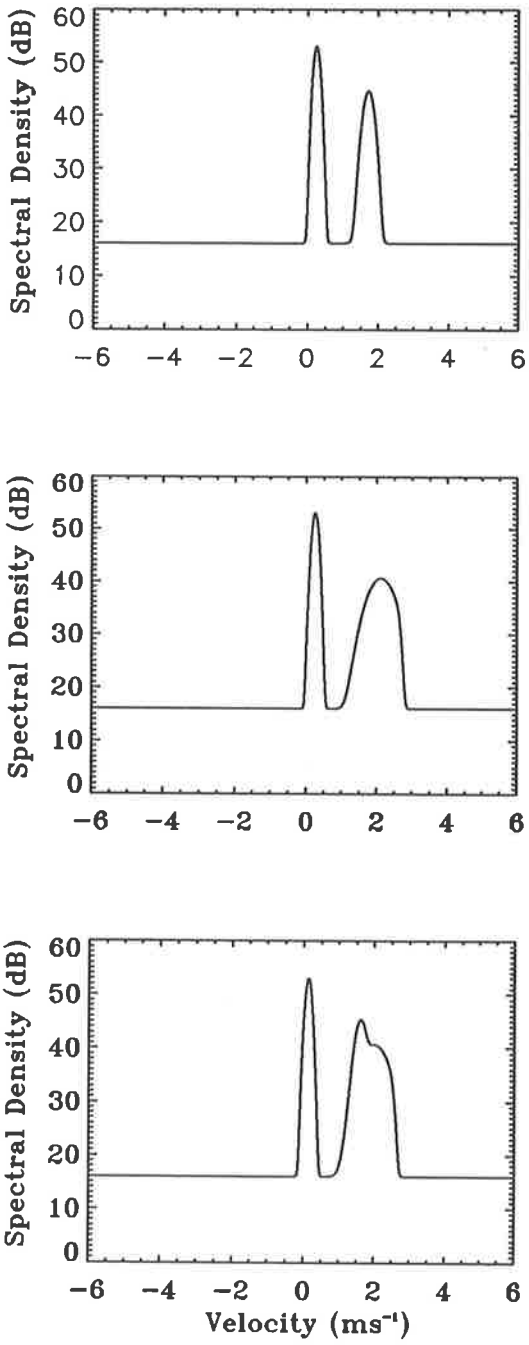

Figure 6.4: Model clear-air and precipitation spectra (without realistic statistical variations) for (a) plates, columns and bullets, (b) dendrites, and (c) a composite spectrum of dendrites and plates. Here the clear-air spectral width was 0.2 ms^{-1}.

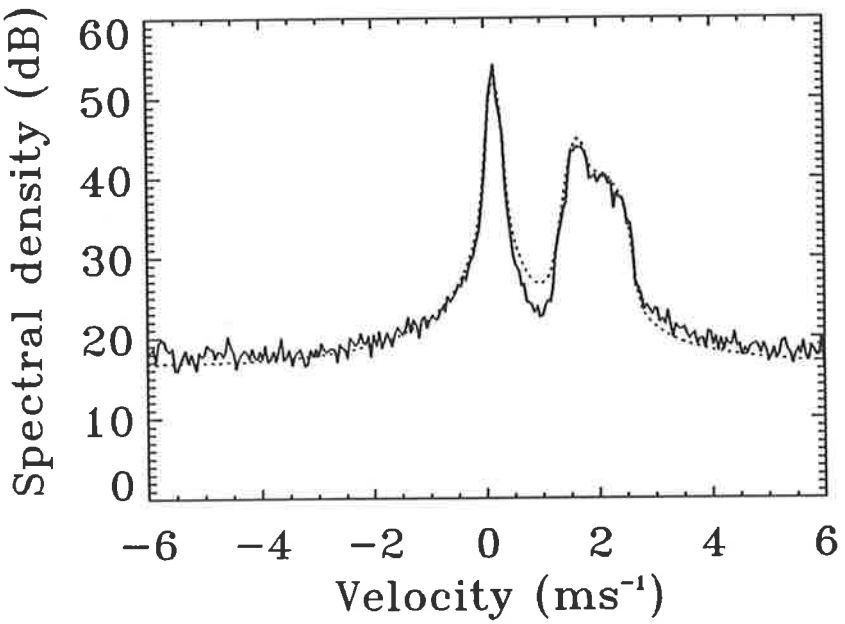

Figure 6.5: Model clear-air and precipitation spectra but with realistic statistical variations (solid lines) and the recovered spectra (dotted lines).

3.5 mm^{-1} respectively, and the corresponding values of N_0 are 2500 and 6000 $m^{-3}mm^{-1}$. These values lie within the range predicted by Eqns. 6.2 and 6.3 (§ 6.3). Since the backscattered power from the solid hydrometeors is equal to the sum of the backscattered power due to different types of ice crystals (see Eqn. 6.9), spectra of dendrites and plates were combined to produce a composite spectrum of the solid-precipitation echo and then the total backscattered power due to clear-air and solid precipitation particles was calculated from using Eqn. 6.7. Fig. 6.4c is the model composite spectrum without considering realistic statistical variations and Fig. 6.5 (solid lines) is the same model spectrum but with realistic "noise" included.

In order to demonstrate that the population spectra can be recovered in the presence of realistic statistical variations, a curve was fitted to the model "observed" spectrum by

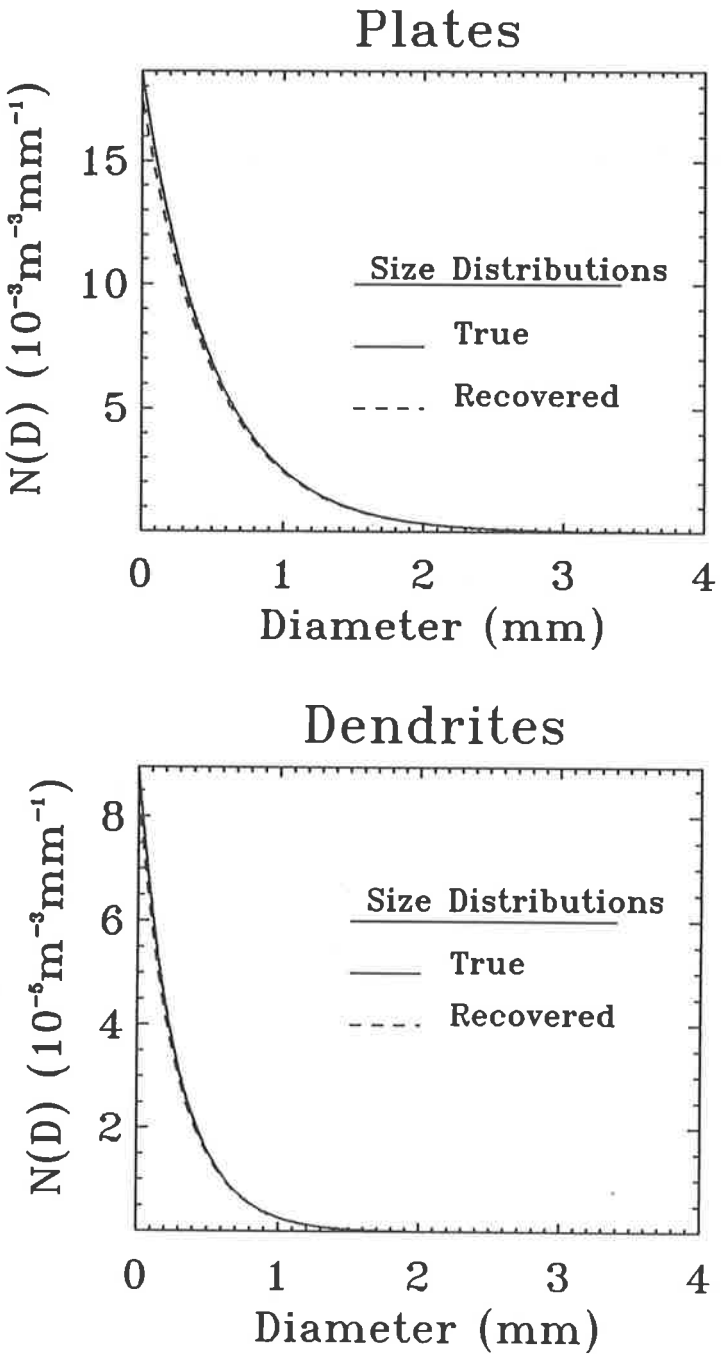

Figure 6.6: Estimated (solid line) and model (broken line) size distributions for plates (upper diagram) and dendrites (lower diagram).

the method described above. It was found that if the initial guesses are close to the true parameters, then the population spectra can be recovered, as shown in the Fig. 6.5 (dotted lines). (Here the window function is also included using Eqn. 6.13 to match with the observed spectra). Comparing this with the observed spectrum (solid lines), we found that the fit is, on the whole, excellent. However, to keep the equations stable, the maximum diameter of dendrites, plates and columns has to be limited. Otherwise, the contamination of the echo due to one ice type on that of another will be very large. In the present study, the maximum diameter of plates, columns and bullets is taken as 3 mm, whereas for dendrites diameters of 5 mm are considered.

The estimated size-distributions of dendrites and plates are shown in Fig. 6.6 by a pair of lines; one representing the recovered size distribution (broken line) and the solid line the actual distribution. The estimated size-distribution curve coincides almost exactly with the true curve, except in the very large–and small-diameter regions. This clearly indicates that the size distributions can be accurately recovered, even after the addition of realistic statistical variations. Here the upper diagram corresponds to plates, columns and bullets whereas the lower diagram is for dendrites.

What are the limitations involved in this technique? To what extent do the estimated values represent the true values? The main limitation of the technique is the overlapping of echoes due to one ice type on those of another. There is no obvious approach to objectively decide on an initial guess of the parameters in the least squares fitting process. So, it is essential to see the deviations of the retrieved values from the actual values as various parameters are changed. The limitations of the technique are studied first by changing the random numbers used to simulate the statistical variations. Fig. 6.7 shows scatter plots of recovered values of λ for dendrites and plates, for the situation in which the clear-air spectral

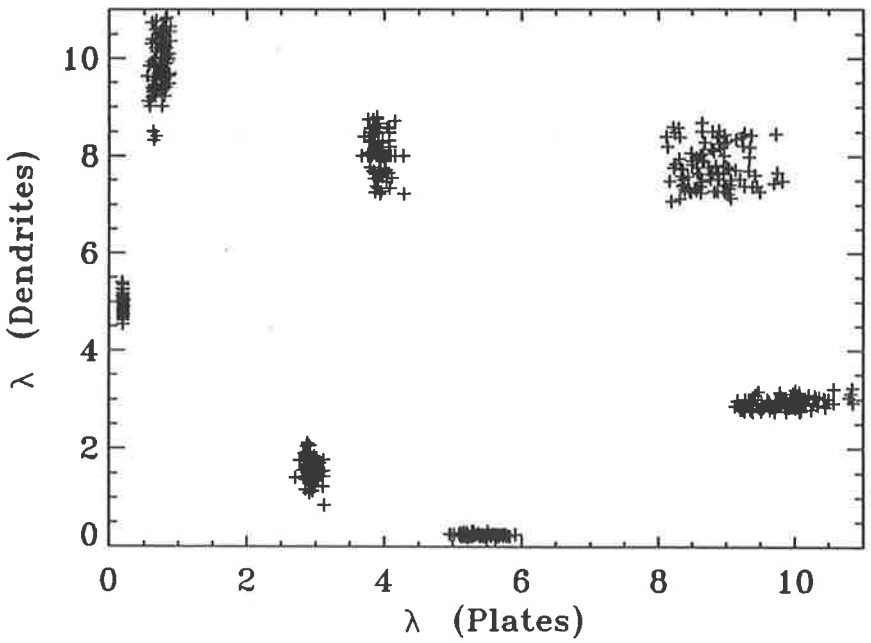

Figure 6.7: Scatter plots of recovered values of λ for dendrites and plates from one hundred different simulations for fixed values of λ and N_0, but with different random numbers. The clear-air spectral width was 0.1 ms^{-1}.

width was fixed at 0.1 ms^{-1}. One hundred different simulations were carried out for each of seven different combinations of λ and N_0. These values were selected using Eqns. 6.2 and 6.3 for wide range of precipitation rates such as from .05 to 100 mm hr^{-1}. However, these equations are not general. The values of λ and N_0 can vary from one occasion to another. We can improve the retrieval technique by estimating λ and N_o using the assumption that they are independent of r. It is apparent that the points cluster around the correct values of λ, with a tendency for the distributions to be elongated along the plot-axis corresponding to the larger value of λ. However, the *relative*, or percentage, variations in the recovered values are about the same. It was also found that the deviation from the actual distribution is very small.

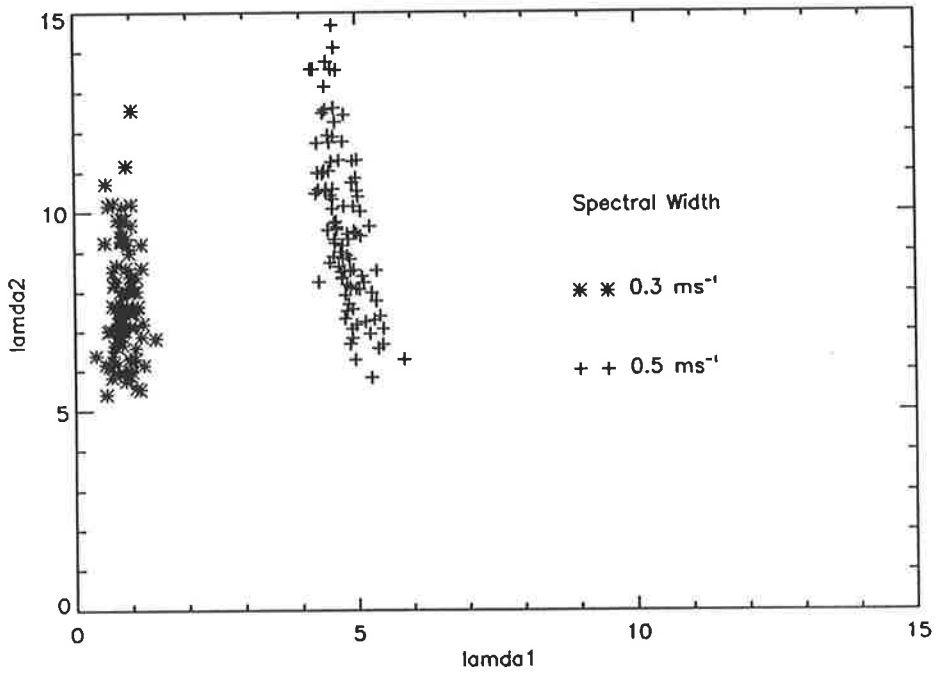

Figure 6.8: Scatter plots of recovered values of λ for dendrites and plates from one hundred different simulations, for fixed values of λ and N_0, but with different random numbers. The clear-air spectral width was 0.3 and 0.5 ms^{-1}.

To study the effect of the clear-air spectral width on the fitting processes, the spectral width was successively increased from 0.1 to 0.3 and 0.5 ms^{-1}. The parameters involved in the fitting process were again recovered for one hundred different simulations achieved by changing the random numbers (Fig. 6.8). The values of λ and N_0 used are selected again from Eqns. 6.4 and 6.5 for wide range of precipitation rates as mentioned earlier. It can be seen that, although the recovered values scatter about the correct values, the deviations from the actual distributions are greater than before. The deviations increase as the clear-air spectral width increases, becoming very large when the clear-air spectral width is 0.5 ms^{-1}.

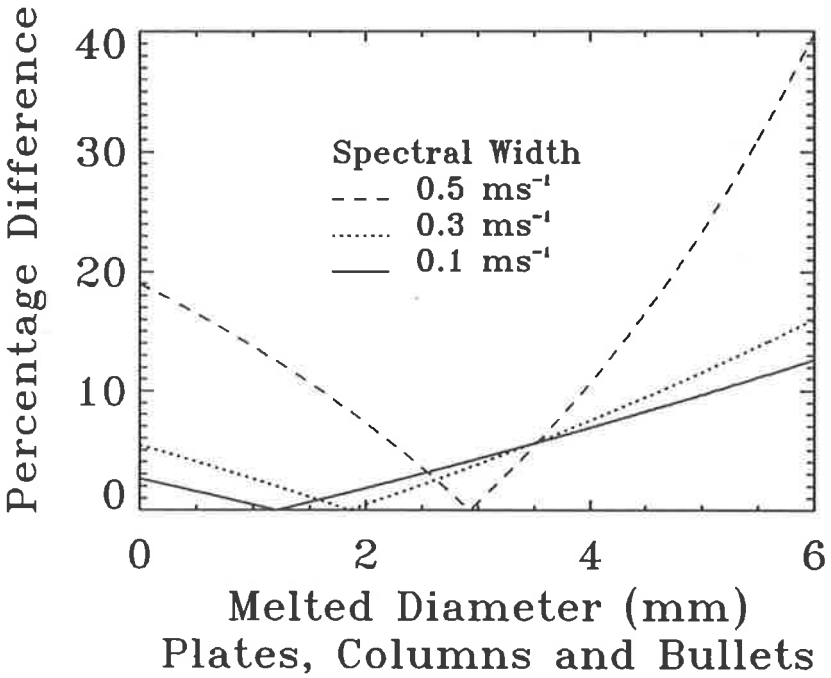

Figure 6.9: The relative difference between the recovered dropsize distributions and model size distributions for plates, columns and bullets.

To summarize the results, the relative, or percentage difference, between the true and so-called "observed" values of size distributions was calculated for plates, columns and bullets. The observed values were estimated by taking a mean from one hundred simulations with different statistical variations. When the clear-air spectral width is 0.5 ms^{-1}, the relative difference for dendrites is up to 20% in the small-diameter region and up to 40% in the large-diameter region (Fig. 6.9). When the clear-air spectral width is 0.3 ms^{-1}, the percentage difference is 20%. However, when the clear-air spectral width is 0.1 ms^{-1}, the relative difference is near 10% for plates, columns and bullets.

The percentage differences between the actual and estimated values are very large when the clear-air spectral width is 0.5 ms^{-1}, but there is a certain diameter range for which the percentage error is small. For example, between 1.2 mm and 3.8 mm diameter, the

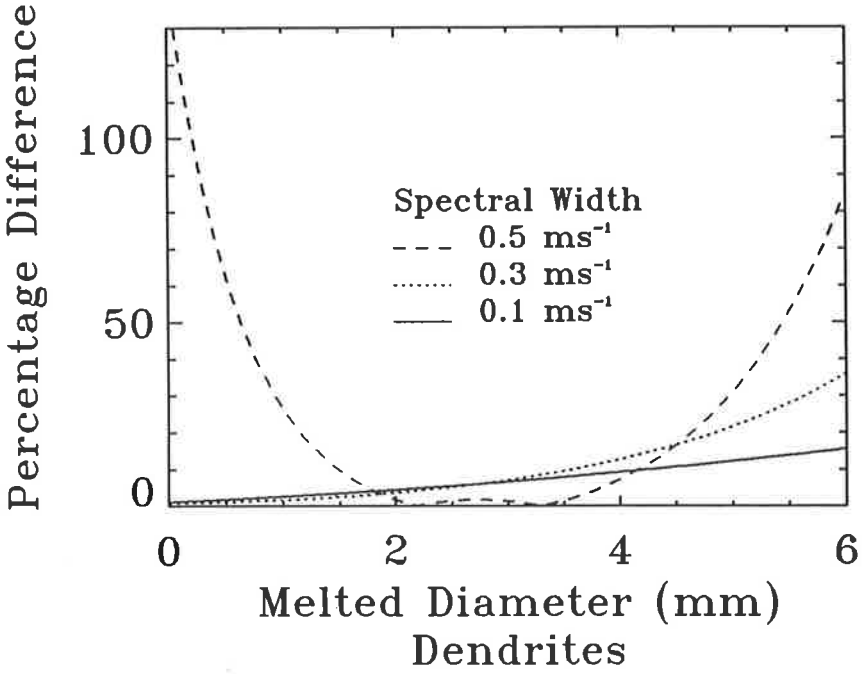

Figure 6.10: The relative difference between the recovered dropsize distributions and model size distributions for dendrites.

percentage error is below 10 % for a clear air-spectral width of 0.5 ms^{-1}.

The relative, or percentage, difference between the true and "observed" values of size distributions for dendrites is shown in Fig 6.10. The estimated error is almost the same as for plates, columns and bullets. A large discrepancy in error is obtained mainly in the small and large-diameter regime. The percentage error for plates is slightly smaller, about 40% in this regime. For the clear-air spectral width of 0.1 or 0.3 ms^{-1} the percentage error is less than 10% when the maximum diameter considered for dendrites is less than 3.75 mm.

Finally, instead of keeping all the parameters constant, the values of N_0 and λ were varied for each value of the clear-air spectral width in order to develop a model spectrum, and then these parameters were recovered. Figs. 6.11a–6.11d are plots for thirty different combinations of N_0 and λ, evaluated with a clear-air spectral width of 0.1 ms^{-1}. The upper

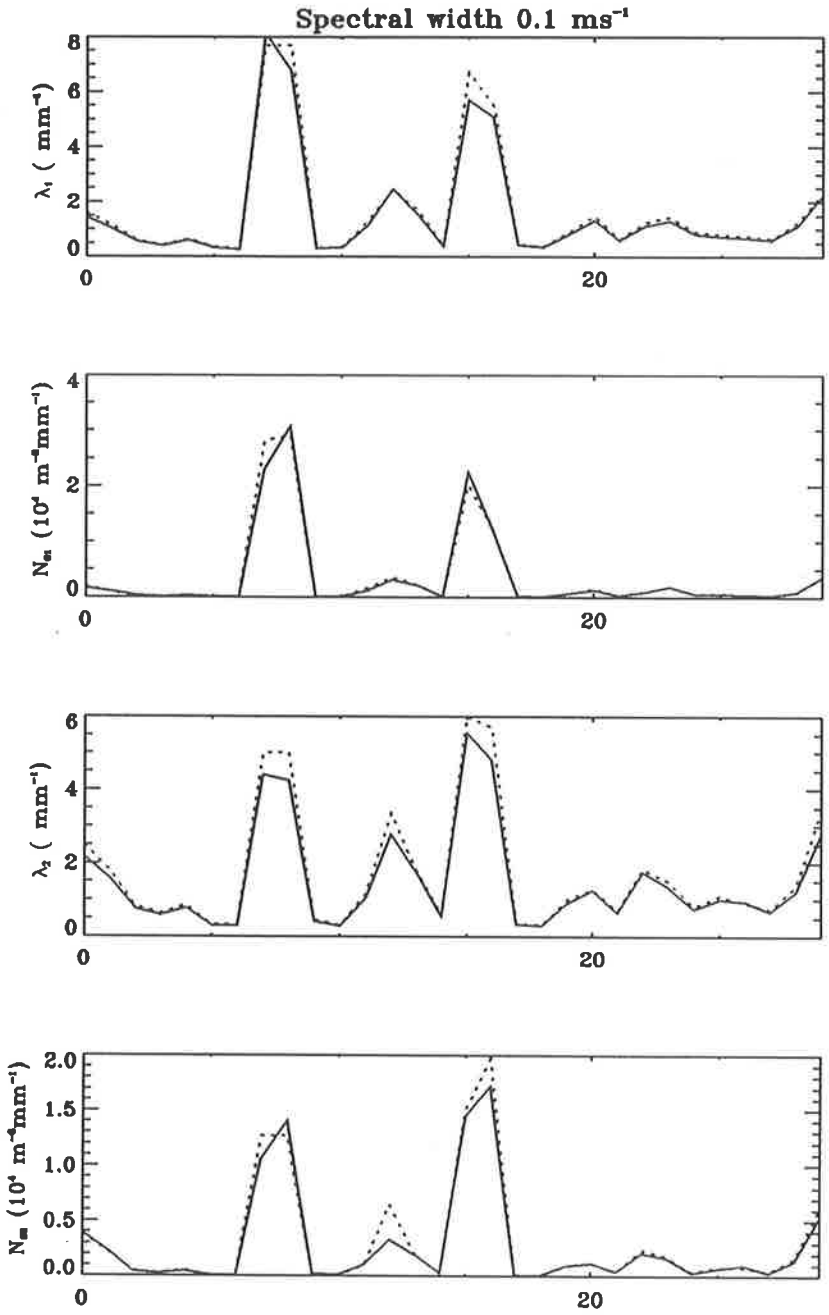

Figure 6.11: A comparison between a series of thirty different "samples" showing recovered (solid lines) and model (dotted lines) parameters for dendrites (top two plots: a, b) and plates (bottom two plots, c, d). The clear-air spectral width was 0.1 ms^{-1}.

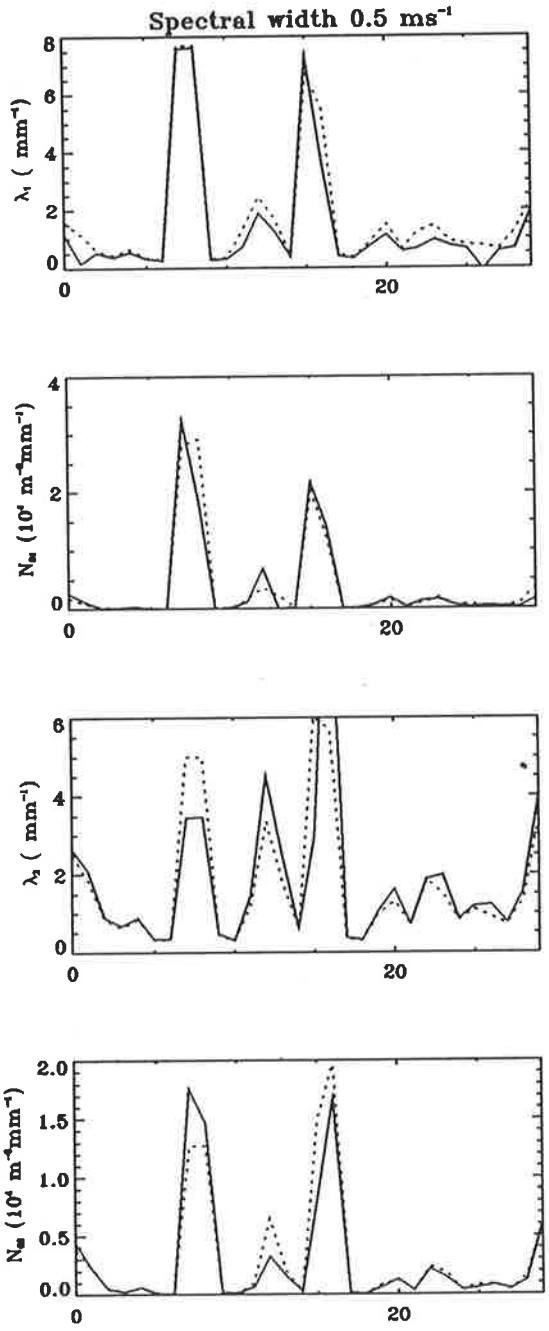

Figure 6.12: A comparison between a series of thirty different "samples" showing recovered (solid lines) and model (dotted lines) parameters for dendrites (top two plots a, b) and plates (bottom two plots: c, d). The clear-air spectral width was 0.5 ms^{-1}.

two plots are for plates and the lower two are for dendrites. The solid lines correspond to the true values and the dotted lines represent the recovered values.

In most cases there is good agreement when the clear-air spectral width was 0.1 ms^{-1}, but when the spectral width was 0.5 ms^{-1} there was a slight departure of the recovered from the actual values (Figs. 6.12a–6.12d). Here the relative errors may be as large as 100%.

6.6 Single ice-crystal types

It has already been mentioned that the consideration of more than one ice crystal type is time consuming in the fitting process by the least-squares method. Additionally, the initial guess of the parameters is much more difficult and contamination of echoes from one type to another is most likely. To make it simpler, let us assume that there is only one ice-crystal type, which is rather unrealistic. However, it can be assumed that the particular ice-crystal types taken into consideration represent an average of all the ice-crystal types within the natural cloud.

Various fall-velocity relations have been discussed in § 5.6. Which of these relations represent the average fall velocity of the various solid hydrometeors? This must be decided from the type of precipitating cloud and the ambient conditions. In this study, the method adopted by Gossard et al. (1992) for snowfall has been used. Recalling equation 5.11,

$$w = 8.8\,[(\rho_s - \rho_a)(0.1)\,D]^{\frac{1}{2}} = 2.78(\rho_s - \rho_a)^{\frac{1}{2}}\,D^{\frac{1}{2}}\,. \tag{6.15}$$

Incorporating air density, the relation can be written as

$$w(p) \approx 2.78\left[\frac{\rho_0}{\rho(p)}\right]^{\frac{1}{2}}\left[\frac{\rho_s - \rho(p)}{\rho_L}\right]^{\frac{1}{2}} D^{\frac{1}{2}} \tag{6.16}$$

where, $\rho(0)$ and $\rho(p)$ are the densities of the air at the surface and at pressure level p

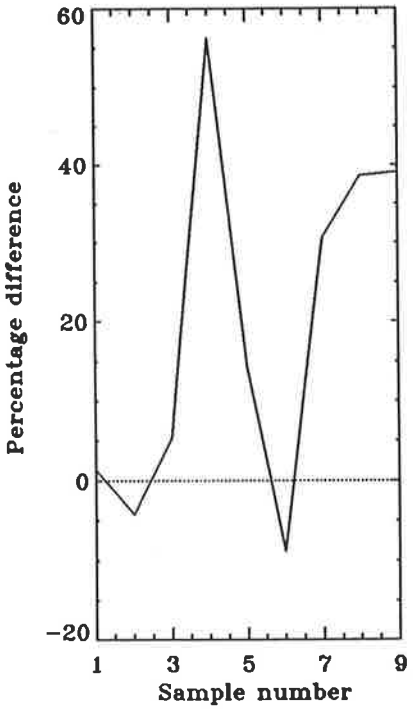

Figure 6.13: Percentage difference of χ^2 values for one and two ice-crystal types.

and ρ_L is the liquid water density.

All together 9 samples are chosen from the data observed on 11 Nov, 1990, and for each a power spectrum is fitted considering one and two ice-crystal types. The coefficient 2.78 has been altered when the ice echo is very close to the clear-air echo.[1] χ^2 values between the observed and the theoretical spectra are estimated for cases of both one and two ice-crystal types.

Finally, the percentage difference between the estimated χ^2 values for these two cases were estimated for all 9 samples. Fig. 6.13 is a plot of the percentage difference of χ^2 values against sample numbers. Here a positive percentage difference indicates that the estimated χ^2 is greater for one ice-crystal type than for two ice-crystal types. It can be seen clearly that in some cases, the fit for one type is better than for two types, but for most cases fitting

1. When the peak of the observed ice echo is very close to the clear-air echo (fall velocity less than 1 ms^{-1}) the empirical Eqn. 6.16 cannot be used. For this reason, the factor 2.78 of this eqn has been altered slightly in order to produce a precipitation spectrum close to the clear air spectrum.

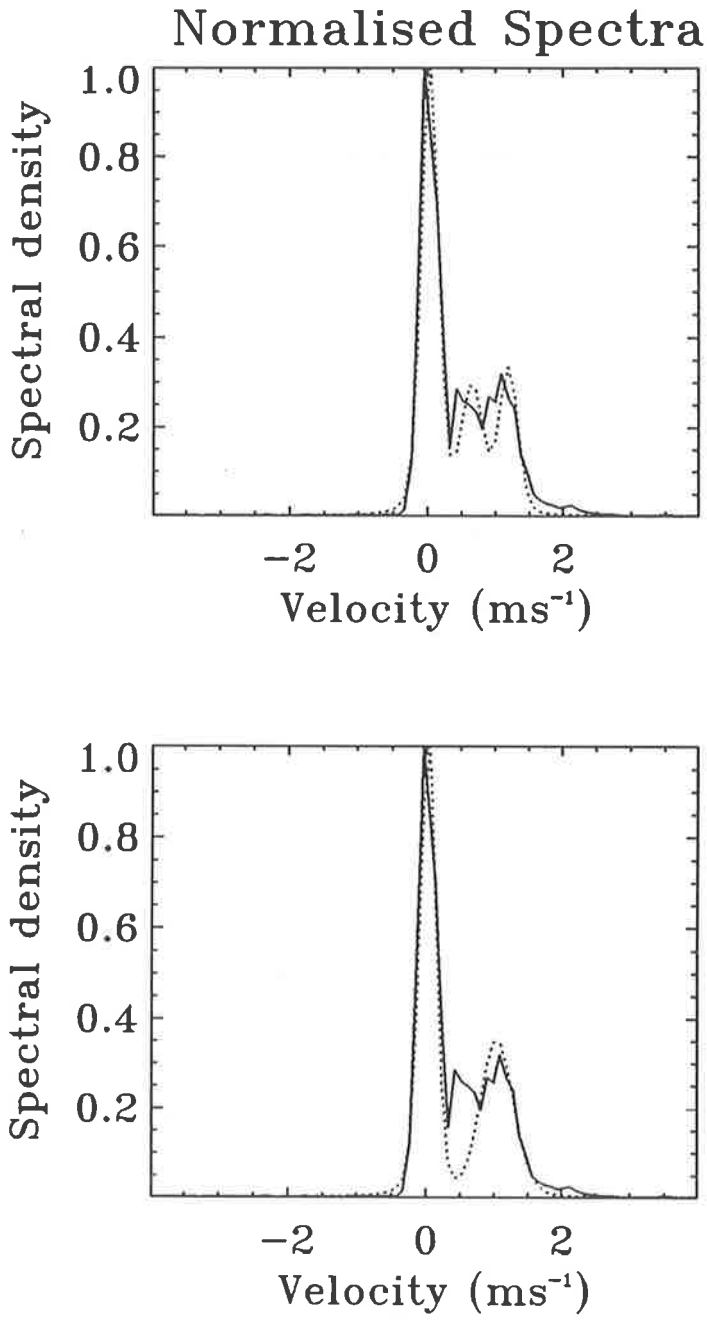

Figure 6.14: Comparisons between spectra for one and two ice-crystal types spectra. Fitted spectrum (dotted line) by assuming one ice-crystal type (lower diagram) and two types (upper diagram) in natural clouds.

two types of ice results in significantly smaller values of χ^2 i.e. better fits. Additionally, two ice-type fitting is essential where two separate ice-echo peaks exist as shown in Fig. 6.14.

In the upper diagram, the dotted line represents a spectrum fitted by considering two ice-crystal types, dendrites and plates. The solid line represents the observed spectrum. The theoretical spectrum matches with the observed spectrum. In the lower diagram, the theoretical spectrum (dotted line) fitted by considering only one ice-crystal type to be present does not match the observed spectrum. Here two peaks in the precipitation echo are clearly visible, whereas the fitting process for one ice-crystal type, of course produces only one peak. Hence, even if the fitting of two types is time consuming, if there are clearly two peaks, then the fitting process for two types has to be considered.

6.7 Conclusion

A radar technique for the determination of ice-particle size distributions within a large volume of cloud using a VHF wind-profiling radar has been demonstrated. The method has been restricted to consider only two types of ice particles (dendrites and plates) in order to make the retrieval problem tractable. This restriction is based on experimental evidence which shows that dendrites are the most commonly observed ice crystals in natural cloud. It is necessary to include more than one ice-crystal type in order to fit the observed radar spectra well. For this reason, in addition to dendrites, aggregates of plates, bullets and columns are included in the simulations, to represent the average of many types in the sample volume in the natural cloud.

The technique was tested by running repeated simulations with different random statistical variations. By changing the slope and shape of the "observed" spectra it was found that the technique has good accuracy, of about 10-30% for the clear-air spectral widths

of 0.1-0.3 ms^{-1}. With hundreds of simulations, it has been shown that the greater the clear-air spectral width the more difficult it is to recover the population spectra. For example, when the clear-air spectral width is as high as 0.5 ms^{-1}, the relative error in the lower-diameter region exceeds 100% and it is also significant in the large-diameter region. It should be noted that off sets of ice echo in the vertical velocity spectrum are small so that for large spectral widths smearing is important. However, in real data obtained with a VHF wind-profiler located at Darwin typical spectral-widths of about 0.25 ms^{-1} were found for scattering from stratiform regions.

The possibility of fitting with only one ice-crystal type is also tested and it has been shown that this gives poor results. If two distinct peaks are visible in the radar power spectra and the precipitation spectra is wide, two ice-type fitting process is essential.

Efforts are continuing to improve the technique, which has obvious limitations. The first is that the retrievals will not be sensitive to small diameter crystals because of the D^6 reflectivity dependence. More importantly, the restriction on the number of ice-types and the *a priori* assumption of ice-type is a major limitation. Additionally, the ice crystals have random shapes and this nonsphericity of the particles may lead to a considerable error in our retrieval technique because the backscatter power from spherical and non spherical particles may be quite different. The wind profiler cannot deal with this problem. The retrieval technique may be improved by combining the results from the profiler with the information obtained from a dual polarization radar which can determine the orientation, size and shapes of the hydrometeors. The coefficients in the fall-velocity relation may also vary from one instant to another because of the random shapes and densities of the ice particles. When the peaks due to individual crystals are distinguishable, the accuracy of the retrieval technique is high. The initial guess of ice parameters is very difficult, because two different

ice crystals moving with different speeds can produce the same echo. To make the retrieval problem tractable, the maximum possible diameter of the crystal is varied with the position of the precipitation peak in the observed spectrum and the different maximum diameters are considered for different crystals to reduce the contamination problem in the observed precipitation spectrum. These two assumptions may also lead to a considerable error in our retrieval technique. However, the observed retrievals do fit the observed spectra very well. Despite these limitations the observation of clearly separated clear-air and ice-peaks in the Doppler spectrum presents a significant opportunity for studies of cloud microphysics and this should be exploited.

Chapter 7

Mesoscale convective systems

7.1 Introduction

Precipitation such as rainfall or snowfall has a big impact on day-to-day human activities. Numerous studies of precipitation formation mechanisms have been carried out all around the world using various experimental and theoretical techniques. Comprehensive theoretical models of precipitation formation and growth are now well developed. However, these models are based largely on laboratory observations and their applications in the atmosphere is very challenging. A lack of profiles of size distributions of hydrometeors and their shape makes precipitation studies more difficult.

A major portion of the precipitation in the tropics and in mid-latitude regions falls in mesoscale convective systems, which cover a horizontal length scale of 50 to 1000 km. In the tropics these systems range from isolated storms to cloud clusters. A cloud cluster is generally associated with multiple storm and tropical squall lines whereas in mid-latitudes the mesoscale convective systems (MCC) are associated with squall lines (Maddox, 1980). The structure of cloud clusters has been discussed by Houze and Betts (1981) and Houze

(1982). Maddox (1980) has discussed the structure of the mid-latitude MCC. In satellite imagery, they had been classified into cloud cluster and squall lines because of their circular and linear appearance. However, many investigators have commented on the similarity between the MCC and cloud clusters.

This chapter is mainly a discussion of squall lines, the vertical up- and down-draughts in the convective systems and their relationship to the precipitation formation and heating and cooling of the atmosphere.

7.2 Squall line systems

The tropical squall line was first described as a distinct meteorological phenomenon by Hamilton and Archbold in 1945, quoted by Gamache and Houze (1982) The first experimental observations of a tropical squall line were carried out by Zipser (1969). The term "squall line" refers to a linearly oriented region of gusty winds, and originated with French mariners (Bluestein and Jain, 1985). Sometimes they are also called disturbance lines.

In the early 20th century, the term squall line was applied not only to convective systems but also to cold fronts, but here we apply the term only to active convective storms.

In the tropics and in middle-latitudes, cumulonimbus convection frequently becomes organized into energetic and very active mesoscale systems. Numerous studies have shown that only a small fraction of tropical convective rain falls from isolated cumulonimbus clouds and the rest from the mesoscale convective systems formed by organized squall lines.

What is the difference between a thunderstorm cell and a squall line? A thunderstorm cell has a very strong updraught and so it carries precipitation particles to upper levels. The life cycle of a thunderstorm cell is very short, such as 30–60 minutes.

A squall line is a band of active thunderstorms which last for several hours. It is formed

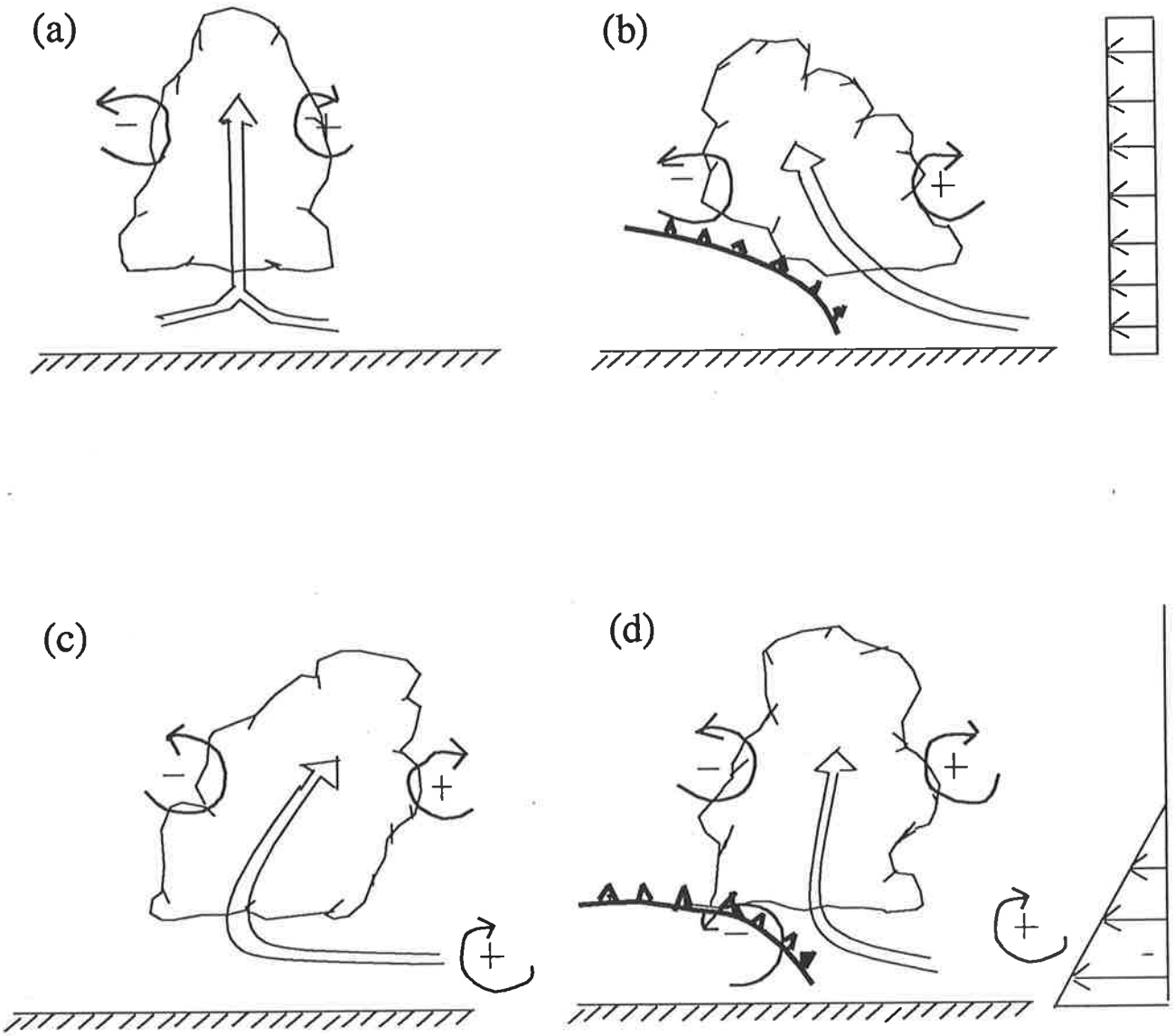

Figure 7.1: Diagrams showing the effect of wind shear and a cold pool on a convective cell. Lifting (a) in the absence of wind shear and no cold pool (b) in the presence of a cold pool, but no wind shear (c) in the absence of a cold pool, but with wind shear and (d) with both a cold pool and wind shear [After Rotunno et al (1988)].

by the combination of individual active cumulonimbus cells called line elements. Why does a squall line last for several hours? One possible explanation is by a balance between the horizontal vorticity associated with low level wind shear and a cold pool, as shown in Fig. 7.1.

When there is no wind shear and no cold pool (fig. 7.1a), the buoyancy force produces a positive vorticity on one side and an equal amount of negative vorticity on the other side. This helps to keep the axis of the convective cell vertical. In the presence of a cold pool alone, the negative vorticity will be stronger and so the axis of the cell leans towards the cold-pool side (fig. 7.1b). This axis will be displaced away from the cold pool side if there is only wind shear (fig. 7.1c). However, a straight updraught is possible if the effect of one is cancelled by the other (fig. 7.1d).

Thus there should be a certain value of the wind shear called the optimal value for a stable updraught. If the environmental wind shear is less than the optimal value for a given cold pool, the convective cell will be slanted and so will be weak (Rotunno et al., 1988)

7.3 Mesoscale convective systems

The precipitation structure of a Mesoscale convective system has been studied by many investigators e.g. Over the equator by Zipser(1969), the equatorial Atlantic by Houze (1977), Zipser (1977), Gamache and Houze (1982, 1983, 1985) and Wei and Houze (1987), equatorial land masses of West Africa by Chong et al. (1987), and the tropical region of North Australia by Drosdowsky (1984), Keenan and Carbone (1992) and Keenan and Rutledge (1993).

7.4 Life cycle

Squall lines and extensive mesoscale complexes have a definite life cycle. Detailed descriptions of this life cycle have been given by many investigators (e.g. Maddox, 1980; Houze, 1977 and Leary and Houze, 1979). Here only a short description is presented. Generally the life cycle can be divided into four major stages, namely, formative, developing, mature, and dissipating.

7.4.1 Formative stage

As soon as the environmental conditions are favorable for convective activities (i.e. weak upward motion in the lower troposphere and an unstable moist lapse rate), a number of individual thunderstorm cells begin to form. These cells generally form a line and move in a direction perpendicular to the line. New cells are likely to form at the lower level in the region between the existing cell and ahead of and in the direction of the low-level wind.

The favourable condition for the development of a new cell is the existence of convergence resulting from downdraughts in the existing cell and the lower level relative ambient wind blowing towards the convective cells. The rainfall at this stage from these isolated cells is around 10 mm h^{-1} or more.

7.4.2 Developing stage

Continuous formation of new cells before the decay of previously formed cells helps to broaden the width of the system. The top of the cell may eventually rise to the tropopause level. Continuous warming due to latent heat release then forms an active convective system. At this stage, the system can produce very strong wind, hail and tornadoes. A distinct upper-level outflow at the rear of the system develops. The precipitation on the ground

may rise as high as 100 mmh^{-1}.

7.4.3 Mature stage

A steady low-level inflow allows the convective cells to continue to form. Severe thunderstorm activity is still likely to occur. The heavy rainfall still persists. The convective activities take place in a moist environment with weak vertical wind shear. There will be a continuous increase in the area covered by the precipitation on the ground and, after a while, a distinct mesoscale high will develop at the upper levels above the system. At this stage the radar detects a maximum echo in both horizontal and vertical sections.

This stage is almost the same as the developing stage, with the main difference being the formation of an an extensive region of horizontally uniform precipitation cloud (called the anvil region) to the rear of the broad convective system. This is the result of the dissipation of cells at the rear of the active system. Once they become weaker, they will diffuse and finally merge together. This region of the mesoscale system is called the stratiform region. A detailed description of the stratiform region is given in §7.5. At this stage maximum precipitation is produced on the ground.

7.4.4 Decaying stage

The active convective cells become increasingly shallow. As time passes they cease to develop and so the area covered by the system begins to decrease. Because of the strengthening of the cold air pool beside the system, the low-level convergence begins to be displaced away from the region of the mesoscale updraught. For this reason the transfer of warm moist air from the lower level to the upper level will be cutoff and the mesoscale system begins to dissipate. The light showers from the stratiform regions may last for several hours.

7.5 Stratiform region

The stratiform region often forms behind an actively convective region of a squall line. This stratiform region has great significance because a large portion of the total precipitation within a squall line lies in this region, covering a wide horizontal area. For this reason numerous theoretical and experimental observations have been carried out in past decades to obtain a clear idea about the vertical air motions and precipitation forms and thermodynamical behaviour within the trailing stratiform regions of the squall line.

The stratiform region generally extends in the vertical direction from the mid-troposphere to the top of the cirrus cloud, whereas in the horizontal direction it covers a distance of 100-200 km.

The main characteristic of this horizontally stratiform region is its melting layer which is often picked up by the radar as a strong echo, called the bright band. Does this strong echo correspond to the presence of very large drops in the melting layer? If not, why should the backscattered signal from the melting layer be very strong? Stewart et al. (1984) and Fovell and Ogura (1988) gave an explanation for this strong echo from the melting layer, based on the phase change within it. Above the melting layer, the hydrometeors are solid particles, which scatter radar signals much more poorly than raindrops. However, the ice particles can aggregate as they fall and so their size will increase. As they begin to melt in the melting layer, the solid hydrometeors will be covered by a very thin film of liquid water, producing a sudden enhancement in the gradient of the refractive index, making these particles better reflecting targets for the radar. The radar detects these particles as a large drop and since, backscattered power is proportional to D^6, the melting layer appears as a very strong echo in every radar cross section of the stratiform region.

The radar reflectivity pattern in the anvil region is consistent with the wind and thermodynamic patterns (Houze, 1977). Many investigators have reported that there is a very broad region of downdraught below the melting layer. This downdraught is of mesoscale extent and has different characteristics from that on the convective scale. The vertical velocity in the mesoscale downdraught is in the range 0.01-0.1 ms^{-1}, which is slow compared to the vertical velocity of 1-10 ms^{-1} in the convective region (e.g. Zipser, 1977; Brown, 1974).

What factor is responsible for producing these mesoscale downdraughts? What is the role of mesoscale downdraught in the stability of the atmosphere? In order to answer these questions, many theoretical and experimental studies of the heat budget and up- and downdraught motions in the stratiform region have been carried out. It has been concluded that the mesoscale downdraught is the result of air-mass contraction below the melting layer because of the cooling due to the melting of ice crystals in the melting layer and the evaporation of raindrops below the melting layer. Even if there is no precipitation on the ground, the mesoscale downdraft can still exist because the precipitating particles can evaporate before reaching the ground, i.e. virga.

The evaporation is the result of the mixing of the mesoscale downdraft with dry midtropospheric air. The relative humidity generally increases with the increase in the rate of evaporation as it descends. However, it has been observed that, despite its high relative humidity, the mesoscale downdraft can sometimes reach the ground.

The rainfall rate from the trailing stratiform region is often around 1-3 mm h^{-1}, whereas the rainfall rate from the convective part may exceed 50 mm h^{-1}. Even if the rainfall rate is very low in the stratiform region, its large area and longlasting behaviour gives it great importance. Houze (1977) estimated a total rainfall of 1.8×10^{12} kg from a trailing stratiform

region during its lifetime, whereas the total estimated rainfall from the squall line region (convective region) was around 2.8×10^{12} kg. Thus the rainfall received from the stratiform region is about 40% of the total rainfall from the whole system. It clearly indicates that the anvil region can give an enormous amount of rain and this is due to the continuous entry of decaying cells into the stratiform region from the convective region.

7.6 Updraught and downdraught motions

Updraught and downdraught motions of a convective mesoscale system play a vital role in the precipitation features on the ground and in heat and momentum transfer to the upper level. Here only a short review of the profiles of vertical velocities of the MCS in the convective and stratiform regions are presented.

7.6.1 Stratiform profiles

A mesoscale downdraught and updraught in the stratiform region of a squall line has been simulated by Brown in 1979, quoted by Leary and Houze (1979). Generally in stratiform regions there will be a mean upward motion in the upper troposphere and downward motion in the lower troposphere. The existence of downward motion has already been mentioned in § 7.5 The upward motion is very often located from 0–2 km above the melting layer (Houze, 1989).

The upward motion above the melting layer and downward motion below the melting layer have been confirmed by many other investigators. Fig. 7.2 is a compilation of vertical velocities obtained by previous investigators in the stratiform regions, for tropical oceanic and island cases.

Chong et al. (1987) found that the continental tropical stratiform velocity profiles also

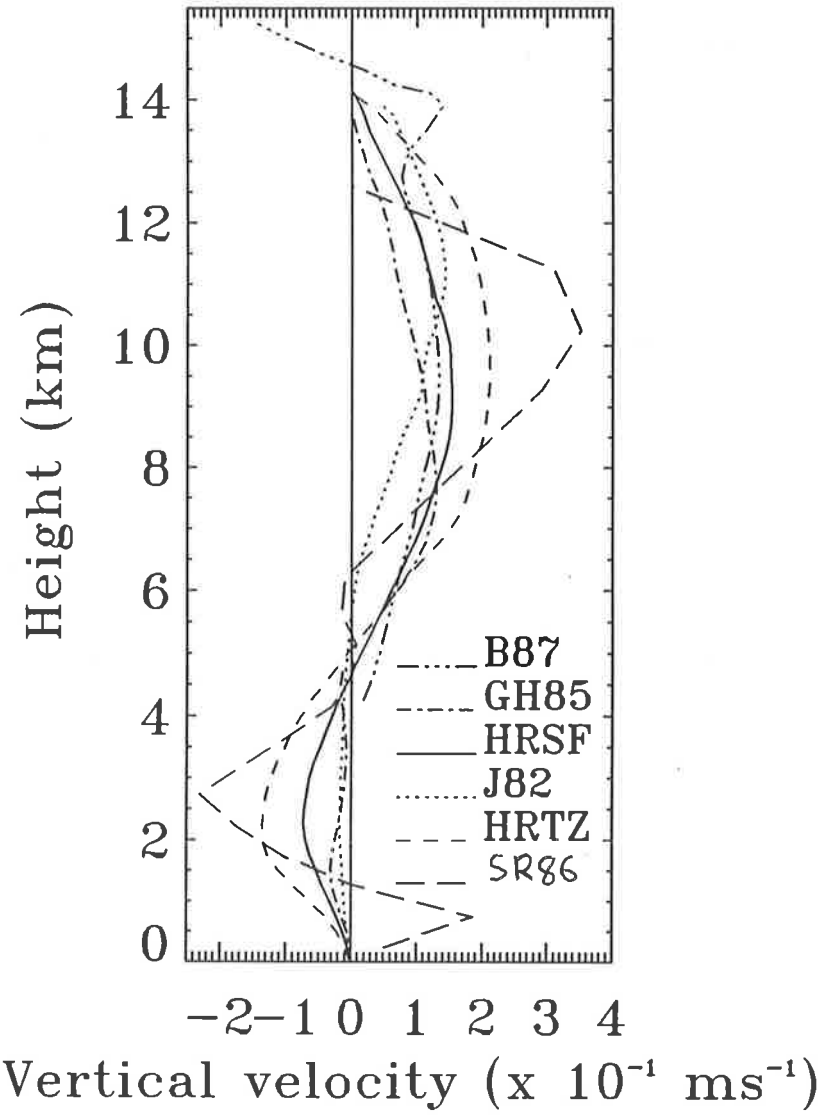

Figure 7.2: Tropical, Oceanic and Island stratiform-region vertical velocity profiles presented by Houze and Rappaport (1984) in stratiform regions (HRSF) and transition region (HRTZ); Johnson in 1982 (J82); Gamache and Houze in 1985 (GH85); Balsely et al. in 1988 (b87); and Srivastava et al., 1986 (SR86). [Reproduced from Houze (1989) and Srivastava et al. (1986)]

have the downward motion below the melting layer and upward motion above the melting layer, but the magnitudes of these velocities are much more intense in the continental type. Here the melting layer is at a height between 4.5 and 5.5 km.

Unlike the profiles of other researchers, Srivastava et al. (1986) observed a weak ascending motion in the boundary layer (below 1 km in height). They commented that this weak ascending motion is the result of intense convergence near the surface. They estimated the vertical velocity by numerical integration of the continuity equation. The vertical air velocity is difficult to estimate by this method due to poorly defined boundary conditions and contamination problems caused by the fall velocity of the hydrometeors.

Without using the continuity equation Balsley et al. (1988) observed more complicated distributions near the tropopause (see Fig. 7.2, labelled as "B87"). Using a 50-MHz wind profiler, they have found a secondary maximum around 14 km, and near the tropopause, there was a distinct downward motion. Their results have been confirmed by Johnson et al. (1990). If there are updraught motions above the melting level, how it is possible to get a continuous influx in the melting layer from the upper troposphere to produce widespread rain? Houze and Churchill (1987) found that, above the melting level in the stratiform region, the mesoscale updraft motion is strong enough to hold the growth of ice particles which are growing by vapour deposition, but not strong enough to stop bigger ice particles and their aggregates from drifting down towards the melting level.

7.6.2 Convective profiles

From past observations it has been found that in stratiform regions, the variation of the shape of the vertical velocity profile from one system to another is very small. The observations also showed that the vertical-velocity profiles of convective motions do vary from one

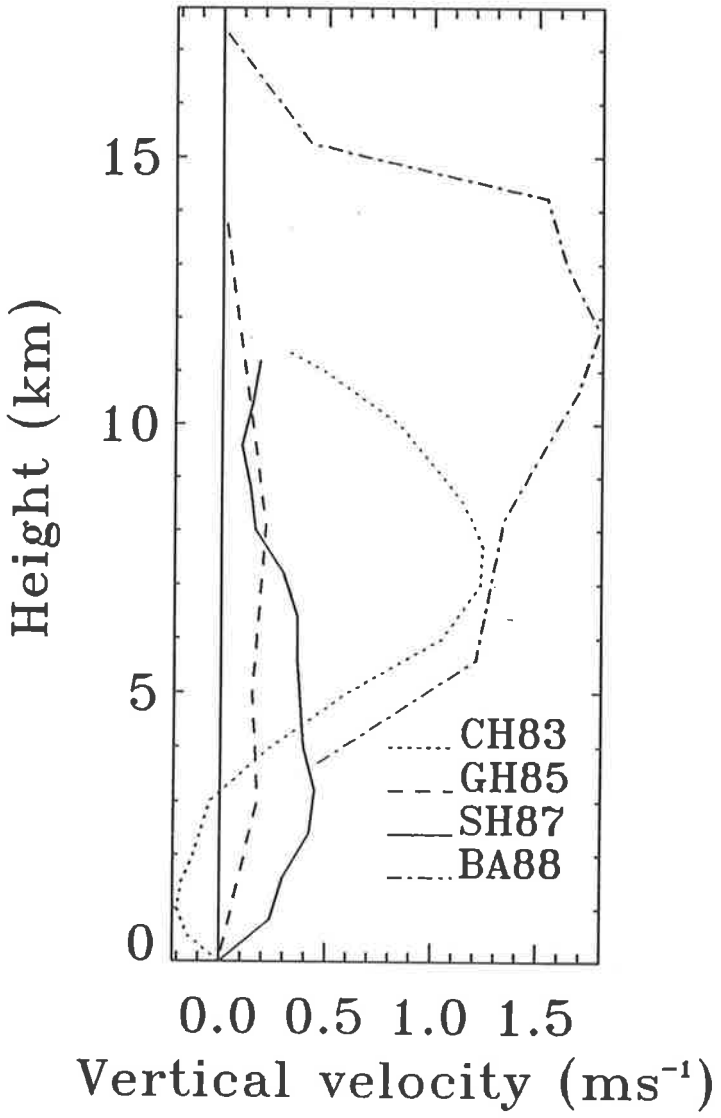

Figure 7.3: The convective region's vertical-velocity profiles, presented by Gamache and Houze in 1985(GH85); Balsley et al. in 1988 (BA88); Chong et al. in 1983 (CH83); and Smull and Houze in 1987 (SH87). [Reproduced from Smull and Houze (1987) and Houze (1989).]

observation to another. These differences may be due either to different meteorological conditions or to the use of different techniques and sampling rates in the analysis of the data. The largest difference in magnitude, shape and in the position of maximum wind was found in the middle to the upper troposphere (Houze, 1989). The analysis of convective regions is complicated by the existence of many individual small-scale up- and down-draughts, so a comprehensive comparison of the vertical-velocity profiles in the convective regions of one system with another has to be carried out.

Fig. 7.3 shows the observations of mean vertical velocities obtained by previous investigators in the convective regions of mesoscale convective systems. In general, deep convective updraughts have been observed in the convective region of a squall line. The updraught is intense in the leading edge of the cell.

Chong et al. (1983) observed an average downward component in the lower level of the convective motions. Upper-level downdraught in the convective regions near the tropopause has been reported on various occasions (Smull and Houze, 1987; and Heymsfield and Schotz, 1985). They commented that this downdraft is due to the existence of upper level convergence resulting from the interactions of outflows from adjacent cells.

7.6.3 Heating rates

What is the relation between the vertical velocity profiles and corresponding heating rates at various levels? This aspect has been studied by many investigators. Here, some of the results obtained in past observations in stratiform and convective regions are presented in Fig. 7.4

Comparing Fig. 7.4 with 7.2 and 7.3, it can be concluded that the shapes of the heating-rate profiles are similar to those of the vertical-velocity profiles. For example, the very large

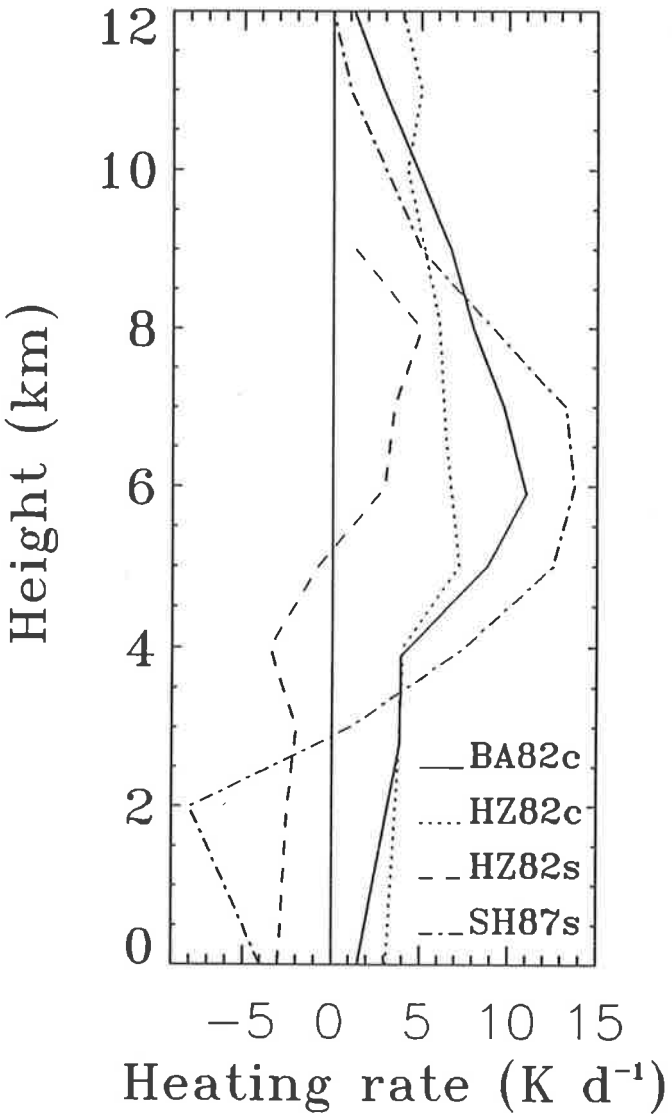

Figure 7.4: Convective and stratiform regions heating profiles. The curves BA82c and HZ82c are the heating rates of covective regions computed from the vertical velocities of Balsley et al. (1988) and Houze (1982). Similarly, thc curves HZ82s and SH87s are the heating rates computed from the data presented by Houze (1982) and Smull and Houze (1987) for stratiform regions. [Reproduced from Gamache and Houze (1989)].

heating rate of Balsley et al. (1988) at the 12-km height in the convective region corresponds to a peak vertical velocity of $\approx 1.85\,\mathrm{ms}^{-1}$ at that level. The mesoscale descent in the stratiform region below the melting layer corresponds to net cooling of the atmosphere, whereas upward air motion in the stratiform and convective regions produces heating at the upper level. Thus it is clear that the MCC is playing a vital role in taking heat to the upper troposphere from the lower troposphere and boundary layer.

7.7 Climatology of tropical cyclones in Darwin

Darwin is situated in the northern part of Australia and lies at the boundary of the maritime continent region. Darwin gets 90% of its annual rainfall in its wet season from November to March.

Widespread convective activity is observed in January and February in the monsoon period. Onset of the Australian monsoon is regarded as the reversal of low level wind from easterly to westerly. During this period, there will be a southward movement of the monsoon equatorial trough and the southern hemisphere equatorial trough (Gunn et al., 1989). Small cells evolved from zonally forced convective systems often develop into deep meridionally oriented squall lines (Keenan and Carbone, 1992).

The convective activity in Northern Australia is also enhanced by the diurnally generated storms formed by the interactions between the diurnal heating cycle and the local topography. Storms over the islands to the North of Darwin are regarded as the deepest convectively generated storms found on a regular basis anywhere in the world (Keenan et al., 1989).

In order to understand the behaviour of convective cells and their rainfall characteristics, a Doppler weather radar called "NOAA-TOGA" (National Oceanographic and Atmospheric

Administation- Tropical Ocean and Global Atmosphere) was installed in Darwin in 1987 by the US National Aeronautics and Space Adminstration (NASA) and the Australian Bureau of Meteorology Research Centre (BMRC). Since then a series of comprehensive experiments such as Tropical Rainfall Measuring Mission (TRMM), Island Thunderstorm Experiment (ITEX), Down Under Doppler and Electricity Experiment (DUNDEE) have been carried out. For the DUNDEE program, the MIT (Massachusetts Institute of Technology) Doppler radar was also deployed in Darwin.

7.8 Conclusion

Mesoscale precipitation fields are the result of a combination of several isolated convective cells. The orientation of the cells relative to the low-level wind direction is a crucial factor in the intensification of the system, because the alignment of the cells in the direction perpendicular to the low level wind is the most favourable case for the evolution of new cells.

What environmental factors are most responsible for longlasting features of cloud and storm and their intensity? How do clouds evolve in a storm? How is the heat budget maintained in the troposphere? To answer these questions, comprehensive studies of mesoscale convective motion in well defined squall lines have been carried out by many investigators. There are variations from one occasion to another. e.g. sometimes the stratiform regions are visible on both sides of slow moving convective cells. However, in most cases, the system has been observed with leading convective cells. These cells are arranged in an arc-shaped line, trailed by a large area of stratiform clouds (Leary and Houze, 1979; Barnes and Sieckman, 1984 and Houze, 1989). Much remains to be done to get an overall picture of the nature of vertical-velocity profiles in the convective regions of MCCs. The variation of these profiles

from one system to another is also an area for investigation. A better understanding of the physical process involved in maintaining a long lived squall line is essential, because of their impact on day-to-day human activity.

It has been discussed earlier that the heating rate in the atmosphere is a function of the mean updraught and downdraught motions. The precipitation field also depends upon the ascending and descending motions of the air. For this reason, a better understanding of wind and thermodynamic fields is essential. Furthermore, the importance of an understanding of the dynamics and thermodynamic state of these systems cannot be ignored in the study of the general circulation and precipitation mechanisms in the tropics.

Many different techniques and instruments have been used to explore the behaviour of mesoscale convective systems. However, the capability of ground based radars to penetrate through these systems made it possible to reveal their entire internal structure, because these radars have the capacity to obtain information such as reflectivity and mean horizontal and vertical velocities, with good height and time resolution, within the cloud. This makes it possible to estimate the size distributions of cloud particles, liquid water content and rainfall intensities.

A brief discussion of Australian monsoons and the occurrence of tropical cyclones in Darwin have been presented. Accordingly, the next chapter deals mainly with mesoscale observations of vertical-velocity profiles, size distributions of hydrometeors and thermodynamic variability observed under DUNDEE program in 1989/1990, using a Darwin wind profiler and a Doppler weather radar.

Chapter 8

Observations of tropical squall lines

8.1 Introduction

A brief discussion of the dynamics of a mesoscale system and its relation to the precipitation system and heating rates have been presented in the previous chapter. The growth, intensity and dynamical properties of many storms are strongly dependent upon environmental factors, such as the thermodynamic stability and vertical wind shear.

This chapter deals with the cloud and precipitation fields of two deep, well organised squall lines that passed over the Darwin windprofiler on the evenings of Dec 5, 1989 and Jan 12, 1990, hereafter referred to as D0589 and J1290 respectively. The D0589 case was formed south of Darwin during a monsoon break period and the leading edge of the convective region of the system reached the profiler site from the south at about 18:30 local time (LT), whereas the J1290 case reached the profiler site from North at about 18:00 LT.

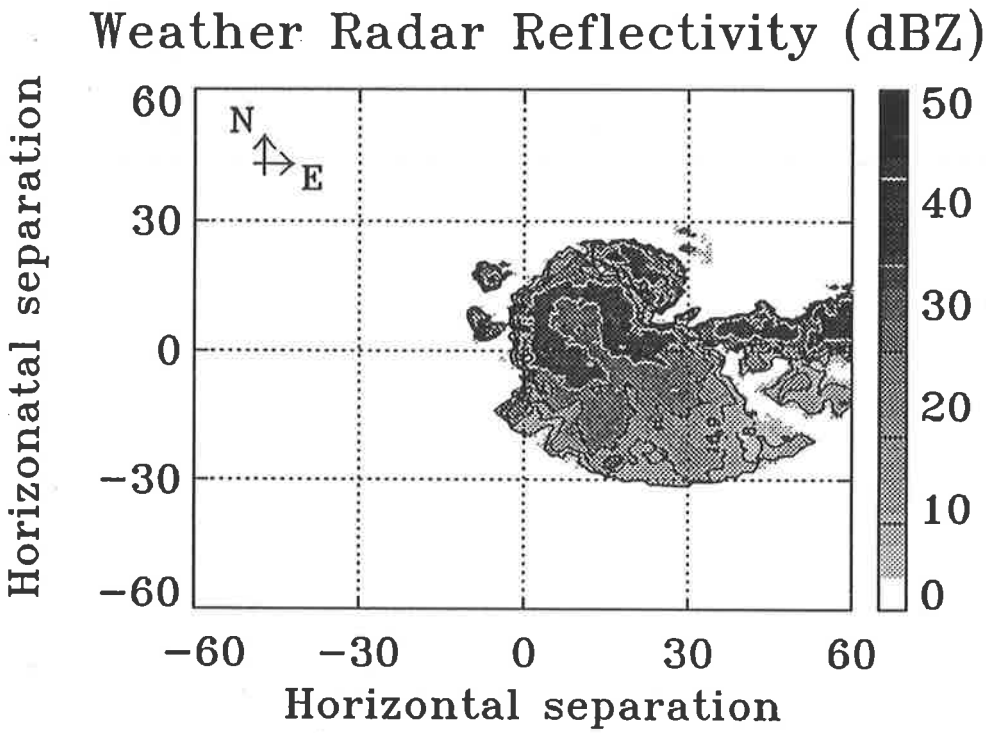

Figure 8.1: Horizontal pattern of reflectivity at 1 km altitude for the tropical squall line at 18:30 (LT) in Dec 5, 1989. The weather radar is located at the origin (0,0), whereas the profiler is at (3,-1) km.

To give a horizontal extension of these squall line, horizontal reflectivities detected by the weather radar at 1 km height level are shown in Figs. 8.1 and 8.2. Here the weather radar is located at the origin (0,0), whereas the profiler is at (3,-1) km.

In the D0589 case, the pattern was moving at a rate of $\approx$ 10 m s^{-1} and the maximum reflectivity recorded at 1 km height level was $\sim$ 51 dBZ at 18:40 (LT). The maximum value of the rainfall from the convective region was $\sim$ 75 mm hr^{-1}. In the J1290 case, the pattern was moving at a rate of $\approx$ 6 m s^{-1} and the maximum reflectivity at 1 km height level was $\sim$ 37 dBZ.

A case study of the evolution of the D0589 storm has been presented by Keenan and

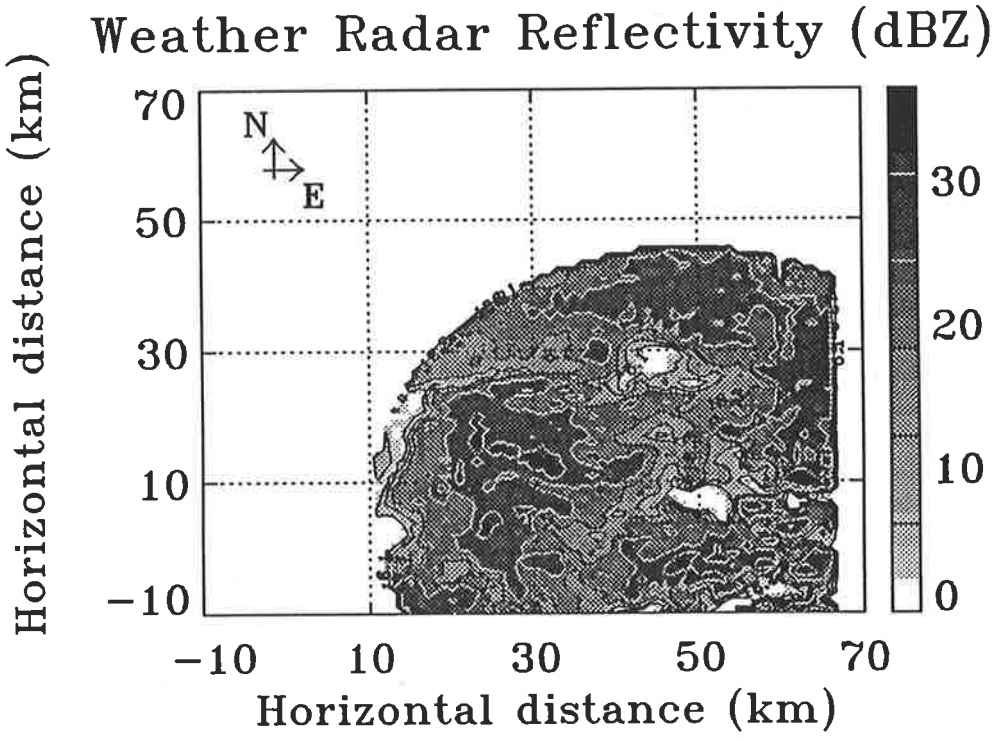

Figure 8.2: Horizontal pattern of reflectivity at 1 km altitude for the tropical squall line at 19:40 (LT) in Jan 12, 1990. The weather radar is located at the origin (0,0), whereas the profiler is at (3,-1) km.

Rutledge (1993) and Cifelli and Rutledge (submitted manuscript, 1994). A case study of J1290 has been presented by Cifelli and Rutledge (submitted manuscript, 1994). The previous findings will be compared with the results of this study, allowing verification of both. The profiler provides information complimentary to the dual-doppler weather radar analysis of Keenan and Rutledge. In particular, direct estimation of the vertical motions and cloud to a height level of 10 km, such as the relation of vertical velocity field to the precipitation size distibution spectrum and their particle concentation, ice water and liquid water content and vertical heating profile will be explored.

In the first part of this chapter, the precipitation echo detected by the profiler will be

discussed. This will be followed by a discussion on updraught and downdraught motions in the convective, moat and stratiform regions. Then the interpretation of the precipitation intensity in terms of the size distribution of precipitation particles (water drops and ice particles) will be presented. The time and height profiles of the size distribution of precipitation particles is used to estimate water content within the system. Finally, the latent heating rate is estimated by measuring the vertical gradient of integrated water content.

8.2 Precipitation echo and bright band

The Darwin profiler was able to detect the precipitation echo during the passage of D0589 and J1290. A strong echo from the liquid drops was visible for more than 3 hours. Precipitation echoes were observed even above the freezing level in high spectral resolution data and they are due to the existence of ice particles in the upper layer. Ice echoes are detected only in the stratiform region and not in the convective region. In the convective region, the large vertical velocity, and the velocity variance obscures the ice echo. For this reason, it was difficult to observe the ice echo above the freezing level and the rain echo below the melting layer in the convective region.

In order to study the intensity of the precipitation echo, the spectrum is separated at the position of minimum signal strength between the clear-air peak and the precipitation peak. A tail is extrapolated from the precipitation echo in order to represent a complete precipitation echo. In the convective region, the precipitation echo is separated only for the lower heights. The area enclosed by the precipitation echo in the vertical-velocity spectrum represents the relative precipitation intensity. For this reason, the integration is performed over the entire range of the precipitation echo in order to calculate the area under the curve.

Fig. 8.3 is a contour plot of the relative intensity in the convective and stratiform regions

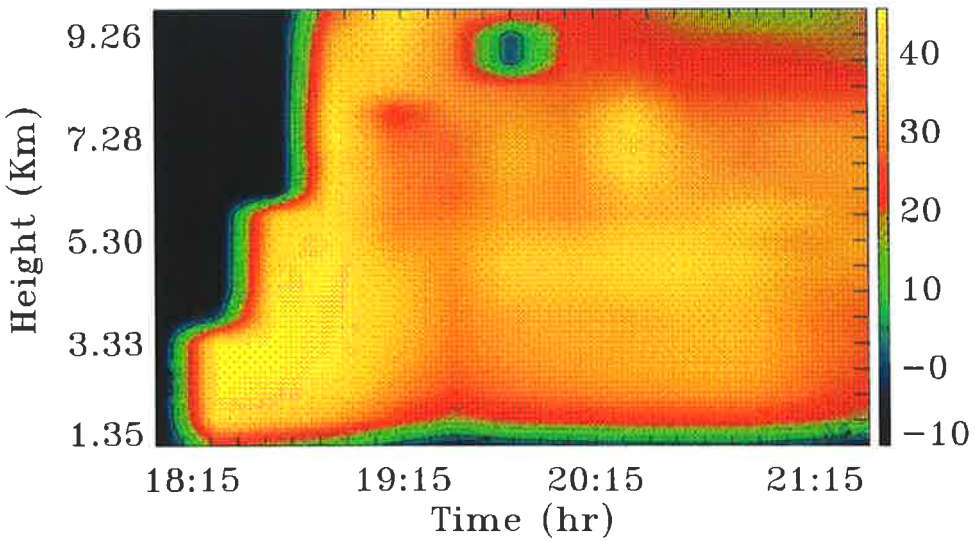

Figure 8.3: A Contour plot showing the relative precipitation intensity measured by the wind profiler in the convective, and stratiform regions on Dec 5, 1989. A region of signal strength of -10 dBZ indicates that the precipitation echo cannot be separated from the clear-air echo in that region. The upper levels of the active convection are obscured by the clear-air echo.

at various heights. A strong precipitation echo is visible in the convective region at the lower heights. In the stratiform region a uniform weak precipitation intensity is observed, except in the height range 3.8-5 km where the precipitation echo was very strong and corresponds to the bright band (see §7.5). The precipitation echo was visible even up to the 9-km height level. In the moat region, the precipitation intensity is low compared to the stratiform region and the bright band is absent. The pattern of the precipitation echo against time and height matches that for the vertical velocity presented in the previous section.

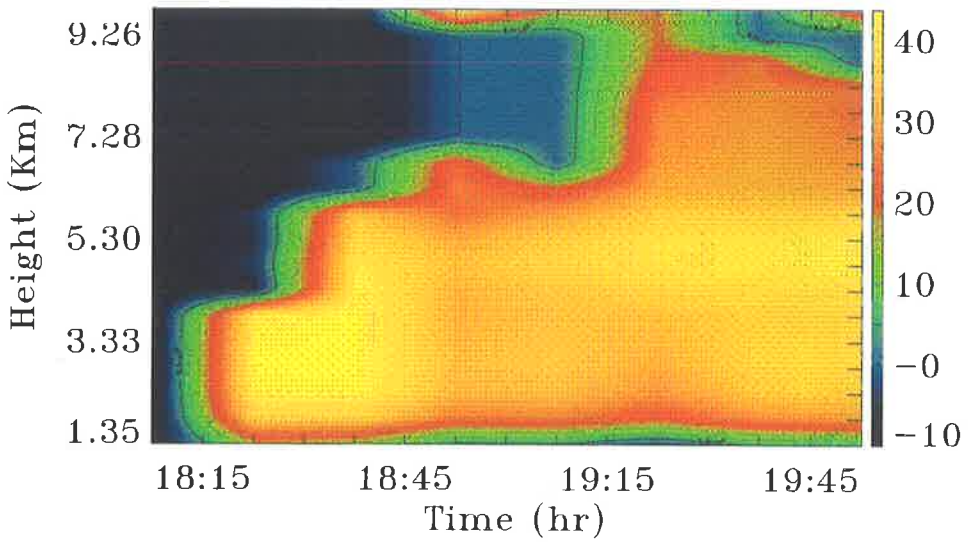

Figure 8.4: As for fig 8.3 but for Jan 12, 1990.

Fig 8.4 is a similar contour plot of relative intensity with height, but for J1290. Here the intensity pattern is almost the same as in Fig. 8.3, but the bright band is much more intense and extends to higher altitudes. The change in the precipitation intensity in the moat region at lower heights is hard to see. However, at upper heights, above the freezing level in the moat, the precipitation echo was negligibly small.

8.3 Calibration of wind profiler

The precipitation echo strengths presented in the previous section are only relative echoes. The Darwin profiler echo strength needs to be calibrated before performing absolute precipitation intensity measurements. The calibration can be done by comparing the precipitation

intensity observed by the wind profiler with the reflectivity obtained from a calibrated 5-cm weather radar located about 4km from the profiler. If R_w and R_p are the reflectivity observed by the weather radar and profiler then

$$R_p = K\, R_w \tag{8.1}$$

where K is a calibration factor. Converting R_w and R_p to dBZ and representing them by P and W respectively, then

$$P = W + C \tag{8.2}$$

where the constant C is also in dBZ. Thus the graph of P against W should be a straight line with slope unity and the y-intercept is C.

Fig. 8.5 is a plot of profiler reflectivity and weather radar reflectivity in dBZ. Here the data are included from Dec 5, 1989 and Jan 12, 1990 and for heights ranging from 1.35 to 9 km. The profiler data were 15-minute averages whereas the weather radar data were essentially instantaneous. Additionally, data obtained from the profiler and weather-radar were not for the same heights, so interpolation has been applied to produce identical height intervals.

A line of best fit was obtained using regression analysis and the slope of the best fit is 1.1, which is very close to the theoretical slope of unity. Since the two radars are in different places with different averaging times and since interpolation has been applied, exact agreement cannot be expected. Additionally, only limited weather-radar data were available for the heights and times observed with the profiler. The calibration constant C, found from the y-intercept, is 26.5 dBZ. This calibration factor has been used to calculate the absolute size distributions of hydrometeors in the following sections.

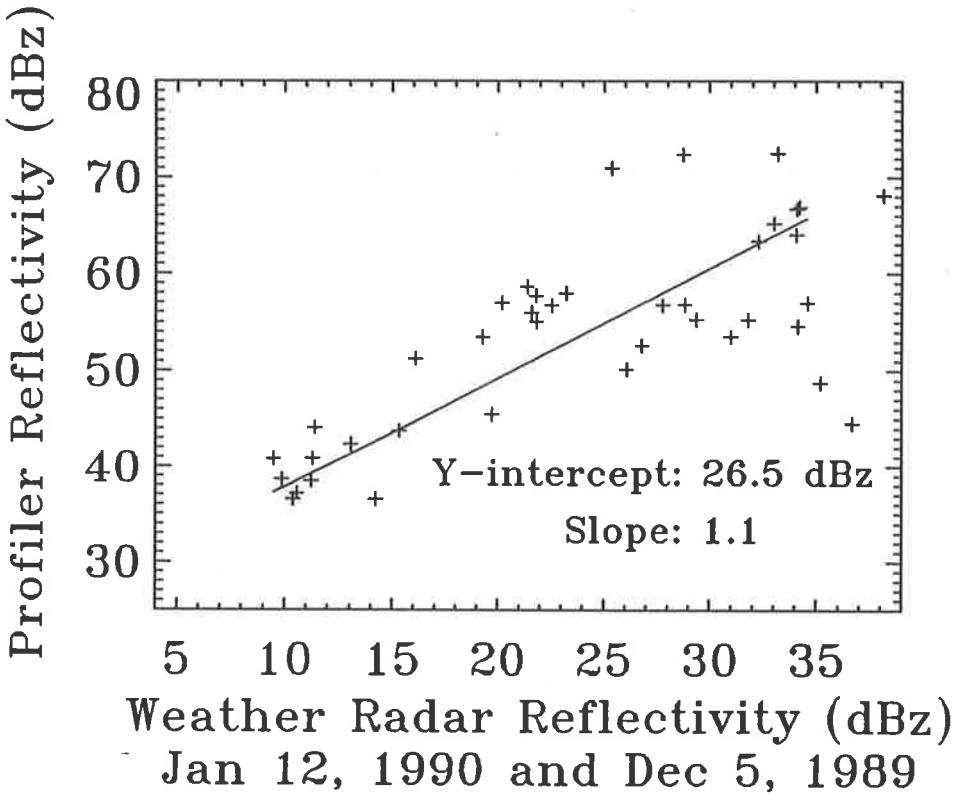

Figure 8.5: A plot of relative intensity observed by the profiler in dBZ versus calibrated weather radar reflectivity in dBZ. Data are from Dec 5, 1989 and Jan 12, 1990.

8.4 Vertical velocity

In order to estimate the vertical velocity, a power spectrum of vertical velocity is obtained and a Gaussian curve fitted to the clear-air part of the spectrum. To reduce contamination from the precipitation echo, the parameters of the Gaussian curve are estimated from the first side (low-velocity side) of the clear-air curve, opposite to the precipitation echo, as stated in Chapter 6. Elimination of such contamination is much more important in the stratiform region, where the peak of the clear-air echo is very close to zero velocity because the vertical velocity in this region is generally less than 0.3 m s^{-1}.

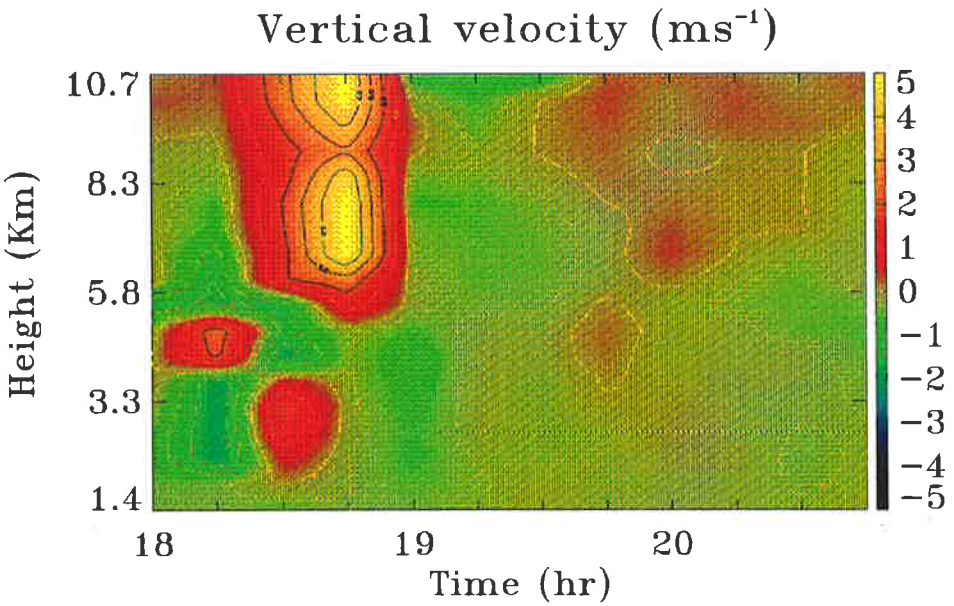

Figure 8.6: A contour plot showing the vertical updraught and downdraught motions of the convective (18:00 to 19:00 LT), moat (19:00 to 19:30 LT) and stratiform (19:30 to 20:45 LT) regions of a tropical squall line which passed over on Dec 5, 1989. Here the time resolution of the data is 90 seconds and the averaging time is 15 minutes.

A contour plot of 15-minute averages of the vertical velocity on Dec 5, 1989 is shown in Fig. 8.6. The strong vertical updraught motion in the convective region above the 4-km height level can be seen between 18:00 and 19:00 LT (Local Time). The instantaneous vertical velocity sometimes exceeds 12 m s^{-1}, although motions of only up to 5 m s^{-1} are shown in the figure. The vertical velocity is strongest above the melting layer, which indicates that glaciation is taking place in order to produce a considerable acceleration in the upper heights. Underneath the convective cell (below 3.5 km), a new small convective cell was emerging. Another small convective cell also can be seen between 18:00 and 18:15 LT. These new cells appear to be developing ahead of the mature cell (see § 7.4.1 and §

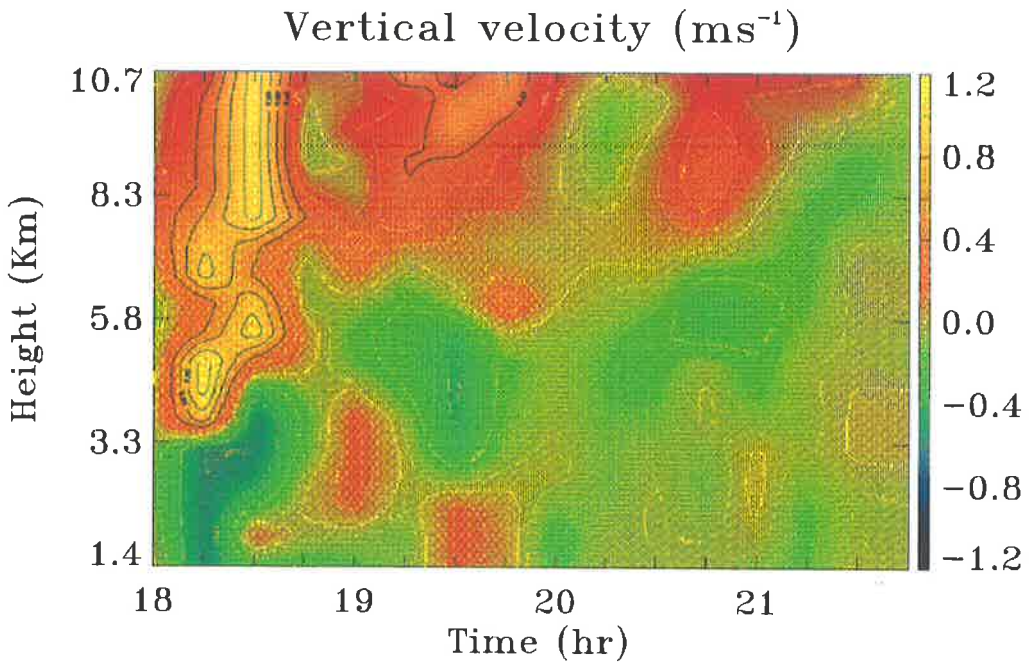

Figure 8.7: As for Fig. 8.6 but for Jan 12, 1990.

7.4.2), indicating the cold pool is advancing ahead of the mature cell and shallow warm rain processes are taking place within the cells.

In the moat region, there is a clear downdraught motion can be seen up to 11 km. The magnitude of the vertical velocity is around 0.3 m s^{-1}.

In the stratiform region, above 5.8 km, there is a weak updraught motion, whereas below the 5.8 km level a weak downdraught is observed. The magnitude of these velocities are of the order of 0.1 m s^{-1}. Note the transition from down to up-draughts occurs significantly higher than the freezing level at about 5 km.

Fig 8.7 is a similar plot of vertical velocity estimated for J1290. An active convective cell with a strong updraught motion can be seen between 18:00 and 19:00 hours LT. A distinct

cool pool lies just underneath the cell. As for D0589, the downdraught in the moat region did not last for a long time.

Some cellular structure is visible in the stratiform region of the J1290 case, as was observed by Keenan and Rutledge. In this case the stratiform region formed from decaying convective cells. Thus even in the stratiform region, some remnants of convective structure remained, in contrast to the D0589 case which appeared as a more classical squall line structure with a uniform stratiform region. The updraught in the stratiform region above the melting layer was distinct and lasted for a long time. Here the upward velocity is larger than that in the stratiform region of the D0589 case by 0.1-0.15 m s^{-1}. In the convective region, the maximum upward vertical velocity is about 2.5 m s^{-1}, which is significantly less than the very large velocity of 12 m s^{-1} for D0589. However, the subsidence below the freezing level is comparable with the D0589 case.

These results are similar to those obtained by Johnson (1982), Houze and Rapport (1984), Gamache and Houze (1985), Srivastava et al. (1986), Smull and Houze (1987) and Chong et al., (1987), as shown in figures 8.4 and 8.5.

A comprehensive explanation of the occurrence of these up- and down-draught motions is presented in § 7.6. A qualitative explanation of the occurrence of these up- and down draught motions is presented in Fig. 8.8. The vertical velocities in convective, moat and stratiform regions are indicated by thick arrows. These motions have a direct influence on the temperature and humidity of the air (Houze, 1977) and their direct impact on the precipitation field is examined more fully in the following section.

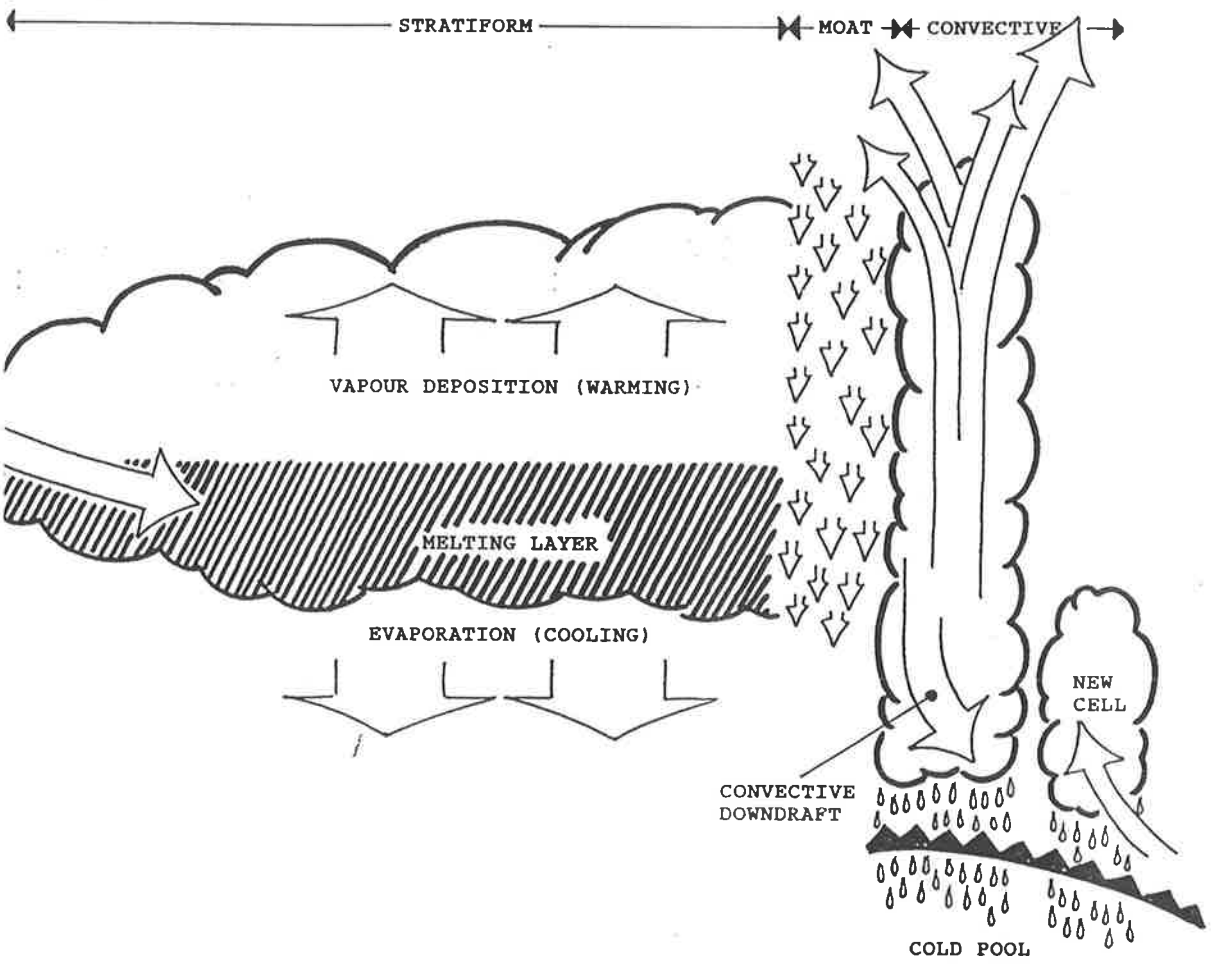

Figure 8.8: A schematic diagram of vertical velocity in convective, moat and stratiform regions and their relation to precipitation and heating rates.

8.5 Dropsize distribution

The dropsize distribution is an essential factor in the study of cloud microphysics. For example, variations in this distribution with time and height affect the cloud optical properties and the estimation of rainfall intensity from radar observations.

Here the size distribution of liquid drops have been estimated for both the D0589 and J1290 cases using the technique discussed in § 6.4. The Nyquist velocity in the vertical-velocity spectrum was 20.07 ms^{-1}. To see the contribution from smaller and larger drops, a median volume diameter has been estimated using Eqn. 3.27. Dropsize distributions were recovered both for the stratiform region and the edge of the convective region. In the stratiform region, precipitation echoes were observed even above 4 km, but in the convective region precipitation echoes were visible from 1.35 km to an approximate height of 3 km as previously noted in §8.2. Above this height, it was hard to separate the precipitation echo from the clear-air echo. The estimated size distributions in the convective region are generally less accurate than those retrieved from the stratiform regions (see § 4.3.1).

Fig. 8.9 is a height profile of the size distribution at the edge of the convective region for 1.35-km to 3.82-km height levels in the D0589 case at 18:55 LT. The lower solid line is the dropsize distribution while the dotted line is a fitted size distribution using a Marshall and Palmer (1948) exponential distribution. Slight departures from the exponential distribution can be seen at all heights. Here the profiles of dropsize distributions have been estimated for about two and a half hours (18:52 to 21:07 LT).

Sometimes, a distinct double peaked spectrum was detected using high-resolution data for which the Nyquist velocity is 6.02 m s^{-1}. However, these peaks are very close to the position of zero velocity, which makes it difficult to separate the precipitation echo from the clear-air spectrum and the absolute amplitude has a large uncertainty. In some cases,

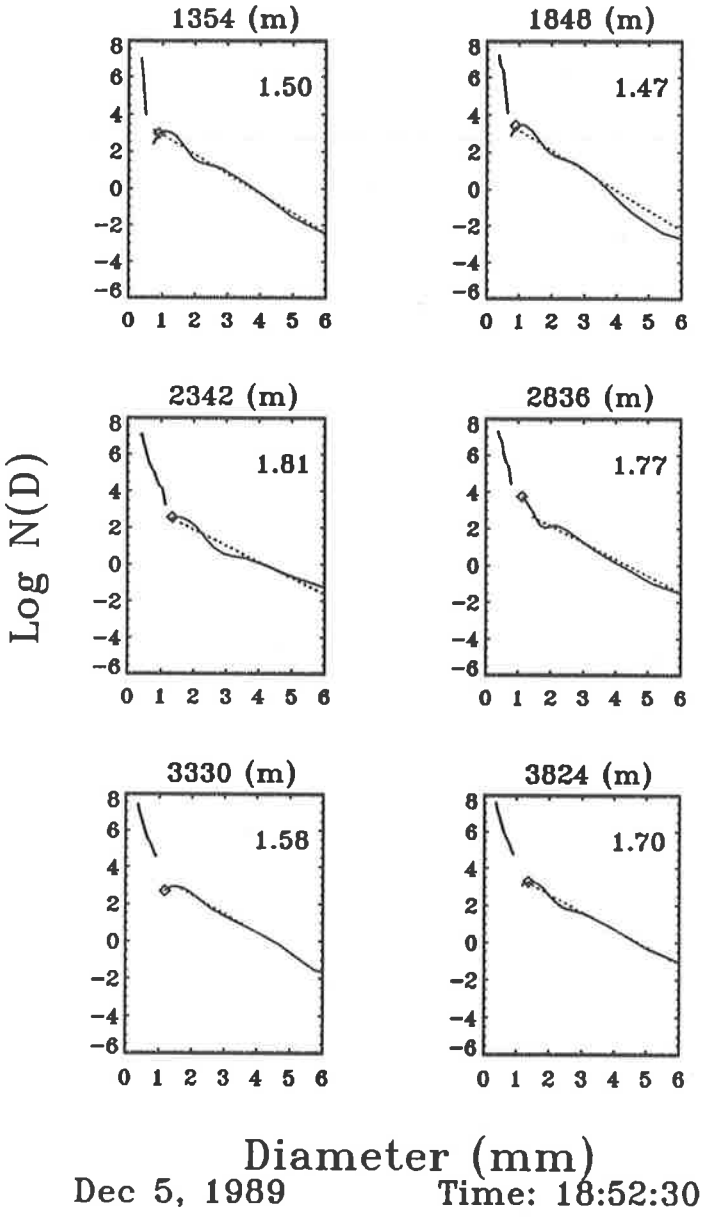

Figure 8.9: Height profiles of dropsize distributions at the edge of the convective region. The solid line corresponds to the estimated size distribution and the dotted line to the exponential distribution. The upper solid line on the left side of the diagram represents the size distribution for small drops estimated from high resolution data. The number in the right upper corner represents the estimated value of median volume diameter. [Dec 5, 1989]

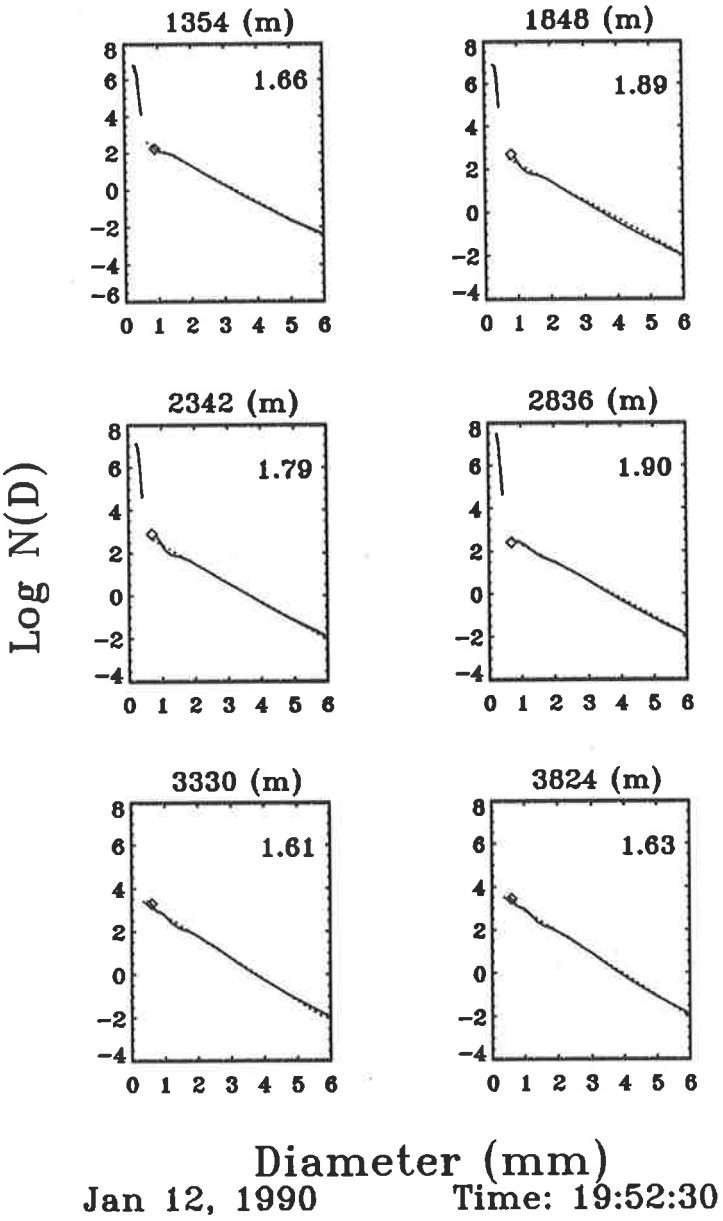

Figure 8.10: As for fig. 8.9 but for Jan 12, 1990 in the stratiform region.

size distributions of these small drops were estimated as shown by solid lines in the top left corner of the diagrams (Fig. 8.9 and Fig. 8.10). This population of small drops may be associated with drop breakup and collision near the melting level, but they appear to account for a significant part of the total water content.

The median volume diameter divides the water content in the cloud in such a way that half of the total volume of water resides in drops larger than this diameter (see § 3.6.1). It is convenient to discuss the distributions as a whole and as parameterised by the median volume drop diameter and total water content. Here the median volume diameter of rain drops has been calculated using Eqn. 3.27 for the large drop part of the spectrum for both the D0589 and J1290 cases.

The cloud microphysical structure of the convective, moat, and trailing stratiform region shows considerable detail. For example, the shape of the size distribution of the drops does not change much with height in the moat and stratiform regions, but there is a considerable change in the dropsize distribution with height in the convective region. There is also a considerable change in the dropsize distribution with time at all levels in these regions. Height and time profiles of dropsize distribution in the convective region for the D0589 case are shown in Fig. 8.9. Here, the median volume drop diameter at 18:55 LT in the convective region of the storm at six different heights varied from 1.47 to a maximum value of 1.81 mm. In the moat region (not shown in the figure), the median volume drop diameter at 19:20 LT at six different height levels varied from 0.82 to just 0.99 mm, whereas, the median volume drop diameter in the stratiform region varied from 0.18 to 0.30 mm between 19:40 and 21:10 LT.

In the J1290 case, the size distributions were estimated for the height range 1.35-3.82 km, but only for one and a half hours (18:22 to 19:52 LT). The results (Fig. 8.10) show

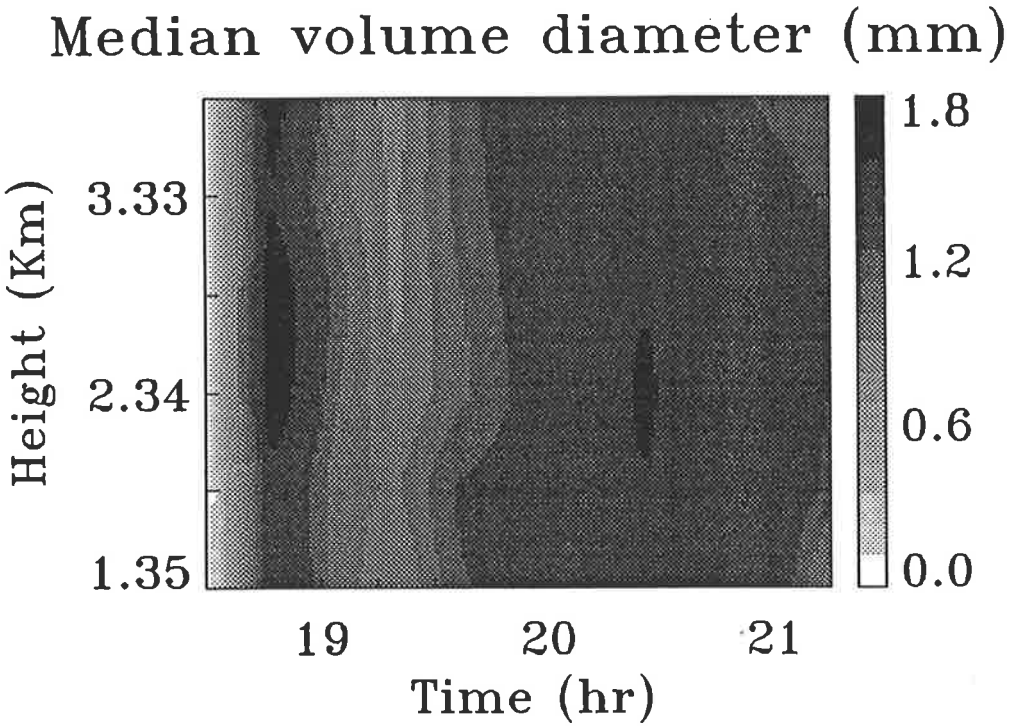

Figure 8.11: Height and time profiles of median volume diameter.

that the median volume drop diameter is larger than that observed in D0589 case. In the convective region, it varied from 1.53 to 1.82 mm and in the moat region, it varied from 1.00 to 1.22 mm. Occasionally, much larger drops were observed in the stratiform region, for example, the median drop diameter varied from 1.13 to a maximum value of 2.24 mm.

Height and time profiles of median volume diameter for the D0589 case are shown in Fig 8.11. The main characteristic in this diagram is the sharp decrease of median volume diameter in the moat region (19:00 to 91:45 LT). In the stratiform region, the median volume diameter is almost uniform. The pattern of this distribution matches perfectly against the time and height pattern of the vertical velocity profiles presented in fig. 8.6 and 8.7.

Fig 8.12 is a similar plot for Jan 12, 1990. As before, a sharp decrease in the value of

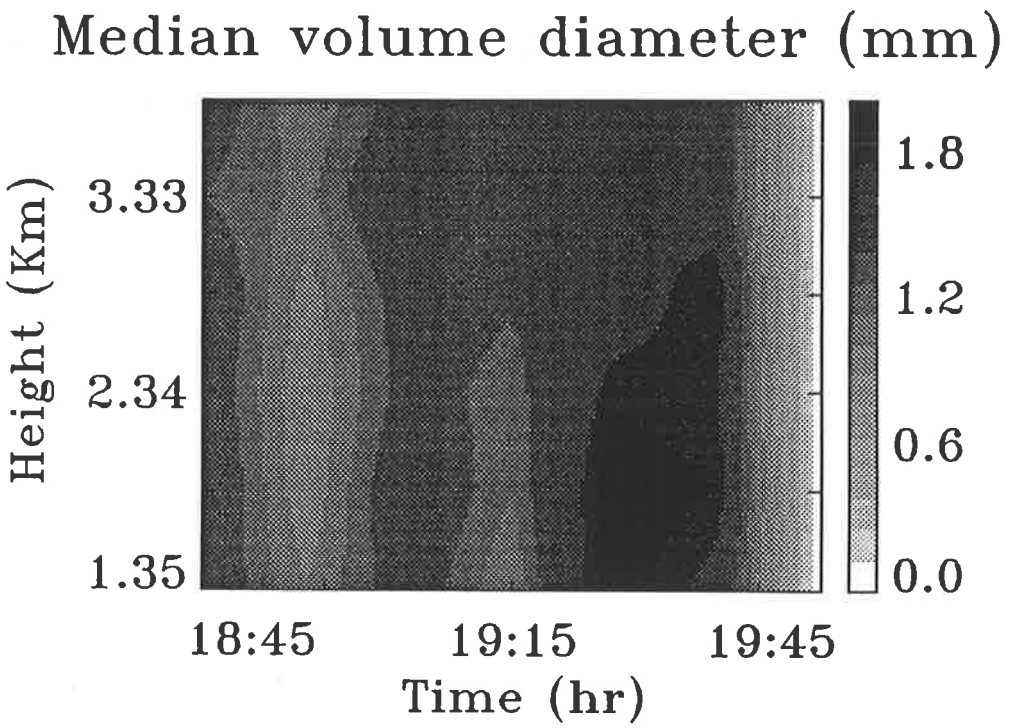

Figure 8.12: As for fig. 8.11 but for Jan 12, 1990.

median volume diameter can be seen in the moat region (18:45 to 19:00 LT). A secondary minimum was detected somewhere around 19:15 LT at the lower heights (below 2.8 km). A sharp increase in the median volume diameter was observed, reaching a value greater than 2 mm at levels below 3.3 km at around 19:30 LT. This indicates that the size increased by coalescence as the drops descended from the cloud base.

8.6 Ice crystals size distributions

In the atmosphere, above the melting layer, the precipitation particles are either in the form of ice crystals or in the form of super-cooled water droplets. In the convective region, because of the presence of strong updraughts, supercooled water droplets are likely to be

found even well above the melting layer. However, in the stratiform region, which has only weak updraughts above the melting layer, supercooled water droplets are unlikely to occur. The melting layers in the present studies (for both D0589 and J1290) were somewhere between heights of 4 and 5 km. So, above the 6-km height, it is safe to assume that the major portion of precipitation particles are ice particles and that phase transitions are possible only from ice to vapour or vice versa. This assumption simplifies the model that the growth of ice particles is possible either by aggregation of ice crystals or by deposition of vapour on the existing ice crystals, but not by the process that produces rimed ice particles(see Rutledge, 1986).

What is the source of ice crystals above the melting layer which have a horizontal dimension of 100 km or even more and a thickness of about 1 km? Gamache and Houze (1982) mentioned that with their model it is possible for the ice particle to travel $\approx$ 100 km horizontally before reaching the melting layer. However, Rutledge (1986) indicated that the influx of ice particles from the convective cell to the stratiform region may extend horizontally only to 50-60 km and precipitation extending beyond this is directly generated by the mesoscale updraught. However, this horizontal distance travelled by the ice crystal before reaching the melting layer depends upon the strength of the wind, shear, and the ice crystal's dimension and its density.

As ice crystals descend, they start to melt at freezing level. As they are the main source of precipitation reaching the ground, a comprehensive knowledge of the size distribution of ice crystals is essential for the improvement of radar estimates of rainfall intensity. However, because of the existence of a large number of ice crystal types, retrievals of size distributions of ice crystals are not as straight forward as in dropsize retrieval. For this reason, only two ice-types, namely dendrites and plates, are considered. This aspect has been discussed in

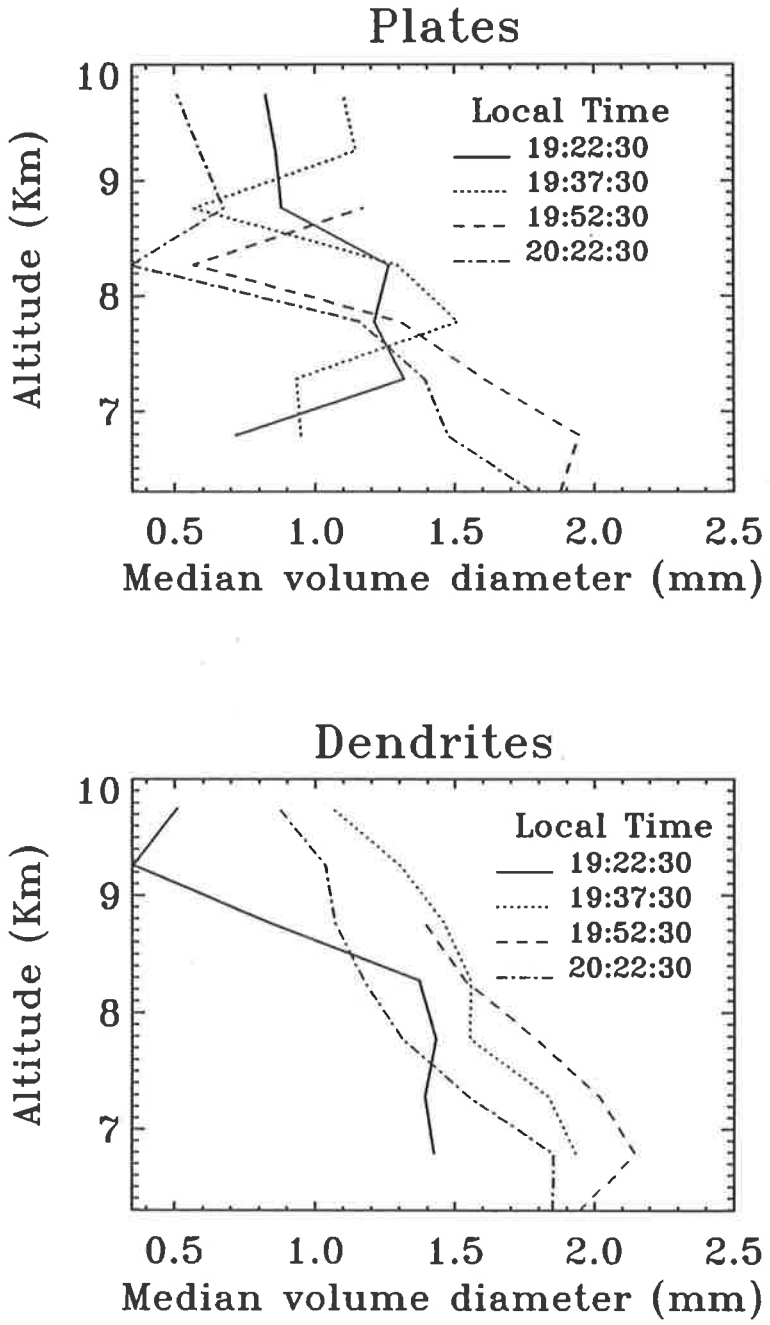

Figure 8.13: Height and time profiles of median volume diameter of ice crystals in the moat and stratiform regions. The solid line is for the moat region. The upper diagram is for plates and the lower one for dendrites. [Dec 5, 1989].

detail previously in Chapter 5.

The size distributions of ice crystals have been determined for heights in the range 6.2-9.8 km for both D0589 and J1290, using the technique explained in §6.3. To estimate absolute values of N_0, the same calibration factor as mentioned in §8.2 of this chapter is used. Additionally, this factor has to be corrected to incorporate the refractive index of ice crystals instead of that of water, and the low bulk density of the ice particles. The radar reflectivity, Z, for the raindrops is (see Zrnic et al., 1993 and Ziegler, 1985)

$$Z = 3.6 \times 10^{12} N_r V_r^2 \frac{\nu_r + 2}{\nu_r + 1} \tag{8.3}$$

where N_r is the drop number concentration, V_r the fall speed of the drop and ν_r the permittivity of the drop. For ice particles, a correction for the dielectric constant K and low bulk density of the ice particles is applied[1], so that

$$Z = 3.6 \times 10^{12} N_s V_s^2 \left(\frac{|k_i|^2}{|k_r|^2}\right) \frac{\nu_s + 2}{\nu_s + 1} \tag{8.4}$$

where,

$$|k_i|^2 = 0.243\,\rho_s^2 \qquad \textit{and} \qquad |k_r|^2 = 0.93 \tag{8.5}$$

Here subscripts i, r and s stand for ice, rain, and snow respectively. The density of snow ρ_s is taken as 0.4 gm cm^{-3}. This gives the correction factor as $\left(\frac{|k_i|^2}{|k_r|^2}\right) = 0.04$.

Using these calibration and the correction factors, the size distributions of ice particles are now estimated. The height profiles of size distributions of plates and dendrites for D0589 in four different time intervals are shown in Fig. 8.13. The median diameter of plates in the stratiform region varied from 0.35 to about 2.0 mm. In the moat region (solid line), there was not much variation in the size distribution of plates with height; for example,

1. Eqn. 8.3 refers to a model based on Gamma distribution. This eqn. is not used in this thesis. However, a correction factor for the dielectric constant K and low bulk density of the ice particles given in this equation is used in this study.

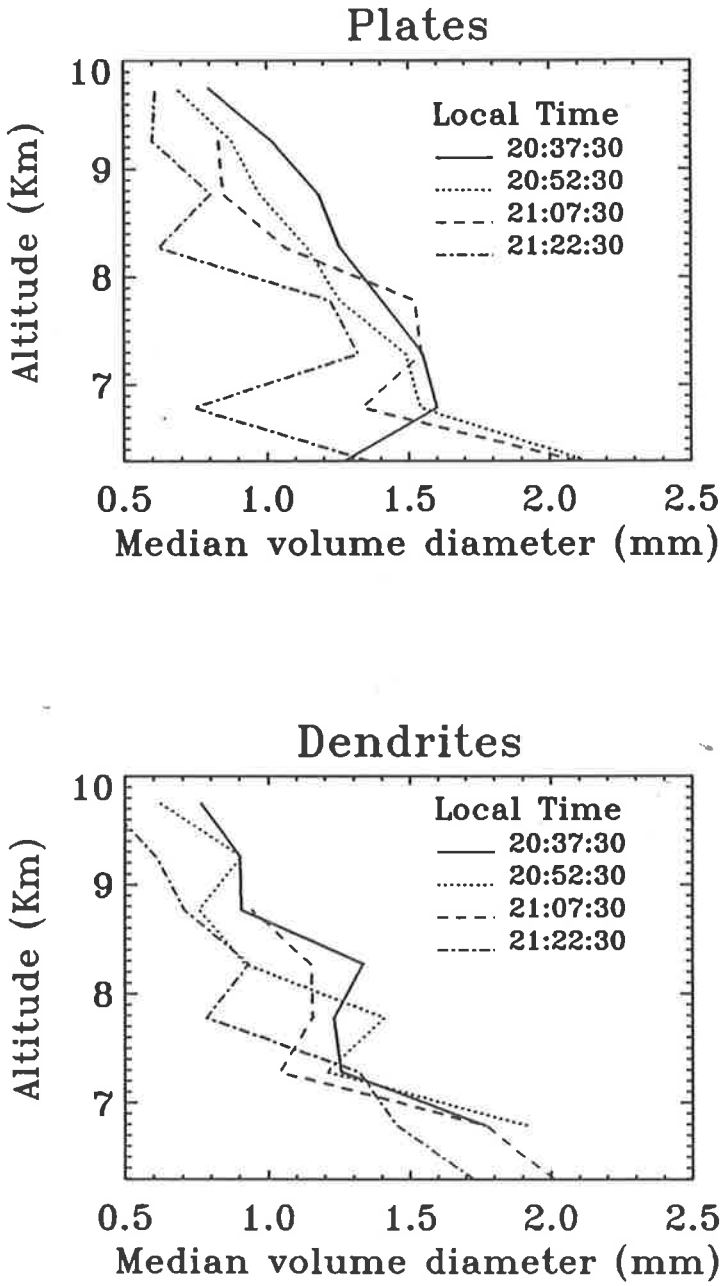

Figure 8.14: Height and time profiles of the median volume diameter of ice crystals in the stratiform region. The upper diagram is for plates and the lower one for dendrites. [Jan 12, 1990]

the median diameter varied from 0.7 to 1.3 mm. For dendrites in the moat region it varied from 0.35 to 1.43 mm, whereas in stratiform region, it varied from 0.11 to 2.17 mm. For both plates and dendrites in the layer close to the melting layer, ice crystals are smaller in the moat region compared to the stratiform region. However, above the 9-km height level, the ice crystals were similar in size in the moat and stratiform regions. Generally there is a tendency for the size distribution to shift towards smaller particles with an increase in height. This indicates a considerable growth of ice crystals, either by aggregation or by vapour deposition on the existing ice crystals, as they descend through various cloud layers.

Fig. 8.14 is a set of plots of height profiles of the median-volume diameter of dendrites and plates at four different times of observation for the J1290 case. These profiles are for the stratiform region only. The median-volume diameter of plates varied from 0.53 to 2.11 mm, whereas it varied from 0.42 to 2.01 mm for dendrites. For plates, there was some tendency to increase in median-volume diameter with height somewhere between 7 to 8 km in height. However, this is unusual and the main change was a continuous increase of median-volume diameter for both plates and dendrites as they descended from the 10 to 6 km height level, indicating growth of ice particles. The rate of growth is much more rapid here than in the D0589 case.

8.7 Liquid water content

So far the size distribution of hydrometeors has been discussed in terms of median volume diameter which is a function only of λ (i.e. one of the parameters of the size distribution of precipitation particles). The second parameter is N_0, which is the amplitude of the size distribution. So it is worthwhile calculating the water content in the cloud from the size distribution using both N_0 and λ. The variation of water content with height and time,

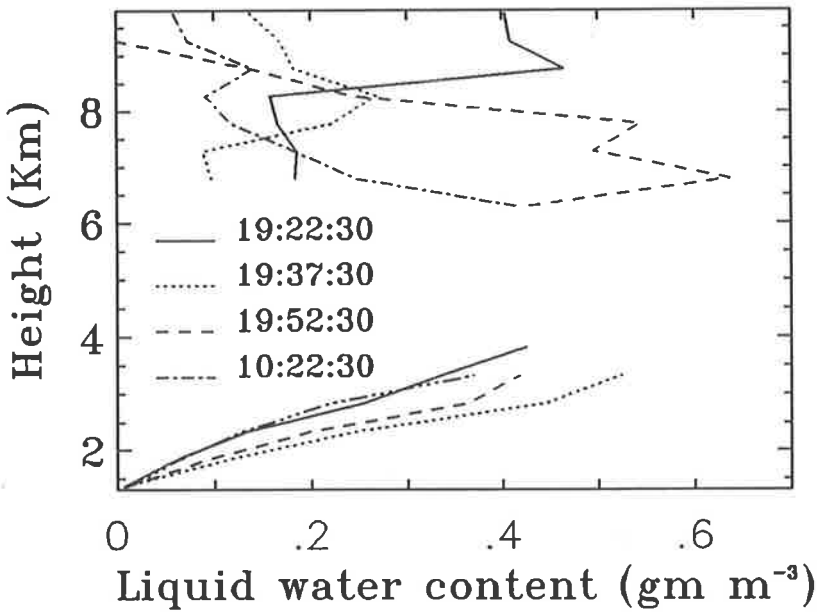

Figure 8.15: Height and time profiles of water content, estimated from the size distribution of solid and liquid particles above and below the freezing level on Dec 5, 1989.

and its spatial distribution is directly related to evaporation and drop-breakup processes, cooling and heating of the atmosphere, and the precipitation reaching the ground.

Fig. 8.15 shows time and height profiles of water content in the moat and stratiform regions estimated from the eqn. 3.26 for the D0589 case. The lower curves are deduced from dropsize distributions and the upper curves from ice crystal size distributions. Over-all the water content varied from 0.05 to 0.7 gm m^{-3}. It can be seen that water content is less in the moat region, varying from 0.05 to about 0.48 gm m^{-3}. This variation is mainly due to variation in height rather than time. The maximum water content occurs somewhere around 3.5 km. In estimating dropsize distributions, the maximum diameter range has been chosen as 6 mm. Still there is a possibility of enhancement in water content at the 3.5-5 km height level because of the bright-band effect. Additionally, lower-level values are influenced

by ground clutter. Despite the presence of these effects, clearly it can be concluded that, while descending from 3.5 to 2 km, more than fifty percent of the water evaporates and this significantly cools the lower atmosphere. This is discussed further in the following section.

Above the freezing level, the ice water content was significantly less than that below the freezing level, although this difference may be associated with uncertainties in the corrections of Equations 8.4 and 8.5. It varied from 0.02 to about 0.64 gm m^{-3}. In general, there is a decrease of water content with increasing height. This indicates that there is considerable growth of the ice particles as they fall from the upper levels. Rapid growth is possible near the bright band as melting particles collide with frozen crystals. '

The water content above the melting level and below the melting level should be same. This can be seen that if extrapolated the ends of the curves below the freezing level and the beginings of the curves above the freezing level would meet. So the estimation of water content above and below the freezing level provides a means of investigating the physical processes taking place in the melting layer. However, more detailed study is necessary to understand the behaviour of the melting layer.

Figs. 8.16 and 8.17 are similar plots of height and time profiles of water content below and above the freezing level in the stratiform region for J1290 case. The dropsize retrieval requires a large Nyquist interval while the ice retrieval needs high spectral resolution, in the J1290 case these modes were not intermixed with sufficient time resolution. Therefore, in fig. 8.16 and 8.17, the profiles above and below the freezing level are plotted separately because their times of observation are different. Below the freezing level, the water content varied from 0.02 to 0.69 gm m^{-3}, whereas above freezing level the variation was from 0.02 to 0.17 gm m^{-3}. As in the D0589 case, a considerable amount of evaporation below the freezing level and considerable growth above the freezing level can be observed.

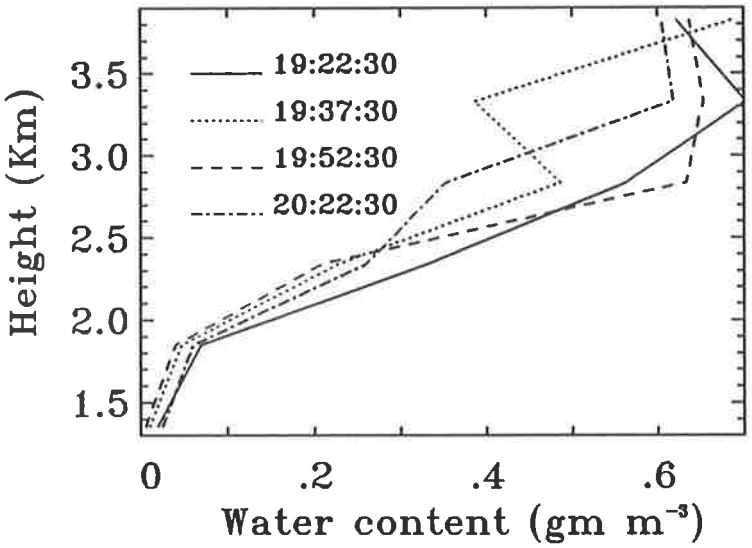

Figure 8.16: Height and time profiles of water content estimated from the size distribution of liquid particles below the freezing level on Jan 12, 1990.

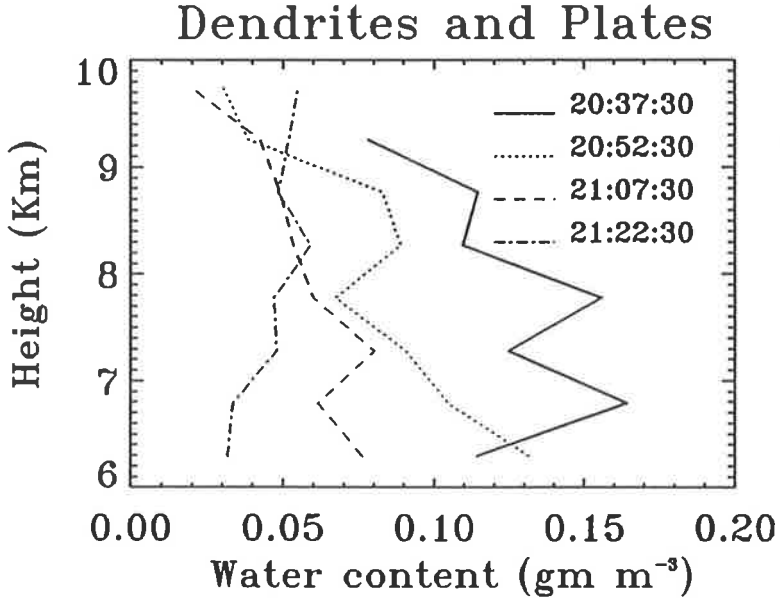

Figure 8.17: Height and time profiles of water content estimated from the size distribution of solid particles above the freezing level on Jan 12, 1990.

8.8 Heating Profiles

The heating and cooling of the atmosphere is a subject of common interest to everyone. Individual thunderstorm cells, tropical squall lines, storms, and mesoscale convective system are responsible for transfering heat from the boundary layer to the upper troposphere and lower stratosphere. The whole circulation of the atmosphere and change in the weather pattern are directly related to the heating rates. A brief discussion on the heating profiles of the atmosphere using vertical-velocity profiles has been given in §7.6.3.

In this thesis, heating profiles were estimated by using the change of water content from one height to another. The change of water content is due to its phase transition and the latent heat released or absorbed during this process acts to heat or cool the atmosphere. It is assumed that the change of phase below the melting layer is only from vapour to liquid or liquid to vapour, whereas above the melting layer it is from solid to vapour or vapour to solid, (i.e the total content is dominated by the precipitating particles and not cloud particles). Hence, if ΔQ is the amount of latent heat released when a mass Δm changes phase, then

$$\Delta Q = L \Delta m \tag{8.6}$$

where L is the latent heat released or absorbed during the phase change. The latent heat of vapourisation of water and latent heat of sublimation of ice are taken as 2.50×10^3 and 2.83×10^3 J gm^{-1} at 0°C respectively. In this study these values of latent heat were used to estimate the heating rate from the change in water content with height. In general, the air temperature decreases with height in the troposphere and the value of latent heat is a function of temperature. So the variation of latent heat with height is also considered in

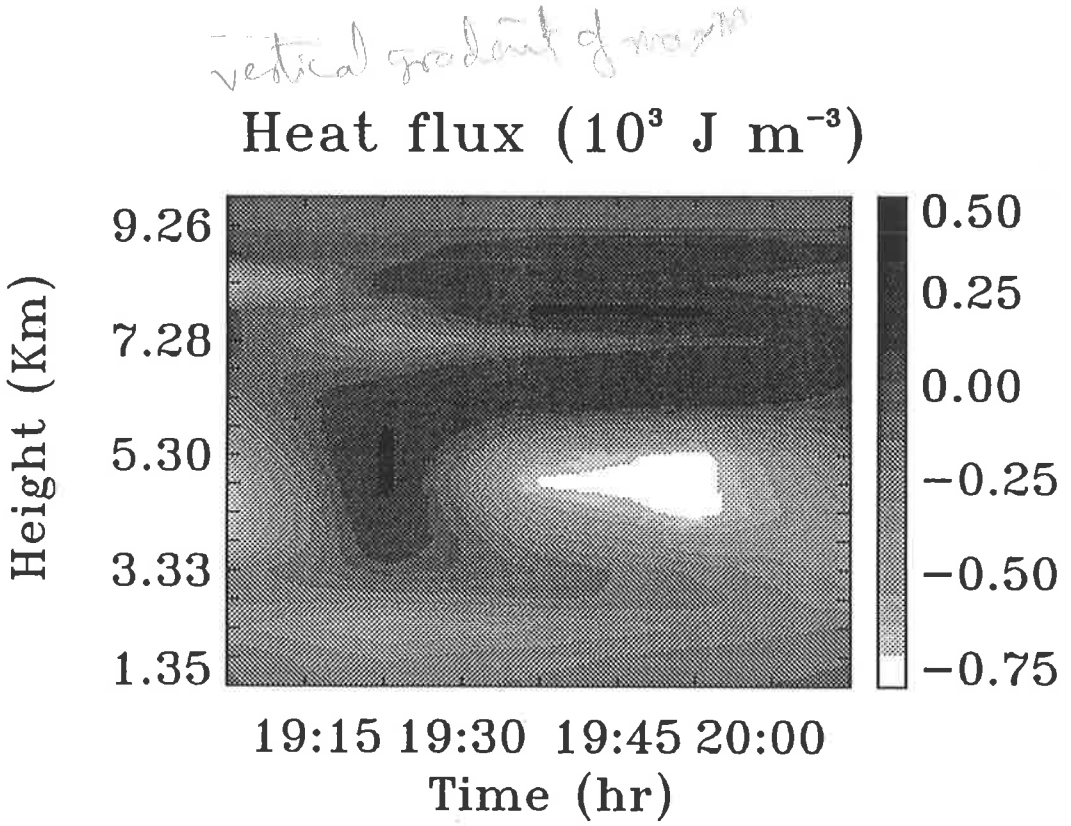

Figure 8.18: Heating profile estimated from the change in water content at various heights on Dec 5, 1989.

the estimation of the heating profiles. However, these variations are very small compared to the variation of mass involved in the phase transition.

Fig. 8.18 shows a contour plot of heating rate against height and time. Interpolation is applied to obtain the heating rate in the melting layer by using the estimated surplus of heat above and below the layer. The result indicates that there was a net deficit of heat below the melting layer with a maximum value of 709 J m^{-3}, whereas there was a positive heat flux above the melting layer with a maximum heat surplus of 657 J m^{-3}. These values are enough to reduce or increase the temperature of the air by more than 1°C (Keenan and Carbone, 1992). A strong heating rate in the melting layer is due to the melting of ice.

The heating profiles of J1290 are not calculated because the times of observation above and below the melting layers are different. However with the pattern of the liquid water content, it can be concluded that the heating profiles of J1290 should be similar to that of the D0589 case.

8.9 Aggregation of ice particles

These radar investigations also enable us to study other important processes in clouds, in particular aggregation of ice particles, because aggregation is regarded as a major process for the

growth of ice particles. This effect can be seen in fig 8.119. The top two plots are for D0589 case for plates and dendrites respectively, whereas the other two sets are for J1290.

In the D0589 case, the slope of the curves for both the dendrites and plates are opposite in lower heights. Additionally, the profiles of dendrites at 19:22 LT is different from other curves.

Despite these variations, in all plots we can see that there is a tendency to increase the value of N_0 with height. These plots clearly indicate that the aggregation is taking place while the particles descend from the upper level to the melting layer.

In the J1290 case, there is not much difference between the profiles observed at different times for both the plates and the dendrites. As before, aggregation is taking place in all heights.

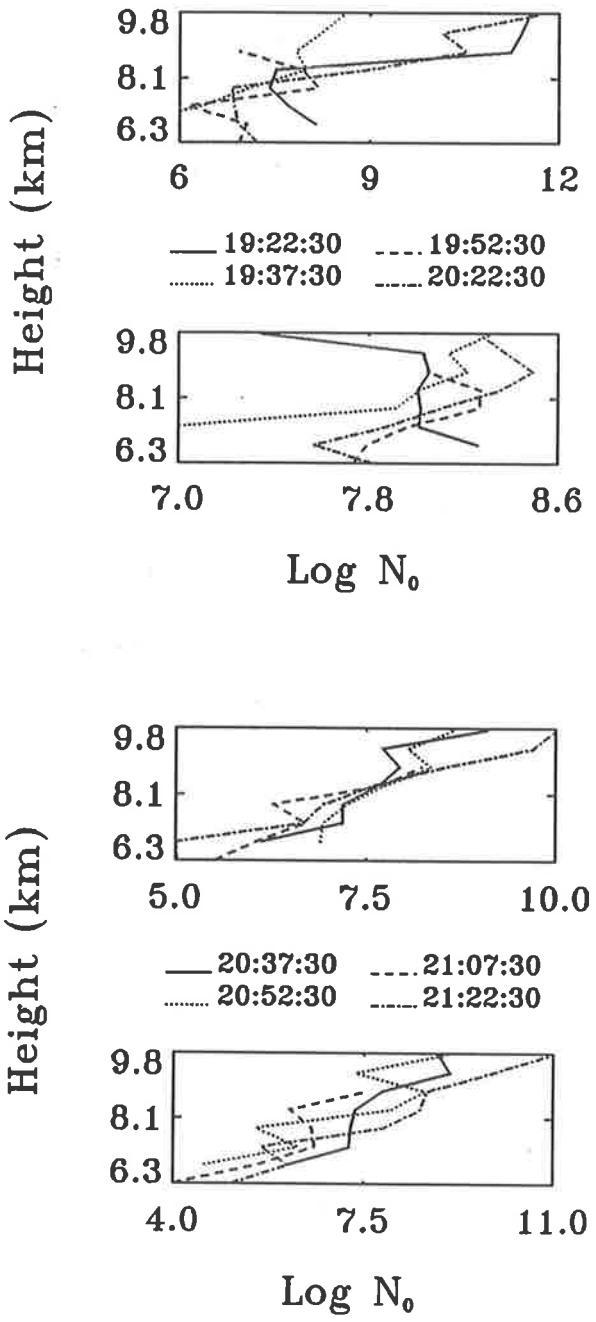

Figure 8.19: Height and time profiles of ice crystal number density N_0. The top two diagrams for plates and dendrites for Dec 5, 1989 and the lower two diagrams for plates and dendrites for Jan 12, 1990.

8.10 Conclusion

The strong vertical velocity in the convective region is associated with a very high precipitation rate. A strong updraught below 4 km is associated with warm rain processes in the leading cells. This is followed by a mature cell with a weak vertical updraught at lower levels. Above 7 km, glaciation and decreased drop loading causes a strong acceleration in the vertical wind. Convective downdraughts are also visible in the raw data (90 seconds resolution data, not shown) and result in the mean down motion in the lowest 2 kms.

The moat region shows descending motions throughout the depth of the storm. Convergence of convective outflow with the ambient wind causes a descending motion at the upper level (Heymsfield and Schotz, 1985), whereas the lower level descending motion is probably due to the water loading and the cooling due to melting and evaporation (submitted manuscript, Cifelli and Rutledge, 1994).

A weak mesoscale vertical updraught in the stratiform region above the melting layer and a weak downdraft below the melting layer, with the cross-over at about 1-2 km above the melting layer, corresponds to widespread precipitation reaching the ground. Nearly fifty percent of liquid water evaporates below the freezing level before reaching the ground which is consistent with the modelling results obtained by Rutledge (1986). This enormous amount of evaporation of water helps to cool the lower atmosphere and to maintain the mesoscale downdraught below the melting level. Above the melting level, the atmosphere is warmer because of the release of latent heat in the phase transition from vapour to ice. This helps to maintain the mesoscale updraught in that region.

It has been demonstrated that windprofilers are able to give insight by producing a picture of a tropical squall line and its trailing stratiform regions. Using these profilers, information can be obtained not only on the windfield but also on the precipitation field

from each part of the system. However, there is always a limit to the information that can be extracted from the signal recorded using these profilers. The interpretation of results and their validation requires many experimental studies. The accuracy of results can be increased by comparing results obtained by various equipment and various techniques. These observations agree in general with our conceptual understanding of these storm systems. Much of the microphysical structure has been quantitatively measured and will provide a test of model simulations.

It is expected that the results provided in this chapter, combined with other similar studies will provide a valuable tool for the understanding of the nature of these tropical squall lines. More detailed study can be done in order to understand the physical processes taking place in the freezing layer. Comparisons of these observed parameters of cloud with the existing cloud model and vertical motion are also a field for further work.

Chapter 9

Summary and Further work

The discovery of radio waves by Hertz and Marconi led not only to the development of a powerful tool for the detection of material objects in their path but also to a revolution in the study of atmospheric science. The rapid development of this technology in the VHF and UHF bands in the past 2–3 decades helps in the study of many interesting atmospheric phenomena such as mesoscale dynamics of the atmosphere (especially in the stratosphere and troposphere), small and large-scale clear-air turbulence, momentum fluxes, gravity waves, meteor echoes in the mesosphere and so on. The capacity of weather radar to present a comprehensive picture of cyclones, storms and squall lines plays a vital role in short- and medium-range weather forecasting.

The observed backscattered power caused by the variation in the gradient of radio refractive index, can be used in atmospheric research using radar equations. As a further application, the windfield of the atmosphere can be determined by using the DBs and SA methods. The radar measured windfield has to be validated by comparing these measurements with the other existing techniques.

However, the backscattered signal from the atmosphere contains not only information which can be used to obtain winds but may also contain information on precipitation particles. hte backscattered power depends on the sixth power of the diameter of the precipitation particles. So, the measured radar power spectrum can be used to obtain valuable information about the size of the precipitation particles present in the radar volume.

The first step in determining the size distribution of drops, is to estimate their terminal velocities. On account of the departure of the drop from a spherical shape the numerical calculations of the terminal fall velocity are complicated. However, with much experimental evidence now available, the droplet fall velocity relations are well established for small and large drops.

The physical mechanisms which affect the size of the drops are micro-physical processes such as condensation, accretion of cloud droplets, evaporation, collision-coalescence, collisional breakup and aerodynamic breakup. Clearly, evaporation and collision-coalescence reduce the small-drop concentration whereas collisional and aerodynamic breakup will reduce the large drop concentration within the cloud volume. The distribution is also controlled by the cloud dynamics that determine the cloud dimensions, the degree of mixing with the environment, the distribution of vertical velocities, the scale and intensity of turbulence and the time interval for which the drops remain within the cloud volume. Thus the growth of precipitation in nature is a complicated physical process. Additionally, internal circulation within the drop, produced by the viscous drag between the surface and the air has been predicted. This makes the study of cloud parameters more complicated. The ground-based doppler radar is now widely used as an essential tool to understand these processes. The estimation of dropsize distribution using VHF radar has just begun in the past 6-7 years.

There is no doubt that the clear-air information obtained by VHF radar make it a potentially powerful tool for remotely determining dropsize distributions. However, on going efforts are still being made to develop an accurate technique to study the cloud optical properties governed by many complicated physical processes.

Accordingly, a technique is demonstrated for the recovery of rain-dropsize distributions in chapter 4, after the addition of realistic statistical variations. The shape of the distributions and the accuracy of their estimation is still uncertain. For this reason, no particular shape of the precipitation spectrum is assumed, the technique is quite general in its application. The technique is shown to have good accuracy ($\sim 10-20\%$) for reasonable averaging, especially in the dropsize region ranging from about 1.5 to 4 mm. With this technique, the existence of cutoffs in the spectrum can be identified over a wide range of drop diameters. It was also found that the accuracy of the technique depends upon the spectral width of the clear-air echo. If the clear-air spectral width is about 1.5 ms^{-1} or more, the reliability of the recovered values will be reduced. It is also demonstrated that this technique can resolve multiple peaks in the back-scattered spectrum.

The technique is also applied to analyse Adelaide VHF radar data during the passage of cold fronts and Darwin profiler data to obtain the height profiles of dropsize distribution in deep convective tropical squall line.

There are, however, some limitations at the very small and very large ends of the dropsize distribution. This is mainly due to the existence of sidelobes produced by deconvolution in the recovered spectra and small variation of fall speed from the large diameter and the finite width of the clear-air echo.

The fundamental shape of the ice crystals is hexagonal. However, there are an infinite number of variations ranging from flat six sided plates to six branched crystals and six sided

prisms and so on. Generally the ice particles observed on the ground are not perfect. The collision between the crystals, melting and riming can lead to these irregularities.

The information on the motion of ice crystals is an essential factor in the understanding of the precipitation forms above the ground. As theoretical models of cloud and precipitation processes have become well established, the study of the relationship between the fall speeds, masses and dimensions of various ice crystals has become more important. The terminal fall velocity of ice crystals is a function of crystal orientation, crystal diameter, and axis ratio. However, a complicated spread of terminal velocities of ice crystals has been observed and it has been suggested that the mass distribution and crystal shape are responsible for complicated fall patterns.

It is well understood that dust particles play an important role in the formation of ice crystals. It has been reported that particular types of dust particles are essential to initiate the phase change, and the change of phase from vapour to solid (ice) is a more favourable process in the atmosphere than from supercooled water drops. Many researchers have also reported the existence of supercooled water drops.

No matter whether the crystals are formed from supercooled drops or from vapour, meteorologists are interested in the type of ice crystals present in natural clouds. As a growing crystal penetrates through the various parts of the cloud, its crystal form will change according to the changing ambient conditions and during this time the crystals can pass through many stages such as diffusion, riming and aggregation. An understanding of these processes is necessary to estimate the density and eventually the mass of the crystals which depend upon their type, aggregation and the riming.

Excess vapour density over ice is a maximum at about -15°C, which is also the temperature of the maximum growth rate. The preferred crystal types in this growth region are

seen to be dendrites and sectors. A clear understanding of the three dimensional velocity vector and rotational motions is essential in explaining the dominance of dendritic crystals in the aggregation processes.

Thus the size distribution of cloud droplets is determined not only by the micro-physical processes of crystal growth by sublimation, riming and aggregation, but it is also affected by the cloud dynamics, such as the degree of mixing with the environment, the distribution of vertical and horizontal velocities within the cloud, the period for which the individual crystals remain in the cloud, the three dimensional fall velocity of the crystal and its rotational motion during its fall, the intensity of turbulence and so on. Knowledge of the evolution of solid hydrometeors with time and height can make a significant contribution to the understanding of the phase change, the latent heat released within the cloud and the rainfall intensities on the ground.

A radar technique for the determination of ice-particle size distributions within a large volume of cloud using a VHF wind-profiling radar has been demonstrated in chapter 6. The method has been restricted to the consideration of only two types of ice particles (dendrites and plates) in order to make the retrieval problem tractable.

It was found that the technique has good accuracy, of about 10-30% for the clear-air spectral widths of 0.1-0.3 ms^{-1}. With hundreds of simulations, it has been shown that the greater the clear-air spectral width the more difficult it is to recover the population spectra. For example, when the clear-air spectral width is very high, such as 0.5 ms^{-1}, the relative error in the lower-diameter region exceeds 100% and also significant in the large-diameter region. It should be noted that off sets of ice echoes in the vertical velocity spectrum are small so that for large spectral widths smearing is important.

The possibility of fitting with only one ice-crystal type is also tested and it has been

shown that this gives poor results. If two distinct peaks are visible in the radar power spectra and the precipitation spectra is wide, the two ice-type fitting process is essential.

This technique has obvious limitations and efforts to improve it are continuing. The retrievals will not be sensitive to small diameter crystals because of the D^6 reflectivity dependence. More importantly, the restriction on the number of ice-types and the *a priori* assumption of the ice-type is a major limitation. Additionally, the ice crystals have random shapes and this nonsphericity of the particles may lead to a considerable error in our retrieval technique because the backscattered power from spherical and non spherical particles may be quite different. The wind profiler cannot deal with this problem. The coefficients in the fall-velocity relation may also vary from one instant to another because of the random shapes and densities of the ice particles. When the peaks due to individual crystals are distinguishable, the accuracy of the retrieval technique is high. The initial estimation of ice parameters is very difficult, because two different ice crystals moving with different speeds can produce the same echo. To make the retrieval problem tractable, the maximum possible diameter of the crystal is varied with the position of the precipitation peak in the observed spectrum and the different maximum diameters are considered for different crystals to reduce the contamination problem in the observed precipitation spectrum. These two assumptions may also lead to a considerable error in our retrieval technique. However, the observed retrievals do fit the observed radar spectra very well. Despite these limitations the observation of clearly separated clear-air and ice-peaks in the Doppler spectrum presents a significant opportunity for the study of cloud microphysics and this should be exploited.

Mesoscale precipitation fields are the result of a combination of several isolated convective cells. The orientation of the cells relative to the low-level wind direction is a crucial factor in the intensification of the system, because the alignment of the cells in the direction

perpendicular to the low level wind is the most favourable case for the evolution of new cells.

Comprehensive studies of mesoscale convective motion in well defined squall lines have been carried out by many investigators. There are variations from one occasion to another. However, in most cases, the system has been observed with leading convective cells. These cells are arranged in an arc-shaped line, trailed by a large area of stratiform clouds (Leary and Houze, 1979; Barnes and Sieckman, 1984 and Houze, 1989).

The heating rate in the atmosphere is a function of the mean updraught and downdraught motions. The precipitation field also depends upon the ascending and descending motions of the air. For this reason, a better understanding of wind and thermodynamic fields is essential. Furthermore, the importance of an understanding of the dynamics and thermodynamic state of these systems cannot be ignored in the study of the general circulation and precipitation mechanisms in the tropics.

Many different techniques and instruments have been used to explore the behaviour of mesoscale convective systems. However, the capability of ground based radars to penetrate through these systems made it possible to reveal their entire internal structure, because these radars have the capacity to obtain information such as reflectivity and mean horizontal and vertical velocities, with good height and time resolution, within the cloud. This makes it possible to estimate the size distributions of cloud particles, liquid water content and rainfall intensities.

Accordingly, a brief discussion of Australian monsoons and the occurrence of tropical cyclones in Darwin have been presented in Chapter 7. Mesoscale observations of vertical-velocity profiles, size distributions of hydrometeors and thermodynamic variability observed under DUNDEE program in 1989/1990, using a Darwin wind profiler and a Doppler weather

radar have been presented in chapter 8. It has been found that the strong vertical velocity in the convective region is associated with a very high precipitation rate: A strong updraught below 4 km is associated with warm rain processes in the leading cells. This is followed by a convective downdraught and a mature cell with a weak vertical updraught. Above 7 km, glaciation and decreased drop loading causes a strong upward acceleration in the vertical wind.

The moat region shows descending motions throughout the depth of the storm. Convergence of convective outflow with the ambient wind causes a descending motion at the upper level (Heymsfield and Schotz, 1985), whereas the lower level descending motion is due to water loading and cooling due to melting and evaporation (submitted manuscript, Cifelli and Rutledge, 1994).

A weak mesoscale vertical updraught in the stratiform region above the melting layer and a weak downdraft below the melting layer, with the cross-over at about 1-2 km above the melting layer, corresponds to widespread precipitation reaching the ground. Nearly fifty percent of liquid water evaporates below the freezing level before reaching the ground which is consistent with the modelling results obtained by Rutledge (1986). This enormous amount of evaporation of water helps to cool the lower atmosphere and to maintain the mesoscale downdraught below the melting level. Above the melting level, the atmosphere is warmer because of the release of latent heat in the phase transition from vapour to ice. This helps to maintain the mesoscale updraught in that region.

Thus with these results, it has been shown that windprofilers are able to give insight by producing a picture of a tropical squall line and its trailing stratiform regions. Using these profilers, information can be obtained not only on the windfield but also on the precipitation field. These observations agree in general with our conceptual understanding of these storm

systems. Much of the microphysical structure has been quantitatively measured and will provide a test of model simulations.

It is expected that the results provided in this thesis, combined with other similar studies will provide a basis for the understanding of the nature of these tropical squall lines.

9.1 Future work

- In this thesis, the recovered dropsize spectra are somewhat broader than the population spectra. Hence more work needs to be done to overcome these limitations. This technique can be extended to include simulations based on data obtained by 915-MHz profilers, where the precipitation echo is much larger than the clear-air echo for any rain except very light rain. Mixed 50/915-MHz profiler observations are also a field for further work.

- More detailed study can also be done by including other related meteorological parameters in the analysis.

- The technique described in this thesis to obtain the ice crystals size distributions needs to be improved by performing more simulations, because there is no basis to estimate the initial parameters involved in the retrieval process. Additionally, too many assumptions involved in the technique makes the process more difficult. So, more work must be done to make the process automatic.

- The retrieval technique of ice particles may be improved by combining the results from the profiler with the information obtained from a dual polarization radar which can determine the orientation, size and shapes of the hydrometeors.

- The dropsize and ice particles retrieving techniques should have applications in the study of cloud microphysics. The measurements have direct implications for such diverse applications as rainfall estimation from weather radars and the calculation of cloud optical properties.

- More detailed study can be done in order to understand the physical processes taking place in the freezing layer. Comparisons of these observed parameters of cloud with the existing cloud model and vertical motion are also a field for further work.

- Much remains to be done to get an overall picture of the nature of vertical-velocity profiles in the convective regions of squall lines. The variation of these profiles from one system to another is also an area for investigation. A better understanding of the physical process involved in maintaining a long lived squall line is essential, because of its direct impact on day-to-day human activity.

- More detailed study can be done in order to understand the physical processes taking place in the freezing layer by careful estimation of dropsize distribution below the freezing level and ice particles size distributions above the freezing level.

- Comparisons of the observed size distributions with those from a cloud model, where the model vertical motions are constrained to the observed values are planned.

- Finally, there is always a limit to the information that can be extracted from the signal recorded using these profilers. The interpretation of results and their validation requires many experimental studies. The accuracy of results can be increased by comparing results obtained by various equipment and various techniques.

Appendix A

Full Correlation Analysis

The Spaced Antenna technique has been utilized to determine the true wind velocities of the atmosphere and was first proposed by Mitra in 1949, as quoted by Solvang et al. (1977) and the first detailed analysis technique, the so called 'Full correlation analysis', was developed by Briggs et al. (1950). Here only a short description of the technique is presented. An example of a diffraction pattern produced by the interaction of radar echoes scattered by variations of radio refractive index in the atmosphere has been presented in Fig. 2.1. If $f(x, y)$ is a function representing a two-dimensional moving pattern and $f(x + \xi, y + \eta)$ is a new function obtained by shifting the same function $f(x, y)$ through ξ and η in x- and y-directions respectively, then the spatial correlation coefficient between these two functions, assuming zero mean value and taking a spatial average, is given by

$$\rho(\xi, \eta) = \frac{\langle f(x, y) * f(x + \xi, y + \eta) \rangle}{\langle [f(x, y)]^2 \rangle} . \tag{A.1}$$

It has been found that the random changes of the pattern have a tendency to shift the maximum of the correlation coefficient towards zero lag. Clearly, this may lead to a serious error in our calculation. In addition to this, if there is no systematic elongation of the

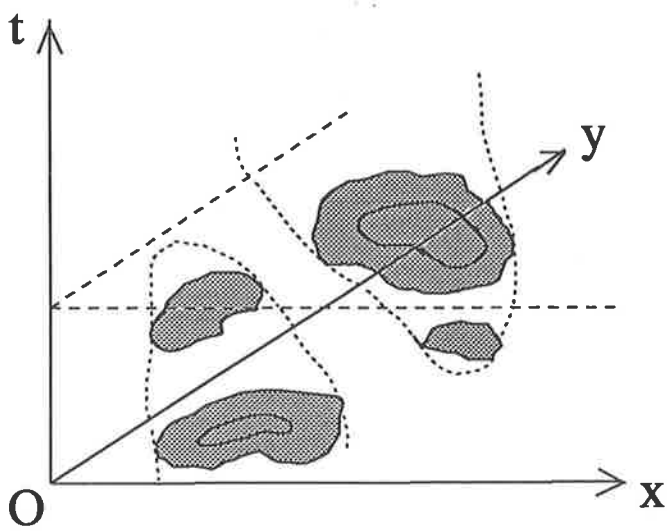

Figure A.1: An isometric two dimensional pattern in x, y, and t space. [after Briggs, 1984].

patterns in a particular direction, then the directional bias in the apparent velocity does not exist. If the patterns are anisometric (*i.e., systematically elongated in a particular direction as they move*) then the line of maxima will have a tendency to shift towards the direction of elongation. Clearly, it will change the mean time shifts and hence the velocity has to be corrected. In the full correlation analysis, the effect of these problems is taken into consideration.

To introduce random changes we consider a co-ordinate system with three axes, x, y (spatial co-ordinates), and t (time co-ordinate). The contours of the pattern are shown in x, y, t space at t=0. But when $t = t + \tau$, the contours in (x,y) space will be as represented by the broken lines and their shape may change in any direction (Fig. A.1). Now the temporal auto-correlation function is defined as

$$\rho(\xi, \eta, \tau) = \frac{\langle f(x, y, t) * f(x + \xi, y + \eta, t + \tau) \rangle}{\langle [f(x, y, t)]^2 \rangle}. \tag{A.2}$$

To introduce the anisometric component of the pattern, we begin with the assumptions that

the auto-correlation function is elliptical in form and that the cross-correlation function and auto-correlation function have the same functional form. If V_x and V_y are the components of the velocity (V) of the pattern at an angle ϕ measured clockwise from the y-axis, then we can derive

$$\rho(\xi,\eta,\tau) = \rho[A(\xi - V_x\tau)^2 + B(\eta - V_y\tau)^2 + K\tau^2 + 2H(\xi - V_x\tau)(\eta - V_y\tau)] \,. \qquad \text{(A.3)}$$

This is equivalent to the form

$$\rho(\xi,\eta,\tau) = \rho[A\xi^2 + B\eta^2 + C\tau^2 + 2F\xi\tau + 2G\eta\tau + 2H\xi\tau] \,. \qquad \text{(A.4)}$$

The two equations above (A.3 & A.4) are the fundamental equations used to determine the wind velocities by the spaced-antenna technique using the full correlation analysis. The parameters $\frac{A}{C}$, $\frac{B}{C}$, $\frac{F}{C}$, $\frac{G}{C}$, and $\frac{H}{C}$ are determined from the cross-correlation and auto-correlation functions assuming that the three receivers have the same auto-correlation function. Here, the values needed to find the above parameters are (see Fig. A.2)

- time lag (τ') corresponding to maximum value of correlation function of a pair of receivers
- time lag (τ) such that mean auto correlation functions of the signal falls to the correlation at zero lag.

Theoretically for any spatial arrangement with more than three sensors Eqn. A.4 can be rewritten.

$$\rho(\xi_{ij},\eta_{ij},\tau_{ij}) = \rho[A\xi_{ij}^2 + B\eta_{ij}^2 + C\tau_{ij}^2 + 2F\xi_{ij}\tau_{ij} + 2G\eta_{ij}\tau_{ij} + 2H_{ij}\eta_{ij}] \,. \qquad \text{(A.5)}$$

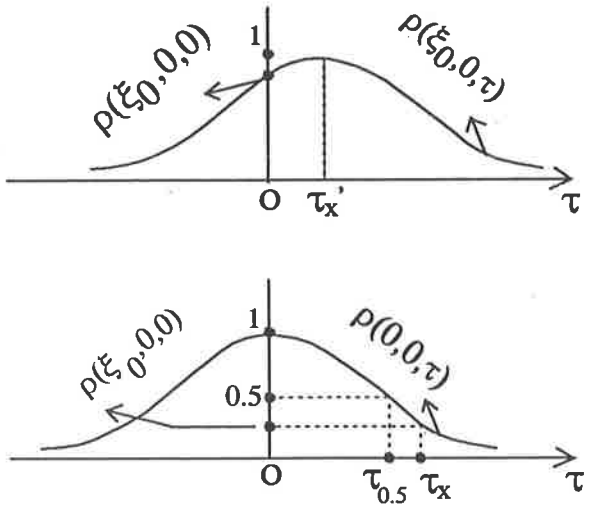

Figure A.2: (a) Cross-correlation between two receivers (a) in the x-axis, separated by ξ_0 and (b) in the y-axis, separated by η_0. [after Briggs, 1984].

Now as before, by assuming τ_{ij} to be the particular time lag for which the auto-correlation function has the same value as that of the cross-correlation function across the two receivers at i and j for zero time lag, all the coefficient ratios can be determined.

A.1 Velocity determination

We begin with the assumptions that the ratios of the coefficients, such as $\frac{A}{C}$, $\frac{B}{C}$, $\frac{F}{C}$, $\frac{G}{C}$, and $\frac{H}{C}$ are already determined as described in previous section. Equating the terms containing $\xi\tau$ and $\eta\tau$ in Eqns. A.3 and A.4 gives: we get

$$AV_x + HV_y = -F \tag{A.6}$$

$$BV_y + HV_x = -G. \tag{A.7}$$

Dividing both sides of these equations by C allows the velocities in the x- and y-direction to be calculated. The magnitude of the velocity vector **V** is given by

$$|V| = V_x^2 + V_y^2 \tag{A.8}$$

and its direction ϕ, measured clockwise from the y-axis, is

$$\tan\phi = \frac{V_x}{V_y} . \tag{A.9}$$

The velocity vector V of the anisometric pattern, obtained by Eqn. A.8 and A.9, is generally referred to as the true velocity V_t. This is the velocity of the diffraction pattern obtained by the ground-based sensors. If the scatterers in the atmosphere have a velocity V, then by geometry the diffraction pattern on the ground must have the velocity 2V. Hence, V_t and V_a have to be divided by 2 to represent the velocity of the scatterers at the selected height (Felgate, 1970; Wright, 1972).

A.2 Directional bias

If right angle triangles are used a directional bias may appear in the calculation. For example, with the observations of the E- and F-regions taken in Halley Bay, Antarctica in November and December, 1964, and January 1965, it was found that there is a greater tendency for the major axis of the correlation ellipse to be aligned with the longest side of the triangular arrangements. (Beynon and Wright, 1969b). They said that the directional bias is expected when the line of maxima of the diffraction pattern is curved rather than straight (Harnischmacher and Rawer, 1963; Beynon and Wright, 1969a). However, not much work has been carried out on the full correlation analysis to get a complete understanding of this directional bias . To minimise the directional bias, because of the asymmetry, it has been recommended that a more appropriate configuration of the sensors is an equilateral triangle (Golley and Rossiter, 1970), as is used in the Adelaide VHF radar. Another suggestion is to use four receivers at the corners of a square to eliminate this directional bias.

A.3 Use of complex signal

In the early use of this technique only the signal amplitude was used. Now SA measurements use coherent radars where both phase and amplitude of signal are recorded. When the function is complex the relation for the correlation ceofficients has to be modified by replacing the functions by their complex conjugate. The modulus of the computed function can then be applied in the full-correlation analysis using the same relationship as in the preceeding discussion.

The advantages of using the complex signal is that it helps to increase the noise power ratio in the coherent averaging process. Apart from this, by using the phase information, we can work out the vertical velocity.

A.4 Statistical errors in the spaced-antenna technique

Although the spaced-antenna technique has been used to measure the wind velocities in the atmosphere for more than three decades, so far only a few observations have been carried out to estimate the random errors involved in the associated full correlation analysis. The reliability of wind measurements can be judged only by knowing those uncertainties. The first attempt to estimate errors was made by Awe (1964a, b) using some numerical simulations. Fedor (1967) estimated the error by assuming the Gaussian form for the correlation functions. The main advantages of this assumption of the Gaussian form are that it retains high-frequency components and that the estimated value is always positive. Buckley (1971), Chandra et al (1972) and Chandra in 1980, quoted by May (1988) also elaborated on the estimation of the random errors associated with the spaced antenna technique. Later May (1988) gave a detailed discussion of the errors involved in the full

correlation analysis. However, Hocking et. al. (1989) argued that May's analysis is only applicable to a one-dimensional mode and the validity of its application in two dimensions is still uncertain.

The estimated parameters in the spaced antenna technique can also be affected by the presence of a significant noise level in the signal. It is well known that the noise will produce a spike at the origin of the auto-correlation function. By careful consideration, it is possible to interpolate (or to renormalise) the correlation coefficients by removing this spike. Apart from the spike at the origin, noise causes errors in the correlation functions which are not related between adjacent time lags. However, unless the sample correlation is very high or the amplitude of the noise level is comparable to that of the signal being analysed, the effect of fluctuation produced by the noise on the estimation of time lags τ and τ' will be negligible (May, 1988).

A.5 Systematic error

Systematic errors arise mainly for the following two reasons:(a) the triangle size effect and (b) the effect of vertical velocities. Kelleher (1966) first reported that the calculated value of the true velocity in the full correlation analysis has a tendency to increase with an increase in the size of the triangle formed by the three receivers. However, he did not mention its optimum value or the effect of the triangle size on the derived direction of the wind speed. Careful studies of this triangle size effect were performed first by Golley and Rossiter (1970) in the E-region of the ionosphere. It was found that in the spaced-antenna technique, the magnitude of the true velocity increases with an increase in the separation between the sensors, but only up to a certain value. At the higher separation it represents the real velocity. Their results showed that the average calculated value of the true and apparent

directions were good estimates of the real direction for all triangle sizes. They found that the correlation ellipse tends to be aligned along the triangle hypotenuse for small triangles, but this tendency decreases as the size of the triangle increases. They also found that the apparent direction does not depend on the size of the triangle, but that there is a tendency for these parameters to show larger r.m.s. deviations from the average of true and apparent directions for small triangle sizes. Thus it is clear that the triangle size effect can be avoided by choosing the optimum separation between the sensors.

The effect of vertical velocity on the horizontal velocity derivation by the Spaced-Antenna technique was first suggested by Royrvik (1982). If the vertical velocity is uniform within the radar beam volume then there will not be any problems in the measurements of horizontal velocities. However, if there is a systematic variation of vertical velocities within the radar volume such as positive in one part and negative in another part, then it will certainly affect the horizontal velocity, because the pattern detected by the sensor is the sum of the diffraction patterns scattered from a variety of off-vertical angles and in such a case each will be scattered with a different Doppler shift. This effect will be significant in the study of high-frequency phenomena, such as gravity waves, but it has little effect for long-term measurements such as taking averages for 30-60 minutes (Hocking et al,1989). The errors induced in the SA technique by horizontal gradients of w are equivalent to those in the Doppler technique by the same effect (May, 1990).

Appendix B

Comparisons of balloon and radar wind measurements

B.1 Introduction

Comparisons between the balloon and radar techniques have been made to become familiar with the MST radar techniques, because MST radars operated in the VHF band are a powerful tool for the study of windfields in the lower and middle atmosphere. These radars are Doppler radars and are able to detect the Doppler shifts caused by radial components of the wind motion along the direction of the radar beam. These radial measurements are then used to estimate the vertical and horizontal components of the wind assuming . An alternative radar technique used to estimate three-dimensional windfield is by determining the the movement of the diffraction pattern due to atmospheric scatterers using the "Spaced Antenna Technique" (for details, see Chapter 2).

The Buckland Park VHF radar (35° S and 138° E), situated on a flat coastal plain about

40 km north of Adelaide, operates in Doppler mode at a frequency of 54.1 MHz and is able to provide measurements of the atmospheric vertical velocity at height levels of 2–20 km, every 2 minutes with a height resolution of half a kilometre. Additionally, it can be operated in a spaced-antenna (SA) mode to obtain the horizontal windfields of the atmosphere every 3 minutes from 2 km to a maximum height level of $\sim$ 15 km with a similar height resolution.

The Bureau of Meteorology is using a classical technique to estimate the horizontal wind up to the 30-km height level, by tracking a meteorological balloon (radiosonde) launched every six hours from the Adelaide airport. The airport is about 12 km to the south-west of Adelaide and about 37 km south of the Buckland Park (VHF radar) site. Assuming the balloon follows the background wind, the windfield of the atmosphere can be estimated by tracking the balloon's path with a radar.

The radiosonde technique is regarded as the standard technique to determine the windfield of the atmosphere. The accuracy of the balloon technique is uncertain, for example Jasperson (1982) showed that the RMS difference between two sets of data from balloons launched close together is about 1 m s^{-1} in the troposphere. As quoted by May (1986), Hoehne (1980) found that the RMS difference of wind velocities measured by a pair of radiosondes attached to a single balloon is of the order of 3.1 m s^{-1}.

Continuous efforts have been made since the early 1940s to develop a remote-sensing technique in order to study the dynamics of the atmosphere. Since the mid 1970s, radars have been used routinely to obtain the wind fields of the atmosphere in various parts of the world. Now the radar is becoming an essential tool for atmospheric research and weather forecasting. This is because, while the balloon can provide only instantaneous values during its ascent, unattended radar can provide quasi-continuous measurements of the velocities of the atmosphere. However, for validation of the radar technique, its observations should

be compared with the observations made by other existing techniques. Such comparisons should be performed in various geographical conditions in different seasons of the year and in different meteorological conditions.

Several comparisons between radar- and balloon-measured velocities have been made in the past to validate the radar technique for wind measurements (e.g, Fukao et al., 1982; Larsen 1983; Vincent et al., 1987; Weber and Wuertz, 1990; and May, 1993). These comparisons have been affected by spatial separation (with the exception of Weber and Wuertz, 1990; and May, 1993) between the radar and balloon site. Weber and Wuertz (1990) considered two years of data, whereas all other investigators considered only a short term data.

Accordingly, this chapter deals with comparisons of the Buckland Park VHF radar wind observations with balloon wind observations. In the first part of the chapter, the time and height profiles of wind velocity are discussed. This is followed by a comparison of the radar and balloon measured wind direction, and finally the effect of the spatial separation between the radar site and the position of balloon is studied.

B.2 Data collection

The horizontal wind vectors in the height range 2-11.5, km collected in the month of August, 1990, using the Buckland Park VHF radar, were used in the present study. The Spaced-Antenna technique (discussed in chapter 2) was applied in the collection of data with the radar. A large array made up of 32 individual coaxial collinear (co-co) type antennas, forming a square of 88 m, is used to transmit the pulse. Three arrays, each consisting of sixteen 5-element Yagi antennas, form an equilateral triangle with sides of 50 m, is used to study the diffraction patterns produced by the atmospheric scatterers. In the vertical mode, the co-co antennas are used for transmitting and receiving the signals. The balloon wind

measurements made at the Adelaide airport during the same period have been obtained from the Australian Bureau of Meteorology.

To compare the instantaneous measurements of the balloon with the radar measurements, it has been assumed that the balloon takes half an hour to ascend from 2 to 11.5 km. Thus the radar measurements were also averaged over the 30 minutes beginning at the time of launch of the balloon. This comparison of an instantaneous with an average value must show some discrepancy, as the variability in the atmospheric wind will affect the instantaneous values more. The radar data were available from 1 to 16 August and then from 20 to 31 August, so the balloon data were also considered during the same period.

In collecting data from the balloon, the wind estimates were generally made every minute, so the actual height of the balloon may vary from a sequence of equal intervals because of variability in the vertical component of the background wind. However, interpolation was used to estimate values for prescribed height levels. Additionally, the prescribed height levels in the balloon observations and the profiler observations were not the same, also requiring that interpolation be applied to the balloon data to produce identical height intervals.

B.3 Height-time profiles of the magnitude of the horizontal wind

Height profiles of wind velocities measured by radar and balloon at four different times on August 22, 1990 are shown in Fig. B.1. In the figure, the radar velocities at a particular height in a particular half-hour interval are indicated by dots and the average radar height profiles are represented by a solid line. The balloon velocities are indicated by diamonds.

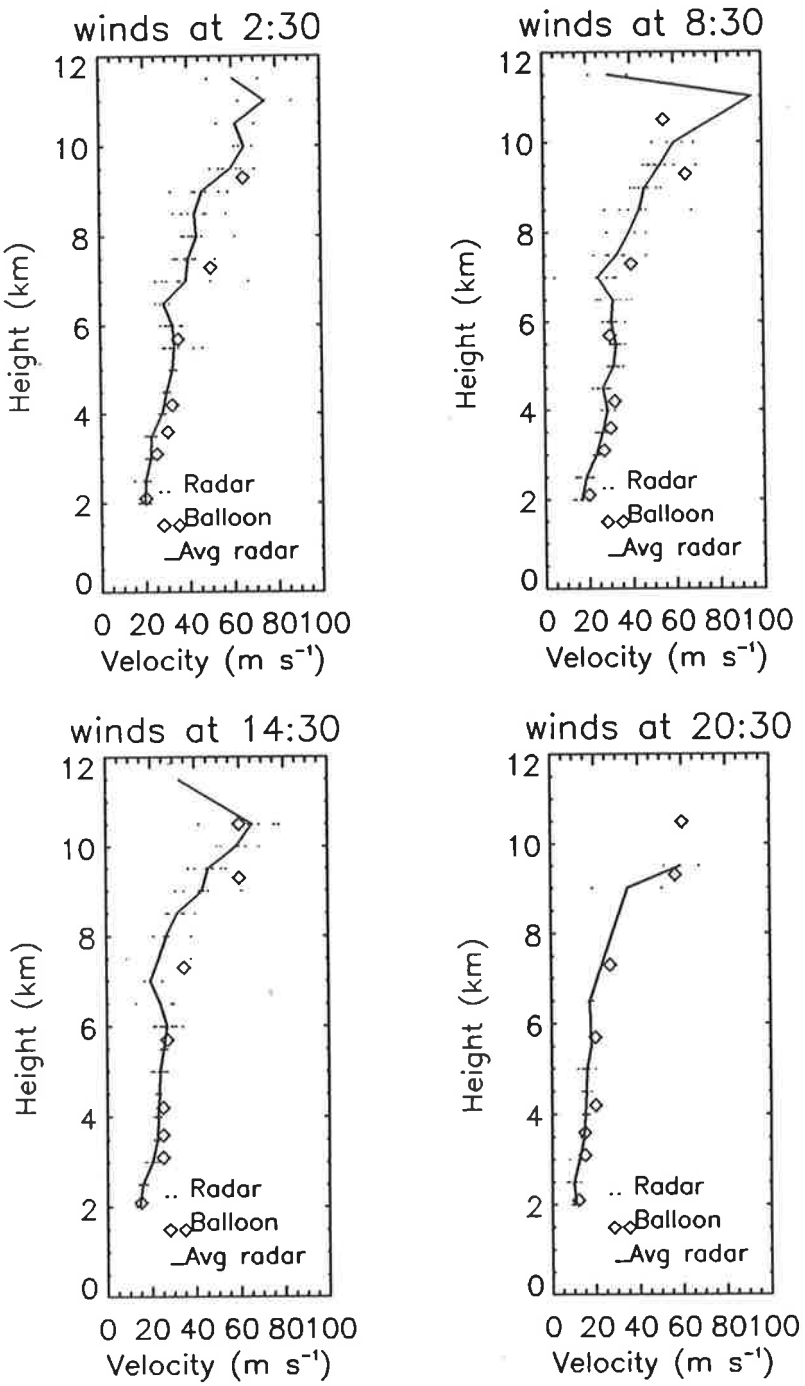

Figure B.1: Height and time profiles of balloon velocity (diamonds) and radar velocity (dots) on 22 August, 1990. The solid line is the average radar velocity during the time of flight of the balloon.

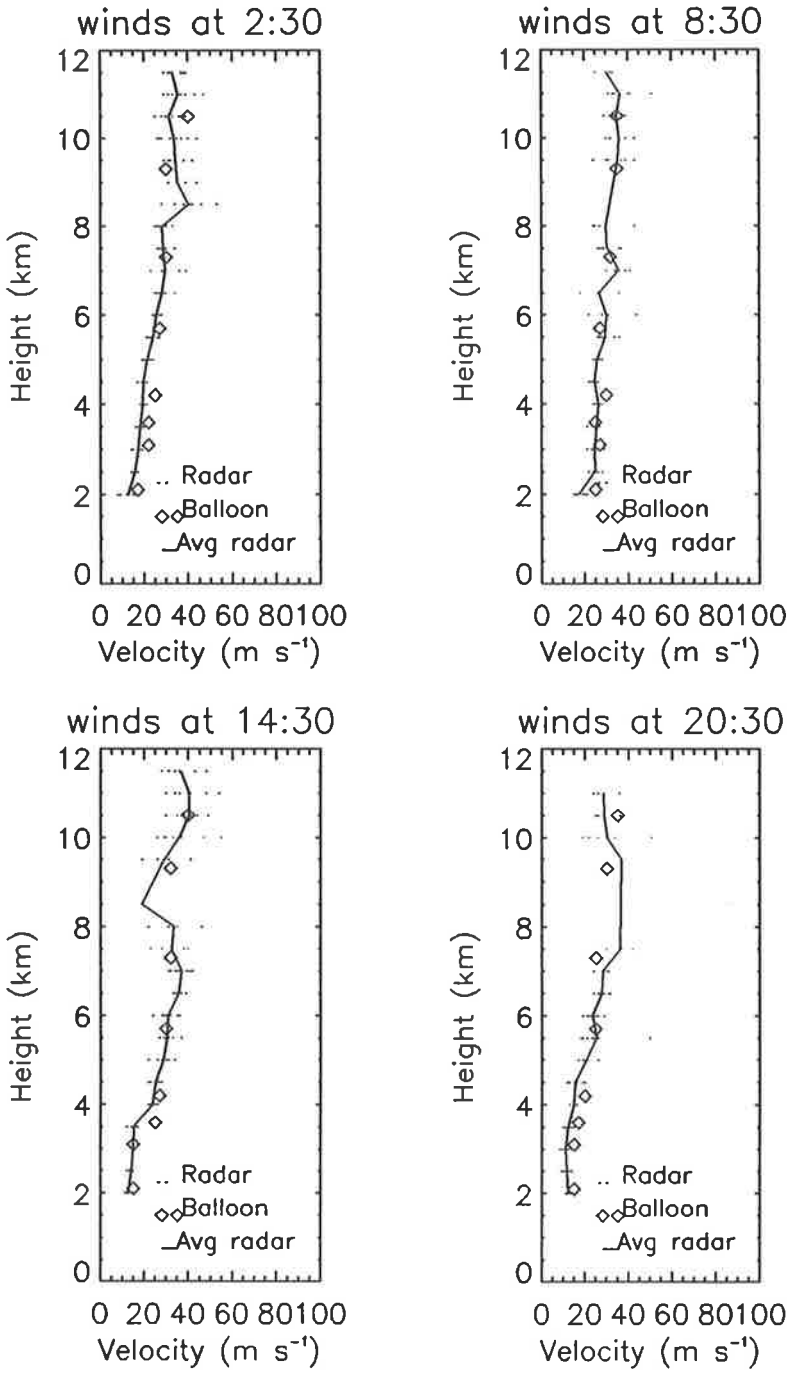

Figure B.2: As for Fig.B.1 but for 29 August, 1990.

It can be seen that the balloon velocities and radar velocities are very close to each other at all heights, but the balloon velocity is slightly larger than the radar velocity in most cases and this discrepancy increases with increasing height.

The radar measured a maximum velocity of $\sim$ 90 m s^{-1} at 08:30 (LT), but at this time, the balloon measured a smaller velocity. The radar and balloon observations are very close up to wind velocities of 60-70 m s^{-1}.

The large discrepancy for the upper heights may be due to the spatial separation between the balloon position and the radar site (see further discussion in § B.5) and the instantaneous variability in the upper-level wind. At times, the discrepancy may also be due to the movement of the balloon towards the Adelaide Hills. These reach a maximum height of about 700 m to the east of Adelaide and can produce lee waves in the region of the balloon site when the wind is from the south-east or east.

Fig. B.2 is another set of height and time profiles of radar and balloon observations made on 22 August 1990. Here unlike previous plots the velocities are generally less than 50 m s^{-1}. It can be seen that at all heights in all four different time intervals the radar velocity agrees well with the balloon velocity.

These results are in good agreement with the results obtained by other investigators (e.g, Vincent et al., 1987; Weber and Wuertz, 1990 and May, 1993). They found that the RMS difference between the balloon and radar wind velocities is of the order of 1-3 m s^{-1}.

B.4 Wind velocity and direction

A scatter plot of radar wind direction with the balloon wind direction is shown in Fig. B.3 (upper diagram). Here R and B stand for radar and balloon; the subscripts d and v stand for the direction and magnitude of wind velocities respectively. The data from all the heights

ranging from 2 to 11 km for 1 August to 31 August has been included. In many cases there are less data available for the upper heights, especially in the radar data, because measurements with low signal-to-noise ratio have been rejected. If the data are in good agreement with each other, the points should fall in a straight line with slope of unity, passing through the origin.

The clustering of all the points along the line of equality (solid line) shows that the balloon and radar directions are very close to each other. Their RMS difference is 1.01°. The satisfactory agreement can be seen not only in lower heights, but for upper heights too.

However, the agreement for wind direction does not occur for the magnitude of wind velocity, where radar estimates are often less than the balloon velocities. Their RMS difference is 3.73 m s^{-1}. This can be seen clearly in the lower diagram of Fig. B.3, where most of the points lie below the line of equality.

The clustering of points along the line of equality is more pronounced when the velocity is less than 20-30 m s^{-1}. However, when the wind speed is large, there is a greater possibility of having nonuniform wind, causing a departure of the observed wind from the line of equality. If the wind is uniform, a better agreement may be expected between the profiler and balloon observations. However, if the winds are changing rapidly during the averaging time, such agreement is unlikely to occur. Thus variability in atmospheric conditions makes the comparison problem more difficult. It has been suggested that the bias is a sampling problem analogous in some way to velocity aliasing, but not as easy to correct after the fact. Faster sampling may minimise the problem (Holdsworth, 1994, personal communication).

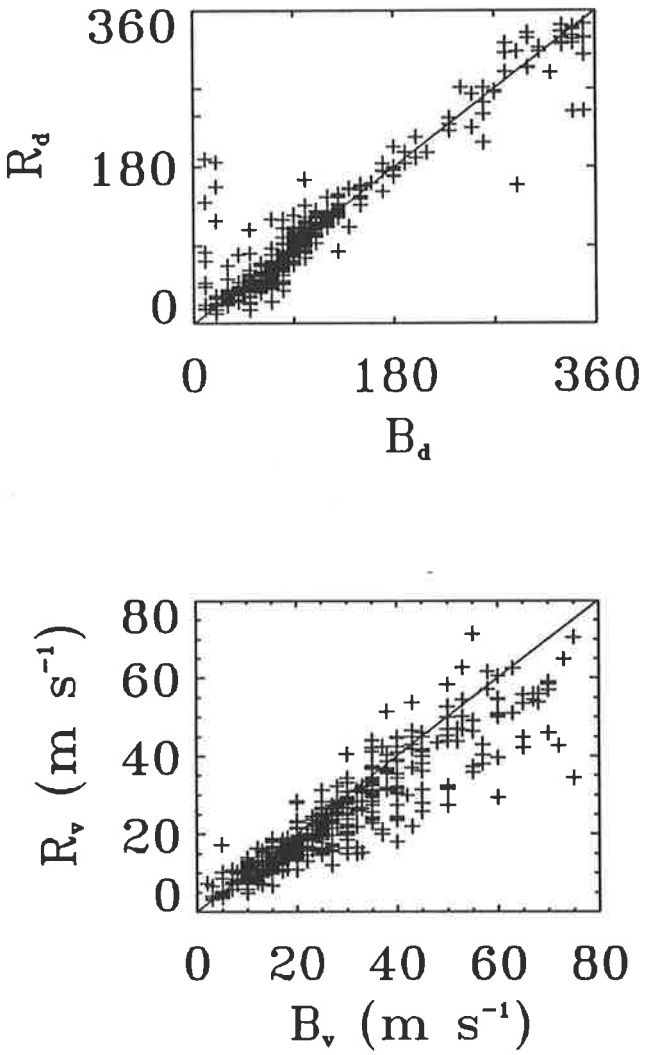

Figure B.3: Scatter plots of balloon and radar velocities observed at all heights during 1-31 August, 1990. The upper plot is for direction and the lower plot for the magnitude of wind velocity. The solid line indicates equal values.

B.5 Effect of horizontal separation

What is the effect of the horizontal separation between the radar site and the position of the balloon during its flight? In general it is expected that the greater the separation, the less likely it will be to get a good agreement between the balloon and radar observations. This aspect has been considered by Jasperson (1982). He found that the RMS difference in wind speed is a function of horizontal separation d and quantified as

$$V_{rms} = f(d^{1/3}). \tag{B.1}$$

Considering this power law separation effect, the RMS difference at the lower heights should be around 4-5 m s^{-1} (May, 1986). The effect will be greater as the balloon ascends to upper heights because the westerly wind (most likely to occur in Adelaide) will rapidly increase the separation d.

Fig. B.4 is a plot of the separation of the balloon from the radar site against the difference of wind velocities between the balloon and radar for all heights and times. Here the radar is at coordinates (0,0). The balloon travelled to a maximum distance of 195 km from the radar site. When the balloon moves towards the radar, the velocity difference tends to be less. In general the larger difference occurs when the balloon goes away from the radar. However, this may be due to the relatively low velocity of the background wind when it happens to blow towards the radar.

To investigate the directional effect, another set of plots is shown in Fig B.5. Here, cases where the balloon is blown towards the radar (i.e. $\pm$ 45° at the line towards the radar) indicated by crosses. When the wind is in this direction, the variation in speed is less than 8 m s^{-1}. However, only a small number of data points are available in the region of $\pm$ 45°

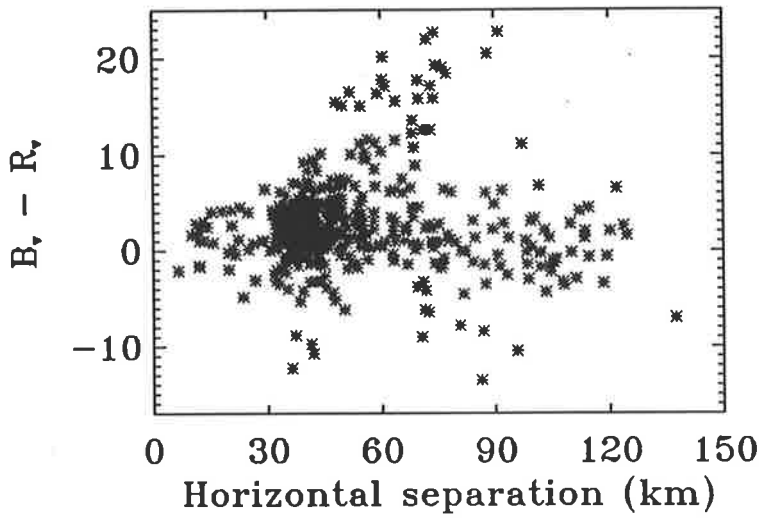

Figure B.4: Scatter plots of difference in balloon velocity (B_v) and radar velocity (R_v) versus the horizontal separation between the radar site and the position of the balloon observed at all heights during 1-31 August, 1990.

towards the radar. So it is not conclusive that the separation effect can produced these results.

B.6 Conclusion

Except for lower heights there can be a large discrepancy between the radar and balloon observations. This discrepancy is more pronounced when the velocity exceeds 25 m s^{-1}.

The effect of horizontal separation between the position of the balloon and the radar site is significant. However, in the present study only one month's data is available which is not enough to make a significant conclusion. The validation of the radar-measured wind speed has to be confirmed with a large set of data, for all the seasons of the year. It should be noted, that these results can be from an initial study of some of the possible causes of

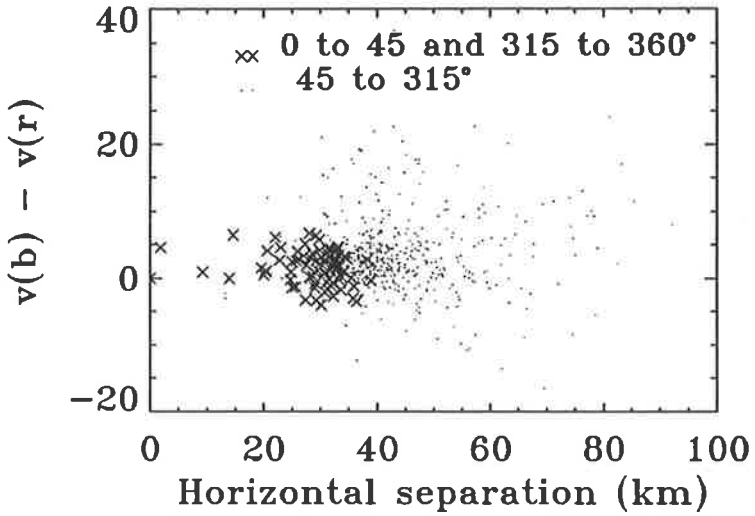

Figure B.5: As for Fig. B.4 but with an indication of the direction of wind velocity

differences between radar and balloon winds. However, the backscattered signal from the atmosphere contains not only information which can be used to obtain winds but may also contain information on precipitation particles. The measured radar power spectrum can be used to obtain the valuable information about the size of the precipitation particles present in the radar volume. So this thesis deals with the retrieval and the use of precipitation information.

Appendix C

Median volume diameter

Referring to Eqn. 3.26, the volume V_1 of water in the diameter range 0 to D_0 is

$$V_1 = \frac{\pi}{6}\int_0^{D_0} D^3 N(D) dD \tag{C.1}$$

and the volume V_2 of water in the diameter range D_0 to ∞ is

$$V_2 = \frac{\pi}{6}\int_{D_0}^{\infty} D^3 N(D) dD\,. \tag{C.2}$$

The median volume diameter D_0 divides the drops into two size ranges for which the total water volume is the same. Hence,

$$V_1 = V_2\,. \tag{C.3}$$

Subsituting for $N(D) = N_0 e^{-\lambda d}$, and by simplification, we can arrive at

$$e^{-\lambda D_0}\left(\lambda^3 D_0^3 + 3\lambda^2 D_0^2 + 6\lambda D_0 + 6\right) - 3 = 0\,. \tag{C.4}$$

This eqn is solved by numerical method and the value of D_0 obtained is

$$D_0 = \frac{3.67206}{\lambda}\,. \tag{C.5}$$

Appendix D

A General Approach to the Retrieval of Raindrop Size Distributions from Wind Profiler Doppler Spectra: Modeling Results

This is a reprint of the paper,

D.K.Rajopadhyaya, P.T.May and R.A.Vincent, 1993: A general approach to the retrieval of raindrop size distributions from wind profiler Doppler spectra: Modeling results. *Journal of Atmospheric and Oceanic Technology*, **10**, 710-717.

Rajopadhyaya, D.K., May, P.T., and Vincent, R.A., (1993) A general approach to the retrieval of raindrop size distributions from wind profiler doppler spectra: modeling results.
Journal of Atmospheric and Oceanic Technology, v. 10 (5), pp. 710-717.

Appendix E

The Retrieval of Ice Particle Size Information from VHF Wind Profiler Doppler Spectra

This is a reprint of the paper,

D.K.Rajopadhyaya, P.T.May and R.A.Vincent, 1994: The retrieval of ice particle size information from VHF wind profiler Doppler spectra. *Journal of Atmospheric and Oceanic Technology*, (in press).

Rajopadhyaya, D.K., May, P.T., and Vincent, R.A., (1994) The retrieval of ice particle size information from VHF wind profiler doppler spectra.
Journal of Atmospheric and Oceanic Technology, v. 11 (6), pp. 1559-1568.

References

Arking, A., 1991: The radiative effects of clouds and their impact on climate. *Bull. Ame. Meteo. Soc.*, **72**, 795-813.

Atlas, D., R.C.Srivastava, and R.S.Sekhon, 1973: Doppler radar characteristics of precipitation at vertical incidence. *Rev. Geophys Space Physics*, **11**, 1-35.

Atlas, D. and C.W.Ulbrich, 1977: Path- and area-integrated rainfall measurement by micro-wave attenuation in the 1-3 cm band. *Journal of Applied Meteorology*, **16**, 1322-1331.

Atlas, D., C.W.Ulbrich, and R.Meneghini, 1984: The multi parameter remote measurement of rainfall. *Radio Science*, **19**, 3-22.

Awe, O., 1964a: Errors in correlation between time series. *Journal of Atmospheric and Terrestrial Physics*, **26**, 1239-1256.

Awe, O., 1964b: Effects of errors in correlation on the analysis of the fading of radio waves. *Journal of Atmospheric and Terrestrial Physics*, **26**, 1257-1271.

Bailey, D.K., R.Bateman, L.V. Berkner, H.G. Booker, G.F.Montgomery, E.M.Purcell, W.W.Salisbury and J.B.Weisner, 1952: A new kind of radio propagation at very high frequencies observable over long distances. *Phys. Rev.*, **86**, 141-145.

Balsley, B.B., W.L.Ecklund, D.A.Carter, A.C.Riddle and K.S.Gage, 1988: Average vertical motions in the tropical atmosphere observed by a radar wind profiler on Pohnpei (7°N latitude, 157°E longitude). *Journal of the Atmospheric Sciences*, **45**, 396-405.

Barnes, G.M. and K.Sieckman, 1984: The environment of fast- and slow-moving tropical mesoscale convective cloud lines. *Mon. Weath. Rev.*, **112**, 1782-1794.

Battan, L.J., 1964: Some observations of vertical velocities and precipitation sizes in a thunderstorm. *Journal of Applied Meteorology*, **3**, 415-420.

Bean, B.R. and E.J.Dutton, 1968: *Radio Meteorology*, US Government printing office, Washington D.C.

Beard, K.V., 1985: Simple altitude adjustments to raindrop velocities for Doppler radar analysis. *Journal of Atmospheric and Oceanic Technology*, **2**, 468-471.

Beard, K.V. and A.J.Heymsfield, 1988: Terminal velocity adjustment for plate-like crystals and graupel. *Journal of the Atmospheric Sciences*, **45** 3515-3518.

Beard, K.V., D.B.Johnson and A.R.Jameson, 1983: Collisional forcing of raindrop oscillations. *Journal of the Atmospheric Sciences*, **40**, 455-462.

Beard, K.V., R.J.Kubesh and H.T.Ochs(III), 1991: Laboratory measurements of small raindrop distortion. I. Axis ratios and fall behaviour. *Journal of the Atmospheric Sciences*, **48**, 698-710.

Beard, K.V. and H.R.Pruppacher, 1969: A determination of the terminal velocity and drag of small water drops by means of a wind tunnel. *Journal of the Atmospheric Sciences*, **26**, 1066-1072.

Bevington, P.R., 1969: Data reduction and error analysis for the physical sciences, least-square fit to an arbitrary function. *McGraw-Hill*, pp 204-214.

Beynon, W.J.G., 1975: Marconi, radio waves, and the ionosphere. *Radio Science*, **10**, 657-664.

Beynon, W.J.G. and J.C.Wright, 1969a: Ionospheric drift measurements on adjacent aerial arrays. *Journal of Atmospheric and Terrestrial Physics*, **31**, 119-133.

Beynon, W.J.G. and J.C.Wright, 1969b: The analysis of ionospheric drift data in the closely spaced receiver method. *Journal of Atmospheric and Terrestrial Physics*, **31**, 593-596.

Bluestein, H.B. and M.H.Jain, 1985: Formation of mesoscale lines of precipitation: Severe squall lines in Oklahoma during the spring. *Journal of the Atmospheric Sciences*, **42**, 1711-1732.

Bowles, K.L., 1958: Observation of vertical incidence scatter from the ionosphere at 41 Mc/sec. *Phy. Res. Lett.*, **1**, 454-455.

Boyenval, E.H., 1960: Echoes from precipitation using pulsed Doppler radar. *Proc. 8th Weather radar conference*, Boston, Amer. Metor. soc., 57-64.

Bracewell, R.N., 1978: The fourier transform and its application. McGraw-Hill, New York, pp 444.

Braham, R.R., 1990: Snow particle size spectra in lake effect snows. *Journal of Applied Meteorology*, **29**, 200-207.

Briggs, B.H., 1968: On the analysis of moving patterns in geophysics–I. Correlation analysis. *Journal of Atmospheric and Terrestrial Physics*, **30**, 1777-1788.

Briggs, B.H., 1980: Radar observations of atmospheric winds and turbulence: A comparison of techniques. *Journal of Atmospheric and Terrestrial Physics*, **42**, 823-833.

Briggs, B.H., 1984: The analysis of spaced sensor records by correlation techniques. *Handbook for MAP*, ed. R.A.Vincent, **13**, 166-186, SCOSTEP Secr., Univ. of Ill., Urbana.

Briggs, B.H., G.J.Phillips, and D.H.Shinn, 1950: The analysis of observations on spaced receivers of the fading radio signal. *Pro. Roy. Soc. London*, B63:106.

Brown, J.M., 1974: Mesoscale motions induced by cumulus convection: A numerical study. *Ph.D. thesis, MIT*, pp 206.

Brown, J.M., 1979: Mesoscale unsaturated downdrafts driven by rainfall evaporation: A numerical study. *Journal of the Atmospheric Sciences*, **36**, 313-338.

Brown, P.S., Jr., 1988: The effects of filament, sheet and disk breakup upon the drop spectrum. *Journal of the Atmospheric Sciences*, **45**, 712-718.

Brown, S.R., 1970: Terminal velocities of ice crystals. *M.S. thesis*, Colorado State University, pp 52.

Buckley, R., 1971: Some notes on practical digital power spectral and auto- and cross-correlation analysis using the FFT. *Department of Physics Report*, University of Adelaide.

Caton, P.G.F., 1963: Measurement of wind and convergence of Doppler radar. *Proc. Tenths Weather Radar Conf.*, Washington DC, Amer. Meteor. Soc. 290-296.

Caton, P.G.F., 1966: A study of raindrop-size distributions in the free atmosphere. *Quarterly Journal of the Royal Meteorological Society*, **92**, 15-30.

Chandra, H., M.R. Deshppande, and R. C. Rastogi, 1972: Errors in the correlation analysis of ionospheric drift records. *J. of the Institute of Telecommunication Engineers*, New Delhi, **18**, 340.

Cheng, C-P and R.A.Houze, Jr., 1979: The distribution of Convective and Mesoscale precipitation in GATE radar echo Patterns. *Mon. Weath. Rev.*, **107**, 1370-1381.

Chong, M., P.Amayenc, G.Scialom, and J.Testud, 1987: A tropical squall line observed during the COPT 81 experiment in West Africa. Part I: Kinematic structure inferred from dual-Doppler radar data. *Mon. Weath. Rev.*, **115**, 670-694.

Cifelli, R. and S.A.Rutledge, 1993: Vertical motion structure in maritime continent mesoscale convective systems: Results from a 50 MHz profiler. *Journal of the Atmospheric Sciences*, (Submitted manuscript).

Cooper, M.J., 1977: Deconvolution: If in doubt, don't do it. *Physics Bulletin*, 463-466.

Cornford, S.G., 1965: Fall speeds of precipitation elements. *Quarterly Journal of the Royal Meteorological Society*, **91**, 91-94.

Currier, P.E., S.K.Avery, B.B.Balsley, K.S.Gage, and W.L.Ecklund, 1992: Combined use of 50 MHz and 915 MHz wind profilers in the estimation of raindrop size distributions. *Geophysical Research Letters*, **19**, 1017-1020.

Doviak, R.J., and D.S.Zrnic, 1984: Doppler radar and weather observations. *Academic Press*, New York, 184-191.

Dowling, D.R. and L.F.Radke, 1990: A summary of the physical properties of cirrus clouds. *Journal of Applied Meteorology*, **29**, 970-979.

Drosdowsky, W., 1984: Structure of a northern Australian squall line system. *Aus. Meteo. Mag.*, **32**, 177-183.

Du Toit, P.S., 1967: Doppler radar observations of drop sizes in continuous rain. *Journal of Applied Meteorology*, **6**, 1082-1087.

Fedor, L.S., 1967: A statistical approach to the determination of 3-dimensional ionospheric drifts. *Journal of Geophysical Research*, **72**, 5401-5415.

Fedor, L.S., and W.Plywaski, 1972: The interpretation of ionospheric radio drift measurements. IV-The effects of signal coupling among spaced sensor channels. *Journal of Atmospheric and Terrestrial Physics*, **34**, 1285-1303.

Felgate, D.G., 1970: On the point source effect in the measurement of ionospheric drifts. *Journal of Atmospheric and Terrestrial Physics*, **32**, 241-245.

Flock, W.L. and B.B.Balsley, 1967: VHF radar returns from the D-region of the equatorial ionosphere. *Journal of Geophysical Research*, **72**, 5537-5541.

Foote, G.B. and P.S. duToit, 1967: Terminal velocity of raindrop aloft. *Journal of Applied Meteorology*, **8**, 249-253.

Fovell, R.G., and Y.Ogura, 1988: Numerical simulation of a midlatitude squall line in two dimensions. *Journal of the Atmospheric Sciences*, **45**, 3846-3879.

Friend, A.W., 1949: Theory and practice of tropospheric sounding by radar. *Proc. IEEE*, **37**, 116-138.

Fukao, S., T.Sato, N.Yamasaki, R.M.Harper and S.Kato, 1982: Winds measured by a UHF Doppler radar and rawinsondes: Comparisons made on 26 days (August-September, 1977) at Arecibo, Puerto Rico. *Journal of Applied Meteorology*, **21**, 1357-1363.

Fukao, S., K.Wakasugi, T.Sato, S.Morimoto, T.Tsuda, I.Hirota, I.Kimura, and S.Kato, 1985: Direct measurement of air and precipitation particle motion by VHF Doppler radar. *Nature*, **316**, 712-714.

Gage, K.S. and B.B.Balsley, 1980: On the scattering and reflection mechanisms contributing to clear air radar echoes from the troposphere, stratosphere, and mesosphere. *Radio Science*, **15**, 243-257.

Gage, K.S., and J.L.Green, 1978: Evidence for specular reflection from monostatic VHF radar observations of the stratosphere. *Radio Science*, **13**, 991-1001.

Gamache, J.F. and R.A.Houze, Jr., 1982: Mesoscale air motions associated with a tropical squall line. *Mon. Weath. Rev.*, **110**, 118-135.

Gamache, J.F. and R.A.Houze, Jr., 1983: Water budget of a mesoscale convective system in the tropics. *Journal of the Atmospheric Sciences*, **40**, 1835-1850.

Gamache, J.F. and R.A.Houze, Jr., 1985: Further analysis of the composite wind and thermodynamic structure of the 12 September GATE squall line. *Mon. Weath. Rev.*, **113**, 1241-1259.

Gokhale, N.R. and J.Goold, 1968: Ice-nucleating properties of meteoritic material and

soil particles. *Proceedings of the International conference on cloud physics*, Toronto, Canada.

Golley, M.G. and D.E.Rossiter, 1970: Some tests of methods of analysis of ionospheric drift records using an array of 89 aerials. *Journal of Atmospheric and Terrestrial Physics*, **32**, 1215-1233.

Gorelik, A.G., I.V.Gritskiv, L.A.Penyax and V.V.Tsykunov, 1967: Results of simultaneous radar and ground measurements of the microstructure of precipitation. *Izv. Akad. Nauk SSSR, Ser. Fiz. Atmos. Okeana*, **3**, 961-966.

Gori, E.G. and S.G.Geotis, 1981: Comparison of raindrop size distributions observed in New England and Switzerland. *20th conf. on radar meteor.*, Boston, Ame. Meteor. Soc., 282-286.

Gossard, E.E., 1988: Measuring drop-size distributions in clouds with a clear-air-sensing Doppler radar. *Journal of Atmospheric and Oceanic Technology*, **5**, 640-649.

Gossard, E.E. and R.G.Strauch, 1983: Radar observation of clear air and clouds. *Elsevier Amsterdam*, Oxford, New York.

Gossard, E.E., R.G.Strauch, and R.R.Rogers, 1990: Evolution of dropsize distributions in liquid precipitation observed by ground-based Doppler radar. *Journal of Atmospheric and Oceanic Technology*, **7**, 815-828.

Gossard, E.E., R.G.Strauch, D.C.Welsh, and S.Y.Matrosov, 1992: Cloud layers, particle identification, and rain-rate profiles from ZRV_f measurements by clear-air Doppler radars. *Journal of Atmospheric and Oceanic Technology*, **9**, 108-119.

Gunn, B.W., J.L.McBride, G.J.Holland, T.D.Keenan, N.E.Davidson, and H.H.Hendon, 1989: The Australian summer monsoon circulation during AMEX phase II. *Mon. Weath. Rev.*, **117**, 2554-2574.

Gunn, K.L.S., 1967: The number flux of snow crystals at the ground. *Mon. Weath. Rev.*, **95**, 921-924.

Gunn, K.L.S., and J.S.Marshall, 1958: The distribution with size of aggregate snowflakes. *J. Meteo.*, **15**, 452-461.

Gunn, R., and G.D.Kinzer, 1949, The terminal velocity of fall for water droplets in stagnant air. *J. Meteo.*, **6**, 243-248.

Harnischmacher, E. and K.Rawer, 1963: Research on Ionospheric structure and motion. AF 61 (052)-81, Ionospharen Institute, Breisach.

Heymsfield, A.J., 1972: Ice crystal terminal velocities. *Journal of the Atmospheric Sciences*, **29**, 1348-1357.

Heymsfield, A.J., and L.J.Donner, 1990: A scheme for parameterizing ice-cloud water content in general circulation models. *Journal of the Atmospheric Sciences*, **47**, 1865-1877.

Heymsfield, A.J., and M.Kajikawa, 1987: An improved approach to calculating terminal velocities of plate-like crystals and graupel. *Journal of the Atmospheric Sciences*, **44**, 1088-1099.

Heymsfield, G.M. and S.Schotz, 1985: Structure and evolution of a severe squall line over Oklahoma. *Mon. Weath. Rev.*, **113**, 1563-1589.

Hocking, W.K., 1983: On the extraction of atmospheric turbulence parameters from radar backscatter Doppler spectra. 1 Theory. *Journal of Atmospheric and Terrestrial Physics*, **45**, 89-102.

Hocking, W.K., 1988: Lecture notes: Target parameter estimation. *International school on atmospheric radars*, ed. S.Fukao, Kyoto.

Hocking, W.K., P.May, and J.Rottger, 1989: Interpretation, reliability and accuracies of parameters deduced by the spaced antenna method in middle atmosphere applications. *PAGEOPH*, **130**, 571-604.

Hoehne, W.E., 1980: Precision of national weather service upper air measurements. *NOAA Tecl Memo*, NWS TED-16.

Holdsworth, D., 1994: Private communication. *Dept. of Phys.*, The University of Adelaide.

Holroyd, E.W.III and J.E.Jiusto, 1971: Snowfall from a heavily seeded cloud. *Journal of Applied Meteorology*, **10**, 266-269.

Houze, R.A.Jr., 1977: Structure and dynamics of a tropical squall-line system. *Mon. Weath. Rev.*, **105**, 1540-1567.

Houze, R.A.Jr., 1982: Cloud clusters and large-scale vertical motions in the tropics. *Journal of the Meteorological Society of Japan*, **60**, 396-410.

Houze, R.A.Jr., 1989: Observed structure of mesoscale convective systems and implications for large-scale heating. *Quarterly Journal of the Royal Meteorological Society*, **115**, 425-461.

Houze, R.A.Jr. and A.K.Betts, 1981: Convection in GATE. *Rev. Geophys Space Physics*, **19**, 541-576.

Houze, R.A.Jr. and D.D.Churchill, 1987: Mesoscale organization and cloud microphysics in a Bay of Bengal depression. *Journal of the Atmospheric Sciences*, **44**, 1845-1867.

Imai, I., 1950: On the velocity of falling rain drops. *Journal of the Meteorological Society of Japan*, **28**, 113-118.

Jasperson, W.H., 1982: Mesoscale time and space wind variability. *Journal of Applied Meteorology*, **21**. 831-839.

Johnson, D.B. and K.V.Beard, 1984: Oscillation energies of colliding raindrops. *Journal of the Atmospheric Sciences*, **41**, 1235-1241.

Johnson, R.H., W.A.Gallus, M.D.Vescio, 1990: Near-tropopause vertical motion within the trailing stratiform region of a midlatitude squall line. *Journal of the Atmospheric Sciences*, **47**, 2200-2210.

Jiusto, J.E. and G.E.Bosworth, 1971: Fall velocity of Snowflakes. *Journal of Applied Meteorology*, **10**, 1352-1354.

Jiusto, J.E. and H.K.Weickmann, 1973: Types of snowfall. *Bull. Ame. Meteo. Soc.*, **54**, 1148-1162.

Joss, J. and E.G.Gori, 1978: Shapes of raindrop size distributions. *Journal of Applied Meteorology*, **17**, 1054-1061.

Joss, J., and A.Waldvogel, 1970: A method to improve the accuracy of radar measured amounts of precipitation. *14th Radar meteor. conf.*, 237-238.

Kajikawa, M., 1972: Measurement of falling velocity of individual snow crystals. *Journal of the Meteorological Society of Japan*, **50**, 577-583.

Kajikawa, M., 1975: Experimental formula of falling velocity of snow crystals. *Journal of the Meteorological Society of Japan*, **53**, 267-275.

Kajikawa, M., 1982: Observation of the falling motion of early snowflakes. Part I: Relationship between the Free-fall pattern and the number and shape of component snow crystals. *Journal of the Meteorological Society of Japan*, **60**, 797-803.

Kajikawa, M., 1989: Observation of the falling motion of early snowflakes. Part II: on the variation of falling velocity. *Journal of the Meteorological Society of Japan*, **67**, 731-737.

Kajikawa, M., 1992: Observation of the falling motion of plate-like snow crystals Part I: The free-fall patterns and velocity variations of unrimed crystals. *Journal of the Meteorological Society of Japan*, **70**, 1-9.

Keenan, T.D. and R.E.Carbone, 1992: A preliminary morphology of precipitation systems in tropical northern Australia. *Quarterly Journal of the Royal Meteorological Society*, **118**, 283-326.

Keenan, T.D., B.R.Morton, M.J.Manton, and G.J.Holland, 1989: The Island Thunderstorm Experiment (ITEX)-A study of tropical thunderstorms in the maritime continent. *Bull. Ame. Meteo. Soc.*, **70**, 152-159.

Keenan, T.D. and S.A.Rutledge, 1993: Mesoscale characteristics of monsoonal convection and associated stratiform precipitation. *Mon. Weath. Rev.*, **121**, 352-374.

Kelleher, R.F., 1966: Some statistical properties of the ground diffraction patterns of vertically reflected radio waves. *Journal of Atmospheric and Terrestrial Physics*, **28**, 213-224.

Kepler, J., 1966: The six-cornered snowflake. *Clarendon press*, Oxford.

Kumai, M. and K.Itagaki, 1954: Shape and fall velocity of rain drops. *Journal of the Meteorological Society of Japan*, **32**, 11-18.

LaLonde, L.M., 1966: Incoherent backscatter observations of sporadic E. *Journal of Geophysical Research*, **71**, 5059-5065. Langleben, M.P., 1954: The terminal velocity of snowflakes. *Quarterly Journal of the Royal Meteorological Society*, **80**, 174-181.

Larsen, M.F., 1983: Can a VHF Doppler radar provide synoptic wind data? A comparison of 30 days of radar and radiosonde data. *Mon. Weath. Rev.*, **111**, 2047-2057.

Leary, C.A. and R.A.Houze, Jr., 1979: The structure and evolution of convection in a tropical cloud cluster, *Journal of the Atmospheric Sciences*, **36**, 437-457.

Laws, J.O., 1941: Measurements of the fall-velocity of water-drops and rain-drops. *Trans. Am. Geophys. Un.*, **22**, 595-597.

Lhermitte, R., 1960: The use of special "pulsed Doppler radar" in measurements of particle fall velocities. *Proc. 8th Wea. Radar Conf.*, San Francisco, Amer. Meteor. Soc., 269-275.

Lin, Y-L, R.D.Farley and H.D.Orville, 1983: Bulk parameterization of the snow field in a cloud model. *J. of Cli. and App. Meteo.*, **22**, 1065-1092.

List, R., N.R.Donaldson, and R.E.Stewart, 1987: Temporal evolution of drop spectra to collisional equilibrium in steady and pulsating rain. *Journal of the Atmospheric Sciences*, **44**, 362-372.

List, R, D. Hudak, R. Nissen, N. P. Tung, S. K. Soo and T. S. Kang, 1988: Results from warm rain studies in Penang, Malaysia. *Proc. 10th Inter. Cloud Conf.*, Bad Homburg, Germany, 446-448.

List, R., and G.McFarquhar, 1990: The role of breakup and coalescence in the three-peak equilibrium distribution of raindrops. *Journal of the Atmospheric Sciences*, **47**, 2274-2292.

Litvinov, I.V., 1956: Determination of falling velocity of snow particles. *Izv. Akad. Nauk SSSR, Ser. Fiz. Atmos. Okeana*, **7**, 853-856.

Locatelli, J.D., and P.V.Hobbs, 1974: Fall speeds and masses of solid precipitation particles. *Journal of Geophysical Research*, **79**, 2185-2197.

Low, T.B. and R.List, 1982: Collision coalescence and breakup of raindrops. Part I: Experimentally established coalescence efficiencies and fragment size distributions in breakup. *Journal of the Atmospheric Sciences*, **39**, 1591-1606.

Maddox, R.A., 1980: Mesoscale convective complexes. *Bull. Ame. Meteo. Soc.*, **61**, 1374-1387.

Magono, C., 1951: On the fall velocity of snowflakes. *J. Meteo.*, **8**, 199-200.

Magono, C., 1953: On the growth of snowflakes and graupel. *Sci. Repts*, Yokohama, Natl. Univ., Ser 1, **2**, 18-40.

Magono, C., and C.V.Lee, 1966: Meteorological classification of natural snow crystals. *J. Fac. Sci., Hokkaido Univ.*, Ser 7, **2**, 321-335.

Magono, C., and T.Nakamura, 1965: Aerodynamic studies of falling snowflakes. *Journal of the Meteorological Society of Japan*, Ser 2, **43**, 139-147.

Marshall, J.S., W.Hitschfeld, K.Gunn, 1955: Advances in radar weather. *Adv. in Geophy.*, **2**, Academic Press, New York.

Marshall, J.S. and W.M.Palmer, 1948: The distributions of raindrops with size. *J. Meteo.*, **5**, 165-166.

Mason, B.J., 1971: The physics of clouds. *Clarendon Press*, Oxford.

Matrosov, S.Y. and R.A.Kropfli, 1993: Cirrus cloud studies with elliptically polarized Ka-band radar signals: A suggested approach. *Journal of Atmospheric and Oceanic Technology*, **10**, 684-692.

May, P.T., 1986: VHF radar studies of the troposphere. *Ph.D. thesis*, Univeristy of Adelaide, Australia.

May, P.T., 1988: Statistical errors in the determination of wind velocities by the spaced antenna technique. *Journal of Atmospheric and Terrestrial Physics*, **50**, 21-32.

May, P.T., 1990: Spaced antenna versus Doppler radars: A comparison of techniques revisited. *Radio Science*, **25**, 1111-1119.

May, P.T., 1991: Recent developments and performance of radar wind profilers and RASS. *Aus. Meteo. Mag.*, **39**, 237-245.

May, P.T., 1993: Comparison of wind-profiler and radiosonde measurements in the tropics. *Journal of Atmospheric and Oceanic Technology*, 10, 122-127.

May, P.T., and R.G.Strauch, 1989: An examination of wind profiler signal processing algorithms. *Journal of Atmospheric and Oceanic Technology*, **6**, 731-735.

McDonald, J.E., 1960: An aid to computation of terminal fall velocities of spheres. *J. Meteo.*, **17**, 463-465.

Mossop, S.C., R.E.Cottis and B.M.Bartlett, 1972: Ice crystal concentrations in cumulus and stratocumulus clouds. *Quarterly Journal of the Royal Meteorological Society*, **98**, 105-123.

Mossop, S.C. and A.Ono, 1969: Measurements of ice crystal concentration in clouds. *Journal of the Atmospheric Sciences*, **26**, 130-137.

Nakaya, U., 1954: Snow crystals, natural and artificial. *Harvard University press.*

Nakaya, U., and T.Terada, 1935: Simultaneous observation of the mass, falling velocity and form of snow crystals. *J. Fac. Sci., Hokkaido Univ.*, Ser 2, **1**, 191-201.

Ottersten, H., 1969: Mean vertical gradient of potential refractive index in turbulent mixing and radar detection of CAT. *Radio Science*, **4**, 1247-1249.

Passarelli, R.E., 1978: Theoretical and observational study of snow-size spectra and snowflake aggregation efficiencies. *Journal of the Atmospheric Sciences*, **35**, 882-889.

Passarelli, R.E. and R.C.Srivastava, 1979: A new aspect of snowflake aggregation theory. *Journal of the Atmospheric Sciences*, **36**, 484-493.

Phillips, J.G., and M.Spencer, 1955: The effects of anisometric amplitude patterns in the measurement of ionospheric drifts. *Proceedings of the Physical Society*, **68B**, 481-492.

Probert-Jones, J.R., 1960: The analysis of Doppler radar echoes from precipitation. *Proc. 8th Wea. Radar Conf.*, Boston, Amer. Metor. Soc., 347-354.

Pruppacher, H.R., and J.D.Klett, 1978: Microphysics of clouds and precipitation. *D. Reidel Publishing Company*, pp 6-22.

Rajopadhyaya, D.K., P.T.May, and R. A. Vincent, 1993: A general approach to the retrieval of rain dropsize distributions from wind profiler Doppler spectra: modeling results. *Journal of Atmospheric and Oceanic Technology*, **10**, 710-717.

Ratcliffe, J.A., 1954: The analysis of fading records from spaced receivers. *Journal of Atmospheric and Terrestrial Physics*, **5**, 173-181.

Reynolds, S.E., 1952: Ice-crystal growth. *J. Meteo.*, **6**, 36-40.

Rogers, R., 1967: Doppler radar investigation of Hawaiian rain. *Tellus*, **19**, 432-455.

Rogers, R.R., D.Baumgardner, S.A. Ethier, D.A.Carter, and W.L.Ecklund, 1993: Comparison of raindrop size-distributions measured by radar wind profiler and by airplane. *Journal of Applied Meteorology*, **32**, 694-699.

Rogers, R.R. and R.J.Pilie, 1962: Radar measurements of dropsize distribution. *Journal of the Atmospheric Sciences*, **19**, 503-506.

Rogers, R.R. and M.K.Yau, 1991: A short course in cloud physics, Rain and Snow. *Pergamon press*, pp 170-183.

Rottger, J., 1984: The MST radar technique. *MAP handbook*, 13, ed. R.A.Vincent, 150-163.

Rottger, J. and C.H.Liu, 1978: Partial reflection and scattering of VHF radar signals from the clear atmosphere. *Geophysical Research Letters*, **5**, 357-360.

Rottger, J. and R.A.Vincent, 1978: VHF radar studies of tropospheric velocities and irregularities using spaced antenna techniques. *Geophysical Research Letters*, **5**, 917-920.

Rotunno, R., J.B.Klemp and M.L.Weisman, 1988: A theory of strong, long-lived squall lines. *Journal of the Atmospheric Sciences*, **45**, 463-485.

Royrvik, O., 1982: Drift and aspect sensitivity of scattering irregularities in the upper equatorial E region. *Journal of Geophysical Research*, **87**, 8338-8342.

Rutledge, S.A., 1986: A Diagnostic modeling study of the stratiform region associated with a tropical squall line. *Journal of the Atmospheric Sciences*, **43**, 1356-1377.

Sato, T., H. Doji, H.Iwai, I.Kimura, S.Fukao, M.Yamamoto, T.Tsuda and S.Kato, 1990: Computer processing for deriving drop-size distributions and vertical air velocities from VHF doppler radar spectra. *Radio Science*, **25**, 961-973.

Sekhon, R.S. and R.C.Srivastava, 1970: Snow size spectra and radar reflectivity. *Journal of the Atmospheric Sciences*, **27**, 299-307.

Smull, B.F. and R.A.Houze, Jr., 1987: Dual-Doppler radar analysis of a midlatitude squall line with a trailing region of stratiform rain. *Journal of the Atmospheric Sciences*,

44, 2128-2148.

Solvang, G., A.Brekke, and A.Haug, 1977: Auroral zone E-region motions deduced from spaced receiver observations. *Journal of Atmospheric and Terrestrial Physics*, **39**, 823-831.

Srivastava, R.C., T.J.Matejka, and T.J.Lorello, 1986: Doppler radar study of the trailing anvil region associated with a squall line. *Journal of the Atmospheric Sciences*, **43**, 356-377.

Steiner, M. and A.Waldvogel, 1987: Peaks in raindrop size distributions. *Journal of the Atmospheric Sciences*, **44**, 3127-3133.

Stewart, R.E., J.D.Marwitz, J.C.Pace and R.E.Carbone, 1984: Characteristics through the melting layer of stratiform clouds. *Journal of the Atmospheric Sciences*, **41**, 3227-3237.

Strauch, R.G., 1983: Techniques for measurement of horizontal and vertical velocities: Optimum pointing angle. *Handbook for MAP*, **9**, 232-234, ed. S.A.Bowhill and B.Edwards, SCOSTEP Secr., Dep. Elec. Eng., Univ. IL, Urbana.

Swords, S.S., 1986: Technical history of the beginnings of radar. *Peter Peregrinus Ltd, IEE History of Techno. Ser. 6*, London.

Tatarski, V.I., 1961: Wave propagation in a turbulent medium. *McGraw Hill*, New York.

Tennekes, H., and J.L.Lumley, 1973: A first course in turbulence. *MIT Press*, pp 300.

Tsuda, T., T.Sato, K.Hirose, S.Fukao and S.Kato, 1986: MU radar observations of the aspect sensitivity of backscattered VHF echo power in the troposphere and lower

stratosphere. *Radio Science*, **21**, 971-980.

Ulbrich, C.W., 1983: Natural variations in the analytical form of the rain drop size distribution. *J. of Cli. and App. Meteo.*, **22**, 1764-1775.

Valdez, M.P. and K.C.Young, 1985: Number fluxes in equilibrium raindrop populations. A Markov chain analysis. *Journal of the Atmospheric Sciences*, **42**, 1024-1036.

Villars, F. and V.F.Weisskopf, 1955: On the scattering of radio waves by turbulent fluctuations of the atmosphere. *Proc. IRE*, **43**, 1232-1239.

Vincent, R.A., 1984: Relationship of spaced antenna and Doppler techniques for velocity measurement. *Handbook for MAP*, ed. S. A. Bowhill and B. Edwards, **14**, 126-130, SCOSTEP Secr., Univ. of Ill., Urbana.

Vincent, R.A., P.T.May, W.K.Hocking, W.G.Elford, B.H.Candy and B.H.Briggs, 1987: First results with the Adelaide VHF radar: Spaced antenna studies of tropospheric winds. *Journal of Atmospheric and Terrestrial Physics*, **49**, 353-366.

Volz, F.E., 1960: Some aspects of the optics of the rainbow and the physics of rain. Physics of precipitation. *Amer. Geophys. Union*, Washington, DC, 280-286.

Wakasugi, K., A.Mizutani, M.Matsuo, S.Fukao and S.Kato, 1986: A direct method for deriving drop-size distribution and vertical air velocities from VHF doppler radar spectra. *Journal of Atmospheric and Oceanic Technology*, **3**, 623-629.

Wakasugi, K., A.Mizutani, M.Matsuo, S.Fukao and S.Kato, 1987: Further discussion on deriving drop-size distribution and vertical air velocities directly from VHF Doppler radar spectra. *Journal of Atmospheric and Oceanic Technology*, 4, 170-179.

Waldvogel, A., 1974: The N_0 jump of raindrop spectra. *Journal of the Atmospheric Sciences*, **31**, 1067-1078.

Weber, B.L. and D.B.Wuertz, 1990: Comparison of rawinsonde and wind profiler radar measurements. *Journal of Atmospheric and Oceanic Technology*, **7**, 157-174.

Wei, T. and R.A.Houze, 1987: The GATE squall line of 9-10 August 1974. *Adv. Atmo. Sci.*, **4**, 85-92.

Weickmann, H.K., 1947: Die eisphase inder atmosphare. *Reports and translation*, 716. (Volkenrode), Ministry of Supply, London. (173, 175-177).

Willis, P.T., 1984: Functional fits of observed drops size distributions and parameterization of rain. *Journal of the Atmospheric Sciences*, **41**, 1648-1661.

Wilson, D.A., 1963: Dropsize distribution as recorded by pulsed Doppler radar. *Master's thesis*, University of Arizona.

Woodman, R.F. and A.Guillen, 1974: Radar observations of winds and turbulence in the stratosphere and mesosphere. *Journal of the Atmospheric Sciences*, **31**, 493-505.

Wright, J.R., 1972: The interpretation of inospheric radio drift measurements-V. Demonstration of the point effect in time-averaged correlations and drift calculations. **34**, 1365-1378.

Young, K.C., 1993: Microphysical processes in clouds. Oxford University press.

Zawadzki, I. and M.Antonio, 1988: Equilibrium raindrop size distributions in tropical rain. *Journal of the Atmospheric Sciences*, **45**, 3452-3459.

Ziegler, C.L., 1985: Retrieval of thermal and microphysical variables in observed convective storms Part 1: Model development and preliminary testing. *Journal of the Atmospheric Sciences*, **42**, 1487-1509.

Zikmunda, J, 1972: Fall velocities of spatial crystals and aggregates. *Journal of the Atmospheric Sciences*, **29**, 1511-1515.

Zikmunda, J. and G.Vali, 1972: Fall patterns and fall velocities of rimed ice crystals. *Journal of the Atmospheric Sciences*, **29**, 1334-1347.

Zipser, E.J., 1969: The role of organised unsaturated convective downdrafts in the structure and rapid decay of an equatorial disturbance. *Journal of Applied Meteorology*, **8**, 799-814.

Zipser, E.J., 1977: Mesoscale and convective-scale downdrafts as distinct components of squall-line structure. *Mon. Weath. Rev.*, **105**, 1568-1589.

Zrnic, D.S., 1975: Simulation of weatherlike Doppler spectra and signals. *Journal of Applied Meteorology*, **14**, 619-620.

Zrnic, D.S., N.Balakrishnan, C.L.Ziegler, V.N.Bringi, K.Aydin, and T.Matejka, 1993: Polarimetric Signatures in the stratiform region of a mesoscale convective system. *Journal of Applied Meteorology*, **32**, 678-693.